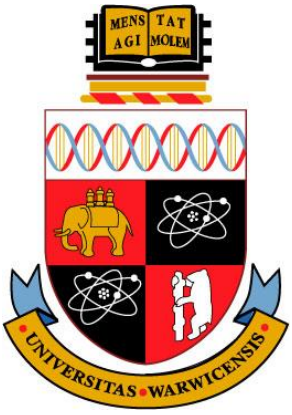

Advanced Electrochemical Techniques for Investigating Electron Transfer Kinetics

by

Sze-yin Tan

Thesis

Submitted to the University of Warwick for a degree of

Doctor of Philosophy

Supervisors: Prof Patrick R. Unwin, Prof Julie V. Macpherson, Dr Jie Zhang and Prof Alan M. Bond

April 2017

MONASH University

WARWICK
THE UNIVERSITY OF WARWICK

To my family

Table of Contents

List of Figures

List of Tables

Abbreviations

1D	One-dimensional
2D	Two-dimensional
3D	Three-dimensional
AC	Alternating current
AFM	Atomic force microscopy
BDD	Boron-doped diamond
CE	Counter electrode
CNT	Carbon nanotube
CV	Cyclic voltammetry
CVD	Chemical vapour deposition
DC	Direct current
DCV	Direct current voltammetry
DOS	Density of states
EDL	Electrical double layer
ET	Electron transfer
$FcCH_2OH$	Ferrocene methanol
$FcTMA^+$	Ferrocenylmethyl trimethylammonium ion
FEM	Finite element method
FTACV	Fourier-transformed large amplitude alternating current voltammetry
GC	Glassy carbon
HOPG	Highly oriented pyrolytic graphite
IC-SECM	Intermittent-contact scanning electrochemical microscopy
LSV	Linear sweep voltammetry
MC	Microcrystalline
NC	Nanocrystalline
Ox	Oxidised form of a redox species
pBDD	Polycrystalline boron-doped diamond
QRCE	Quasi reference counter electrode
Red	Reduced form of a redox species

RE	Reference electrode
SECCM	Scanning electrochemical cell microscopy
SECM	Scanning electrochemical microscopy
SEM	Scanning electron microscopy
SG/TC	Substrate-generation/tip-collection
SICM	Scanning ion conductance microscopy
SMCM	Scanning micropipette contact method
TCNQ	Tetracyanoquinodimethane
TG/SG	Tip-generation/substrate-collection
TLC	Thin layer cell
TTF	Tetrathiafulvalene
UME	Ultramicroelectrode
UNC	Ultra-nanocrystalline
WE	Working electrode

Glossary of Terms

Some symbols are allowed to have multiple definitions as they occur in independent parts of the work.

A	Area of an electrode
a	Radius of an UME
C	Capacitance
C_{dl}	Double layer capacitance
c	Concentration
D	Diffusion coefficient
d	SECM tip-substrate distance
E	Potential
$E^{0'}$	Formal potential of a given redox couple
$E_{1/2}$	Half-wave potential of a steady-state LSV
$E_{1/4}$	Quarter-wave potential of a steady-state LSV
$E_{3/4}$	Three-quarter-wave potential of a steady-state LSV
E_{AC}	AC potential ramp
E_{DC}	DC potential ramp
E_m	Mid-wave potential of a peak shaped CV
e_0	Elementary charge
F	Faradays constant
f	i) Frequency of AC sine wave
	ii) Function
I	Current
i_p	Peak current
J	Flux
K_{ads}	Equilibrium adsorption constant
k^0	Standard rate constant
k_{ox}	Heterogeneous oxidation rate constant
k_{red}	Heterogeneous reduction rate constant

k_t	Mass transport coefficient
L	Normalised distance between the UME tip and substrate
N	Number of data points/data sets
n	Number of electrons transferred per redox event
R	Gas constant
R_u	Uncompensated resistance
r	Radial direction of a cylindrical coordinate
T	Absolute temperature
v	Potential scan rate
W	Probability density function of
z	i) Charge of an ion
	ii) Axial direction of a cylindrical coordinate
α	Transfer coefficient
κ^{-1}	Debye-Hückel length
γ	D ratio of the oxidised to reduced form of the redox couple
ε	Relative dielectric permittivity
ε^0	Permittivity of vacuum
ϕ	Electric potential
η	Overpotential
θ	i) Fractional surface coverage of an adsorbed monolayer
	ii) Fractional area of an electrode
	iii) Circumferential direction of a cylindrical coordinate
λ	Solvent reorganisation energy
$\lambda^{0'}$	Dimensionless ET rate constant
Γ^0	Monolayer surface concentration
ΔE	AC frequency amplitude
ΔE_p	Peak potential separation of a CV
∇	Differential operator
Ψ	Least squares correlation

Acknowledgements

Firstly, I would like to thank my (team of) supervisors, Prof Pat Unwin, Prof Julie Macpherson, Dr Jie Zhang and Prof Alan Bond for your encouragement and enthusiasm throughout my PhD. Your guidance and knowledge has helped drive my projects forward and enabled the academic successes I have achieved. For that I am truly grateful. Thank you for this opportunity and for believing in me from the beginning as we embarked on our visionary Warwick-Monash joint PhD venture.

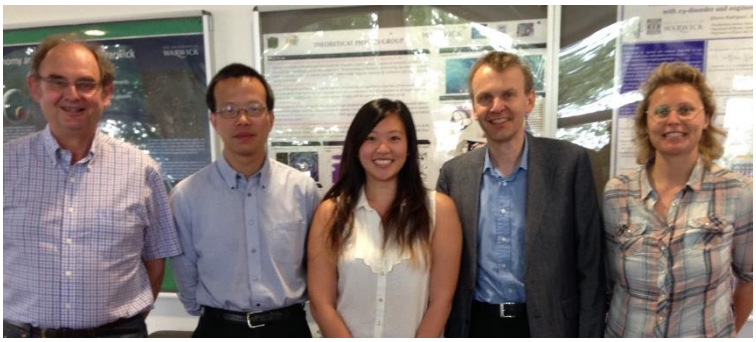

Next, thank you to everyone in the Warwick Electrochemistry and Interfaces group whom culturally, make it such a fun and vibrant place to work in addition to advice and expertise continually shared. A special thanks to FYG – Emma, Faduma, Maria and Minkyung – for making this entire journey so unforgettable.

Thank you to the Monash Electrochemistry group for being so welcoming during my Aussie adventure with a special thanks to Si-Xuan for your friendship.

Thank you Mum and Dad, first for setting up the FAMA foundation but more importantly for all your love and support. Mum, thank you for imparting on me your strength and ambition to succeed, for which I am eternally thankful. Dad, thank you for your unconditional support in whatever I do, you're the only one who will willingly listen to my science rants.

Tianyi, thank you for being with me for the day-to-day. Thank you for your unconditional support through the highs and lows of PhD life and for your unwavering confidence in me. I am truly appreciative. I couldn't have done it without you.

Declarations

The work presented in this thesis is entirely original and my own. This thesis is submitted to the University of Warwick in support of my application for the degree of Doctor of Philosophy. I confirm that it has not been submitted for a degree at another University.

Parts of the Introduction (Chapter 1) have been included in the following book chapter:

A. G. Güell, **S.-y. Tan**, P. R. Unwin, G. Zhang, Electrochemistry at Highly Oriented Pyrolytic Graphite (HOPG): Toward a New Perspective, in Electrochemistry of Carbon Electrodes, P. N. Bartlett, R.C. Alkire, J. Lipkowski (Eds.), Wiley-VCH, **2016**, 31-82.

Chapter 2 was published as:

S.-y. Tan, R. A. Lazenby, K. Bano, J. Zhang, A. M. Bond, J. V. Macpherson, P. R. Unwin, Comparison of Fast Electron Transfer Kinetics at Platinum, Gold, Glassy Carbon and Diamond Electrodes using Fourier-Transformed AC Voltammetry and Scanning Electrochemical Microscopy. *Phys. Chem. Chem. Phys*. **2017**, 19, 8726-8734

Chapter 3 was published as:

S-y. Tan, J. Zhang, A. M. Bond, J. V. Macpherson, P. R. Unwin, Impact of Adsorption on Scanning Electrochemical Microscopy Voltammetry and Implications for Nanogap Measurements. *Anal. Chem*. **2016**, 88, 3272-3280.

Chapter 4 was published as:

S-y. Tan, P. R. Unwin, J. V. Macpherson, J. Zhang, A. M. Bond, Probing Electrode Heterogeneities using Fourier-Transformed Alternating Current Voltammetry: Application to a Dual-Electrode Configuration. *Anal. Chem*. **2017**, 89, 2830-2837.

Chapter 5 was published as:

S-y. Tan, P. R. Unwin, J. V. Macpherson, J. Zhang, A. M. Bond, Probing Electrode Heterogeneities using Fourier-Transformed Alternating Current Voltammetry: Protocol Development. *Electrochim. Acta*. **2017**, 240, 514-521

Additionally, collaborative electrochemical analysis and finite element method modelling projects, not featured in this thesis, have contributed to the following articles:

A. G. Güell, A. S. Cuharuc, Y. Kim, G. Zhang, **S.-y. Tan**, N. Ebejer, P. R. Unwin, Redox-Dependent Spatially Resolved Electrochemistry at Graphene and Graphite Step Edges, *ACS Nano*, **2015**, 9, 3558-3571.

G. Zhang, **S.-y. Tan**, A. N. Patel, P. R. Unwin, Electrochemistry of $Fe^{3+/2+}$ at Highly Oriented Pyrolytic Graphite (HOPG) Electrodes: Kinetics, Identification of Major Electroactive Sites and Time Effects on the Reponses, *Phys. Chem. Chem. Phys*, **2016**, 18, 32387-32395.

T. Troadec, **S.-y. Tan**, C. J. Wedge, J. P. Rourke, P. R. Unwin, A. B. Chaplin, One-Electron Oxidation of $[M(P^tBu_3)_2]$ (M=Pd, Pt): Isolation of Monomeric $[Pd(P^tBu_3)_2]^+$ and Redox-Promoted C-H Bond Cyclometalation, *Angew. Chem. Int. Ed*, **2016**, 11, 3818-3821

Summary

Heterogenous interfacial electron transfer processes are of fundamental and applied importance to electrochemists and are extensively studied by a wide range of electrochemical techniques. This thesis focuses on the development of analysis strategies and electrochemical methodologies for more detailed quantitative investigations of electron transfer kinetics at a plethora of electrode materials, with an emphasis on carbon-based materials. Of interest are the techniques of Fourier-transformed large amplitude alternating current voltammetry (FTACV) and scanning electrochemical microscopy (SECM).

The complementary electrochemical techniques of FTACV and SECM are used for measurements of fast electron transfer to reveal the impact of the complex heterogeneous surface of degenerately-doped polycrystalline boron-doped diamond electrode surfaces compared to conventional electrode materials such as platinum and gold. This part of the work highlights the importance of understanding the influence of measurement technique and further demonstrates how electron transfer at semi-metallic electrodes differ from conventional metallic electrodes.

The oxidation of a ferrocene-derivative at highly oriented pyrolytic graphite is used to demonstrate the effects of reversible reactant adsorption on the SECM response. The high surface area-to-solution volume ratio of nanogap SECM measurements depicts the importance of understanding the impact of such surface effects. Precise quantitative kinetic analysis requires understanding of the mass transport between the SECM probe and electrode surface. Finite element method modelling was used to extensively investigate the effects of electrode reactant processes and the results of the models shed light on important factors that need to be accounted for in quantitative analysis of nanogap voltammetric measurements.

FTACV is further developed as a tool for kinetic selectivity at heterogeneous electrode surfaces. This is achieved by taking advantage of the harmonic-dependent measurement timescale of FTACV to deconvolute a dual-heterogeneity electrochemical response into its individual components. Protocols are developed for this application and demonstrated experimentally using the ruthenium hexamine and ferrocene methanol redox couples.

Chapter 1

Introduction

This thesis is concerned with the development of analysis and modelling strategies for advanced electrochemical methods and their application for electron transfer kinetics measurements. Of specific interest is the application of Fourier-transformed large amplitude alternating current voltammetry and scanning electrochemical microscopy for fast kinetic measurements and the numerical methods and protocols used to understand and quantify the systems studied.

This chapter introduces the fundamentals of electrochemistry as well as the experimental and numerical techniques used in subsequent chapters. The importance of carbon electrode materials in electrochemistry and studies of fundamental electron transfer kinetics at highly oriented pyrolytic graphite and polycrystalline boron-doped diamond electrodes are also reviewed. Finally, a brief summary of the project aims is outlined.

1.1. Equilibrium Electrochemistry

Electrochemistry is concerned with the study of electroactive molecules at an electrode/electrolyte interface. Consider the following redox couple:

$$\mathrm{Red}^{n-}{}_{(aq)} \underset{k_{red}}{\overset{k_{ox}}{\rightleftharpoons}} \mathrm{Ox}_{(aq)} + ne^{-}{}_{(m)} \quad \text{(Eq. 1.1)}$$

where Ox and Red are the soluble oxidised and reduced forms of an electroactive species and n is the number of electrons transferred per redox event. k_{ox} and k_{red} are the first-order heterogeneous oxidation and reduction rate constants, respectively, and are described in detail in Section 1.2. This electrochemical process involves the transfer of charge across the interfacial region of an electrode (usually metallic (m)), and a solution phase (aq) species. For this process, the Nernst equation is used to relate the potential at the electrode and concentration of the electroactive species.

Under equilibrium conditions, the potential established at the electrode is known as the equilibrium potential, E_{eq}, and is given by:

$$E_{eq} = E^{0'} + \left(\frac{RT}{nF}\right)\ln\left(\frac{\gamma_{ox}[\mathrm{Ox}]}{\gamma_{red}[\mathrm{Red}]}\right) \quad \text{(Eq. 1.2)}$$

where $E^{0'}$ is the formal electrode potential of the redox couple of interest, [Ox] and [Red] are the concentrations of species Ox and Red at the electrode surface, which under equilibrium conditions, is the same as the bulk concentration. γ is the activity coefficient, usually assumed to be unity in dilute solutions.[1] R is the gas constant (8.314 J K^{-1} mol^{-1}), T is the absolute temperature of the solution and F is the Faraday constant (96485 C mol^{-1}).[1]

1.2. Dynamic Electrochemistry

Dynamic electrochemistry is the study of charge transfer processes occurring at electrode/electrolyte interfaces under non-equilibrium conditions. Two types of processes can occur at this interface, i.e. non-faradaic and faradaic. A non-faradic process occurs

when a change at the interface results in a current flow without facilitating charge transfer. The most common non-faradaic process is capacitive charging from the electrical double layer (Section 1.2.3) and requires consideration when interpreting electrochemical measurements.

Faradaic current flows when a potential is applied to an electrode to promote oxidation or reduction of a redox species in solution. The magnitude of current, *I*, generated is related to the flux, *J*, of the species in solution, by the following:

$$I = nFAJ \quad \text{(Eq. 1.3)}$$

where *n* is the number of electrons transferred per redox event and *A* is the area of the electrode.

Numerous factors are known to influence the dynamics of an electrochemical reaction and the rate of the charge transfer processes. These are the electrode potential, mass transport of the electroactive species to the electrode surface, the reactivity of the molecule of interest, the activity of the electrode material and the structure of the interfacial region where the electron transfer occurs. Figure 1.1 shows a schematic of the basic processes that occur during dynamic electrochemistry of a redox species in solution, which is the type of process considered in this work. Although each step can be more complicated, ultimately the rate of the electrochemical reaction depends on the slowest step.

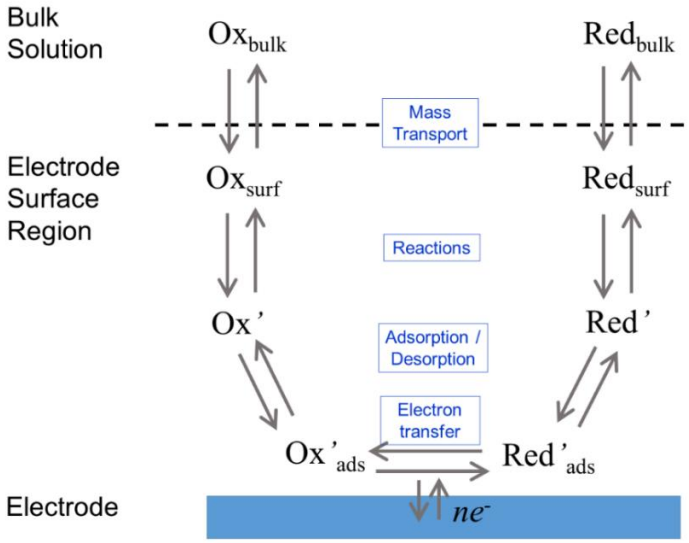

Figure 1.1. A schematic representation of processes involved in basic dynamic electrochemistry.

1.2.1. Mass Transport

Mass transport is the term used to describe the movement of material in the solution phase and can be split into diffusion, migration and convection processes. The sum of all three of these processes dictates the total mass transport rate. The overall partial differential equation used to describe mass transport is the Nernst-Plank equation:[1]

$$J_i = J_{i,d} + J_{i,m} + J_{i,c} \quad \text{(Eq. 1.4)}$$

$$= -D_i \nabla c_i - \frac{z_i F}{RT} D_i c_i \nabla \phi + c_i v_s \quad \text{(Eq. 1.5)}$$

J_i, $J_{i.d}$, $J_{i.m}$ and $J_{i.c}$ represent the total, diffusive, migrative and convective flux elements of species i, D_i is the diffusion coefficient of species i, c_i is the concentration of species i, z_i is the charge on species i, ϕ is an electric potential and v_s represents the velocity of the solution.

1.2.1.1. Diffusion

Diffusion is the net flux that occurs due to Brownian motion of molecules (neutral and charged) and is described by Fick's first (Eq. 1.6) and second (Eq. 1.7) laws of diffusion.

$$J_{i.d} = -D_i \nabla c_i \quad \text{(Eq. 1.6)}$$

$$\frac{\partial C_i}{\partial t} = D_i \nabla^2 c_i \quad \text{(Eq. 1.7)}$$

∇ is the Laplace operator in the form of $\frac{\partial}{\partial x} + \frac{\partial}{\partial y} + \frac{\partial}{\partial z}$ for the Cartesian coordinate and $\frac{\partial}{\partial r} + \frac{1}{r}\frac{\partial}{\partial \theta} + \frac{\partial}{\partial x}$ for a cylindrical coordinate.

The first law describes flux in terms of a concentration gradient, towards an electrode, at a specific time. It has a negative sign because molecules move from a higher

to lower concentration region. The second law describes variations in concentration with time and is the equation solved to predict current at an electrode.

The size of an electrode determines the diffusion profile that is established at the electrode surface. When a concentration gradient develops at a large electrode, species will diffuse to the electrode in a planar diffusion field (Figure 1.2(a)). When the electrode is sufficiently smaller, there is a significant contribution from radial diffusion, ultimately leading to a hemispherical diffusion field, and a greater flux density (Figure 1.2(b)).

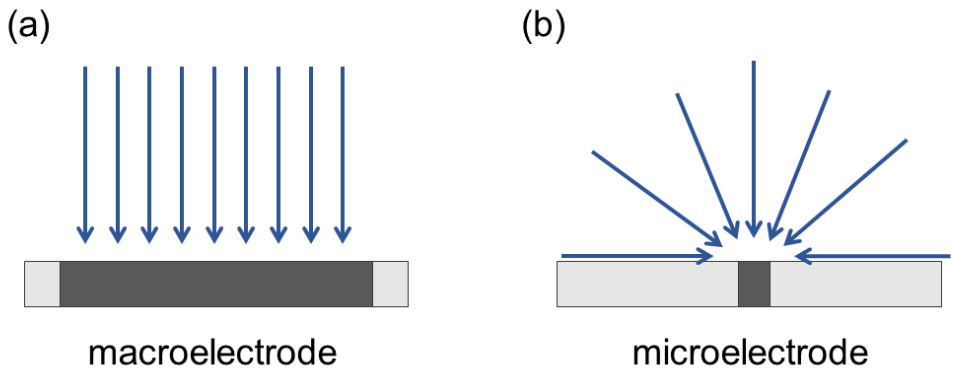

Figure 1.2 Diffusion profile for a (a) macroelectrode (linear) and (b) microelectrode (hemispherical).

1.2.1.2. Migration

Migration describes the movement of charged species in an electric field gradient, $\nabla\phi$, with ϕ being the potential of the field. This exerts an electrostatic force onto the charged species pushing it towards or away from an electrode surface. Migrative flux is described by:

$$J_{i,m} = \frac{z_i F}{RT} D_i c_i \nabla\phi \quad \text{(Eq. 1.8)}$$

where $\frac{z_i F}{RT} D_i$ is a coefficient often referred to as the mobility of ion and can be denoted as μ_i.

Migration can be minimised experimentally by adding supporting electrolyte (typically ≥ 0.1 M for mM levels of charged analyte). This reduces the range of the potential gradient to a region very close (*i.e.* < 1 nm) to the electrode interface, so that the electron transfer process experiences the full potential driving force at the electrode/solution interface. The addition of supporting electrolyte also functions to reduce ohmic drop (iR_u) effects.

1.2.1.3. Convection

Convection refers to the flux caused by a mechanical force, either natural or forced and is described by the Navier-Stokes equation:

$$J_{i,c} = c_i \nu_s \quad \text{(Eq. 1.9)}$$

Natural convection could arise from thermal gradients or density changes across a solution while forced convection controlled by hydrodynamic systems are based on electrodes that move with respect to the electrolyte solution, such as the rotating disk electrodes,[2–5] or systems where the electrolyte solutions flow over a static electrode, such as in channel[6–12] or micro-jet[13–15] electrodes.

1.2.2. Electron Transfer

1.2.2.1. ET at Metal Electrodes

Electron transfer (ET) occurs at the electrode/electrolyte interface when thermodynamically favourable. In a metallic electrode material, the overlap of atomic orbitals allows for electrons to move freely within the crystal lattice. These electrons occupy a continuum of energy levels with a maximum state known as the Fermi level, E_F, tuneable by applying an electrical potential. If this level is lower than the highest occupied molecular orbital (HOMO) or higher than the lowest unoccupied molecular orbital (LUMO) of the redox species in the electrolyte than oxidation and reduction processes,

respectively, become thermodynamically viable as depicted in Figure 1.3.[1] The Fermi level density of states (DOS) of the electrode material plays an important role in the ET process.[16] Platinum and gold, which are typical metallic electrodes used in electrochemistry, have DOS values ~ 10^{23} cm^{-3} eV^{-1}.[17]

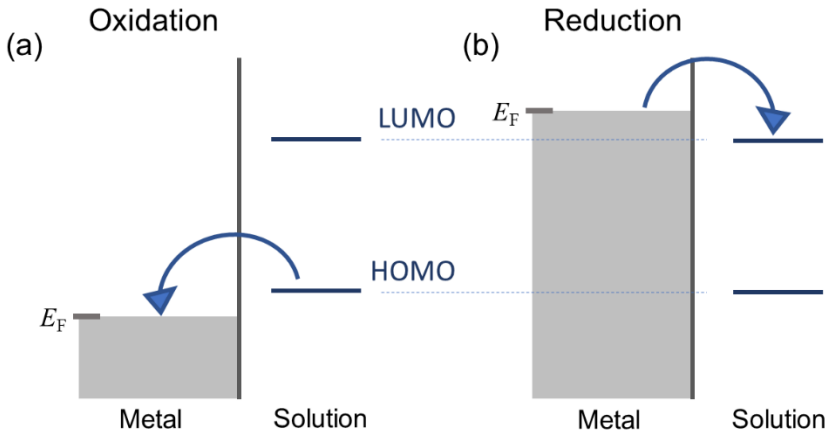

Figure 1.3 A metal electrode in contact with a solution containing a redox species undergoing (a) oxidation and (b) reduction.

For non-spontaneous electron transfer processes to occur, as studied in dynamic electrochemistry, an overpotential, η, must be applied to the electrode surface. This describes the extent to which the reaction is driven beyond the formal electrode potential, $E^{0'}$, of the redox couple of interest.

$$\eta = E_{appl} - E^{0'} \quad \text{(Eq. 1.10)}$$

In the case where the electron transfer kinetics is so fast that the response is governed by mass transport, we can assume Nernstian behaviour at the electrode surface such that Eq. 2 can be adapted to describe the local concentration of the redox species at the electrode surface:

$$E_{appl} = E^{0'} + \left(\frac{RT}{nF}\right)\ln\left(\frac{[Ox]}{[Red]}\right) \quad \text{(Eq. 1.11)}$$

When Nernstian behaviour does not hold and the electrode is kinetically-limited, the Butler-Volmer relationship is often used to describe the potential-dependence of

electron transfer at the electrode/electrolyte interface. The first-order heterogeneous oxidation and reduction rate constants, k_{ox} and k_{red}, respectively, from Eq. 1.1, are given by

$$k_{ox} = k^0 \exp\left[(1-\alpha) f \eta\right] \quad \text{(Eq. 1.12)}$$

$$k_{red} = k^0 \exp\left[-\alpha f \eta\right] \quad \text{(Eq. 1.13)}$$

where k^0 is the standard rate constant, α is the transfer coefficient and $f = \frac{nF}{RT}$ is a collection of constants.

The transfer coefficient, also known as the symmetry coefficient, is used to describe how closely the transition state is to the reduced form of the redox couple. α takes a value between 0 and 1 but experimentally it is typically found between 0.3 and 0.7. The standard rate constant, k^0, is a characteristic property of the redox couple used to quantify the rate of the electron transfer reaction.

More complex electron transfer models[18–21] have also been developed but are beyond the scope of this thesis.

1.2.2.2. ET at Semiconductor Electrodes

Semiconductor materials used in electrochemistry are usually based on extrinsic semiconductor materials where the electronic properties of an insulting material are tuned by doping. Doping involves the incorporation of different elements into a crystalline insulator to generate charge carriers. The energy spectrum in ideal crystalline materials consists of allowed energy levels and no energy levels (band gaps). As shown in Figure 1.4(a), for an intrinsic semiconductor, the upper unfilled band is called the conduction band and the lower filled band is called the valence band. The energy levels in a semiconductor are characterised by the conduction band edge, E_C, the valence band edge, E_V, and the Fermi level, E_F, which is located at the mid-point of the band gap, E_g.

The simplest example of an extrinsic (doped) semiconductor involves the introduction of a group V element (e.g., P) or a group III element (e.g., Al) into a group IV

element (e.g., Si). The addition of P into the Si lattice structure introduces an energy level, E_D, close to the conduction band edge which facilitates the movement of electrons into the conduction band. This is known as a *n*-type semiconductor (Figure 1.4(b)). The addition of Al into the Si lattice, introduces a vacant energy level, E_D, close to the valence band edge which allows promotions of electrons from the valence band leading to the formation of holes in the valence band. This is known as a *p*-type semiconductor (Figure 1.4(c)).

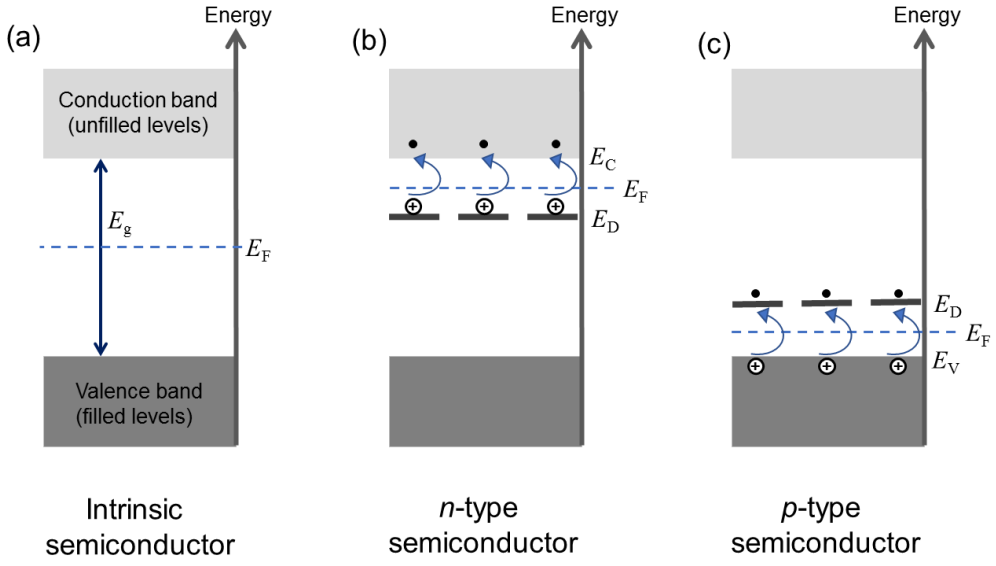

Figure 1.4 Schematic showing the band structure of an (a) intrinsic, (b) *n*-type and (c) *p*-type semiconductors.

The electron transfer at semiconductors can be described by the Marcus-Gerischer model[22–26] which states that the current depends on the overlap integral between the occupied/unoccupied states at the valence and conduction band edges and the unoccupied/occupied states of the redox system as shown in Eq. 1.14.

$$\mathrm{Red}_{(aq)} + (\text{vacant state})_{(solid)} \rightleftharpoons \mathrm{Ox}_{(aq)} + (\text{occupied state})_{(solid)} \quad \text{(Eq. 1.14)}$$

Eq. 1.15 and Eq. 1.16 describe the oxidative and reductive components of the microscopic current of electron transfer:

$$i_{ox} = e^0 \cdot N_{red} \cdot \sigma_{red} \cdot \sigma_{el} \cdot \nu_n \cdot \kappa_{el} \cdot \int_{-\infty}^{\infty} W_{red}(E) \cdot \mathrm{DOS}_{vac}(E) dE \quad \text{(Eq. 1.15)}$$

$$i_{red} = e^0 \cdot N_{ox} \cdot \sigma_{ox} \cdot \sigma_{el} \cdot \nu_n \cdot \kappa_{el} \cdot \int_{-\infty}^{\infty} W_{ox}(E) \cdot DOS_{occ}(E) dE \quad \text{(Eq. 1.16)}$$

where e^0 is the electric charge on an electron, N_i are the number of reactants, σ_i is reaction cross section of the reaction partners at the interface, ν_n is the averaged frequency of the nuclear nodes, κ_{el} is the adiabaticity coefficient and DOS(E) is the density of vacant or occupied electronic states. W_{ox} and W_{red} are the distribution functions for the oxidised and reduced species, respectively. The distribution of energy level of a redox couple can be described in terms of a Gaussian distribution function:

$$W_{ox} = \exp\left[-\frac{(E - E_{F,redox} - \lambda)^2}{4k_B T \lambda}\right] \quad \text{(Eq. 1.17)}$$

$$W_{red} = \exp\left[-\frac{(E - E_{F,redox} + \lambda)^2}{4k_B T \lambda}\right] \quad \text{(Eq. 1.18)}$$

where, λ is the solvent reorganisation energy and $E_{F,redox}$ is the redox potential on an absolute scale. An illustrative representative of the Marcus-Gerischer formulisation is shown in Figure 1.5.

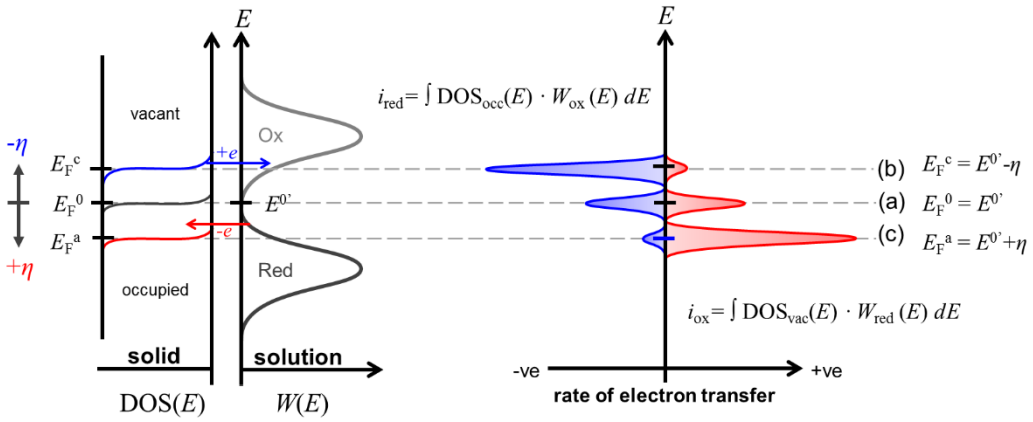

Figure 1.5 Illustrative representation of the overlap of electronic states for an electrode with those of the redox species as described in the Marcus-Gerischer theory. (a) At equilibrium, the Fermi level of the electrode is aligned with that of the redox couple. Both cathodic (reductive) and anodic (oxidative) current components are equal. (b) At a negative overpotential, -η, applied between the bulk of the solution and the electrode, the Fermi level of the electrode rises resulting in an increased cathodic current component and a reduced anodic current component. (c) At a positive overpotential, + η, applied to the electrode relative to the bulk solution, the Fermi level of the electrode is lower and facilitates an increased anodic current component and a reduced

cathodic current component. The overall current is the sum of the area under the curves on the current axis.

1.2.2.3. ET at Semi-metal Electrodes

Semi-metals are materials which behave as a metal in some instances but like a semiconductor in others.[17,22,27–30] The band structure of a semi-metal is like that of a semiconductor, but where the top of the valence band overlaps with the bottom of the conduction band such that there is no band gap but rather, negligible DOS at the Fermi level. Graphite is an example of a semi-metal due to a slight overlap of the valence and conduction bands.[22,31,32] Investigations of the structural-dependency of electron transfer can be traced back to earlier studies of heterogeneous electron transfer kinetics on highly ordered pyrolytic graphite (HOPG).[33–41] Boron-doped diamond is another example of a semi-metal material where the extent of overlap between the valence and dopant band depends on the amount of boron incorporation.[17,42,43] The implications of the electronic band structure on the electrochemistry at these examples are further discussed in Section 1.5.

1.2.3. Electrical Double Layer

Various successive models have been proposed to describe how the charge density at the electrode interface is compensated by the analyte in solution phase. A typical model is presented in Figure 1.6. The inner Helmholtz plane (IHP) and the outer Helmholtz plane (OHP) represent the plane at the centre of specifically adsorbed ions into the electrode and the plane of closest approach of solvated ions, respectively,

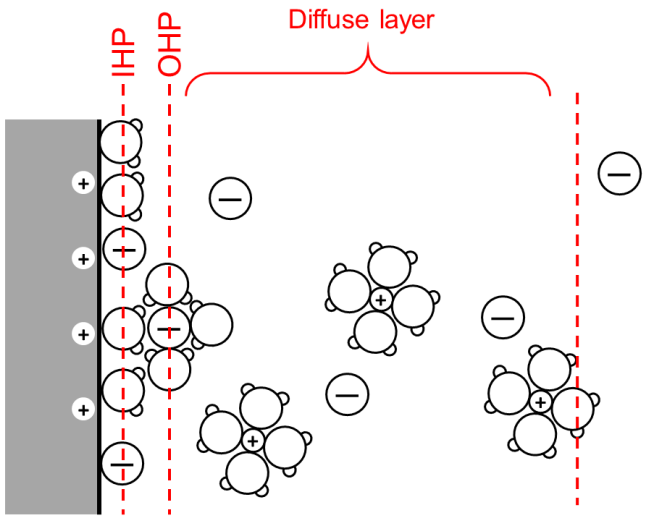

Figure 1.6 The electrical double layer at the electrode/electrolyte interface of a positively charged electrode.

The thickness of the diffuse layer is given by the Debye-Hückel length, κ^{-1}, which is the measure of a charge carrier's net electrostatic effect in solution.

$$\kappa^{-1} = \left(\frac{\varepsilon\varepsilon_0 kT}{2N_A c z_i^2 e_0^2}\right)^{1/2} \quad \text{(Eq. 1.19)}$$

where ε is the relative dielectric permittivity of the solvent, ε^0 is the permittivity of vacuum, N_A is the Avogadro constant, z is the ion charge and e_0 is the elementary charge.

The term double layer refers to the simplified model where the balancing charges are described as two sets of charges in parallel and is typically represented in an equivalent circuit as a parallel plate capacitor. The current that flows due to the compositional change of the double layer is termed the charging current, I_c. For a capacitor:

$$I_c = C_{dl}\frac{\partial E}{\partial t} \quad \text{(Eq. 1.20)}$$

where C_{dl} is the double layer capacitance and $\frac{\partial E}{\partial t}$ is the scan rate of an electrochemical measurement. I_c temporally limits the sensitivity of the electrochemical measurement.

1.3. Electrochemical Methods

1.3.1. Voltammetry

In an electrochemical cell, a potential is applied to the working electrode (WE) with respect to a quasi-reference counter electrode (QRCE). This setup is adequate for small currents (< 1 μA). For currents larger (>1 μA) in aqueous solution, a three-electrode setup in which a third electrode, known as the counter electrode (CE) (or auxiliary electrode), is used to facilitate the passage of electrical current through the solution.[1]

1.3.1.1. Cyclic Voltammetry at Macroelectrodes

Cyclic voltammetry (CV) employs a linear potential scan between two potential values, E_1 and E_2 at a steady scan rate, v, as shown in Figure 1.7(a). E_1 is normally a potential at which there is no electrochemical activity and E_2 is a potential where the reaction is mass transport controlled. CV is the most widely used technique for the characterisation of redox species and can provide quantitative information about the number of oxidation states and their stability,[44–47] as well as, surface adsorption mechanisms[48–51] and coupled chemical reactions.[52–54] Furthermore, multiple potential cycles can also be employed to study film formation, for example.[55–58] Current-voltage curves obtained from a cyclic voltammetry experiment are characteristic of the reaction mechanism and kinetic conditions. Figure 1.7(b) shows a typical CV current-voltage plot for a simple oxidation reaction at a macroelectrode (~mm dimensions) where planar diffusion conditions prevail.

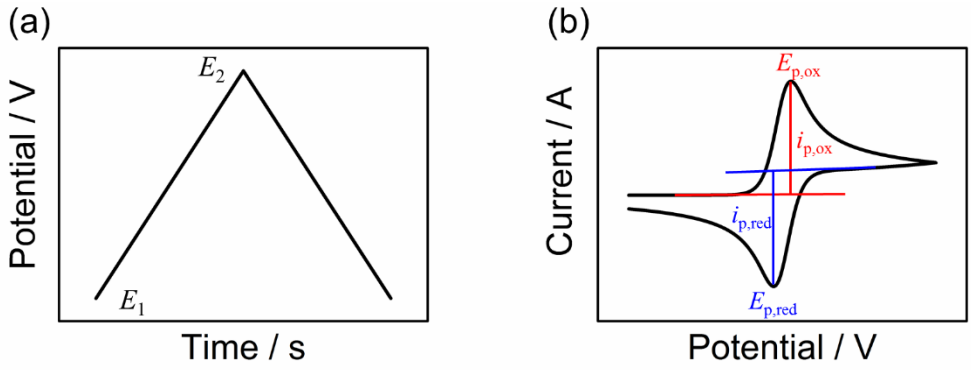

Figure 1.7 (a) Time-dependent potential waveform employed in cyclic voltammetry. (b) Typical current-potential plot of a cyclic voltammogram under planar diffusion conditions.

During the forward sweep of the potential scan, the reduced species is consumed (oxidised) at the electrode surface and an oxidation current is observed. On the reverse potential scan, the reduced species is regenerated at the electrode resulting in a reduction current. The change of sign in the current is directly related to the inversion of the concentration gradient of the reduced species at the electrode surface. The peaks in the voltammogram occur at the potential at which mass transport can no longer keep up with the electrode kinetics and so a depletion occurs. A key feature of cyclic voltammetry is the current peak height, i_p, which is given by the Randles-Sevcik equation:

$$i_p = 2.69\times10^5 n^{3/2} A D^{1/2} c v^{1/2} \text{ at 298 K (Eq. 1.21)}$$

Hence, a fully reversible (fast ET mechanism) voltammogram will have the following characteristics:

(1) $i_p \propto v^{1/2}$

(2) $\Delta E_p = E_{p,ox} - E_{p,red} = 59/n$ mV at 298 K

(3) $\left| i_{p,ox} / i_{p,red} \right| = 1$

The shape of voltammograms alter when the rate of mass transport overcomes the rate of electron transfer, i.e. increasing v or decreasing k^0. This results in peak broadening and increased separation of the oxidation and reduction peaks, ΔE_p, as shown in Figure 1.8.

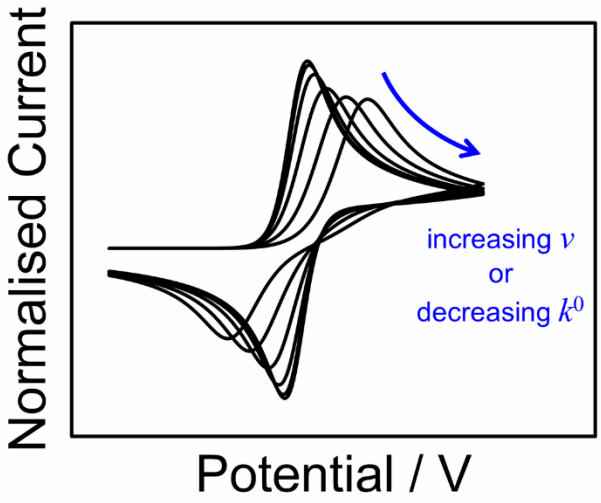

Figure 1.8 Cyclic voltammograms which are kinetically limited. The currents are normalised to demonstrate the effects of changing the potential scan rate or the electron transfer rate constant.

1.3.1.2. Voltammetric behaviour of Ultramicroelectrodes

Ultramicroelectrodes (UMEs) are electrodes that have micrometre-dimension (typically ≤ 25 μm). UMEs come in many shapes, e.g. disk,[59–62] spherical,[63–65] band[9,66,67] or cylindrical[68,69] and in some cases, constructed down to a few nm in size. UMEs offer advantages over larger (macro-) electrodes, such as high mass transport rates due to hemispherical diffusion where the mass transport layer is larger than the electrode size,[1] low ohmic drop (iR_u drop) due to the small currents generated, and low double-layer charging and capacitances due to the small surface area.[59,70,71]

In electrochemical scanning probe microscopy, specifically scanning electrochemical microscopy (SECM), a disk-shaped UME is typically used as a probe. The plane of the electrode can be characterised by the size ratio of the radius of the insulating material to that of the active electrode, known as the RG (typically 2 to 20). For a disk-shaped UME, the high mass transport rates result in a diffusion-limited steady-state current, i_∞, expressed by:

$$i_\infty = 4nFaDc \quad \text{(Eq. 1.22)}$$

where n is the number of electrons transferred per redox event, F is the Faraday constant, a is the radius of the electrode and D and c are the diffusion coefficient and concentration of the redox species, respectively. UMEs have been used in the measurements of electron transfer kinetics using both steady-state voltammetry[72–75] and fast scan cyclic voltammetry[58,75–77] methods.

In the case where mass transport reaches a steady-state, e.g. at a microelectrode where hemispherical diffusion dominates, the current-voltage curve has a sigmoidal shape as shown in Figure 1.9. The kinetic parameters can be determined from the slope of the sigmoidal voltammogram, $\Delta E_{1/2}$, which is the difference between the two quartile potentials (quarter-wave and three quarter-wave).[72]

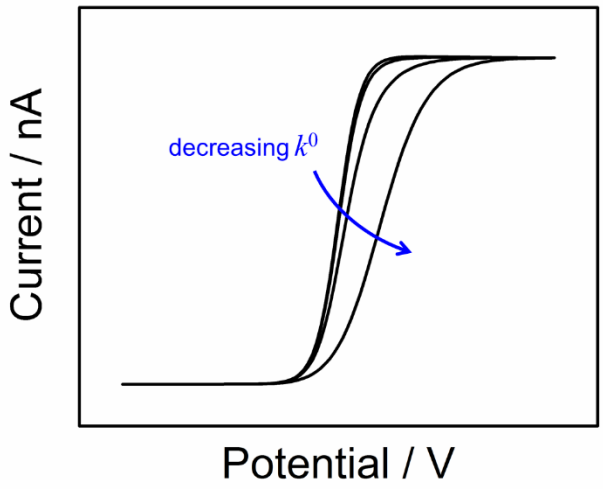

Figure 1.9 Steady-state voltammograms which are kinetically limited.

1.3.1.3. Adsorption Voltammetry

Cyclic voltammetry experiments are sensitive to redox reactions involving adsorption of both the reactant and product and differs from when both species are in solution. This is because mass transport need not be considered. Figure 1.10 shows a typical cyclic voltammogram for ideal Nernstian ET with the Langmuir isotherm describing the adsorption. It consists of two symmetrical peaks, where the charges (area under the peak)

for the oxidation and reduction are equal and tell us about the amount of reactant present. Hence, if the potential scan rate is increased, the peak current must also increase and is given by:

$$i_p = \frac{n^2F^2}{4RT}\nu A\Gamma^0 \quad \text{(Eq. 1.23)}$$

where Γ^0 is the maximum surface coverage of the reactant.

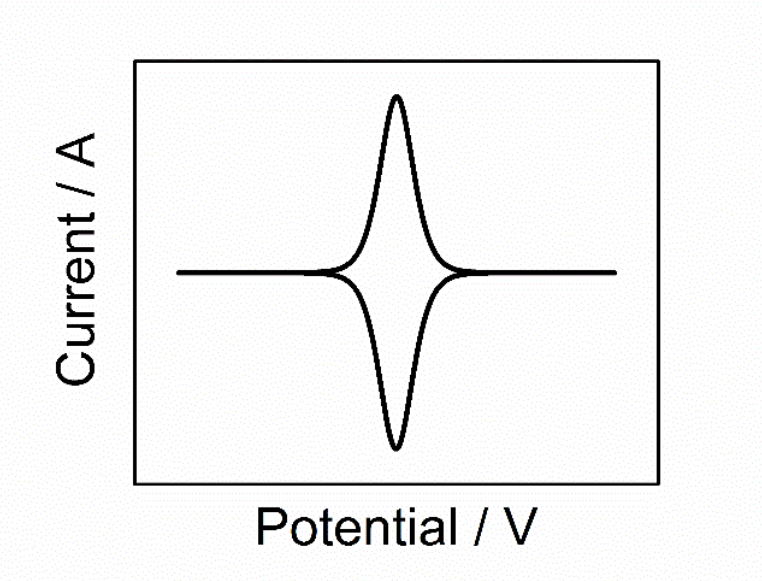

Figure 1.10 Typical current-voltage curve for a surface-confined process.

1.3.2. Fourier-Transformed Large Amplitude Alternating Current Voltammetry

Fourier-transformed large amplitude alternating current voltammetry (FTACV)[78,79] is a powerful electrochemical technique which utilises a sinusoidal potential waveform of amplitude, ΔE, and frequency, f, superimposed onto the linear potential ramp used in cyclic voltammetry. The output current from such an experiment contains components of the fundamental frequency and the higher order harmonics. Spectral analysis is realised by employing the Fourier-transform (FT) algorithm to determine the frequency domain

representation of the time domain signal given by the following (as shown in Figure 1.11(a)):

$$X_k = \sum_{n=0}^{N-1} x_n . e^{-i2\pi k \frac{n}{N}} \quad \text{(Eq. 1.24)}$$

where N is the number of time samples, n is the current sample considered, x_n is the value of the signal at n, k is the current frequency considered and X_k is the amount of frequency, k, in the signal.

The fundamental (1st) harmonic is the component that has the same frequency, f, as applied in the alternating current (AC) waveform while higher harmonic components have frequencies, $2f$, $3f$, $4f$, etc. There is also an aperiodic direct current (DC) component located near 0 Hz that resembles, but is not identical to, the conventional DC CV response. The aperiodic DC and AC components are resolved by selecting the regions of interest from the power spectrum using frequency band filtering and nulling the remaining unwanted signal as shown in Figure 1.11(b). Inverse FT (IFT) of the selected signals gives the resolved DC (Figure 1.11(c)) and AC harmonic components (Figure 1.11(d-f). The equation for the inverse FT is given by:

$$x_n = \frac{1}{N} \sum_{k=0}^{N-1} X_k . e^{i2\pi k \frac{n}{N}} \quad \text{(Eq. 1. 25)}$$

The data obtained from this FT-band filtering-IFT sequence can be analysed by applying suitable models analogous to strategies employed in direct current voltammetry (DCV) methods.

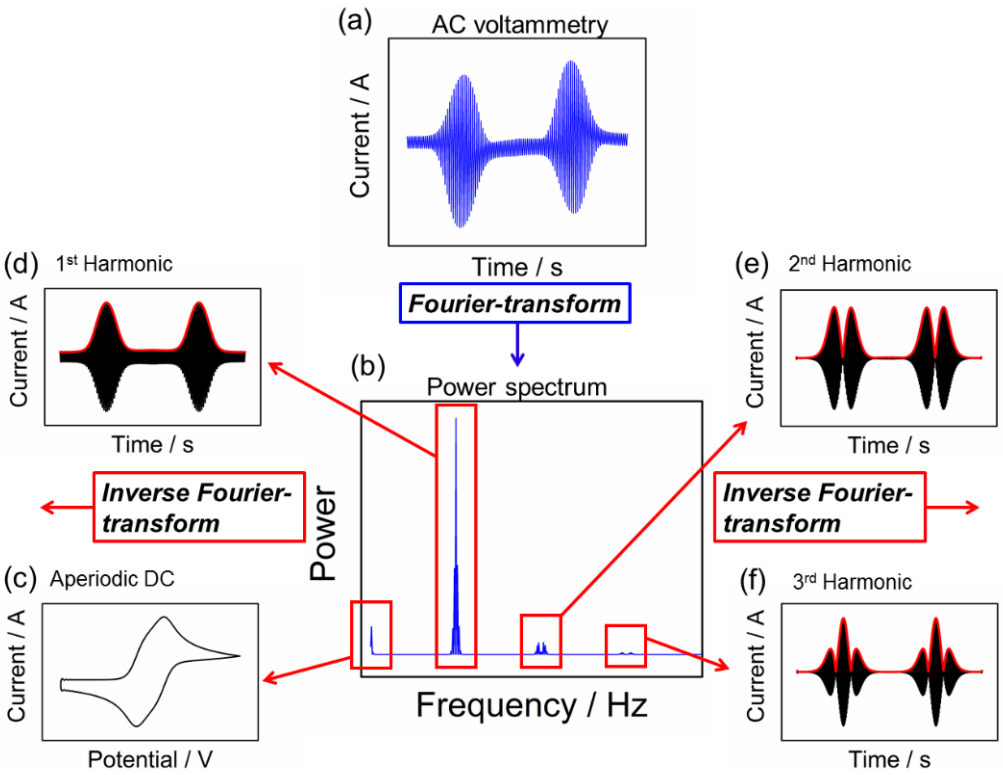

Figure 1.11 Schematic showing the experimental protocols of Fourier-transformed large amplitude alternating current voltammetry.

1.3.4.1. Advantages of FTACV

The FTACV method is highly advantageous over traditional DCV for the following reasons:

(1) The higher AC harmonics components are extremely sensitive to electrode kinetics such that the peak currents decrease with decreasing k^0. Furthermore, the individual AC harmonic components display a different level of kinetic sensivity (different measurement timescale).

(2) The 3rd and higher AC harmonic components are insensitive to background charging processes which allows selectivity of the faradaic components as well as exceptionally favourable faradaic-to-background current ratios.

(3) The phenomenologically similar effects of slow electron transfer kinetics and ohmic drop in DC CV are distinguishable under FTACV conditions, i.e. odd AC harmonic components show easily identifiable peak splitting due to ohmic drop.[80,81]
(4) All FTACV higher order harmonic components are derived from a single experiment and hence all the same electrode conditions apply unlike with DCV techniques where each data set is obtained from a series of measurements at variable potential scan rates which are potentially complicated by experiment-to-experiment variations.

1.3.4.2. Applications of FTACV

FTACV has been used to assess the electron kinetics at a plethora of electrode materials for a variety of redox couples including ferrocene (Fc),[82] tetrathiafulvalene (TTF),[82,83] tetracyanoquinodimethane (TCNQ),[84] $Ru(NH_3)_6$,[46,85] and $Fe(CN)_6$[85] and realises a higher upper limit of detection for the study of electron transfer kinetics at macroelectrodes compared to previously reported studies which employed DCV methods at similar potential sweep rates.

Furthermore, the power of the FTACV technique has been demonstrated for analysis of the surface-confined azurin redox process which gave large background charging currents that were barely distinguishable from the faradaic currents with CV.[86] Using FTACV, the DC and fundamental AC harmonic component was used to quantify the background process while the second and higher AC harmonic components where used to analyse the faradaic component, exemplifying a novel form of kinetic selectivity (faradaic vs. non-faradaic). Additionally, a study of the reversible $Ru(NH_3)_6^{3+/2+}$ redox couple in the presence of the irreversible reduction of oxygen found that the 4th and higher AC harmonic components only contained current contributions from the reversible process, further demonstrating the theme of kinetic selectivity (reversible vs. irreversible, in this case) of FTACV.[85]

The technique of FTACV has been further developed to increase reliability of electrode kinetic measurements by the introduction of an internal reference strategy. This

has been demonstrated using a reversible electrode process as an internal calibration to minimise systematic errors when analysing the target quasi-reversible processes.[82] A dual-frequency FTACV protocol has also been developed where the target process is reversible at the lower frequency and quasi-reversible at the higher frequency applied.[87]

1.3.3. Scanning electrochemical microscopy (SECM)

Scanning electrochemical microscopy (SECM) has been developed into a powerful technique to investigate interfacial physicochemical processes within a wide variety of applications as described in recent reviews.[88–94] SECM also forms the basis for many techniques, where it is combined with another technique usually capable of sensing the distance to the substrate surface, and is used to extend and improve SECM such as intermittent contact (IC)-SECM[95–99] and combined SECM-atomic force microscopy (AFM)[100–104] and SECM-scanning ion conductance microscopy (SICM).[105–107]

Simply, an UME (typically disk-shaped), also known as a SECM tip, is held in close proximity to a surface of interest to locally perturb the redox state or concentration of charge carriers within the UME-substrate gap. High mass transport conditions are formed due to the shuttling of the oxidised and reduced forms of the redox couple between the two electrodes. The steady-state mass transport coefficient, k_t, is a function of tip-substrate separation, d ($k_t \sim D/d$), so that high mass transport rates are obtained by decreasing the UME size and tip-substrate distances,[108] fuelling the trend of miniaturising electrochemical systems, leading to the development of nanoelectrodes[109–115] and various nanogap systems.[49,116–121]

1.3.3.1. SECM Modes of Operation

Typically, the SECM tip is operated in amperometric mode (held at a fixed potential) and the current generated from an electrochemical reaction is measured. As illustrated in Figure 1.12, when the tip is held in close proximity to the substrate surface, the current measured will depend on the experimental configuration which includes feedback,[108,122–127] substrate-

generation/tip-collection (SG/TC),[117,128–130] tip-generation/substrate-collection (TG/SG),[131–134] and competition mode.[135–139]

In feedback mode, the current will increase or decrease depending on whether the substrate is conducting or insulating, respectively. At an insulting substrate, the diffusion field around the UME is hindered resulting in a lowered tip current. This is known as negative feedback (Figure 1.12(a)). At a conducting substrate, however, the substrate can regenerate the oxidised species produced at the tip, resulting in an increased availability of reduced species in the tip-substrate gap. This is known as positive feedback (Figure 1.12(b)) and results in an enhancement of the tip current. The magnitude of the current reduction/enhancement depends on the tip-substrate separation, d, and a plot of tip current, i_T against d is known as an approach curve (Figure 1.12(c)). Many models have been proposed in literature to describe negative[123] and positive[140] feedback approach curves.

In SG/TC mode (Figure 1.12(d)), the reaction driving potential is applied to the substrate, the current measured at the tip tells us about the ET at the substrate. In TG/SC mode (Figure 1.12(e)), the driving potential is applied to the tip and the current is measured at the substrate. Redox-competition mode (Figure 1.12(f)) is when the tip competes with the substrate for the same analyte and leads to a reduction in the tip current when the tip is positioned above a catalytic site on the substrate.[135]

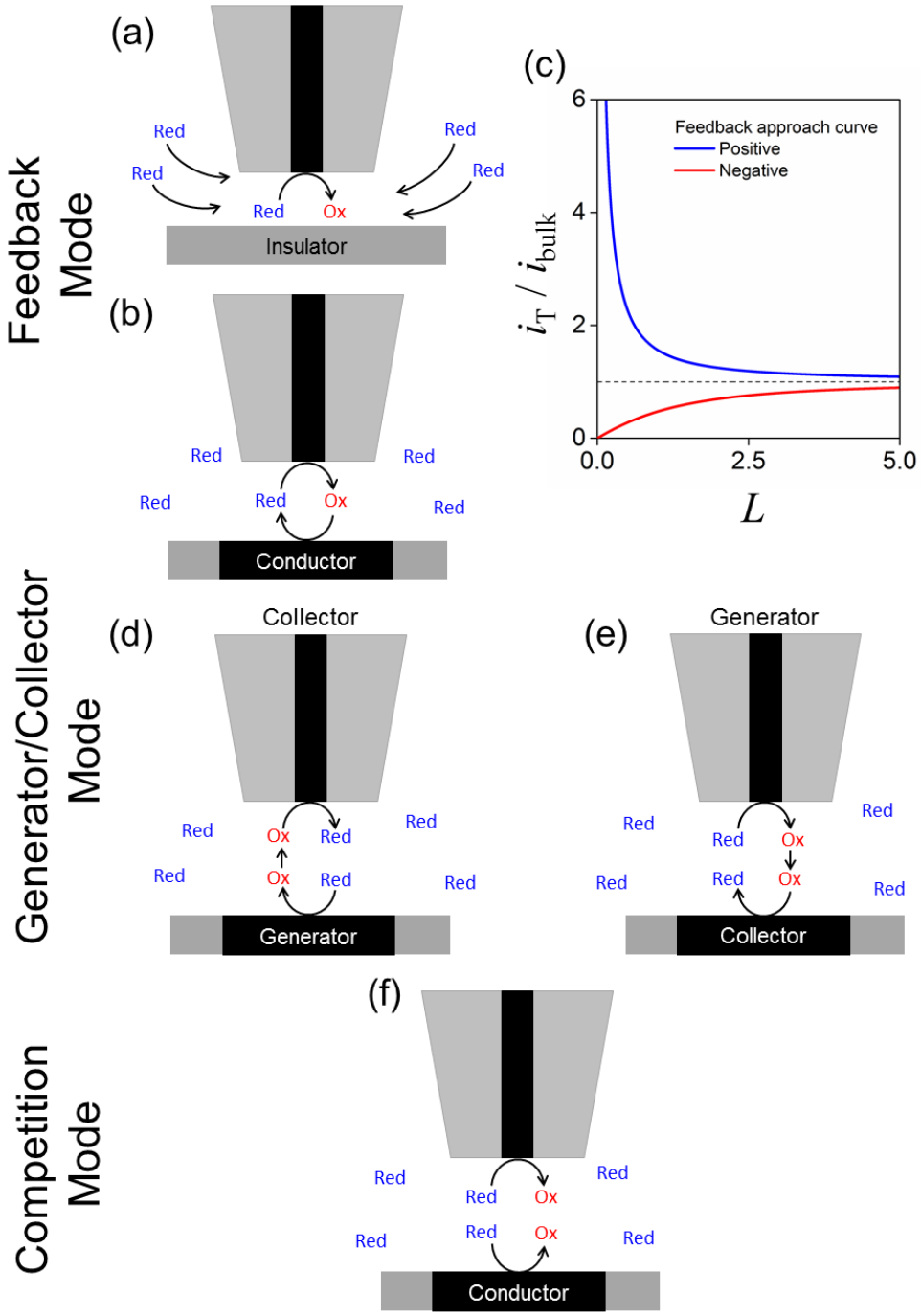

Figure 1.12 SECM modes of operation. (a) Negative and (b) positive feedback modes. (c) Approach curves (Plot of normalised distance, L, vs. normalised tip current, i_T/i_{bulk}). (d) Substrate-generation/tip-collection and (e) tip-generation/substrate-collection modes. (f) Redox-competition mode.

1.3.3.2. Applications of SECM

SECM has many interesting applications including the study of electron transfer kinetics,[52,112,119,128,141–146] movement of charge across[147–151] and along[152–156] an interface, studying processes in organic solvents[52,112,128,141,142,157] and ionic liquids,[74,158–160] and investigating a plethora of electrode materials such as carbon nanotubes,[109,145,146,161,162] nanowires,[25,44] individual nanoparticles,[164–168] graphene[111,119,169–172] and boron-doped diamond,[99,125,173] to name a few.

Of interest in this thesis, is the ability of SECM to deliver the highest known mass transport rates for measurement of ultrafast electron transfer at nanogap/nanoscale dimensions. Quantitative kinetic studies require the precise knowledge of electrode geometry. For example, unaccounted for irregularities in the electrode shape from idealised models,[72] tip recession[97,174,175] or 'lagooned' geometries[176,177] may produce highly erroneous determination (overestimation) of ET kinetic parameters.[178] Significant efforts have thus aimed at developing easy and reproducible electrode preparation alongside improved means of geometric characterisation such as with scanning electron microscopy (SEM),[56,179,180] tunnelling electron microscopy (TEM)[181,182] and AFM.[177,183] Furthermore, under these conditions of high surface area to solution volume ratios, surface effects such as adsorption[49,98,184] and migration[118,185–187] become very important as explored herein.

1.3.4. Scanning electrochemical cell microscopy (SECCM)

Scanning electrochemical cell microscopy (SECCM)[188,189] is a pipette-based imaging technique designed for the simultaneous measurement of electrochemical, conductance and topical visualisation of surfaces. The probe in SECCM is a double-barrelled (theta) pipette pulled to a sharp point, filled with electrolyte solution, together with contacting quasi-reference counter electrodes (QRCEs) in each channel. A potential is applied between the two QRCEs inducing migration of ions between the two barrels, through the meniscus that protrudes from the end of the pipet. Contact between the meniscus and the substrate creates a portable electrochemical cell approximately the size of the pipet end (90 nm – 3

μm).[180,190] The tip is oscillated to allow changes in the conductance to be measured when the meniscus is in contact with the electrode and to maintain positional feedback during scanning.

SECCM has been used for the fabrication of nanostructures,[56,57] molecular functionalisation and modification of surfaces,[58] and performing electrochemistry at individual nanoparticles,[191–195] graphene,[180,196–198] graphite[56,57,180,199,200] and carbon nanotube[162,201–203] electrodes.

1.4. Finite Element Method

Quantitative analysis of electrochemical signals (voltammetric current responses) require the solution of the mass transport problem which depend on the geometry of the system and the underlying mass transport equations. At simple geometries, under strict mass-transport conditions, the current-potential-time responses can be predicted analytically. However, at more complex geometries, or when the mass transport characteristics are more complicated, custom numerical simulations are needed to solve the mass transport problem and quantify the electrochemical signals.

The finite element method (FEM) is a numerical technique that can be used to solve these problems and is available in commercial software packages like COMSOL Multiphysics. In the application of these approaches for electrochemistry,[204,205] the concentrations as a function of time and space are described in terms of discrete values at prescribed locations, i.e. at the nodes of a grid dissecting the diffusion field as shown in Figure 1.13(a) for a simple 2D-axissymetric disk electrode geometry.

The FEM simulations numerically solves the partial differential equation that describes the mass transport within the domain of interest, namely the Nernst-Plank equation (Eq. 1.4), and is subject to boundary and initial conditions. The boundary conditions define the concentration or flux on the boundary and usually represent the bulk solution or electrode/electrolyte interface, respectively. The initial conditions describe an initial estimation for a solution at steady-state or the conditions for time = 0 for a time-

dependent simulation. From the numerical solution, the flux or concentration gradient of the active species to the electrode can be used to determine the current at an electrode. Figure 1.13(b) depicts the concentration profile at the end of a simulated linear sweep voltammetry (LSV) experiment in COMSOL at a 2D-axissymertic representation of a disk electrode. Note that it is important to check that the solution makes sense as the FEM makes a numerical approximation which can contain errors.

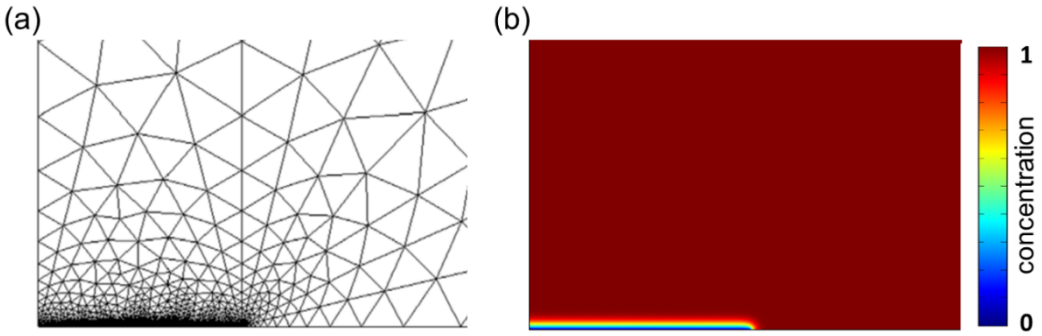

Figure 1.13 COMSOL generated (a) 2D mesh grid where finer mesh points are set at boundaries that have the highest concentration change and (b) the concentration profile at the end of an LSV simulation. The concentration of the reactant is zero at the electrode boundary.

The use of FEM in electrochemical analysis is becoming increasingly popular with the advent of various micro/nano-scale/gap electrode geometries. Some examples of these problems include scanning electrochemical microscopy (SECM),[52,99,128,206] scanning electrochemical cell microscopy (SECCM),[180,188,207] scanning ion-conductance microscopy (SICM), thin-layer electrochemical cell (TLC)[49,117,118,185,208] and nanopore[209–211] geometries. A range of applications of FEM simulations have been conducted and include the study of electrode kinetics,[52,99,162,180] mass transport properties (diffusion coefficient ratios),[52,117] adsorption,[49,50,98] ion migration[118,185,187] and ion rectification[210,212,213] phenomenon.

1.5. Carbon Electrode Materials

Carbon forms a variety of materials including graphite, diamond, carbon fibres as well newly discovered nanostructures such as graphene, fullerene and carbon nanotubes. While being composed of the same atoms, different carbon materials display considerably different physical and chemical properties. Despite their widespread use, there is still significant debate as to which surface features govern the electroactivity of carbon electrodes.[214]

1.5.1. Highly Oriented Pyrolytic Graphite (HOPG)

Graphite is the most common allotrope of carbon and is particularly useful as an electrode material for its high electrical conductivity and other unique properties. Highly oriented pyrolytic graphite (HOPG)[215] is the synthetic analogue of naturally occurring graphite and is prepared by stress annealing of pyrolytic graphite. It has been studied intermittently over several decades as an electrode material and is of enduring interest as a comparison to other types of carbon materials.

1.5.1.1. Structure of HOPG

HOPG is a polycrystalline material composed of multiple layers of graphene sheets stacked on top of each other and held together by weak attractive intermolecular forces, making a three-dimensional structure.

Graphene is an atom-thick sheet of sp^2-bonded carbon atoms that are arranged in a two-dimensional honeycomb crystal lattice. Each carbon atom in graphene is bonded to each of its three nearest neighbours by a strong planar σ-bond from sp^2 hybridised orbitals. The C-C σ-bonds are 0.142 nm long, at an angle of 120˚ to each other and are responsible for the planar structure of graphene as well as its exceptional mechanical and thermal properties (Figure 1.14(a)). The fourth valence electron of carbon, in the half-filled $2p_z$

orbital form weak π-bonds by overlap with other $2p_z$ orbitals orthogonal to the graphene plane as shown in Figure 1.14(b). This layered property results in anisotropy of the bulk HOPG material shown by significant differences in the mechanical strength and electrical conductivity between and within the graphene planes.

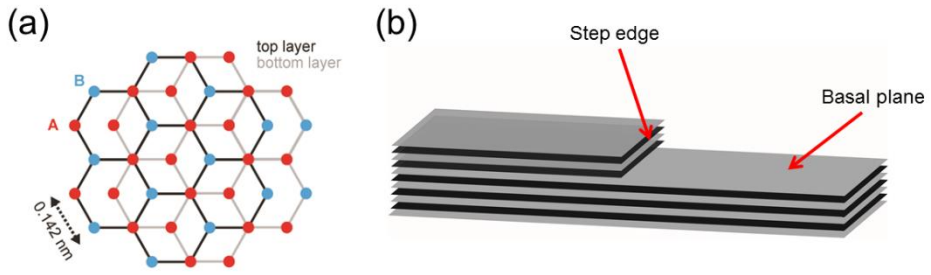

Figure 1.14 Schematic showing (a) the arrangement of carbon atoms and (b) the layered structure of HOPG with basal and edge plane.

Mis-orientation of the graphene layers with respect to each other is known as the "mosaic spread" and is a parameter to quantify the degree of perfection of HOPG. Commercially available HOPG samples are termed SPI-1 and SPI-2 from SPI Supplies and ZYA, ZYB, ZYD and ZYH from GE Advanced Ceramics. The highest quality samples are ZYA and SPI-1 with mosaic spread of 0.4 ± 0.1˚. HOPG grades of lower quality are: ZYB and SPI-2 (mosaic spread 0.8 ± 0.2˚); ZYD (1.2 ± 0.2˚); and ZYH or SPI-3 grades (3.5 ± 1.5˚). An exceptionally high-quality but ungraded HOPG sample, originating from Dr. A. Moore, Union Carbide (now GE Advanced Ceramics), termed AM herein, exhibits a low density of step edges and large basal plane areas, and has been used extensively.[33,36,39,40,55,184,216–223]

HOPG is particularly suitable for providing large areas of pristine, clean atomically flat surfaces by simple exfoliation using Scotch tape to peel off the top layers of HOPG revealing a fresh surface.[180,184,186–189] Although this is common practice mechanical cleavage procedures are also available.[55,58,221,223,224,227] Figure 1.15 shows typical AFM images of the surface topography of 6 different grades of HOPG clearly illustrating that both basal and edge plane sites can be found, with a wide range of step-edge densities

evident across these different samples. AM HOPG provides the most superior surface in terms of low step density with other grades of HOPG showing increasing step-edge densities in the order ZYA, ZYH, SPI-1, SPI-2 and SPI-3.

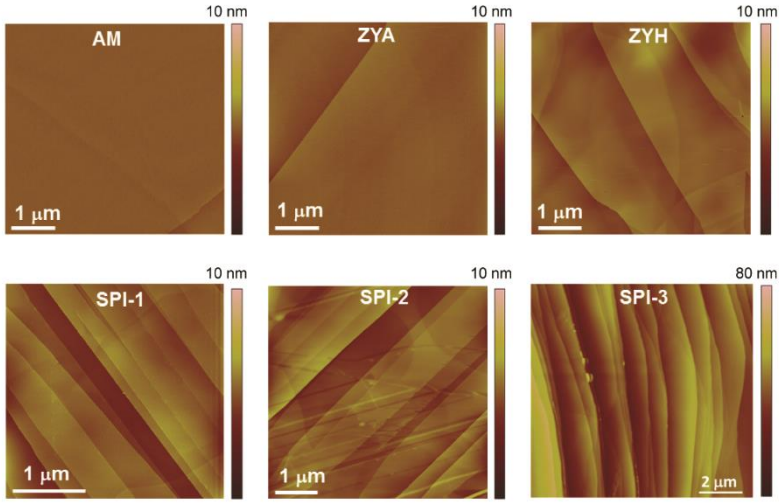

Figure 1.15 AFM images of freshly cleaved HOPG surfaces of different grades, highlighting the significant differences in topographical structure. Note the differences in scale bars (lateral and height).[55,215,227]

The step-edge character is defined in two ways: (i) as the step-edge length (μm) in unit area of the surface (μm^2), not taking account of the step height (monolayer, bilayer, etc.) and (ii) as the total step edge area per unit geometric area of the surface, which takes account of different step edge height. These measures highlight the fact that the average step-edge coverage varies significantly across the different grades by more than 2 orders of magnitude, and that within a grade the range can vary by approximately an order of magnitude from one area (image) to another and is summarised in Table 1.1.

Table 1.1 Summary of some of the key properties of the different grades of HOPG.[55,215,227]

	AM	**ZYA**	**ZYH**	**SPI-1**	**SPI-2**	**SPI-3**
mosaic spread	–	0.4 ± 0.1˚	3.5 ± 1.5˚	0.4 ± 0.1˚	0.8 ± 0.2˚	3.5 ± 1.5˚
Step-edge density range (μm μm^{-2})	0.003 – 0.12	0.1 – 0.7	0.5–2.3	0.3–3.6	1.0 – 3.5	2.5 – 21.9
Mean step edge density (μm μm^{-2})	0.02 ± 0.02	0.5 ± 0.1	1.2 ± 0.6	1.5 ± 0.2	2.1 ± 0.9	8.0 ± 5.8
Step-edge coverage range (%)	0.006 – 0.48	0.03 – 1.0	0.2 – 2.1	0.5 – 3.4	0.6 – 6.7	10.1 – 78.0
Average step-edge coverage (%)	0.09 ± 0.09	0.3 ± 0.25	0.8 ± 0.4	1.7 ± 1.6	2.2	30 ± 24
Capacitance (μF cm^{-2})	2.4 ± 1.5	2.0 ± 0.3	–	2.9 ± 1.2	–	–

1.5.1.2. Electronic Properties of HOPG

A particular feature of the band structure of HOPG is that around the intrinsic Fermi level, the density of state (DOS) is low (about 0.0022 states atom^{-1} eV^{-1}),[215] as shown in Figure 1.16(a) along with the position of the standard potential of some commonly studied redox couples. This contrasts with metals such as Au, for which the DOS is around 0.28 states atom^{-1} eV^{-1} and is constant for a wide range of energies.[37] An important – and still open – general question in electrochemistry is whether (and when) the DOS of metal (and metal-like) electrodes is important in determining ET kinetics and whether the low DOS of graphite has a particularly significant effect. The low DOS of graphite also leads to a low interfacial capacitance between the electrode and electrolyte, of the order of a few μF cm^{-2} (Table 1.1), compared with metal electrodes that exhibit values of at least 1 order of magnitude larger.[46,55,227] Scanning tunnelling spectroscopy (STS) studies have also led to the determination the DOS of step-edges of different chirality (zigzag or armchair),[228] showing clear enhancement in the DOS at zigzag edges, compared to the basal surface, but not at the armchair edges. The DOS at graphitic materials can also be modified due to disorder in the crystal structure, and by the presence of step edges,[228,229] local defects,[230,231] or rotation/detachment of the graphene planes due to the turbostratic nature of HOPG.[232–234] The implications of the DOS of graphite materials for electrochemistry are further discussed in Section 1.5.1.4.

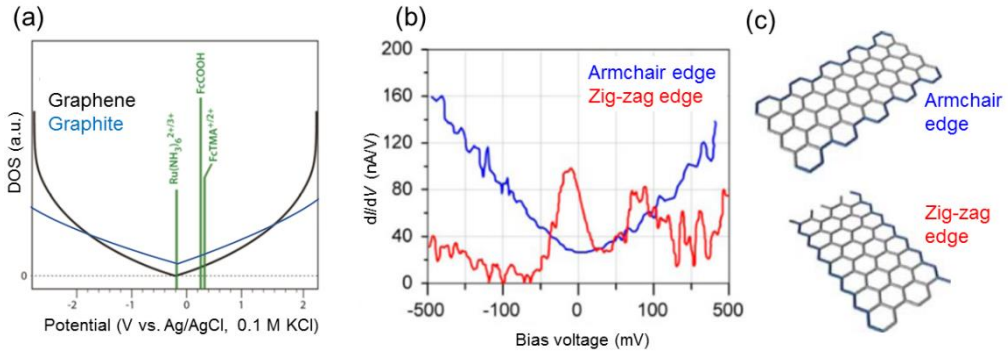

Figure 1.16 (a) The position of standard potentials for commonly used redox couples plotted against the band structure for graphene and graphite.[215] (b) Experimental STS spectra as a function of edge termination.[235] (c) Structure of armchair and zigzag edges.[214]

1.5.1.3. Macroscopic Studies at HOPG

Early electrochemical studies of redox reactions at graphite predominantly with cyclic voltammetry (CV) found that the apparent standard rate constant, k^0, for several redox processes, especially the ferri/ferrocyanide redox couple, $Fe(CN)_6^{3-/4-}$ in aqueous solution, were extremely variable (by many orders of magnitude) even on the same grade of HOPG.[33] CVs of $Fe(CN)_6^{3-/4-}$ resulted in a mean peak-to-peak separation, ΔE_p of 459 ± 331 mV and a range of 58 – 1200 mV[39–41] which can be interpreted as the standard rate constant (for the entire surface) changing by at least 6 orders of magnitude. It was postulated that the reaction could be driven by surface defects[37,38] and so surface modification procedures were introduced to determine the relationship between carbon microstructure and heterogeneous ET.[33–38] Increased edge plane density (as revealed by Raman spectroscopy (~1360 cm^{-1} band or D-band)) appeared to correlate with increased electron transfer rates from which it was concluded that the basal surface of HOPG was essentially inactive or of very low activity, with edge plane defects providing essentially all the activity. However, it is important to comment on the usefulness of Raman analysis for quantifying step-edge density on HOPG samples, as Raman spectra can only highlight relatively highly defective samples. Many different grades of HOPG yield the same defect-free spectra.[55]

Comparisons were often made between electrochemical activities of the highest quality (low step-edge density) AM grade HOPG and laser-activated glassy carbon (GC).

For eight quasi-reversible one electron redox systems, the GC rates were 1-5 orders of magnitude higher than those measured at AM grade HOPG samples and this effect was attributed to the high density of edge sites on GC and the low DOS of HOPG.[40] The impact of laser ablation of HOPG resulting in k^0 increasing by more than 5 orders of magnitude was concluded to be due to increase in the capacitance, C^0, by a factor of 8, and, by inference, the step-edge density. However, more recent studies on the double layer capacitance of graphite suggest that capacitance is a weak indicator of surface quality.[236]

The advancement of modern modelling techniques found HOPG as a model sample for the development of spatially heterogeneous electron transfer modelling strategies.[65,237–239] Finite difference simulations were developed with some spatial zones (edges) being more active than others (basal surface), with the ratio depending on the quality of the HOPG sample. This large body work concluded that the oxidation of $Fe(CN)_6^{4-}$ only occurs at HOPG step edges, with the k^0 for the basal plane < 10^{-9} cm s^{-1}, at least 10^7 times lower than at edge planes, such that the basal plane had essentially no influence on voltammetry. However, this model could not be used quantitatively to determine the edge plane coverage of cleaved HOPG surfaces because in order to model the data, the edge plane coverage applied theoretically had to be 100 times smaller than the actual step-edge coverage value (from AFM).[65,239]

Recent CV measurements[227] of the $Fe(CN)_6^{3-/4-}$ couple found reversible (fast ET) on 4 grades of freshly cleaved HOPG samples contrasting previous studies.[39–41] However, repetitive potential cycling found the ΔE_p values increasing monotonically with a dramatic change in wave shape and decreased current magnitude.[227] This phenomenon of surface passivation/blocking has a serious impact on previous models of electron transfer at graphite electrodes which relied heavily on $Fe(CN)_6^{3-/4-}$ as a 'validation' method for identifying low defect samples.

1.5.1.4. Microscopic Studies at HOPG

Electrochemical scanning probe microscopy (EC-SPM) techniques are able to test the models derived from earlier measurements, producing results that lead to a new perspective on HOPG electrochemistry for a range of reactions, including classical outer-sphere couples,[180,188,207] multistep electron-proton coupled reactions,[55,56] and processes leading to adsorption[98,240] and the modification of the HOPG surface.[58]

Notably, the development of scanning electrochemical cell microscopy (SECCM)[188,198] provided the means of probing the electroactivity of tiny regions upon a HOPG surface, defined by a small area of meniscus contact between an electrolyte solution in a micropipette or nanopipette and a surface (electrode) of interest. The SECCM technique is particularly powerful when complemented by other forms of microscopy applied to the same areas as the electrochemical imaging, in a methodology termed 'the multi-microscopy approach'.[188,202,203,241–245]

Reactive Patterning of Neurotransmitter Oxidation

Neurotransmitters, such as dopamine (DA) and epinephrine (EP) are catecholamines that undergo complex multistep oxidation processes in aqueous solution via coupled ET, proton transfer ($2e^-$, $2H^+$ at physiological pH), but with the complication of side reactions to form melanin-like compounds that can block electrode surfaces.[246] Such processes are expected to follow a classical scheme of squares[247] and are of considerable interest for the practical detection of neurotransmitters, as carbon electrodes have become the electroanalytical platform of choice.[9,55] This is due to a desirable range of properties including biocompatibility, chemical inertness and low background current which provides lower detection limits, wide potential windows and low cost. Understanding the electrochemical activity of neurotransmitters on carbon electrodes is thus of considerable importance in the design of optimal bio-sensor platforms.

Recent reappraisals of the electrochemical oxidation of DA and EP on HOPG using macroscale CV, SECCM, and SECM has demonstrated that the long-standing view of

graphite edges being solely responsible for catalysing the electro-oxidation of neurotransmitters[239,248,249] is incorrect.[55–57,250] Rather, the electrochemical response of catecholamines has been shown to be rapid on the basal surface of HOPG, but with surface fouling occurring readily due to oligomeric side-products. SECCM studies were designed to take advantage of this by moving the liquid meniscus across the surface at a rate such that the electrode reaction was measured on the basal surface at high resolution, but polymeric products were left behind on the surface that acted as surface markers ('reactive patterning'). This allowed the electrochemical activity (Figure 1.17(b)), complemented by the DC (Figure 1.17(c)) and the AC (Figure 1.17(d)) conductance current maps, to be related directly to the local surface character by use of complementary microscopy techniques, namely AFM (Figure 1.17(e)) or SEM,[56] applied to the same area.[56,57]

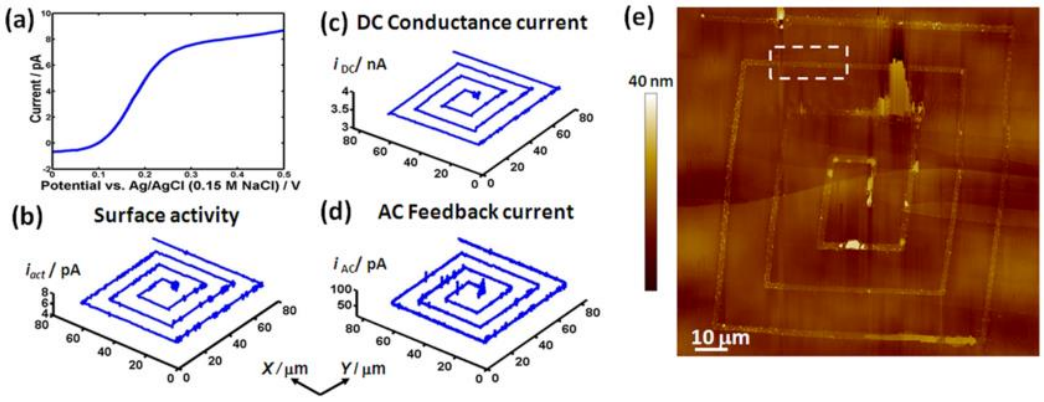

Figure 1.17 (a) SECCM LSV for the oxidation of 100 µM DA at 0.1 V s^{-1}. (b–d) SECCM reactive patterning maps for DA electro-oxidation, (b) surface activity, (c) DC component of the conductance current and (d) AC component of the conductance current used for feedback. (e) AFM image of the HOPG surface showing the SECCM deposited pattern.[57]

The responses for DA and EP electro-oxidation on ZYA and SPI-3 grades of HOPG were studied by recording consecutive CVs (Figure 1.18).[55,56] In both cases, the recorded CVs are near identical in terms of both the initial response and the subsequent deterioration pattern on successive potential cycling. Given that the two surfaces differ dramatically in step-edge coverage (2 orders of magnitude), a reasonable deduction would be that the reaction is dominated by the basal surface. In fact for DA electro-oxidation, many different

grades of HOPG were investigated and the CV responses (10 cycles) were essentially similar across all grades.[55,56]

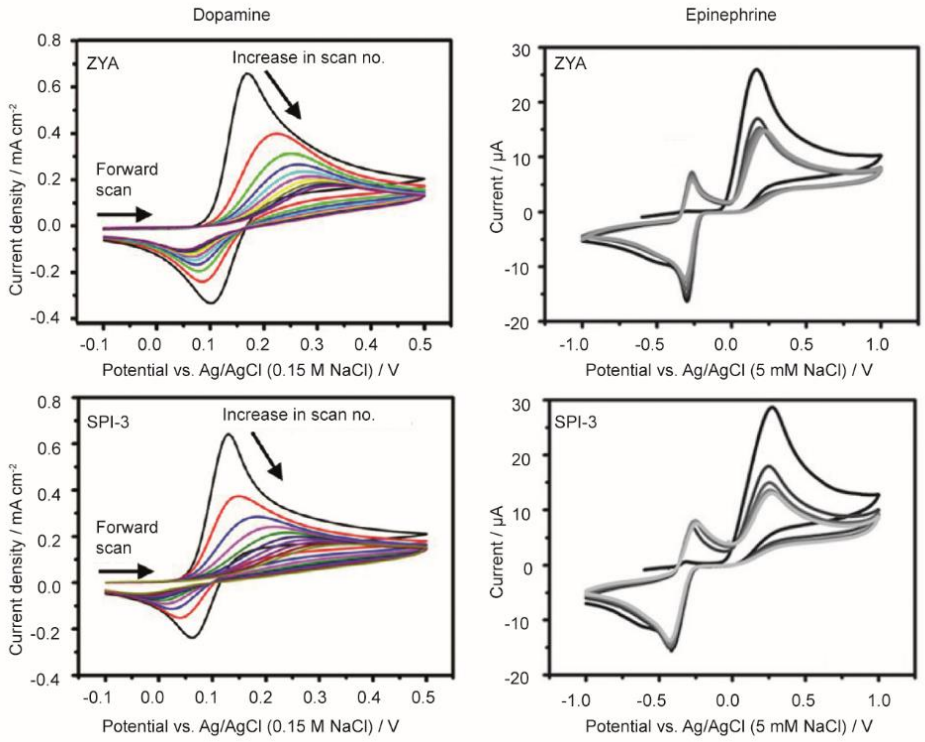

Figure 1.18 Macroscopic CVs for the oxidation of 1 mM DA (left panel) and 1 mM EP (right panel) on freshly cleaved surfaces of ZYA and SPI-3 grade HOPG, at a scan rate of 0.1 V s^{-1}.[55,56]

Dynamic Imaging of Outer-Sphere Redox Couples

A wide range of outer-sphere redox couples, including $Fe(CN)_6^{4-/3-}$, $IrCl_6^{3-/2-}$ and ferrocenylmethyl trimethylammonium ($FcTMA^{+/2+}$), undergo fast, reversible ET at HOPG[180,198,220,227] on the typical voltammetric timescale, as found using both macroscopic CV[220,223,227] and high resolution SECCM.[180,198,199,251] Indeed the kinetics are similar to, or faster than, on platinum,[220] in contrast to earlier work which reported ultra-slow kinetics.[38–41]

Contrastingly, macroscopic voltammetric measurements reveal a time-dependent behaviour after HOPG cleavage, peculiar to the $Ru(NH_3)_6^{3+/2+}$ redox couple and is not associated with surface contamination.[227] This behaviour is found to be attributed to the

spontaneous delamination of the HOPG with time to create partially coupled graphene layers, further supported by conductive AFM measurements.[180,227] This delamination process has a major impact on the density of states on the graphite basal and edge sites, particularly at the intrinsic Fermi level to which $Ru(NH_3)_6^{3+/2+}$ redox couple is most sensitive.[215]

For a more detailed assessment of the electrochemical behaviour of aged AM grade HOPG samples, SECCM was operated in SECCM-LSV mode to allow both potential and spatial resolution of the HOPG electrochemical activity. Figure 1.19(a) shows a snapshot of the electrochemical activity of the scanned area at approximately the mid-wave potential and shows enhanced activity at the step edges of the HOPG surface. Analysis of the individual LSVs obtained on pure basal surfaces and basal-and-edge surfaces using the Butler-Volmer formulation gave $k^0 \sim 0.5$ cm s^{-1} and $\alpha = 0.5$ (at the reversible limit) as shown in Figure 1.19(b). However, the formal potentials needed to produce a good data fit were more cathodic than the values obtained from CV measurements at Pt or freshly cleaved HOPG, which clearly indicates an inapplicability of the classical model. This however suggested that the observed overpotential of the voltammetric wave on the basal plane, at least in part, is related to the position of the standard (formal) potential of $Ru(NH_3)_6^{3+/2+}$ redox couple which is close to the intrinsic Fermi level of graphene where the DOS is theoretically zero. Likewise, the smaller overpotential on the edge is a consequence of the higher DOS at graphene edges, near the intrinsic Fermi level.

On this basis, a so-called potential-dependent pre-exponential factor, A_{basal} and A_{edge}, was introduced to in place of k^0 in the Butler-Volmer formulation to demonstrate how electrochemical activity of the individual structural components of a HOPG substrate varied with potential applied. Figure 1.19(c) shows $A_{edge} >> A_{basal}$ for all potentials, as expected based on the enhanced activity at the step edges. This approach is reasonable and somewhat analogous to the unified expression for the rate constant for adiabatic and non-adiabatic ET in the quantum perturbation theory where the rate constant from the Butler-Volmer model is multiplied by a potential-dependent ratio that originates from a consideration of both the electronic states in the electrode and a redox couple (see Section 1.2.2.2).

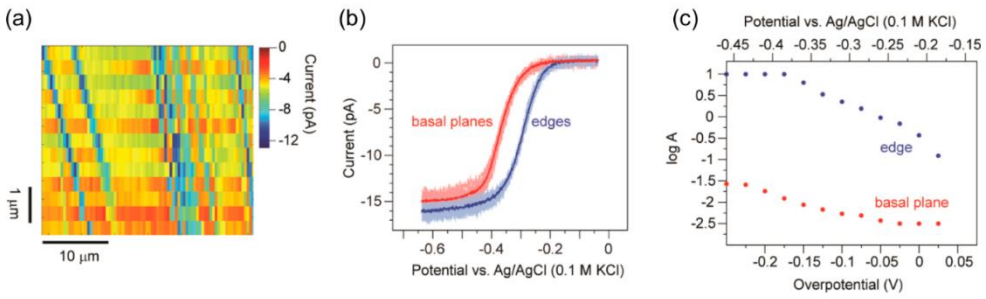

Figure 1.19 (a) The electrochemical SECCM map for the reduction of $Ru(NH_3)_6^{3+}$ at aged AM grade HOPG at η = -0.11 V. (b) SECCM-LSV taken at pure basal (red) and basal-and-edge (blue) regions fitted to Butler-Vomer kinetics. (c) Pre-exponential factors, A_{basal} and A_{edge}, as a function of potential extracted from curves in (b).

1.5.2. Polycrystalline Boron-Doped Diamond (pBDD)

Diamond electrodes gained interest in the field of electrochemistry for its favourable electrochemical properties including wide solvent windows, low capacitive currents, resistance to surface fouling and the ability to be used in extreme (high temperatures and corrosive) environments as well as biocompatibility.[43]

1.5.2.1. Structure and Electronic Properties of pBDD

Diamond is an allotrope of carbon made up of sp^3-bonded atoms tetrahedrally arranged as shown in Figure 1.20. The fundamental properties of diamond can be attributed to the single σ-bonds (0.154 nm) that bind the carbon atoms at a 109.5^o angle.

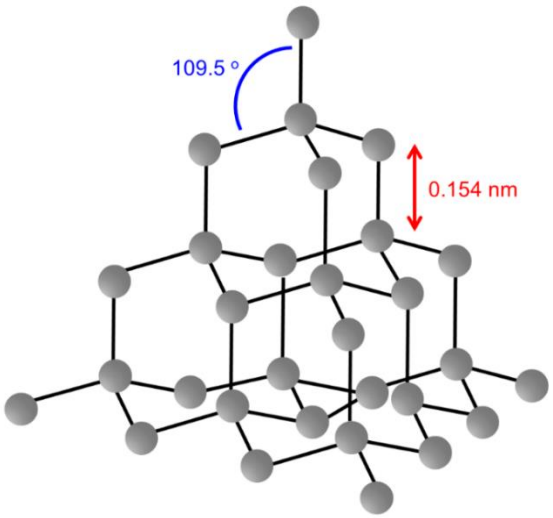

Figure 1.20 Schematic showing the arrangement of carbon atoms in a diamond crystal lattice.

Intrinsically, diamond is a very wide band gap semiconductor (5.47 eV at 300 K).[17,43] However, incorporation of dopants into the diamond lattice is a means of imparting electrical conductivity into the diamond material for electrochemical applications. Doping with an n-type dopant (such as nitrogen atoms) gives electron charge carriers while p-type dopants (such as boron) produce holes as charge carriers in the now conducting material. As boron dopant replaces carbon atoms in the lattice structure with a relatively small activation energy (0.37 eV) compared to nitrogen (1.7 eV), high dopant concentrations are achievable and hence boron-doped diamond (BDD) is the preferred diamond material for electrochemical studies.

Boron dopant concentration, [B], significantly affects the conductivity of the diamond electrode as shown in Figure 1.21.[17,42,43] The incorporation of boron dopants creates a band acceptor level at 0.37 eV above the valence band. When [B] ~ 10^{16} – 10^{19} cm^{-3}, the material has the resistivity behaviour of a p-type semi-conductor. The implication is the depletion of charge carriers at electrode potentials negative to the flat band potential, E_{fb}. As the [B] is increased to ~ 10^{19} – 10^{20} cm^{-3}, the resistivity of the material drops and the electrical conduction is expected to occur via a hopping mechanism. At [B] ≥ 10^{20} cm^{-3}, the diamond electrode is degenerately doped and has semi-metallic or metal-like

properties, but has a reduced number of charge carriers or density of states compared to metallic electrodes.

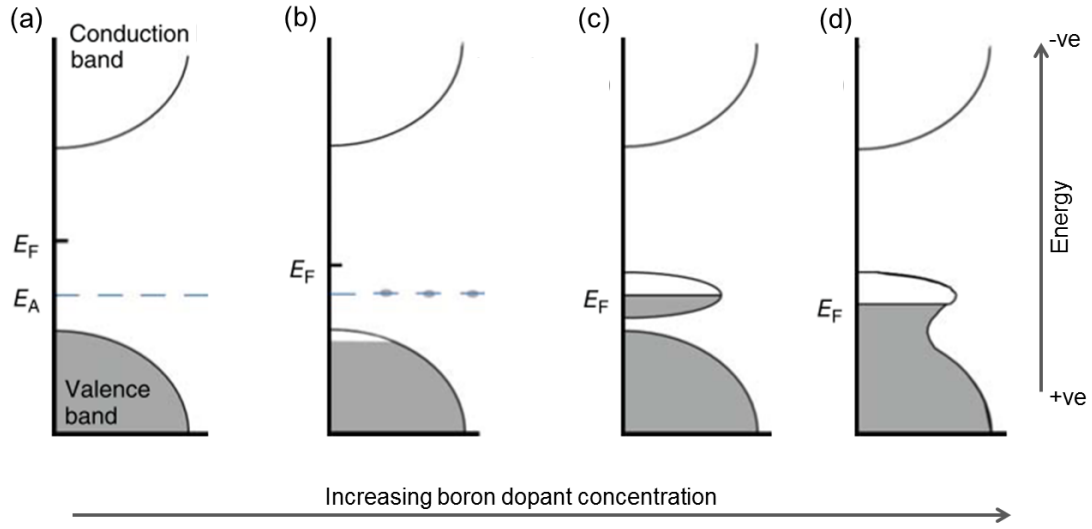

Figure 1.21 The evolution of the electronic density of states and band structure of diamond with increasing concentrations of boron dopants. (a) Insulating diamond has a wide band gap with the Fermi level, E_F, located mid-gap. (b) The number of charge carriers in the valence band depends on the concentration and the ionisation energy of the boron acceptors, E_A. The Fermi level moves towards the top of the valence band. (c) Metal-insulator transition takes place. (d) Very high [B] ($\geq 10^{20}$ cm^{-3}) modifies the acceptor activation energy and reduces the intrinsic band gap energy.[17,42,43]

Commercially available diamond electrodes are grown using the chemical vapour deposition (CVD) methodologies on suitable polycrystalline substrates for the growth of polycrystalline boron-doped diamond (pBDD) electrodes. The resultant grain size depending on growth conditions such as time, temperature, pressure and gas composition. Hence, BDD electrode can be categorised as follows: (i) ultra-nanocrystalline (UNC), grain size < 10 nm, (ii) nanocrystalline (NC), grain size in the range of 10 nm – 1 μm and (iii) microcrystalline (MC), grain size > 1 μm. Scanning electron microscopy (SEM) is the best way of visualising the different categories of pBDD electrode as shown in Figure 1.22. The uptake of boron dopants is also grain-dependent ((111) > (110) > (100)) and results in a highly heterogeneously doped electrode material. The implication for electrochemistry are discussed below.

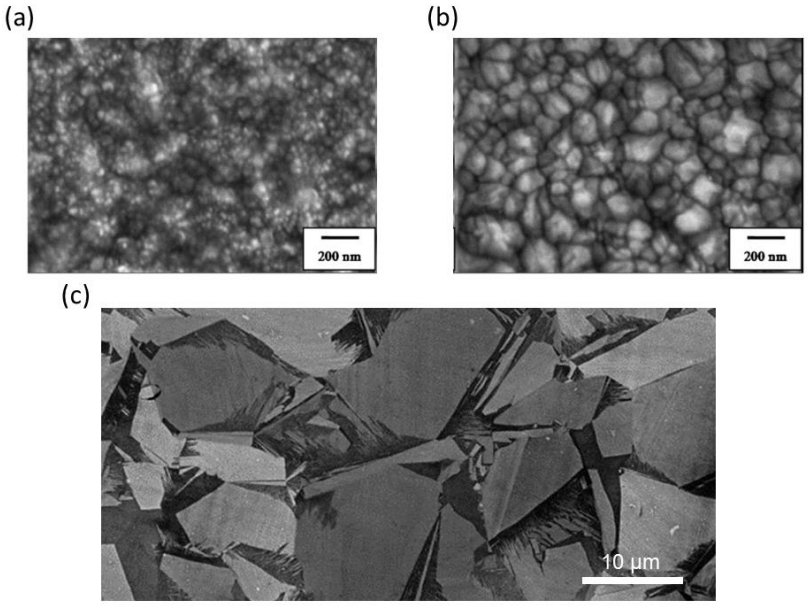

Figure 1.22 SEM images of (a) UNC BDD thin film electrode,[252] (b) NC BDD thin film electrode[252] and (c) polished MC BDD free-standing electrode. The darker areas in the image represent regions of higher boron dopant content.[99,253]

1.5.2.2. Electrochemistry at pBDD Electrodes

The electrochemical response of pBDD, with a range of boron concentrations have been studied with CV for a range of outer-sphere redox couples.[28,55,252,254–263] In almost all investigations, faster electron transfer rates have been observed at heavily doped samples.[25,99,262] CVs for two such examples are shown in Figure 1.23 for the redox reactions of $FcTMA^+$ and $Ru(NH_3)_6^{3+}$ at MC BDD samples containing boron dopant densities ranging from $9.2 \times 10^{16} – 3 \times 10^{20}$ B atoms cm^{-3}. For both redox species, as the boron concentration increases, the peak separation values, ΔE_p, decrease indicative of faster electron transfer. This is as expected given the material approaches 'metal-like' behaviour at concentration ~ > 10^{20} B atoms cm^{-3}. However, it is evident for all boron dopant concentrations < 10^{20} B atoms cm^{-3}, that the ΔE_p measured for $Ru(NH_3)_6^{3+/2+}$ is larger than for $FcTMA^{+/2+}$. This phenomenon is attributed to the more negative potential of the $Ru(NH_3)_6^{3+/2+}$ redox couple, where the overall concentration of charge carriers is

depleted. Further investigation of different parts of the electronic band structure using simple redox mediators with different standard potentials is discussed in Chapter 2.

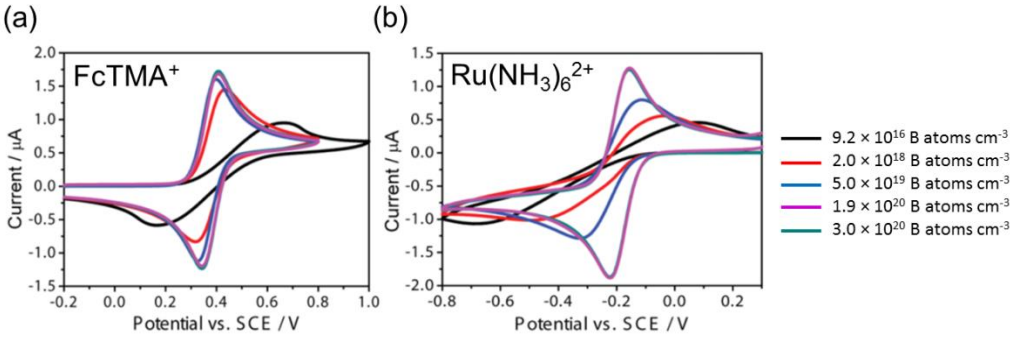

Figure 1.23 CV for the (a) oxidation of $FcTMA^+$ and (b) reduction of $Ru(NH_3)_6^{3+}$ at pBDD at a scan rate of 0.1 V s^{-1}.

While most investigations focus on the study of pBDD electrode as a whole – macroscopic response (as discussed above) – BDD is a highly heterogenous electrode material due to its polycrystalline structure and varying boron dopant content. Electrochemical imaging techniques, such as SECM in particular, have been employed to investigate this heterogeneous nature, with the main debate involving the electrochemical activity of grain boundaries.[173,264,265] Early studies of pBDD electrodes with SECM constant height mode in both SG/TC[125] and feedback mode[173] with 2 µm and 25 µm probe sizes, respectively, revealed heterogeneous electron transfer activity at MC BDD substrates for the $Ru(NH_3)_6^{3+/2+}$ process.

More recently, quantitative SECM studies on MC BDD samples with both $FcTMA^+$ and $Ru(NH_3)_6^{3+}$ reveals two distinct electron transfer rate constants, differing by a factor of ~ 4, corresponding to high and low doped grains on the electrode surface, corroborated by SEM imaging,[99] and are 10^2 – 10^3 times smaller than at metallic electrode.[112,141,185] Voltammetry measurements at macroelectrodes have also found that, in general, k^0 values measured at pBDD are smaller than at conventional metal electrodes[28,46,263] and is attributed to the reduced DOS of pBDD.

By using the small probe of SECCM, it was possible to measure the capacitance for these two different regions: 5.2 ± 0.8 and 3.1 ± 0.4 µF cm^{-2} at 0 V versus Ag|AgCl.

From these values, a local DOS was determined[31,32,266] to be ~ 6.3 (± 2.0) × 10^{20} cm^{-3} eV^{-1} and ~ 1.7 (± 0.7) × 10^{20} cm^{-3} eV^{-1}, respectively, that is, a difference of about 4, correlating well with the factor of 4 difference in k^0 for the differently doped regions of the surface.[99] Dual-electrode micro-trench diamond geometries have also been reported.[267]

1.6. Thesis Aims

The major aim of this thesis is to improve analysis strategies and electrochemical methodologies using both macroscale and microscale techniques while testing present views on electron transfer, particularly at complex electrode materials such as polycrystalline boron-doped diamond (pBDD). Each chapter is self-contained and based on published journal articles.

Chapter 2 concerns a direct comparison of the use of Fourier-transformed large amplitude alternating current voltammetry (FTACV) and substrate-voltammetry scanning electrochemical microscopy (SECM) for measurements of fast electron transfer processes in organic media. Differences in the capabilities of each techniques are highlighted along with a detailed description of established numerical and analytical analysis strategies. The impact of both techniques is studied on the complex heterogeneously active surface of pBDD further highlighting the importance of understanding the influence of the measurement technique and demonstrating how electron transfer kinetics at pBDD differs from conventional electrode materials.

Chapter 3 focuses on the importance of understanding the physicochemical characteristics of an electrochemical system in the SECM configuration. The development of nanoscale and nanogap electrode configurations with surface area-to-solution volume ratios realises the need for more vigorous data analysis procedures where surface effects (adsorption onto the electrode and glass surfaces, in this case) are important and impact the voltammetric response. The consequence of these surface effects on the interpretation of the apparent electron transfer and mass transport are highlighted.

Electrode heterogeneity is ubiquitous in modern electrochemistry, particularly with the emergence of a plethora of carbon based electrode materials. Chapter 4 describes a novel analysis strategy for kinetic selectivity at a dual-heterogeneity macroelectrode surfaces using FTACV. The high kinetic sensivity of FTACV facilitates the deconvolution of electrochemical response complicated by surface heterogeneities into its individual responses in an initial study of a highly-simplified example where the k^0 values of the different kinetic regimes were at least an order of magnitude apart.

Chapter 5 further explores the capabilities of FTACV for kinetic selectivity by taking advantage of the harmonic-dependent measurement timescales to elucidate a dual-heterogeneity electrochemical response into its individual components regardless of domain size ratio and provided one of the processes is reversible, while the other is quasi-reversible (achievable with careful selection of the FTACV measurement timescale) and mass transport is appropriately described by 1D diffusion with overlap of diffusion layers being negligible.

Lastly, concluding remarks and the direction of future work are presented in Chapter 6.

1.7. References

(1) Bard, A. J.; Faulkner, L. R. *Electrochemical Methods: Fundamentals and Applications*, 2nd ed.; Wiley: New York, 2001.

(2) Gabe, D. R.; Walsh, F. C. *J. Appl. Electrochem.* **1983**, *13* (1), 3–21.

(3) Treimer, S.; Tang, A.; Johnson, D. C. *Electroanalysis* **2002**, *14* (3), 165.

(4) Opekar, F.; Beran, P. *J. Electroanal. Chem. Interfacial Electrochem.* **1976**, *69* (1), 1–105.

(5) Barnes, E. O.; Lewis, G. E. M.; Dale, S. E. C.; Marken, F.; Compton, R. G. *Analyst* **2012**, *137* (5), 1068.

(6) Zevenbergen, M. A. G.; Wolfrum, B. L.; Goluch, E. D.; Singh, P. S.; Lemay, S. G. *J. Am. Chem. Soc.* **2009**, *131*, 11471–11477.

(7) Amatore, C.; Lemmer, C.; Sella, C.; Thouin, L. *Anal. Chem.* **2011**, *83* (11), 4170–4177.

(8) Wang, R. L.; Tam, K. Y.; Compton, R. G. *J. Electroanal. Chem.* **1997**, *434*, 105–114.

(9) Sansuk, S.; Bitziou, E.; Joseph, M. B.; Covington, J. A.; Boutelle, M. G.; Unwin, P. R.; MacPherson, J. V. *Anal. Chem.* **2013**, *85* (1), 163–169.

(10) Fietkau, N.; Clegg, A. D.; Evans, R. G.; Villagran, C.; Hardacre, C.; Compton, R. G. *ChemPhysChem* **2006**, *7* (5), 1041–1045.

(11) Singh, P. S.; Chan, H.-S. M.; Kang, S.; Lemay, S. G. *J. Am. Chem. Soc.* **2011**, *133*, 18289–18295.

(12) Compton, R. G.; Unwin, P. R. *J. Electroanal. Chem. Interfacial Electrochem.* **1986**, *205* (1–2), 1–20.

(13) Macpherson, J. V.; Marcar, S.; Unwin, P. R. *Anal. Chem.* **1994**, *66*, 2175–2179.

(14) Martin, R. D.; Unwin, P. R. *J. Electroanal. Chem.* **1995**, *397*, 325–329.

(15) Macpherson, J. V; Jones, C. E.; Unwin, P. R. *J. Phys. Chem. B* **1998**, *102*, 9891–9897.

(16) Gosavi, S.; Marcus, R. A. *J. Phys. Chem. B.* **2000**, *104*, 2067–2072.

(17) Macpherson, J. V. *Phys. Chem. Chem. Phys.* **2015**, *17* (5), 2935–2949.

(18) Zeng, Y.; Smith, R. B.; Bai, P.; Bazant, M. Z. *J. Electroanal. Chem.* **2014**, *735*, 77–83.

(19) Laborda, E.; Henstridge, M. C.; Batchelor-McAuley, C.; Compton, R. G. *Chem. Soc. Rev.* **2013**, *42* (12), 4894–4905.

(20) Kozub, B. R.; Henstridge, M. C.; Batchelor-McAuley, C.; Compton, R. G. *Int. J. Electrochem. Sci.* **2011**, *6* (12), 6047–6062.

(21) Nissim, R.; Batchelor-McAuley, C.; Henstridge, M. C.; Compton, R. G. *Chem. Commun.*

2012, *48* (27), 3294.

(22) Gerischer, H. *Electrochim. Acta* **1990**, *35* (I), 1677–1699.

(23) Gerischer, H. *J. Phys. Chem.* **1991**, *95* (3), 1356–1359.

(24) Peter, L. M. *Semiconductor electrochemistry*; 2016.

(25) Latto, M. N.; Pastor-Moreno, G.; Riley, D. J. *Electroanalysis* **2004**, *16* (6), 434–441.

(26) Marcus, R. A. *J. Chem. Phys.* **1956**, *24* (5), 966.

(27) Yang, D.; Meng, G.; Zhang, S.; Hao, Y.; An, X.; Wei, Q.; Ye, M.; Zhang, L. *Chem. Commun.* **2007**, *1* (17), 1733–1735.

(28) Pleskov, Y. V. *J. Anal. Chem.* **2000**, *55* (11), 1045–1050.

(29) Chen, D.; Tang, L.; Li, J. *Chem. Soc. Rev.* **2010**, *39* (8), 3157.

(30) Eda, G.; Mattevi, C.; Yamaguchi, H.; Kim, H.; Chhowalla, M. *J. Phys. Chem. C* **2009**, *113* (35), 15768–15771.

(31) Gerischer, H. *J. Phys. Chem.* **1985**, *89* (20), 4249–4251.

(32) Gerischer, H.; McIntyre, R.; Scherson, D.; Storck, W. *J. Phys. Chem.* **1987**, *91* (7), 1930–1935.

(33) Bowling, R. J.; Packard, R. T.; McCreery, R. L. *J. Am. Chem. Soc.* **1989**, *111* (4), 1217–1223.

(34) Bowling, R. *J. Electrochem. Soc.* **1988**, *135* (6), 1605.

(35) Rice, R.; Allred, C.; McCreery, R. *J. Electroanal. Chem.* **1989**, *263* (1), 163–169.

(36) Rice, R. J.; McCreery, R. L. *Anal.Chem.* **1989**, *61*, 1637–1641.

(37) McCreery, R. L. *Chem. Rev.* **2008**, *108* (7), 2646–2687.

(38) McCreery, R. L.; McDermott, M. T. *Anal. Chem.* **2012**, *84* (5), 2602–2605.

(39) Cline, K. K.; Mcdermott, M. T.; Mccreery, R. L. *J. Phys. Chem.* **1994**, *98*, 5314–5319.

(40) Kneten, K. R.; McCreery, R. L. *Anal. Chem.* **1992**, *64* (21), 2518–2524.

(41) Mcdermott, M. T.; Kneten, K.; Mccreery, R. L. *J. Phys. Chem.* **1992**, *96* (14), 3124–3130.

(42) Blase, X.; Bustarret, E.; Chapelier, C.; Klein, T.; Marcenat, C. *Nat. Mater.* **2009**, *8* (5), 375–382.

(43) Macpherson, J. V. In *Electrochemistry of Carbon Electrodes*; Bartlett, P. N., Alkire, R. C., Lipkowski, J., Eds.; Wiley-VCH, 2016; pp 163–210.

(44) Zhang, J.; Bond, A. M.; Richardt, P. J. S.; Wedd, A. G. *Inorg. Chem.* **2004**, *43* (26), 8263–8271.

(45) Zhang, J.; Bond, A. M.; MacFarlane, D. R.; Forsyth, S. A.; Pringle, J. M.; Mariotti, A. W. A.; Glowinski, A. F.; Wedd, A. G. *Inorg. Chem.* **2005**, *44* (14), 5123–5132.

(46) Bano, K.; Zhang, J.; Bond, A. M.; Unwin, P. R.; Macpherson, J. V. *J. Phys. Chem. C* **2015**, *119* (22), 12464–12472.

(47) Li, J.; Bond, A. M.; Zhang, J. *Electrochim. Acta* **2015**, *178*, 631–637.

(48) Murphy, M. A.; Wilcox, G. D.; Dahm, R. H.; Marken, F. *Electrochem. commun.* **2003**, *5* (1), 51–55.

(49) Mampallil, D.; Mathwig, K.; Kang, S.; Lemay, S. G. *J. Phys. Chem. Lett.* **2014**, *5*, 636–640.

(50) Cuharuc, A. S.; Zhang, G.; Unwin, P. R. *Phys. Chem. Chem. Phys.* **2016**, *18* (6), 4966–4977.

(51) Bond, A. M.; Mclennan, E. A.; Stojanovic, R. S.; Thomas, F. G. *Anal. Chem.* **1987**, *59*, 2853–2860.

(52) Ekanayake, C. B.; Wijesinghe, M. B.; Zoski, C. G. *Anal. Chem.* **2013**, *85* (8), 4022–4029.

(53) Cannan, S.; Cervera, J.; Steliaros (née Haskins), R. J.; Bitziou, E.; Whitworth, A. L.; Unwin, P. R. *Phys. Chem. Chem. Phys.* **2011**, *13* (12), 5403.

(54) Amatore, C.; Savéant, J. M. **1979**, *102*, 21–40.

(55) Patel, A. N.; Tan, S.-y.; Miller, T. S.; Macpherson, J. V; Unwin, P. R. *Anal. Chem.* **2013**, *85* (24), 11755–11764.

(56) Patel, A. N.; Tan, S.-y.; Unwin, P. R. *Chem. Commun. (Camb).* **2013**, *49* (78), 8776–8778.

(57) Patel, A. N.; Mckelvey, K.; Unwin, P. R. *J. Am. Chem. Soc.* **2012**, *134*, 20246–20249.

(58) Zhang, G.; Kirkman, P. M.; Patel, A. N.; Cuharuc, A. S.; Mckelvey, K.; Unwin, P. R. *J. Am. Chem. Soc.* **2014**, *136*, 11444–11451.

(59) Aoki, K. *Electroanalysis* **1993**, *5* (8), 627–639.

(60) Amatore, C.; Svir, I. *J. Electroanal. Chem.* **2003**, *557*, 75–90.

(61) Pagels, M.; Hall, C. E.; Lawrence, N. S.; Meredith, A.; Jones, T. G. J.; Godfried, H. P.; Pickles, C. S. J.; Wilman, J.; Banks, C. E.; Compton, R. G.; Jiang, L. *Anal. Chem.* **2005**, *77* (11), 3705–3708.

(62) Lee, C.-Y.; Elton, D.; Brajter-Toth, A.; Bond, A. M. *Electroanalysis* **2013**, *25* (4), 931–944.

(63) Belding, S. R.; Dickinson, E. J. F.; Compton, R. G. *J. Phys. Chem. C* **2009**, *113* (25), 11149–11156.

(64) Amatore, C.; Oleinick, A.; Svir, I. *J. Electroanal. Chem.* **2005**, *575* (1), 103–123.

(65) Davies, T. J.; Banks, C. E.; Compton, R. G. *J. Solid State Electrochem.* **2005**, *9* (12), 797–808.

(66) Pebay, C.; Sella, C.; Thouin, L.; Amatore, C. *Anal. Chem.* **2013**, *85* (24), 12062–12069.

(67) Amatore, C.; Oleinick, A.; Svir, I. *J. Electroanal. Chem.* **2004**, *564* (1–2), 245–260.

(68) Dickinson, E. J. F.; Streeter, I.; Compton, R. G. *J. Phys. Chem. C* **2008**, *112* (31), 11637–11644.

(69) Chevallier, F. G.; Fietkau, N.; del Campo, J.; Mas, R.; Muñoz, F. X.; Jiang, L.; Jones, T. G. J.; Compton, R. G. *J. Electroanal. Chem.* **2006**, *596* (1), 25–32.

(70) Forster, R. J. *Chem. Soc. Rev.* **1994**, *23* (4), 289.

(71) Amatore, C.; Pebay, C.; Thouin, L.; Wang, A.; Warkocz, J. S. *Anal. Chem.* **2010**, *82* (16), 6933–6939.

(72) Mirkin, M. V; Bard, A. J. *Anal. Chem.* **1992**, *64* (19), 2293–2302.

(73) Lovelock, K. R. J.; Cowling, F. N.; Taylor, A. W.; Licence, P.; Walsh, D. A. *J. Phys. Chem. B* **2010**, 1–4.

(74) Walsh, D. a; Lovelock, K. R. J.; Licence, P. *Chem. Soc. Rev.* **2010**, *39* (11), 4185–4194.

(75) Bond, A. M. *Analyst* **1994**, *119* (11), 1R.

(76) Hsueh, C.; Brajter-Toth, A. *Anal. Chem.* **1993**, *65* (12), 1570–1575.

(77) Díaz-Ballote, L.; Alpuche-Aviles, M.; Wipf, D. O. *J. Electroanal. Chem.* **2007**, *604* (1), 17–25.

(78) Bond, A. M.; Duffy, N. W.; Guo, S.-X.; Zhang, J.; Elton, D. *Anal. Chem.* **2005**, *77* (9), 186–195.

(79) Guo, S.; Bond, A. M.; Zhang, J. *Rev. Polarogr.* **2015**, *61* (1), 21–32.

(80) Sher, A. A.; Bond, A. M.; Gavaghan, D. J.; Harriman, K.; Feldberg, S. W.; Duffy, N. W.; Guo, S.-X.; Zhang, J. *Anal. Chem.* **2004**, *76* (21), 6214–6228.

(81) Zhang, J.; Guo, S.-X.; Bond, A. M. *Anal. Chem.* **2007**, *79* (6), 2276–2288.

(82) Bano, K.; Bond, A. M.; Zhang, J. *Anal. Chem.* **2015**, *87* (16), 8387–8393.

(83) Bond, A. M.; Bano, K.; Adeel, S.; Martin, L. L.; Zhang, J. *ChemElectroChem* **2014**, *1* (1), 99–107.

(84) Bano, K.; Nafady, A.; Zhang, J.; Bond, A. M.; Inam-ul-Haque. *J. Phys. Chem. C* **2011**, *115* (49), 24153–24163.

(85) Zhang, J.; Guo, S.-X.; Bond, A. M.; Marken, F. *Anal. Chem.* **2004**, *76* (13), 3619–3629.

(86) Guo, S.-X.; Zhang, J.; Elton, D. M.; Bond, A. M. *Anal. Chem.* **2004**, *76* (1), 166–177.

(87) Li, J.; Bentley, C. L.; Bond, A. M.; Zhang, J. *Anal. Chem.* **2016**, *88* (4), 2367–2374.

(88) Amemiya, S.; Bard, A. J.; Fan, F.-R. F.; Mirkin, M. V.; Unwin, P. R. *Annu. Rev. Anal.*

Chem. **2008**, *1*, 95–131.

(89) Bard, A. J.; Fan, F. R. F.; Kwak, J.; Lev, O. *Anal. Chem.* **1989**, *61* (2), 132–138.

(90) Zoski, C. G. *Curr. Opin. Electrochem.* **2017**, *1* (1), 46–52.

(91) Sun, P.; Laforge, F. O.; Mirkin, M. V. *Phys. Chem. Chem. Phys.* **2007**, *9*, 802–823.

(92) Amemiya, S.; Chen, R.; Nioradze, N.; Kim, J. *Acc. Chem. Res.* **2016**, *49* (9), 2007–2014.

(93) Takahashi, Y.; Kumatani, A.; Shiku, H.; Matsue, T. *Anal. Chem.* **2017**, *89* (1), 342–357.

(94) Mirkin, M. V.; Nogala, W.; Velmurugan, J.; Wang, Y. *Phys. Chem. Chem. Phys.* **2011**, *13*, 21196–21212.

(95) McKelvey, K.; Edwards, M. A.; Unwin, P. R. *Anal. Chem.* **2010**, *82* (15), 6334–6337.

(96) Tomlinson, L. I.; Patten, H. V.; Green, B. L.; Iacobini, J.; Meadows, K. E.; McKelvey, K.; Unwin, P. R.; Newton, M. E.; Macpherson, J. V. *Electroanalysis* **2016**, 1–7.

(97) Lazenby, R. A.; McKelvey, K.; Peruffo, M.; Baghdadi, M.; Unwin, P. R. *J. Solid State Electrochem.* **2013**, *17* (12), 2979–2987.

(98) Tan, S.-y.; Zhang, J.; Bond, A. M.; Macpherson, J. V.; Unwin, P. R. *Anal. Chem.* **2016**, *88* (6), 3272–3280.

(99) Patten, H. V.; Meadows, K. E.; Hutton, L. A.; Iacobini, J. G.; Battistel, D.; McKelvey, K.; Colburn, A. W.; Newton, M. E.; Macpherson, J. V.; Unwin, P. R. *Angew. Chem. Int. Ed.* **2012**, *51* (28), 7002–7006.

(100) Kranz, C.; Friedbacher, G.; Mizaikofft, B.; Lugstein, A.; Smoliner, J.; Bertagnolli, E. *Anal. Chem.* **2001**, *73* (11), 2491–2500.

(101) Jones, C. E.; Unwin, P. R.; Macpherson, J. V. *Chemphyschem* **2003**, *4* (2), 139–146.

(102) Bergner, S.; Vatsyayan, P.; Matysik, F. *Anal. Chim. Acta* **2013**, *775*, 1–13.

(103) Avdic, A.; Lugstein, A.; Wu, M.; Gollas, B.; Pobelov, I.; Wandlowski, T.; Leonhardt, K.; Denuault, G.; Bertagnolli, E. *Nanotechnology* **2011**, *22* (14), 145306.

(104) Salomo, M.; Pust, S. E.; Wittstock, G.; Oesterschulze, E. *Microelectron. Eng.* **2010**, *87* (5–8), 1537–1539.

(105) Paulose Nadappuram, B.; McKelvey, K.; Byers, J. C.; Güell, A. G.; Colburn, A. W.; Lazenby, R. a.; Unwin, P. R. *Anal. Chem.* **2015**, 150226143707000.

(106) Takahashi, Y.; Shevchuk, A. I.; Novak, P.; Murakami, Y.; Shiku, H.; Korchev, Y. E.; Matsue, T. *J. Am. Chem. Soc.* **2010**, *132* (29), 10118–10126.

(107) Nadappuram, B. P.; McKelvey, K.; Al Botros, R.; Colburn, A. W.; Unwin, P. R. *Anal. Chem.* **2013**, *85* (17), 8070–8074.

(108) Unwin, P. R.; Bard, A. J. *J. Phys. Chem.* **1991**, *95*, 7814–7824.

(109) Heller, I.; Kong, J.; Heering, H. A.; Williams, K. A.; Lemay, S. G.; Dekker, C. *Nano Lett.* **2005**, *5*, 137–142.

(110) Arrigan, D. W. M. *Analyst* **2004**, *129* (12), 1157.

(111) Zhang, B.; Fan, L.; Zhong, H.; Liu, Y.; Chen, S. *J. Am. Chem. Soc.* **2013**, *135*, 10073–10080.

(112) Sun, P.; Mirkin, M. V. *Anal. Chem.* **2006**, *78* (18), 6526–6534.

(113) Kim, J.; Kim, B. K.; Cho, S. K.; Bard, A. J. *J. Am. Chem. Soc.* **2014**, *136* (23), 8173–8176.

(114) Murray, R. W. *Chem. Rev.* **2008**, *108* (7), 2688–2720.

(115) Cox, J. T.; Zhang, B. *Annu. Rev. Anal. Chem.* **2012**, *5*, 253–272.

(116) Heller, I.; Kong, J.; Williams, K. a.; Dekker, C.; Lemay, S. G. *J. Am. Chem. Soc.* **2006**, *128* (22), 7353–7359.

(117) Mampallil, D.; Mathwig, K.; Kang, S.; Lemay, S. G. *Anal. Chem.* **2013**, *85* (12), 6053–6058.

(118) Chen, Q.; McKelvey, K.; Edwards, M. A.; White, H. S. *J. Phys. Chem. C* **2016**, *120* (31), 17251–17260.

(119) Chen, R.; Nioradze, N.; Santhosh, P.; Li, Z.; Surwade, S. P.; Shenoy, G. J.; Parobek, D. G.; Kim, M. A.; Liu, H.; Amemiya, S. *Angew. Chem. Int. Ed.* **2015**, *54* (50), 15134–15137.

(120) Rassaei, L.; Singh, P. S.; Lemay, S. G. *Anal. Chem.* **2011**, *83*, 3974–3980.

(121) Mathwig, K.; Lemay, S. G. *Electrochim. Acta* **2013**, *112*, 943–949.

(122) Bard, A. J.; Mirkin, M. V; Unwin, P. R.; Wipf, D. *J. Phys. Chem.* **1992**, *96*, 1861–1868.

(123) Cornut, R.; Lefrou, C. *J. Electroanal. Chem.* **2007**, *608* (1), 59–66.

(124) Martin, R. D.; Unwin, P. R. *J. Electroanal. Chem.* **1997**, *439* (1), 123–136.

(125) Neufeld, A. K.; O'Mullane, A. P. *J. Solid State Electrochem.* **2006**, *10* (10), 808–816.

(126) Gabrielli, C.; Huet, F.; Keddam, M.; Rousseau, P.; Vivier, V. *J. Phys. Chem. B* **2004**, *108* (31), 11620–11626.

(127) Cornut, R.; Lefrou, C. *J. Electroanal. Chem.* **2008**, *621* (2), 178–184.

(128) Nioradze, N.; Kim, J.; Amemiya, S. *Anal. Chem.* **2011**, *83* (3), 828–835.

(129) Lazenby, R. A.; Kelvey, K.; Unwin, P. R. *Anal. Chem.* **2013**, *85* (5), 2937–2944.

(130) Martin, R. D.; Unwin, P. R. *Anal. Chem.* **1998**, *70* (2), 276–284.

(131) Bard, A. J. **2004**, *76* (8), 2281–2289.

(132) Johnson, L.; Walsh, D. A. *J. Electroanal. Chem.* **2012**, *682*, 45–52.

(133) Leonard, K. C.; Bard, A. J. *J. Am. Chem. Soc.* **2013**, *135* (42), 15890–15896.

(134) Fernández, J. L.; Bard, A. J. *Anal. Chem.* **2003**, *75* (13), 2967–2974.

(135) Eckhard, K.; Chen, X.; Turcu, F.; Schuhmann, W. *Phys. Chem. Chem. Phys.* **2006**, *8* (45), 5359.

(136) Karnicka, K.; Eckhard, K.; Guschin, D. A.; Stoica, L.; Kulesza, P. J.; Schuhmann, W. *Electrochem. commun.* **2007**, *9* (8), 1998–2002.

(137) Santana, J. J.; González-Guzmán, J.; Fernández-Mérida, L.; González, S.; Souto, R. M. *Electrochim. Acta* **2010**, *55* (15), 4488–4494.

(138) Guadagnini, L.; Maljusch, A.; Chen, X.; Neugebauer, S.; Tonelli, D.; Schuhmann, W. *Electrochim. Acta* **2009**, *54* (14), 3753–3758.

(139) Okunola, A. O.; Nagaiah, T. C.; Chen, X.; Eckhard, K.; Schuhmann, W.; Bron, M. *Electrochim. Acta* **2009**, *54* (22), 4971–4978.

(140) Lefrou, C. *J. Electroanal. Chem.* **2006**, *592* (1), 103–112.

(141) Velmurugan, J.; Sun, P.; Mirkin, M. V. *J. Phys. Chem. C* **2009**, *113* (1), 459–464.

(142) Zoski, C. G.; Luman, C. R.; Fernández, J. L.; Bard, A. J. *Anal. Chem.* **2007**, *79* (13), 4957–4966.

(143) Nioradze, N.; Chen, R.; Kurapati, N.; Khvataeva-Domanov, A.; Mabic, S.; Amemiya, S. *Anal. Chem.* **2015**, *87* (9), 4836–4843.

(144) Chen, R.; Balla, R. J.; Li, Z.; Liu, H.; Amemiya, S. *Anal. Chem.* **2016**, *88* (16), 8323–8331.

(145) Dumitrescu, I.; Unwin, P. R.; Macpherson, J. V. *Chem. Commun.* **2009**, 6886–6901.

(146) Dudin, P. V; Snowden, M. E.; Macpherson, J. V; Unwin, P. R. *ACS Nano* **2011**, *5*, 10017–10025.

(147) Shao, Y.; Mirkin, M. V. *J. Phys. Chem. B* **1998**, *102* (49), 9915–9921.

(148) Barker, A. L.; Unwin, P. R.; Amemiya, S.; Zhou, J.; Bard, A. J. *J. Phys. Chem. B* **1999**, *103* (34), 7260–7269.

(149) Tsionsky, M.; Bard, A. J.; Mirkin, M. V. *J. Phys. Chem.* **1996**, *100* (45), 17881–17888.

(150) Shao, Y.; Mirkin, M. V. *J. Electroanal. Chem.* **1997**, *439* (1), 137–143.

(151) Wei, C.; Bard, A. J.; Mirkin, M. V. *J. Phys. Chem.* **1995**, *99*, 16033–16042.

(152) Zhang, J.; Slevin, C. J.; Morton, C.; Scott, P.; Walton, D. J.; Unwin, P. R. *J. Phys. Chem. B.* **2001**, *105*, 11120–11130.

(153) Zhang, J.; Unwin, P. R. *J. Am. Chem. Soc.* **2002**, *124*, 2379–2383.

(154) O'Mullane, A. P.; Macpherson, J. V.; Unwin, P. R.; Cervera-Montesinos, J.; Manzanares, J. A.; Frehill, F.; Vos, J. G. *J. Phys. Chem. B.* **2004**, *108*, 7219–7227.

(155) Whitworth, A. L.; Mandler, D.; Unwin, P. R. *Phys. Chem. Chem. Phys.* **2005**, *7*, 356–365.

(156) Hauquier, F.; Ghilane, J.; Fabre, B.; Hapiot, P. *J. Am. Chem. Soc.* **2008**, *130*, 2748–2749.

(157) Ekanayake, C. B.; Zoski, C. G. *Electroanalysis* **2016**, *28* (10), 2424–2434.

(158) Ejigu, A.; Lovelock, K. R. J.; Licence, P.; Walsh, D. A. *Electrochim. Acta* **2011**, *56* (28), 10313–10320.

(159) Lovelock, K. R. J.; Ejigu, A.; Loh, S. F.; Men, S.; Licence, P.; Walsh, D. a. *Phys. Chem. Chem. Phys.* **2011**, *13* (21), 10155–10164.

(160) Lovelock, K. R. J.; Cowling, F. N.; Taylor, A. W.; Licence, P.; Walsh, D. a. *J. Phys. Chem. B* **2010**, *114* (13), 4442–4450.

(161) Dumitrescu, I.; Edgeworth, J. P.; Unwin, P. R.; Macpherson, J. V. *Adv. Mater.* **2009**, *21* (30), 3105–3109.

(162) Güell, A. G.; Meadows, K. E.; Dudin, P. V; Ebejer, N.; Macpherson, J. V; Unwin, P. R. *Nano Lett.* **2014**, *14* (1), 220–224.

(163) Lee, H. B. R.; Baeck, S. H.; Jaramillo, T. F.; Bent, S. F. *Nano Lett.* **2013**, *13*, 457–463.

(164) Sánchez-Sánchez, C. M.; Vidal-Iglesias, F. J.; Solla-Gullón, J.; Montiel, V.; Aldaz, A.; Feliu, J. M.; Herrero, E. *Electrochim. Acta* **2010**, *55* (27), 8252–8257.

(165) Sun, T.; Yu, Y.; Zacher, B. J.; Mirkin, M. V. *Angew. Chem. Int. Ed.* **2014**, *53* (51), 14120–14123.

(166) Kwon, S. J.; Bard, A. J. **2012**.

(167) Kim, J.; Renault, C.; Nioradze, N.; Arroyo-Curras, N.; Leonard, K. C.; Bard, A. J. *J. Am. Chem. Soc.* **2016**, *138* (27), 8560–8568.

(168) Yu, Y.; Sun, T.; Mirkin, M. V. *Anal. Chem.* **2015**, *87* (14), 7446–7453.

(169) Azevedo, J.; Fillaud, L.; Bourdillon, C.; Noël, J. M.; Kanoufi, F.; Jousselme, B.; Derycke, V.; Campidelli, S.; Cornut, R. *J. Am. Chem. Soc.* **2014**, *136* (13), 4833–4836.

(170) Zhong, J.-H.; Zhang, J.; Jin, X.; Liu, J.-Y.; Li, Q.; Li, M.-H.; Cai, W.; Wu, D.-Y.; Zhan, D.; Ren, B. *J. Am. Chem. Soc.* **2014**, *136* (47), 16609–16617.

(171) Tan, C.; Rodríguez-López, J.; Parks, J. J.; Ritzert, N. L.; Ralph, D. C.; Abruña, H. D. *ACS Nano* **2012**, *6* (4), 3070–3079.

(172) Ritzert, N. L.; Rodríguez-López, J.; Tan, C.; Abruña, H. D. *Langmuir* **2013**, *29* (5), 1683–1694.

(173) Wilson, N. R.; Clewes, S. L.; Newton, M. E.; Unwin, P. R.; Macpherson, J. V. *J. Phys. Chem. B* **2006**, *110* (11), 5639–5646.

(174) Chang, J.; Leonard, K. C.; Cho, S. K.; Bard, A. J. *Anal. Chem.* **2012**, *84*, 5159–5163.

(175) Nioradze, N.; Chen, R.; Kim, J.; Shen, M.; Santhosh, P.; Amemiya, S. *Anal. Chem.* **2013**, *85*, 6198–6202.

(176) Oldham, K. *Anal. Chem.* **1992**, *64*, 646–651.

(177) Zhang, B.; Galusha, J.; Shiozawa, P. G.; Wang, G.; Bergren, A. J.; Jones, R. M.; White, R. J.; Ervin, E. N.; Cauley, C. C.; White, H. S. *Anal. Chem.* **2007**, *79*, 4778–4787.

(178) Penner, R. M.; Heben, M. J.; Longin, T. L.; Lewis, N. S. *Science* **1990**, *250*, 1118–1121.

(179) Shao, Y.; Mirkin, M. V; Fish, G.; Kokotov, S.; Palanker, D.; Lewis, A. *Anal. Chem.* **1997**, *69*, 1627–1634.

(180) Güell, A. G.; Cuharuc, A. S.; Kim, Y.; Zhang, G.; Tan, S.-y.;Ebejer, N.; Unwin, P. R. *ACS Nano* **2015**, *9* (4), 3558–3571.

(181) Li, Y.; Bergman, D.; Zhang, B. *Anal. Chem.* **2009**, *81*, 5496–5502.

(182) Perry, D.; Momotenko, D.; Lazenby, R. A.; Kang, M.; Unwin, P. R. *Anal. Chem.* **2016**, *88* (10), 5523–5530.

(183) Nogala, W.; Velmurugan, J.; Mirkin, M. V. *Anal. Chem.* **2012**, *84*, 5192–5197.

(184) Unwin, P.; Bard, A. *Anal. Chem.* **1992**, *64*, 113–119.

(185) Xiong, J.; Chen, Q.; Edwards, M. A.; White, H. S. *ACS Nano* **2015**, *9*, 8520–8529.

(186) White, H. S.; Bund, A. *Langmuir* **2008**, *24* (5), 2212–2218.

(187) Bae, J. H.; Yu, Y.; Mirkin, M. V. *J. Phys. Chem. Lett.* **2017**, 1338–1342.

(188) Snowden, M. E.; Güell, A. G.; Lai, S. C. S.; McKelvey, K.; Ebejer, N.; O'Connell, M. A.; Colburn, A. W.; Unwin, P. R. *Anal. Chem.* **2012**, *84* (5), 2483–2491.

(189) Ebejer, N.; Güell, A. G.; Lai, S. C. S.; McKelvey, K.; Snowden, M. E.; Unwin, P. R. *Annu. Rev. Anal. Chem.* **2013**, *6* (1), 329–351.

(190) Aaronson, B. D. B.; Lai, S. C. S.; Unwin, P. R. *Langmuir* **2014**, *30* (7), 1915–1919.

(191) Kleijn, S. E. F.; Lai, S. C. S.; Miller, T. S.; Yanson, A. I.; Koper, M. T. M.; Unwin, P. R. *J. Am. Chem. Soc.* **2012**, *134* (45), 18558–18561.

(192) Lai, S. C. S.; Lazenby, R. A.; Kirkman, P. M.; Unwin, P. R. *Chem. Sci.* **2015**, *6* (2), 1126–1138.

(193) Kim, Y. R.; Lai, S. C. S.; McKelvey, K.; Zhang, G.; Perry, D.; Miller, T. S.; Unwin, P. R. *J. Phys. Chem. C* **2015**, *119* (30), 17389–17397.

(194) Bentley, C. L.; Kang, M.; Unwin, P. R. *J. Am. Chem. Soc.* **2016**, *138* (39), 12755–12758.

(195) Ustarroz, J.; Kang, M.; Bullions, E.; Unwin, P. R. *Chem. Sci.* **2016**, 1841–1853.

(196) Zhang, G.; Güell, A. G.; Kirkman, P. M.; Lazenby, R.; Miller, T. S.; Unwin, P. R. *ACS Appl. Mater. Interfaces* **2016**, acsami.6b00681.

(197) Güell, A. G.; Ebejer, N.; Snowden, M. E.; Macpherson, J. V; Unwin, P. R. *J. Am. Chem. Soc*. **2012**, *134* (17), 7258–7261.

(198) Unwin, P. R.; Güell, A. G.; Zhang, G. *Acc. Chem. Res.* **2016**, *49* (9), 2041–2048.

(199) Lai, S. C. S.; Patel, A. N.; McKelvey, K.; Unwin, P. R. *Angew. Chem. Int. Ed.* **2012**, *51* (22), 5405–5408.

(200) Edwards, M. A.; Bertoncello, P.; Unwin, P. R. *J. Phys. Chem. C* **2009**, *113* (21), 9218–9223.

(201) Miller, T. S.; Macpherson, J. V; Unwin, P. R. *Phys. Chem. Chem. Phys.* **2014**, *16* (21), 9966.

(202) Byers, J. C.; Güell, A. G.; Unwin, P. R. *J. Am. Chem. Soc.* **2014**, *136* (32), 11252–11255.

(203) Momotenko, D.; Byers, J. C.; McKelvey, K.; Kang, M.; Unwin, P. R. *ACS Nano* **2015**, *9* (9), 8942–8952.

(204) Cutress, I. J.; Dickinson, E. J. F.; Compton, R. G. *J. Electroanal. Chem.* **2010**, *638* (1), 76–83.

(205) Dickinson, E. J. F.; Ekström, H.; Fontes, E. *Electrochem. commun.* **2014**, *40*, 71–74.

(206) Zhou, Q.; Wang, Y.; Tallman, D. E.; Jensen, M. B. *J. Electrochem. Soc.* **2012**, *159* (7), H644–H649.

(207) Williams, C. G.; Edwards, M. A.; Colley, A. L.; Macpherson, J. V.; Unwin, P. R. *Anal. Chem.* **2009**, *81* (7), 2486–2495.

(208) Rassaei, L.; Mathwig, K.; Goluch, E. D.; Lemay, S. G. *J. Phys. Chem. C* **2012**, *116* (20), 10913–10916.

(209) White, H. S.; Bund, A. *Langmuir*. 2008, pp 2212–2218.

(210) Lan, W. J.; Edwards, M. A.; Luo, L.; Perera, R. T.; Wu, X.; Martin, C. R.; White, H. S. *Acc. Chem. Res.* **2016**, *49* (11), 2605–2613.

(211) Zhang, B.; Zhang, Y.; White, H. S. *Anal. Chem.* **2004**, *76* (21), 6229–6238.

(212) McKelvey, K.; Kinnear, S. L.; Perry, D.; Momotenko, D.; Unwin, P. R. *J. Am. Chem. Soc.* **2014**, *136*, 13735–13744.

(213) Perry, D.; Al Botros, R.; Momotenko, D.; Kinnear, S. L.; Unwin, P. R. *ACS Nano* **2015**, *9* (7), 7266–7276.

(214) Huang, S.; Weis, J. E.; Costa, S.; Kalbac, M.; Dresselhaus, M. S. *Electrochem. Carbon Electrodes* **2016**, 1–30.

(215) Güell, A. G.; Tan, S.-y.; Unwin, P. R.; Zhang, G. In *Electrochemistry of Carbon Electrodes*; Bartlett, P. N., Alkire, R. C., Lipkowski, J., Eds.; Wiley-VCH, 2016; pp 31–82.

(216) Ray, K.; McCreery, R. L. *Anal. Chem.* **1997**, *69* (22), 4680–4687.

(217) Xu, J.; Chen, Q.; Swain, G. M. *Anal. Chem.* **1998**, *70* (15), 3146–3154.

(218) Byers, J. C.; Güell, A. G.; Unwin, P. R. 1–10.

(219) Shen, M. **2011**.

(220) Zhang, G.; Cuharuc, A. S.; Güell, A. G.; Unwin, P. R. *Phys. Chem. Chem. Phys.* **2015**, *17*, 11827–11838.

(221) Maddar, F. M.; Lazenby, R. A.; Patel, A. N.; Unwin, P. R. *Phys. Chem. Chem. Phys.* **2016**, 26404–26411.

(222) McDermott, C. A. *J. Electrochem. Soc.* **1993**, *140* (9), 2593.

(223) Zhang, G.; Tan, S.-y.; Patel, A. N.; Unwin, P. R. *Phys. Chem. Chem. Phys.* **2016**, *18* (47), 32387–32395.

(224) Ambrosi, A.; Chua, C. K.; Bonanni, A.; Pumera, M. *Chem. Rev.* **2014**, *114* (14), 7150–7188.

(225) Menon, V.; Martin, C. *Anal. Chem.* **1995**, *67* (13), 1920–1928.

(226) Patten, H. V; Velický, M.; Dryfe, R. A. W. 2016; pp 121–162.

(227) Patel, A. N.; Collignon, M. G.; O'Connell, M. A.; Hung, W. O. Y.; McKelvey, K.; Macpherson, J. V.; Unwin, P. R. *J. Am. Chem. Soc.* **2012**, *134* (49), 20117–20130.

(228) Niimi, Y.; Matsui, T.; Kambara, H.; Tagami, K.; Tsukada, M.; Fukuyama, H. *Phys. Rev. B - Condens. Matter Mater. Phys.* **2006**, *73* (8), 1–20.

(229) Nakada, K.; Fujita, M.; Dresselhaus, G.; Dresselhaus, M. *Phys. Rev. B* **1996**, *54* (24), 17954–17961.

(230) Ruffieux, P.; Melle-Franco, M.; Gröning, O.; Bielmann, M.; Zerbetto, F.; Gröning, P. *Phys. Rev. B - Condens. Matter Mater. Phys.* **2005**, *71* (15), 1–4.

(231) Ugeda, M. M.; Brihuega, I.; Guinea, F.; G??mez-Rodr??guez, J. M. *Phys. Rev. Lett.* **2010**, *104* (9), 1–4.

(232) Li, Z. Q.; Lu, C. J.; Xia, Z. P.; Zhou, Y.; Luo, Z. *Carbon N. Y.* **2007**, *45* (8), 1686–1695.

(233) Lopes Dos Santos, J. M. B.; Peres, N. M. R.; Castro Neto, A. H. *Phys. Rev. Lett.* **2007**, *99* (25), 19–22.

(234) Li, G.; Luican, A.; Santos, J. M. B. L.; Neto, A. H. C.; Reina, A.; Kong, J.; Andrei, E. Y.; dos Santos, J. M. B. L.; Neto, A. H. C.; Reina, A.; Kong, J.; Andrei, E. Y. *Nat. Phys.* **2009**, *6* (2), 109–113.

(235) Kobayashi, Y.; Fukui, K. I.; Enoki, T.; Kusakabe, K.; Kaburagi, Y. *Phys. Rev. B - Condens. Matter Mater. Phys.* **2005**, *71* (19), 2–5.

(236) Luque, N. B.; Schmickler, W. *Electrochim. Acta* **2012**, *71*, 82–85.

(237) Amatore, C.; Savéant, J. M.; Tessier, D. *J. Electroanal. Chem. Interfacial Electrochem.*

1983, *147* (1–2), 39–51.

(238) Beriet, C.; Ferrigno, R.; Girault, H. H. *J. Electroanal. Chem.* **2000**, *486*, 56–64.

(239) Davies, T. J.; Moore, R. R.; Banks, C. E.; Compton, R. G. *J. Electroanal. Chem.* **2004**, *574* (1), 123–152.

(240) Unwin, P. R.; Bard, A. J. *Control* **1992**, *5045* (20), 5035–5045.

(241) Aaronson, B. D. B.; Garoz-Ruiz, J.; Byers, J. C.; Colina, A.; Unwin, P. R. *Langmuir* **2015**, acs.langmuir.5b03316.

(242) Aaronson, B. D. B.; Chen, C. H.; Li, H.; Koper, M. T. M.; Lai, S. C. S.; Unwin, P. R. *J. Am. Chem. Soc.* **2013**, *135* (10), 3873–3880.

(243) McKelvey, K.; Perry, D.; Byers, J. C.; Colburn, A. W.; Unwin, P. R. *Anal. Chem.* **2014**, *86* (7), 3639–3646.

(244) Kang, M.; Momotenko, D.; Page, A.; Perry, D.; Unwin, P. R. *Langmuir* **2016**, *32* (32), 7993–8008.

(245) Oja, S. M.; Fan, Y.; Armstrong, C. M.; Defnet, P.; Zhang, B. *Anal. Chem.* **2016**, *88* (1), 414–430.

(246) Hawley, M. D.; Tatawawadi, S. V; Piekarski, S.; Adams, R. N. *J. Am. Chem. Soc.* **1967**, *89* (2), 447–450.

(247) Laviron, E. *J. Electroanal. Chem. Interfacial Electrochem.* **1984**, *164* (2), 213–227.

(248) Banks, C. E.; Compton, R. G. *Analyst* **2005**, *130* (9), 1232.

(249) Banks, C. E.; Moore, R. R.; Davies, T. J.; Compton, R. G.; Road, S. P. *Chem. Commun.* **2004**, *2* (16), 1804–1805.

(250) Lhenry, S.; Leroux, Y. R.; Hapiot, P. *Anal. Chem.* **2012**, *84* (17), 7518–7524.

(251) Snowden, M. E.; Güell, A. G.; Lai, S. C. S.; McKelvey, K.; Ebejer, N.; O'Connell, M. A.; Colburn, A. W.; Unwin, P. R. *Anal. Chem.* **2012**, *84* (5), 2483–2491.

(252) Wang, S.; Swope, V. M.; Butler, J. E.; Feygelson, T.; Swain, G. M. *Diam. Relat. Mater.* **2009**, *18* (4), 669–677.

(253) Miller, J. B.; Brandes, G. R. *J. Appl. Phys.* **1997**, *82* (9), 4538.

(254) Yagi, I.; Notsu, H.; Kondo, T.; Tryk, D. A.; Fujishima, A. *J. Electroanal. Chem.* **1999**, *473* (1), 173–178.

(255) Fujishima, A.; Rao, T. N.; Popa, E.; Sarada, B. V.; Yagi, I.; Tryk, D. A. *J. Electroanal. Chem.* **1999**, *473* (1), 179–185.

(256) Rao, T. N.; Yagi, I.; Miwa, T.; Tryk, D. A.; Fujishima, A. *Anal. Chem.* **1999**, *71* (13), 2506–2511.

(257) Rao, T. N.; Fujishima, A. *Diam. Relat. Mater.* **2000**, *9* (3–6), 384–389.

(258) Duo, I.; Levy-Clement, C.; Fujishima, A.; Comninellis, C. *J. Appl. Electrochem.* **2004**, *34* (9), 935–943.

(259) Notsu, H.; Yagi, I.; Tatsuma, T.; Tryk, D. A.; Fujishima, A. *Electrochem. Solid-State Lett.* **1999**, *2* (10), 522–524.

(260) McEvoy, J. P.; Foord, J. S. *Electrochim. Acta* **2005**, *50* (14), 2933–2941.

(261) Tryk, D. A.; Tachibana, H.; Inoue, H.; Fujishima, A. *Diam. Relat. Mater.* **2007**, *16* (4), 881–887.

(262) Hutton, L. A.; Iacobini, J. G.; Bitziou, E.; Channon, R. B.; Newton, M. E.; Macpherson, J. V. *Anal. Chem.* **2013**, *85* (15), 7230–7240.

(263) Pleskov, Y. V. *Russ. J. Electrochem.* **2002**, *38* (12), 1275–1291.

(264) Holt, K. B.; Bard, A. J.; Show, Y.; Swain, G. M. *J. Phys. Chem. B* **2004**, *108* (39), 15117–15127.

(265) Wang, S.; Swain, G. M. *J. Phys. Chem. C* **2007**, *111* (10), 3986–3995.

(266) Hahn, M.; Baertschi, M.; Barbieri, O.; Sauter, J.-C.; Kötz, R.; Gallay, R. *Electrochem. Solid-State Lett.* **2004**, *7* (2), A33.

(267) Harvey, H. M.; Gross, A. J.; Brooksby, P.; Downard, A. J.; Green, S. J.; Winlove, C. P.; Benjamin, N.; Winyard, P. G.; Whiteman, M.; Hammond, J. L.; Estrela, P.; Marken, F. *Electroanalysis* **2015**, *27* (11), 2645–2653.

Chapter 2

Comparison of Fast Electron Transfer Kinetics at Platinum, Gold, Glassy Carbon and Diamond Electrodes using Fourier-Transformed AC Voltammetry and Scanning Electrochemical Microscopy

Heterogeneous electron transfer kinetics have been extensively studied through a range of electrochemical techniques. This chapter compares studies of fast kinetics using the macroscopic technique of Fourier-transformed large amplitude alternating current voltammetry (FTACV) and the microscopic technique of scanning electrochemical microscopy (SECM) at various electrode materials. This chapter contains the manuscript and supporting information for an article published in *Physical Chemistry Chemical Physics* where electron transfer kinetic measurements were conducted on Pt, Au, glassy carbon and polycrystalline boron-doped diamond electrodes. I was responsible for executing all experimental and simulation work in this chapter and was taught how to conduct SECM and FTACV experiments by Rob Lazenby and Kiran Bano, respectively.

Comparison of Fast Electron Transfer Kinetics at Platinum, Gold, Glassy Carbon and Diamond Electrodes using Fourier-Transformed AC Voltammetry and Scanning Electrochemical Microscopy

Sze-yin Tan, [†,‡] *Robert A. Lazenby,* [†,§] *Kiran Bano,* [‡,ξ] *Jie Zhang,* [*,‡] *Alan M. Bond,* [*,‡] *Julie V. Macpherson,* [†] *Patrick R. Unwin* [*,†]

[†] Department of Chemistry, University of Warwick, Coventry, West Midlands CV4 7AL, United Kingdom

[‡] School of Chemistry, Monash University, Clayton, Victoria 3800, Australia

[§] Present address: Department of Chemistry and Biochemistry, University of Maryland Baltimore County, Baltimore, Maryland 21250, United States

[ξ] Present address: School of Chemistry, University of Connecticut, Storrs, Connecticut 06269, United States

* p.r.unwin@warwick.ac.uk, jie.zhang@monash.edu, alan.bond@monash.edu

2.1. Abstract

Heterogeneous electron transfer (ET) processes at electrode/electrolyte interfaces are of fundamental and applied importance and are extensively studied by a range of electrochemical techniques, all of which have various attributes but also limitations. The present study focuses on the one-electron oxidation of tetrathiafulvalene (TTF) and reduction of tetracyanoquinodimethane (TCNQ) in acetonitrile solution by two powerful electrochemical techniques: Fourier-transformed large amplitude alternating current voltammetry (FTACV); and scanning electrochemical microscopy (SECM), both of which are supported by detailed theoretical models. At conventional Pt, Au and glassy carbon (GC) electrode materials, the apparent (overall) charge transfer kinetic values determined by FTACV give standard ET rate constants, k^0_{FTACV}, that are fast and close to the reversible limit. They are in good agreement with highly localised k^0_{SECM} measurements determined by SECM under conditions of high mass transport rates. In contrast, the impact of both the

complex heterogeneous surface of polycrystalline boron doped diamond (pBDD) and degenerate p-type doping results in a range of k^0_{SECM} values across the electrode surface compared to the overall k^0_{FTACV} measured for both processes studied. Moreover, the reduced availability of charge carriers at the electrode surface, at each energy state, compared to a metal, which decreases as the potential becomes more negative, results in lower k^0 values at pBDD than Pt, Au and GC. The measurement technique also has an influence: SECM measurements are made at much higher local current density than FTACV, and for TCNQ/TCNQ$^{\bullet-}$, which has the more negative formal potential, limited charge carrier availability results in $k^0_{FTACV} > k^0_{SECM}$, with unusual apparent charge transfer coefficients and voltammetric wave-shapes from SECM. These data thus highlight the importance of understanding the influence of the measurement technique and further demonstrate how ET kinetics at pBDD differ from conventional electrodes, in this case for processes in an organic solvent, which has received much less attention compared to aqueous systems for studies with pBDD.

2.2. Introduction

The measurement of electron transfer (ET) kinetics at electrode/electrolyte interfaces is of fundamental importance in the field of electrochemistry.[1,2] Traditionally, direct current (DC) cyclic voltammetry (CV) has been employed with ~ mm-sized macrodisk electrodes to probe ET kinetics under transient conditions. The peak-to-peak separation, ΔE_p, can be used to determine the heterogeneous charge transfer standard rate constant, k^0, via the Nicholson method.[3] However, ΔE_p and the shape of the CVs are significantly affected by uncompensated resistance, R_u. Indeed, the effects of small k^0, on the one hand, and large R_u values, on the other, may be indistinguishable (both lead to increased ΔE_p) in DC CV measurements.[3] Fast-scan CV with ultramicroelectrodes (UMEs) was introduced to increase the temporal resolution of voltammetric measurements.[4,5] However, the current contributions arising from double layer charging currents are linearly dependent on the potential scan rate, v, while faradaic currents are proportional to $v^{1/2}$ resulting in diminished

faradaic-to-background current ratios at high scan rates, complicating the reliability of fast ET kinetic measurements.

Key drawbacks associated with measuring ET rates using traditional DC CV at macroelectrodes can be minimised by the use of Fourier-transformed large amplitude alternating current voltammetry (FTACV).[6–8] In the common form of this technique, a sine wave is superimposed onto the DC potential ramp, as used in DC voltammetry, to generate an alternating current (AC) waveform. Fourier-transform (FT) is then applied to convert the current data from the time to frequency domain to give the power spectrum. Fundamental and higher harmonic components are resolved by selecting the regions of interest from the power spectrum and applying inverse FT procedures (Figure 2.1(a)).[6–8] The major advantage of FTACV over DC voltammetry is that the higher harmonic components (> 3rd harmonic) are essentially free from background charging contributions and the phenomenologically similar effects of k^0 and R_u can be accurately distinguished by systematic analysis of the higher order harmonic components.[6–8] This technique facilitates the study of fast ET processes at macrodisk electrodes under planar diffusion conditions.[6–8]

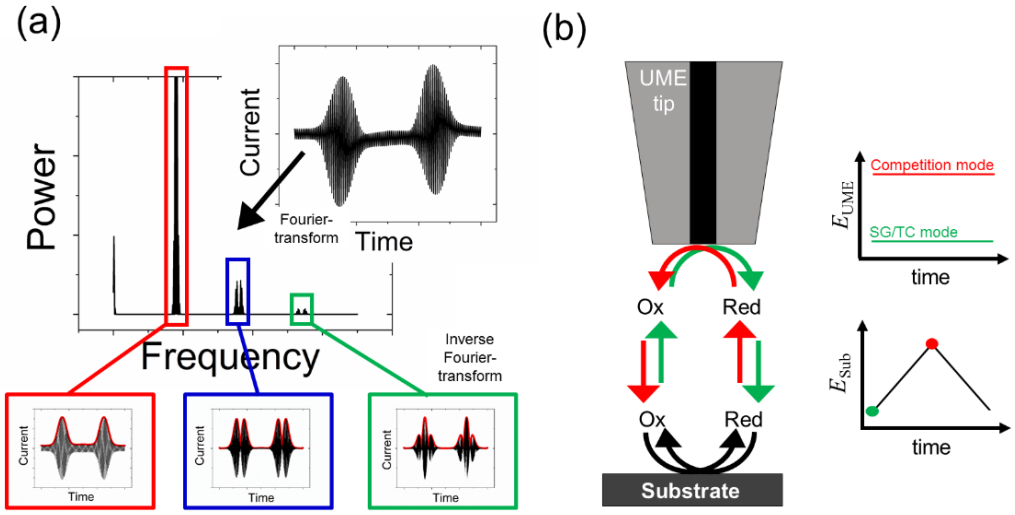

Figure 2.1 Schematic showing the experimental protocols of (a) FTACV and (b) substrate voltammetry SECM.

Fast ET kinetics can also be measured under steady-state conditions, as exemplified by UMEs where radial diffusion dominates at long times.[9,10] UMEs offer a range of advantages including reduced ohmic drop effects, iR_u, fast response times and high mass transport rates under both steady-state (slow scan rate regime) and transient (fast scan rate regime) conditions.[9,10] Of particular relevance to the present study, scanning electrochemical microscopy (SECM) provides even higher mass transport rates to a UME.[11–14]

In SECM experiments, a UME is placed in close proximity to a second (substrate) working electrode and the potential of both electrodes is externally biased relative to the reference electrode. Shuttling of the oxidised and reduced forms of a redox couple between the two electrodes provides high mass transport rates, where the mass transport coefficient, k_t, is inversely proportional to the tip-substrate separation, d. Substrate voltammetry SECM is a variation of SECM that can be used for high spatial resolution measurements of ET kinetics at macroscopic substrate electrodes.[15–17] In this method, the substrate potential is swept about the formal potential, $E^{0'}$, of the redox couple of interest while the UME tip amperometrically monitors the reaction in the redox competition[18] and substrate generation/tip collection (SG/TC)[19] modes (Figure 2.1(b)). A pair of UME tip current-substrate potential curves taken at the same tip-substrate position allows for accurate determination of mass transport, thermodynamic and kinetic parameters.[15–17,20]

The majority of electrode materials employed in electrochemical applications are metallic (e.g. Pt, Au) or semi-metallic (e.g. graphene). However, diamond is gaining increasing interest for electrochemical applications, but is more complicated because the electrical properties depend on the degree of doping. In the undoped state, diamond exhibits a very wide band gap and is essentially useless for electrochemical applications. However, by doping with boron it is possible to change the electrical properties dramatically from ~ insulating to p-type semi-conducting to even "metal-like" (degenerate doping), but with fewer charge carriers available than for a metal, even when highly doped ($> 10^{20}$ B atoms cm^{-3}).[21–23] Boron-doped diamond (BDD) has received substantial attention in recent years in the fields of electroanalytical chemistry and sensor development due to favourable electrochemical properties such as wide potential window, low background currents,

stability in many solvents and biocompatibility.[24–26] These – and future - applications, as well as fundamental studies, require a detailed understanding of ET processes at this electrode material.

Degenerately doped (conducting) polycrystalline boron-doped diamond (pBDD) is the main form of diamond used in electrochemistry, but this material is complicated by surface heterogeneities, including differently doped crystallographic facets and grain boundaries. This also affects the concentration and mobility of charge carriers at the surface of the electrode which may directly impact on the k^0 values measured at individual grains.[23,27] Moreover, the influence of material properties post-processing (e.g. mechanical polishing to reduce the surface roughness), must also be considered.

This report focuses on the one-electron oxidation of tetrathiafulvalene (TTF) to its cation radical, $TTF^{\bullet+}$ and the one-electron reduction of tetracyanoquinodimethane (TCNQ) to its anion radical, $TCNQ^{\bullet-}$ which have been extensively studied as examples of redox couples that undergo simple ET processes. The rapid oxidation of TTF has been reported in both organic[28–30] and ionic liquid media[31,32] while the reduction of TCNQ has been extensively studied over a wide range of electrochemical techniques such as steady-state voltammetry,[33] normal pulse voltammetry,[34,35] ACV[36] and SECM[15,28,37–40] resulting in a wide distribution of reported k^0_{TCNQ} values ranging from 0.005 cm s^{-1} [34] to 8.2 cm s^{-1}.[40] TTF and TCNQ redox processes have also been employed as model systems for the study of diffusion-migration effects at UMEs in low ionic strength solutions.[41] However, neither of these couples have yet been investigated at BDD and, indeed, studies of ET kinetics at BDD in organic solvents are somewhat limited.

A comparison of the ET kinetics determined by FTACV and SECM techniques at three conventional electrode materials: Pt, Au and glassy carbon (GC); and at pBDD is reported. Kinetic parameters obtained using both techniques are close to the reversible limit for both ET processes. However, at pBDD there are kinetic limitations for both the $TTF/TTF^{\bullet+}$ and $TCNQ/TCNQ^{\bullet-}$ processes. In the case of $TCNQ/TCNQ^{\bullet-}$, differences in the kinetics values from the two measurement techniques are found due to the large differences in current density values. Taken as a whole, these data highlight important features for pBDD electrodes: they do not behave like conventional metal electrodes and

under conditions of high mass transport (current density), charge transfer limitations from the material itself become important.

2.3. Experimental

2.3.1. Chemicals

Tetrathiafulvalene (TTF; 97%), 7,7,8,8-tetracyanoquinodimethane (TCNQ; 98%), ferrocene (Fc; ≥ 98%) and n-tetrabutylammonium hexafluorophosphate (Bu_4NPF_6; 98%) were purchased from Sigma-Aldrich and used without further purification. Acetonitrile (CH_3CN; Fisher, HPLC grade) was dried with 3 Å molecular sieves prior to use. All electrochemical studies were undertaken with TTF and TCNQ solutions made up in CH_3CN containing 0.1 M Bu_4NPF_6 as the supporting electrolyte. All voltammetric experiments were carried out at 20 ± 1 °C.

2.3.2. Electrode Materials

Pt (1 mm or 0.5 mm-radius), Au (1 mm or 0.5 mm-radius), GC (1.5 mm or 0.5 mm-radius) macrodisk working electrodes were obtained from CH Instruments, Austin, Texas. The oxygen-terminated pBDD (0.5 mm-radius) was provided by Element 6, Harwell, UK in a free-standing form i.e. not attached to the growth substrate and polished to ~ nm roughness on the growth (electrochemical measurement) face. An in-house procedure for sealing the macroelectrode in a glass support was employed to insulate the pBDD edge and is described in detail elsewhere.[42,43] The boron concentration of the pBDD sample is ~ 3×10^{20} atoms cm^{-3} (average) and is above the metallic threshold.[42,44]

A Pt disk UME was fabricated in-house using an established procedure,[45] involving heat sealing of a 1.0 µm-radius Wollaston wire (Goodfellow, UK), with the Ag layer removed from the end section of ca. 1 mm length, in a borosilicate glass capillary under vacuum. The other end of the Wollaston wire was connected with solder to a larger copper wire inserted into the capillary.[45] After sealing, the end of the UME was polished flat and

conically to obtain an RG value - ratio of the radius of the insulating glass sheath to that of the active electrode - of *ca.* 20. Prior to use, all electrodes were polished with an aqueous alumina slurry (0.05 μm) on a soft microfiber polishing pad (MicroCloth, Buehler Ltd.) and then again on a clean wet microfiber pad, to produce a clean electrode surface, before being left to dry for a brief time. For TTF and TCNQ voltammetric experiments, Ag and Pt wires, respectively, acted as a quasi-reference electrode (QRE) in a 3-electrode arrangement. The QRE wire was separated from the bulk solution (containing TTF or TCNQ) by a glass frit (P4 grade) in order to maintain a constant reference potential during measurements. Potentials derived from the QRE were calibrated against the $Fc^{0/+}$ external reference potential scale.[46] Pt mesh acted as a counter electrode.

2.3.3. FTACV and SECM Instrumentation

FTACV experiments were carried out in a 3-electrode configuration using home-built (Monash) instrumentation, described in detail elsewhere.[7] All FTACV experiments were recorded using a sine wave perturbation of amplitude, ΔE = 80.0 mV and frequency, f = 228.0 Hz. The Fourier-transformed resolved higher order harmonic data were quantitatively modelled using the MECSim program (www.garethkennedy.net/MECSim, details in Section 2.6.11).

A home-built (Warwick) intermittent contact (IC)-SECM setup was used for substrate voltammetry SECM measurements.[47] Details regarding tip positioning are given in Section 2.6.2. A 4-electrode SECM configuration was adopted with the Pt UME tip and substrate (Pt, Au, GC or pBDD) as the working electrodes, with the same counter and reference electrodes as mentioned above. For this purpose, a CHI 760C bipotentiostat was used. All SECM experiments were carried out at a scan rate of 0.05 V s^{-1}. SECM data were analysed and fitted using a relevant model[15] (details in Section 2.6.3.). A schematic showing the basic features of each technique is given in Figure 2.1.

2.4. Results and Discussion

2.4.1. Electron Transfer Studies at Conventional Electrode Materials

Oxidation of TTF

TTF undergoes two well resolved one-electron oxidation processes in CH_3CN.[29] This study considers only the first oxidation process, given by Eq. 2.1:

$$TTF \rightleftharpoons TTF^{\bullet+} + e^- \quad \text{(Eq. 2.1)}$$

DC CVs for the oxidation of 1.0 mM TTF at Pt, Au and GC macrodisk electrodes in the 3-electrode configuration gave mid-point potentials, E_m = - 0.074 ± 0.002 V (vs $Fc^{0/+}$) (Section 2.6.4, Figure 2.9). Diffusion-controlled reversible electro-oxidation processes were observed for all three electrode materials and resulted in ΔE_p values close to 60 mV at v = 0.1 V s^{-1}. The diffusion coefficient, D_{TTF} = 2.10 × 10^{-5} cm^2 s^{-1} was determined from steady-state voltammetry[41] (see Section 2.6.5., Figure 2.11(a)) and the ratio of diffusion coefficients, $D_{TTF}^{\bullet+}/D_{TTF}$ was determined by SECM chronoamperometry in feedback[48] and SG/TC[19] modes (see Section 2.6.6.) to be 0.85 ± 0.02, which is in good agreement with literature values of 2.10 × 10^{-5} cm^2 s^{-1} and 1.90 × 10^{-5} cm^2 s^{-1}, for D_{TTF} and $D_{TTF}^{\bullet+}$, respectively, as determined by macroscale and microscale CVs of 1.0 mM TTF and $TTF^{\bullet+}$ solutions (generated through bulk electrolysis).[29]

FTACV was employed to investigate the ET process for the oxidation of 0.25 mM TTF at Pt, Au and GC electrodes using a sine wave perturbation of ΔE = 80.0 mV and f = 228.0 Hz. $E^{0'}$ = -0.074 ± 0.003 V was determined from the potential minima and maxima of the even and odd harmonics, respectively, and is in good agreement with E_m determined from DC CV (see above). Comparison of the experimental (black lines) conventional DC voltammograms and the 1st to 7th AC harmonic components of FTACV with simulated (red lines) data at a Pt, Au and GC macroelectrode for the TTF/ $TTF^{\bullet+}$ process are shown in Figure 2.2, Figure 2.12 and Figure 2.13, respectively. Excellent agreement between experimental and simulated data shows that this process is essentially reversible on the

time scale of the DC CV and FTACV experiments at all conventional electrode materials studied.

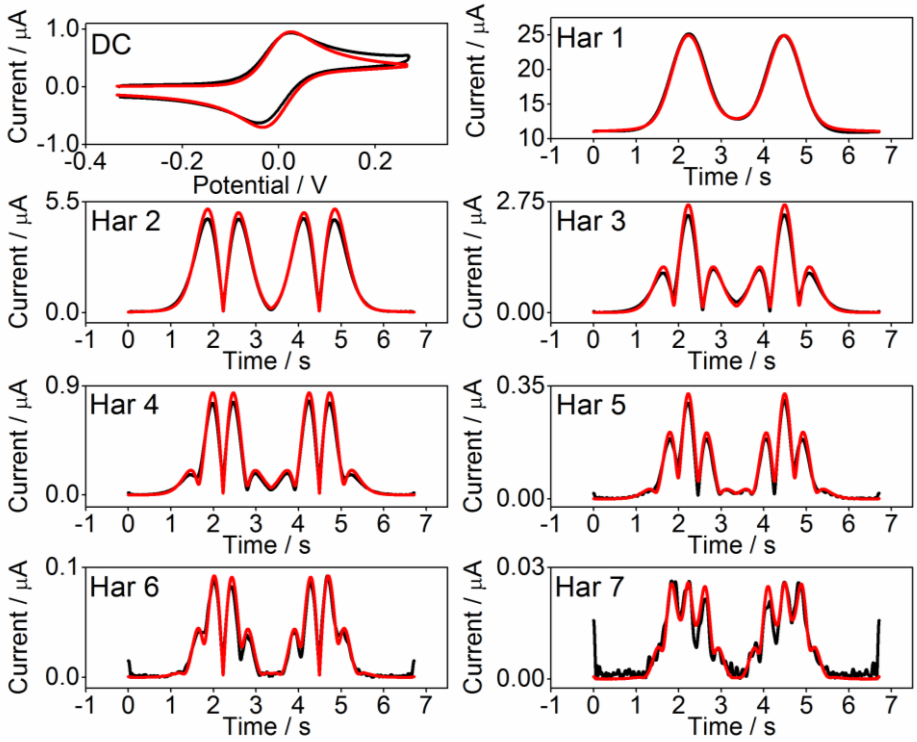

Figure 2.2 Comparison of experimental (black lines) and simulated (red lines, $\Psi = 0.988$) FTACV curves for the one-electron oxidation of 0.25 mM TTF in CH_3CN (0.1 M Bu_4NPF_6) at a Pt macroelectrode. Simulation parameters: $k^0 = 1000$ cm s^{-1} (reversible), $\alpha = 0.5$, $R_u = 550\ \Omega$, $A = 0.00785$ cm^2, $f = 228.0$ Hz, $\Delta E = 80.0$ mV, $D_{TTF} = 2.10 \times 10^{-5}$ cm^2 s^{-1}, $D_{TTF}^{\bullet+} = 1.80 \times 10^{-5}$ cm^2 s^{-1}, $v_{AC} = 0.15$ V s^{-1} and $v_{DC} = 0.1$ V s^{-1}.

In FTACV, k^0 strongly influences the current magnitude obtained at higher harmonic AC components for a quasi-reversible process. For the purpose of this study, the upper kinetic limit of detection is reasonably defined as the k^0 value at which the major peak current magnitude of the selected (7th) harmonic is 90 % of that predicted for a reversible process. Therefore, the k^0 values which represent the upper kinetic limit of detection under these experimental conditions at the Pt, Au and GC macrodisk electrodes are $k^0_{Pt,TTF} \geq 1.5$ cm s^{-1}, $k^0_{Au,TTF} \geq 1.5$ cm s^{-1} and $k^0_{GC,TTF} \geq 1.0$ cm s^{-1}, respectively (α reasonably assumed to be 0.5). Note that the smaller upper limit of detection at the GC electrode is due to the larger capacitance of the electrode material. The complete set of thermodynamic and kinetic parameters associated with the TTF oxidation process is

provided in Table 2.1. The least squares correlation, Ψ (see Section 2.6.1), is also reported to quantify the agreement between experimental and simulated data.

Table 2.1 Parameters used for FTACV simulations and SECM analytical fitting of the TTF/$TTF^{\bullet+}$ process in CH_3CN (0.1 M Bu_4NPF_6) at Pt, Au, GC and pBDD macroelectrodes. Other simulation parameters applicable to either technique: D_{TTF} = 2.10 × 10^{-5} cm^2 s^{-1}, $D_{TTF}^{\bullet+}$= 1.80 × 10^{-5} cm^2 s^{-1}, $E^{0'}$ = -0.074 V, T = 293.2 K and α = 0.50 (assumed).

Electrode Material	FTACV[a]						SECM[b]	
	c / mM	A / mm^2	v_{AC} / V s^{-1}	R_u / Ω	C_{dl} (c_0, c_2 terms) / μF cm^{-2}	k^0 / cm s^{-1}	c / mM	k^0 / cm s^{-1}
Pt	0.25	0.785	0.15	550	12.3, 1.7	≥ 1.5	1.0	≥ 7.0
Au	0.25	0.785	0.07	500	8.0, 1.5	≥ 1.5	1.0	≥ 7.0
GC	0.25	0.785	0.09	525	14.6, 6.0	≥ 1.0	1.0	≥ 3.0
pBDD	0.25	0.785	0.09	550	2.3, 0.8	0.35	1.0	0.05─0.4

[a] ΔE = 80.0 mV, f = 228.0 Hz [b] a_{UME} = 1.0 μm, v = 0.05 V s^{-1}, RG = 20

It is important to note that while it is possible to access higher k^0 values by applying larger f to the AC perturbation, these linear measurements are often complicated by large non-linear capacitance and are subject to ambiguity arising from small uncertainties in R_u values. This limitation can potentially be overcome by use of an internal reference such as the recently reported dual frequency FTACV method, which has been successfully applied to microdisk electrodes.[49] However, the alternative SECM method is chosen to access fast kinetics.

Substrate voltammetry SECM was employed for the quantitative analysis of the kinetic parameters for the oxidation of 1.0 mM TTF at the conventional electrode materials of interest, under high mass transport rates.[15,16] The UME tip (a_{UME} = 1.0 μm, RG = 20) was positioned at a fixed distance, d, from the substrate of interest (normalised distance, L = d/a_{UME}). The substrate potential, E_{sub}, was scanned positively at 0.05 V s^{-1} to oxidise TTF to $TTF^{\bullet+}$.

When the UME tip potential, E_{UME} >> $E^{0'}_{TTF}$, the UME tip gives the positive feedback response at the beginning of the substrate potential scan where E_{sub} << $E^{0'}_{TTF}$. As

E_{sub} is positively scanned, the UME tip competes with the substrate to oxidise TTF and the UME tip current falls to zero. This is known as the redox competition mode.[15,18] In the SG/TC mode ($E_{UME} << E^{0'}_{TTF}$), the UME tip current rises from zero as it collects $TTF^{\bullet+}$ produced at the substrate electrode surface during the voltammetric scan. Hence, a pair of competition and SG/TC mode voltammograms taken at the same tip-substrate distance can be taken at a set of positions to change the inter-electrode mass transport rate. Figure 2.3 shows three pairs of UME tip current responses for both the competition and SG/TC modes, normalised with respect to the steady-state diffusion-limited current for the oxidation of TTF in bulk solution, and plotted as a function of the Pt substrate working electrode potential. Each pair measured at the same tip-substrate distance is shown in the same color. These pairs of competition and SG/TC mode voltammograms can be used to determine all mass transport (from UME tip positive feedback limiting-currents), thermodynamic and kinetics parameters (fitting to an analytical model)[15] associated with the $TTF/TTF^{\bullet+}$ process (detailed in Section 2.6.2.).

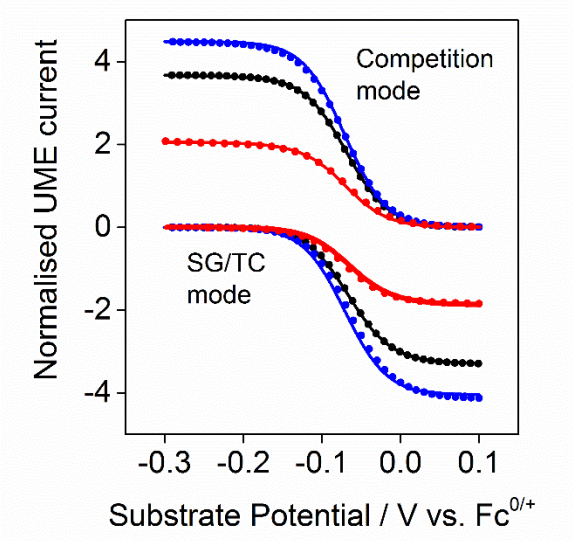

Figure 2.3 Experimental (solid line) and analytical (dotted line) normalised UME tip current-substrate potential curves for the paired competition and SG/TC modes for the one-electron oxidation of 1.0 mM TTF in CH_3CN (0.1 M Bu_4NPF_6) at a Pt macroelectrode with v = 0.05 V s^{-1} at different normalised tip-substrate distances (L = 0.598 (red), 0.265 (black) and 0.206 (blue)).

Here, the kinetic limit of detection of SECM is defined to be the k^0 value at which

$$\frac{\Delta E_{1/2} - \Delta E_{1/2,\mathrm{rev}}}{\Delta E_{1/2,\mathrm{rev}}} \leq 0.1 \text{ (Eq. 2.2)}$$

where $\Delta E_{1/2}$ is the difference between the two quartile (quarter-wave and three quarter-wave) potentials of the sigmoidal competition or SG/TC mode voltammogram.

Reversible tip current-substrate potential voltammograms are measured at the Pt, Au and GC electrodes for the TTF/TTF$^{\bullet+}$ process, indicating that $k^0_{\mathrm{Pt,TTF}} \geq 7.0$ cm s^{-1}, $k^0_{\mathrm{Au,TTF}} \geq 7.0$ cm s^{-1} and $k^0_{\mathrm{GC,TTF}} \geq 3.0$ cm s^{-1} (α reasonably assumed to be 0.5). Other simulation parameters are provided in Table 2.1.

Under experimental conditions considered herein, the upper limit of detection of SECM is larger than FTACV due to the high mass transport rates achievable under steady-state in the SECM configuration. However, the k^0 values determined for the Pt, Au and GC electrodes remain too close to the kinetic limit of SECM to be quantified. k^0_{TTF} values measured herein are consistent with previously reported literature values. Both $k^0_{\mathrm{Pt,TTF}}$ and $k^0_{\mathrm{GC,TTF}}$ were previously found to be ≥ 1.0 cm s^{-1} by FTACV (ΔE = 80.0 mV and f = 233.0 Hz)[29] at 0.12 and 1.0 mM concentrations, while $k^0_{\mathrm{Pt,TTF}}$ and $k^0_{\mathrm{Au,TTF}}$ were found to be 8.8 and 9.0 cm s^{-1}, respectively, in 1,2-dichloroethane using nanoelectrode-voltammetry in the SECM configuration.[28]

Reduction of TCNQ

TCNQ undergoes two well-resolved single-electron reduction processes in CH_3CN.[36] This study considers only the first reduction process, given by Eq. 2.3:

$$\mathrm{TCNQ} \underset{}{\overset{+e^-}{\rightleftharpoons}} \mathrm{TCNQ}^{\bullet-} \text{ (Eq. 2.3)}$$

DC CVs gave E_{m}= -0.170 ± 0.002 V (vs Fc$^{0/+}$). As for the TTF oxidation process, ΔE_{p} for the reduction of TCNQ to TCNQ$^{\bullet-}$ was close to 60 mV at v = 0.1 V s^{-1} (Section 2.6.4., Figure 2.10). $D_{\mathrm{TCNQ}} = 1.66 \times 10^{-5}$ cm^2 s^{-1} was determined from steady-state voltammetry[41] (see Section 2.6.5., Figure 2.11). $D_{\mathrm{TCNQ}^{\bullet-}}/D_{\mathrm{TCNQ}}$ determined by SECM

chronoamperometry in feedback[48] and SG/TC[19] modes (see Section 2.6.6.) gave 0.92 ± 0.04. This is in satisfactory agreement with previously reported literature values of $D_{TCNQ}^{\bullet-}/D_{TCNQ}$ of 0.80 to 0.94.[15,36–38,40]

FTACV was employed to investigate the ET process for the reduction of 0.20 mM TCNQ at Pt, Au and GC electrodes using a sine wave perturbation of ΔE = 80.0 mV and f = 228.0 Hz, where $E^{0'}$ was determined to be -0.170 ± 0.004 V. Agreement of simulated and experimental data for Pt, Au and GC are shown in Figure 2.14, Figure 2.15 and Figure 2.16 (Section 2.6.8.), respectively. Simulation parameters are provided in Table 2.2. In this case, experimental data were in good agreement with simulated data for a reversible process at the Pt electrode and therefore $k^0_{Pt,TCNQ} \geq 1.2$ cm s^{-1} was determined for the TCNQ/TCNQ$^{\bullet-}$ process. However, peak currents measured in the 7th harmonic at the Au and GC electrodes are smaller than the reversible peak magnitude and therefore $k^0_{Au,TCNQ}$ = 1.0 cm s^{-1} and $k^0_{GC,TCNQ}$ = 1.0 cm s^{-1} can be reliably assigned. k^0_{FTACV} values reported herein for the TCNQ/TCNQ$^{\bullet-}$ redox process at a high frequency of 228.0 Hz are consistent with values for $k^0_{Pt,TCNQ}$ and $k^0_{GC,TCNQ} \geq 0.3$ cm s^{-1} determined using a sine wave perturbation of ΔE = 80.0 mV and a lower frequency of 9.0 Hz.

Table 2.2 Parameters used for FTACV simulations and SECM analytical fitting of the TCNQ/TCNQ$^{\bullet-}$ process in CH_3CN (0.1 M Bu_4NPF_6) at Pt, Au, GC and pBDD macroelectrodes. Other simulation parameters applicable to either technique: D_{TCNQ} = 1.66 × 10^{-5} cm^2 s^{-1}, $D_{TCNQ}^{\bullet-}$ = 1.53 × 10^{-5} cm^2 s^{-1}, $E^{0'}$ = -0.170 V, T = 293.2 K and α = 0.50 (assumed).

Electrode Material	FTACV[a]						SECM[b]	
	c / mM	A / mm^2	v_{AC} / V s^{-1}	R_u / Ω	C_{dl} (c_0, c_1, c_2, c_3 terms) / μF cm^{-2}	k^0 / cm s^{-1}	c / mM	k^0 / cm s^{-1}
Pt	0.20	0.785	0.10	550	13.5, 0.0, 1.0, 0.0	≥ 1.2	1.0	2.1 ± 0.6
Au	0.20	0.785	0.05	485	8.5, 0.0, 0.0, 0.0	1.0	1.0	1.6 ± 0.6
GC	0.20	0.785	0.10	475	18.0, 10.3, 7.8, -0.9	1.0	1.0	1.2 ± 0.2
pBDD	0.20	0.785	0.10	300	3.8, 0.0, 0.2, 0.0	0.4	1.0	0.04 ± 0.02[c]

[a] ΔE = 80.0 mV, f = 228.0 Hz [b] a_{UME} = 1.0 μm, v = 0.05 V s^{-1}, RG = 20 [c] anomalous α

Substrate voltammetry SECM was also employed to investigate this system under high mass transport rates. The UME tip (a_{UME} = 1.0 μm, RG = 20) was positioned at a fixed

distance from the substrate of interest and E_{sub} was scanned negatively at 0.05 V s^{-1} to reduce TCNQ to $TCNQ^{\bullet-}$. In the competition mode ($E_{UME} << E^{0'}_{TCNQ}$), the UME tip gives the positive feedback response when $E_{sub} >> E^{0'}_{TCNQ}$. As the substrate potential is scanned (negatively), the UME tip competes with the substrate to reduce TCNQ.[18] In the SG/TC mode ($E_{UME} >> E^{0'}_{TCNQ}$), the UME tip current rises from zero as it oxidises $TCNQ^{\bullet-}$ produced at the substrate surface. Similar to the TTF oxidation process, competition and SG/TC mode UME tip currents, taken as a function of substrate potential, can be used to determine thermodynamic and kinetic parameters[15] and the results are summarised in Table 2.2.

$k^0_{Pt,TCNQ}$ = 2.1 cm s^{-1}, $k^0_{Au,TCNQ}$ = 1.6 cm s^{-1} and $k^0_{GC,TCNQ}$ = 1.2 cm s^{-1} that were determined from SECM measurements are in good agreement with results from FTACV experiments. For comparison, $k^0_{Pt,TCNQ}$ in the range of 3.0–7.0 cm s^{-1} in CH_3CN (0.1 M tetrabutylammonium perchlorate (Bu_4NClO_4)) have previously been found using substrate voltammetry SECM[15] while $k^0_{Pt,TCNQ}$ = 1.1 cm s^{-1} and α = 0.42 in CH_3CN (0.1 M Bu_4NClO_4) was obtained by nanoelectrode-voltammetry in the SECM configuration[28] but it was also found that $k^0_{Au,TCNQ}$ could not be determined at gold nanoelectrodes due to poorly shaped voltammograms, that were inconsistent with theoretical predictions.[28] It has recently been reported that $k^0_{Pt,TCNQ}$ = 8.2 cm s^{-1} [40] at Pt nanoelectrodes that were characterised by atomic force microscopy and analysis of steady-state voltammograms. However, this study,[40] also noted other important factors that should be considered in nanoelectrode voltammetry studies such as possible influences of the electrical double layer and glass surface charge that were not considered. Given the uncertainties associated with each experimental technique, the kinetic values determined herein by both FTACV and SECM are consistent with other reported values.[15,28,33–40]

2.4.2. Electron Transfer Studies at pBDD Electrodes

Oxidation of TTF

FTACV experiments for the oxidation of TTF at pBDD were carried out using a sine wave perturbation of ΔE = 80.0 mV and f = 228.0 Hz. $E^{0'}$ was found to be -0.074 ±

0.002 V (vs $Fc^{0/+}$) and is in good agreement with values determined at the conventional electrode materials (see above). Comparison of the higher harmonic experimental peak current magnitudes for electrodes having the same radii immediately suggests that the electrode kinetics at the pBDD electrode are much lower than that at the Pt, Au and GC electrodes. Comparison of experimental (black lines) and simulated (red lines) data at pBDD (Figure 2.4) gave $k^0_{pBDD,TTF} = 0.35$ cm s^{-1}. The blue line in Figure 2.4 shows that the simulated reversible 7th harmonic component is much larger than the experimental peak currents and validates the reliability of kinetic assignment of k^0_{TTF}. All thermodynamic and kinetic properties associated with the $TTF/TTF^{\bullet+}$ process at pBDD, determined by FTACV, are provided in Table 2.1.

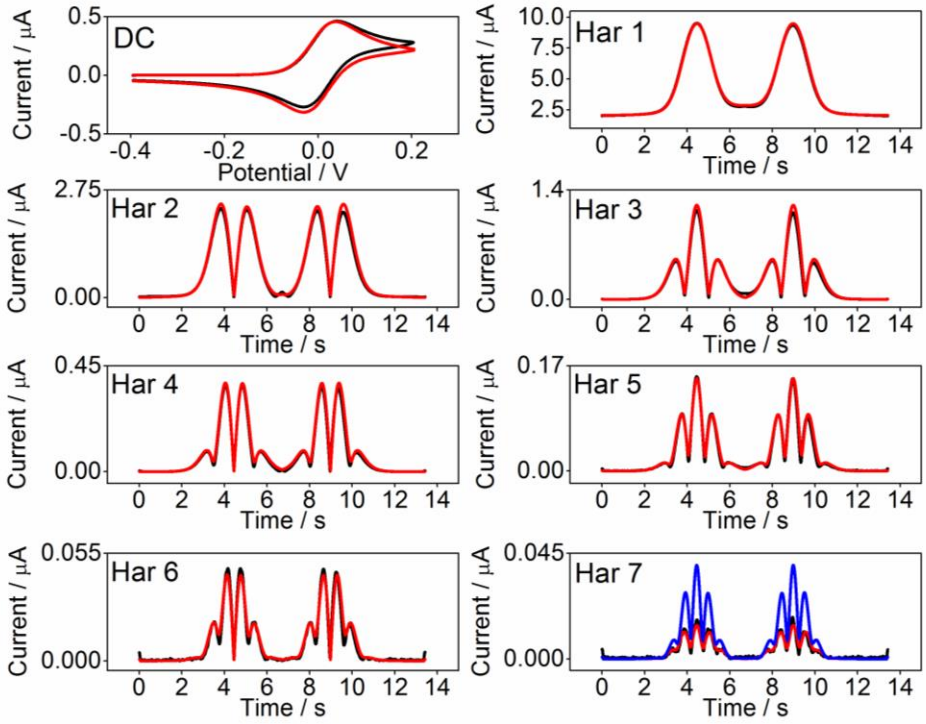

Figure 2.4 Comparison of experimental (black lines) and simulated (red lines, Ψ = 0.989) FTACV curves for the one-electron oxidation of 0.25 mM TTF in CH_3CN (0.1 M Bu_4NPF_6) at a pBDD macroelectrode. Simulation parameters: $k^0 = 0.35$ cm s^{-1}, $\alpha = 0.5$, $R_u = 550\ \Omega$, $A = 0.00785$ cm^2, $f = 228.0$ Hz, $\Delta E = 80.0$ mV, $D_{TTF} = 2.10 \times 10^{-5}$ cm^2 s^{-1}, $D_{TTF^{+\cdot}} = 1.80 \times 10^{-5}$ cm^2 s^{-1}, $v_{AC} = 0.09$ V s^{-1} and $v_{DC} = 0.1$ V s^{-1}. The blue line shows the 7th AC harmonic component response for a reversible process ($k^0 = 1000$ cm s^{-1}) with all other simulation parameters the same.

Substrate voltammetry SECM was performed in the competition and SG/TC modes on pBDD for the oxidation of 1.0 mM TTF. In contrast to the FTACV data, which gave an average $k^0_{pBDD,TTF}$, a series of SECM voltammetric experiments performed on a pBDD substrate in a line scan at 2.0 μm intervals (d ~ 800 nm, N_{total} = 21) gave a large dispersion in $k^0_{pBDD,TTF}$ values lying between 0.05 and 0.4 cm s^{-1} (α assumed to be 0.5). Figure 2.5 provides a histogram showing $k^0_{pBDD,TTF}$ values determined from the SECM line scan. Two distinct regions of ET activity (modal values of 0.1 cm s^{-1} and 0.4 cm s^{-1}) are observed. This could reasonably be expected due to the heterogeneous nature of pBDD, where regions of high and low dopant densities that have distinctly different ET rates have been observed.[22,23,27] Interestingly, the ratio of the high to low k^0 values is similar to previous values (by SECM in SG/TC modes) for two outer-sphere redox mediators, $[Ru(NH_3)_6]^{3+/2+}$ and ferrocenylmethyltrimethyl ammonium, at pBDD electrodes in aqueous solution.[22] This is also in good agreement with SECM studies that show variations in the SECM kinetic response as the UME tip is traversed laterally near to a pBDD surface.[27]

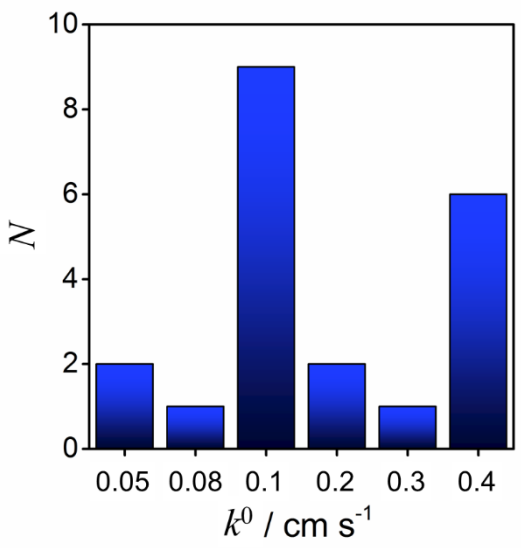

Figure 2.5 Histogram of $k^0_{pBDD,TTF}$ values determined from substrate voltammetry SECM measurements taken in a line scan at 2.0 μm intervals (N_{total} = 21).

This interesting result exemplifies a major difference in SECM compared to FTACV. The high spatial resolution capabilities of SECM allow for highly localised kinetic measurements at a macrodisk electrode relevant to the specific region under the

UME tip. In contrast k^0 values determined by FTACV represent an overall (average) kinetic value for the pBDD macroelectrode, which will tend to be dominated by the faster process when the diffusion layers are fully overlapped.[50] However, regardless of the spatial-kinetic resolution of the two techniques, both FTACV and SECM measurements reveal that the k^0_{BDD} value is at least an order of magnitude smaller than at conventional electrode materials for the TTF/TTF$^{\bullet+}$ process.[51]

Reduction of TCNQ

FTACV for the TCNQ/TCNQ$^{\bullet-}$ process at a pBDD macrodisk electrode was carried out using a sine wave perturbation of ΔE = 80.0 mV and f = 228.0 Hz. $E^{0'}$ was determined to be -0.170 ± 0.002 V (vs $Fc^{0/+}$). The pBDD electrode again showed significantly slower ET rates, $k^0_{pBDD,TCNQ}$ = 0.4 cm s^{-1} compared to the conventional electrode materials considered above. Agreement between simulated and experimental FTACV data, which is excellent for all harmonics, is shown in Figure 2.17. All thermodynamic and kinetic properties are summarised in Table 2.2. Again, lower capacitance is observed at the pBDD electrode (< 4 μF cm^{-2}) compared to the conventional electrode materials (> 8 μF cm^{-2}).

Substrate voltammetry SECM was also performed in the competition and SG/TC mode on pBDD for the reduction of 1.0 mM TCNQ. Figure 2.6(a) shows a plot of current density at the UME tip as a function of the pBDD substrate potential in both competition and SG/TC mode. These voltammograms are considerably broader than predicted for a diffusion-limited reversible process, and can only be fitted with rather low $k^0_{pBDD,TCNQ}$ values (0.04 ± 0.02 cm s^{-1}) compared to those obtained using FTACV (0.4 cm s^{-1}).

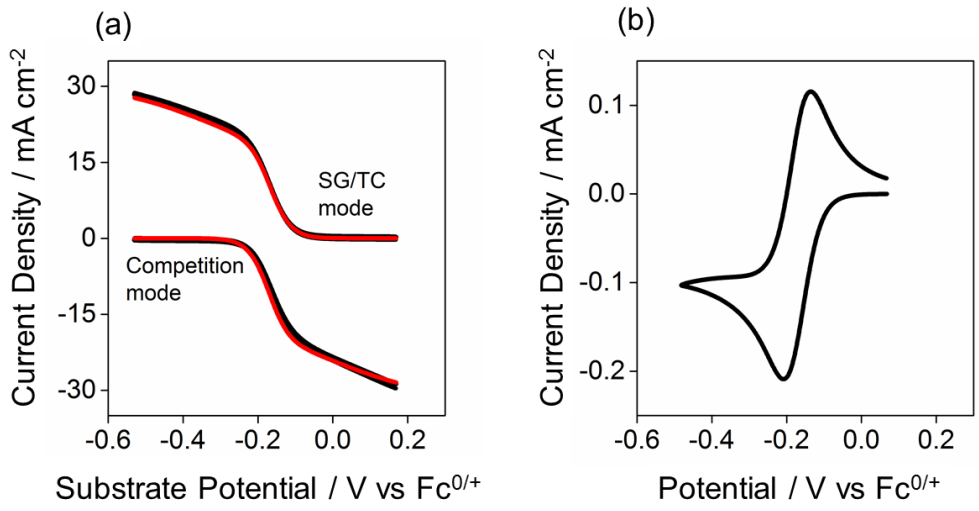

Figure 2.6 (a) Experimental (black lines) and analytical (red lines) UME tip current-substrate potential curves for the competition and SG/TC mode for the one-electron reduction of 1.0 mM TCNQ in CH_3CN (0.1 M Bu_4NPF_6) at a pBDD electrode with v = 0.05 V s^{-1}. (b) CV for the TCNQ/$TCNQ^{\bullet-}$ process at a pBDD macrodisk with v = 0.1 V s^{-1}.

Moreover, these non-characteristic SECM voltammograms fail to reach a diffusion-limited current, even at large substrate overpotentials and do not comply with kinetically-limited voltammograms with the usually assumed α value of about 0.5. Interestingly, for better simulation fits, the competition and SG/TC mode are fitted separately but with different α values, with all other parameters remaining the same. For Figure 2.6(a), the following simulation parameters apply: $k^0_{pBDD,TCNQ}$ = 0.04 cm s^{-1}, D_{TCNQ} = 1.66 × 10^{-5} cm^2 s^{-1}, $D_{TCNQ^{\bullet-}}$ = 1.53 × 10^{-5} cm^2 s^{-1}, $E^{0'}$ = - 0.170 V, a = 1.0 µm and d = 1.0 µm, along with α values of 0.8 and 0.2 for the competition and SG/TC modes, respectively.

The SECM voltammogram shapes imply that both the reduction of TCNQ and oxidation of $TCNQ^{\bullet-}$ appear to be more 'difficult' than expected when large current densities are passed through the pBDD electrode material in the region under the UME tip. The extreme (and unusual) α values are likely a physical manifestation of relatively high resistance within the pBDD substrate (or surface layer) rather than a chemical property associated with the TCNQ/$TCNQ^{\bullet-}$ process. It is proposed that the higher apparent kinetic resistance of the SECM voltammetric behaviour for the TCNQ/ $TCNQ^{\bullet-}$ process can be attributed to depletion of charge carriers at the BDD surface under the UME tip (depicted

in Figure 2.7). The high current density passing through the pBDD electrode is limited by the availability (and/or reduction in mobility) of charge carriers at the electrode surface, which is exacerbated in this potential region.[42]

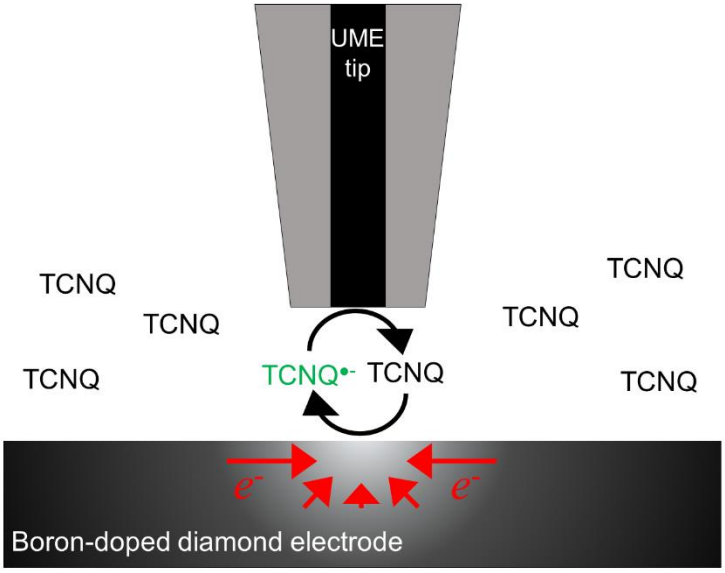

Figure 2.7 Diagram depicting the interaction of the TCNQ redox mediator with pBDD surface in the SG/TC mode of SECM. The lightly shaded region represents the charge depletion effect when high current density is locally passed through the pBDD substrtate.

Anomalous voltammograms have been observed previously in substrate voltammetry SECM measurements at other materials such as < 1% single walled carbon nanotube (SWNT) networks UMEs,[52] where a sloping plateau in the diffusion-limited potential regime was observed for SG/TC voltammograms taken at a < 1% surface coverage (resistive) SWNT network UME under conditions of very high flux to individual SWNTs. In contrast, a 100 % surface coverage (less resistive) SWNT mat UME exhibited well-behaved Nernstian SG/TC voltammograms.[52] A recent SECM study on chemical vapor deposition-grown graphene[53] also reported anomalous UME tip voltammograms for the $Fc(CH_2OH)^{0/+}$ process. However in this study, the odd-shaped voltammograms were attributed to surface contamination by positively-charged polymethylmethacrylate on the graphene electrode limiting the redox feedback process.

In contrast to the SECM results, macroscale CV (Figure 2.6(b)) and FTACV (Figure 2.17) do not provide anomalous α. The current density measured for these

configurations is more than 100 times smaller than for the UME tip in the SECM configuration.

Interestingly, the behaviour in substrate voltammetry SECM measurements for the TTF/TTF$^{\bullet+}$ process at pBDD electrodes do not show the same anomalous behaviour exhibited for the TCNQ/TCNQ$^{\bullet-}$ process. This is most likely a consequence of the electronic properties of pBDD. Although this p-type semi-conductor is degenerately doped, the number of available charge carriers at each energy state is less than that of a typical metal and will decrease as $E^{0'}$ for the redox couple becomes more negative.[54] Furthermore, polishing of the pBDD surface, in post-processing, may also impact deleteriously, causing charge-trap defects which affect charge mobility. This reduced carrier availability and mobility is the likely reason why, in general, k^0 values for pBDD are lower than for classical metal electrode systems, whilst the anomalous behaviour of TCNQ/TCNQ$^{\bullet-}$, is attributed to the more negative $E^{0'}$ value of this redox couple, where the overall concentration of charge carriers in the pBDD is depleted and becomes further depleted as the potential is scanned cathodically, manifested empirically in the (extreme) value of $\alpha = 0.2$ in the SG/TC mode. Figure 2.8 highlights this situation qualitatively, showing a simplified band diagram where there is a depletion of available charge carriers at the pBDD electrode at more negative potentials compared to the continuous availability of states available in a metal. The simple, and usually fast, TTF/TTF$^{\bullet+}$ and TCNQ/TCNQ$^{\bullet-}$ redox couples essentially probe different parts of the band structure given the different standard electrode potentials.

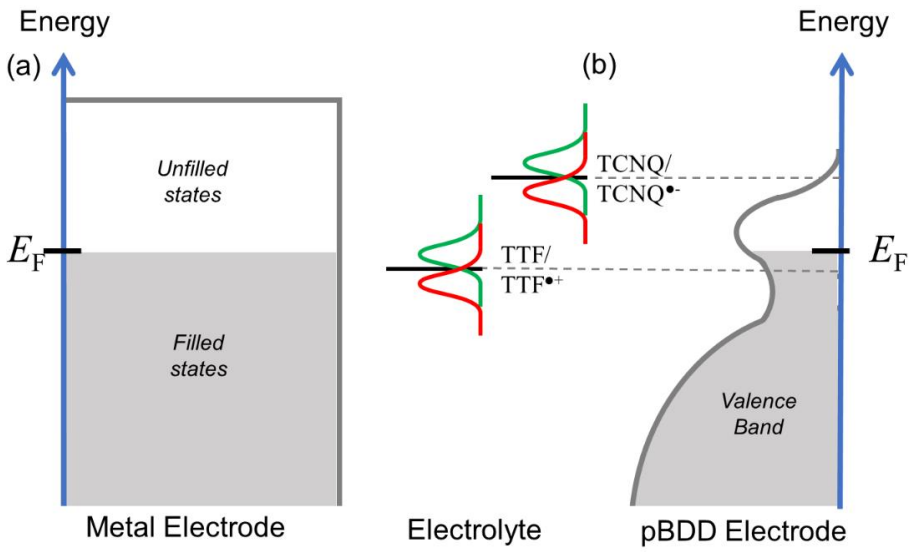

Figure 2.8 Schematic representation qualitatively showing the positon of the TTF/TTF$^{\bullet+}$ and TCNQ/TCNQ$^{\bullet-}$ redox couples with respect to the (a) filled and unfilled states at conventional metal electrodes and (b) the valence band at degenerately doped-pBDD electrodes.[55]

2.5. Conclusions

The studies reported herein provide a comparison of k^0 values determined by macroscopic FTACV and microscopic SECM measurements for the simple one-electron oxidation of TTF and the reduction of TCNQ at three conventional electrode materials; Pt, Au and GC. All results provide very fast k^0 values, close to the upper kinetic limit for both electrochemical techniques, in good agreement with literature reports. These data highlighted these processes to be fast and, most likely, outer sphere, making them particularly suitable to probe more complex materials such as pBDD electrodes.

At pBDD electrodes important key differences emerge in FTACV kinetic measurements, which provide overall kinetic values for the entire macroelectrode, and substrate voltammetric SECM kinetics measurements, which reflect a highly localised kinetic measurement of the macroelectrode sample at the region under the UME tip. For TTF oxidation at pBDD, two distinct regions of ET activity are observed by substrate voltammetry SECM, which are related to the distinct regions of high and low boron dopant density.[21,22,27,42] These data are in good agreement with the overall k^0 values determined by

FTACV. In the case of TCNQ reduction at pBDD, the more negative $E^{0'}$ compared to TTF, results in a lower number of available charge carriers. The result is a k^0_{SECM} that is 10 times smaller than k^0_{FTACV}, due to the high local current density of SECM that imposes a significant challenge on charge flow through the pBDD, and a distorted voltammogram shape, with an apparent α = 0.2 (in the SG/TC configuration) diagnostic of increasing limitations from the electrode material as the potential is scanned in the negative direction, consistent with the degenerate p-doping of pBDD.

These studies thus highlight important differences between pBDD and more conventional electrode materials for electrochemistry that are revealed with simple redox couples. It is also important to note possible influences of surface states, defects, charge-trapping and surface passivation layers. This highlights the need for further work to understand the electronic structure and charge carrier mobility near the surface of pBDD and the effect of post-process (polishing) on the properties of this layer through testing with additional redox couples, along with electrode surface treatments and varying boron doping levels.

2.6. Supporting Information

2.6.1. FTACV: Theory and Simulations

FTACV simulations were carried out with the MECSim program written in Fortran.[6,56] Fick's law of planar diffusion was solved numerically to determine the electrochemical response by applying Butler-Volmer[57,58] formulations to describe the potential-dependence of ET at the electrode/electrolyte interface.

The DC potential ramp applied to the working electrode was superimposed with an AC sine wave of amplitude, ΔE = 80 mV and frequency, f = 228.0 Hz. The FTACV data obtained experimentally and theoretically were converted from the time domain to the frequency domain using a Fourier-transform algorithm. Frequencies corresponding to the AC harmonic components were selected from the power spectrum and were subjected to band filtering and inverse Fourier-transform procedures to obtain the resolved AC

components as a function of time. Electrode area, A, solution concentration, c, uncompensated resistance, R_u, and diffusion coefficients, D, are known from other measurements while the redox couple formal potential, $E^{0'}$, standard heterogeneous rate constant, k^0, transfer coefficient, α and the double layer capacitance, C_{dl}, were computed in FTACV simulations. $E^{0'}$ can also be estimated from the potential minima and maxima of the even and odd harmonics, respectively. The potential-dependent C_{dl} was determined from the fundamental harmonic component in the potential region where there is no faradaic current and is modelled as a fourth-order polynomial function: $C_{dl} = c_0 + c_1E + c_2E^2 + c_3E^3 + c_4E^4$, where c_0, c_1, c_2, c_3 and c_4 are constants. R_u was determined from the 1st and 2nd AC harmonics. The higher order harmonic components (3rd to 7th), which are highly sensitive to electrode kinetics, were used to determine k^0. α is reasonably assumed to be 0.5.

The least squares correlation, Ψ, between experimental and simulated data is given by the following:[59,60]

$$\Psi = 1 - \left[\frac{1}{H} \left(\sum_{h=1}^{H} \sqrt{\frac{\sum_{i=1}^{N} \left[\left(f_h^{\exp}(x_i) - f_h^{sim}(x_i) \right)^2 \right]}{\sum_{i=1}^{N} f_h^{\exp}(x_i)^2}} \right) \right] \qquad \text{(Eq. 2.4)}$$

where h is the number of the AC harmonic component, H is the total number of AC harmonic components considered and $f_h^{\exp}(x_i)$ and $f_h^{\text{sim}}(x_i)$ are the experimental and simulated functions in the corresponding AC harmonic, respectively and N is the number of data points. All calculations of Ψ do not include the first and last 0.5 s of the FTACV scan to ensure effects of 'ringing' artefacts resulting from the experimental Fourier-transform – band filtering – inverse Fourier-transform process do not reduce the reliability of the simulated fit and is described in detail elsewhere.[61]

2.6.2. SECM: Tip Positioning

A scanning electrochemical microscope (SECM) was mounted on a vibration-isolation table inside a Faraday cage. The UME tip (a = 1.0 μm and RG = 20) was mounted in a tip holder on a piezo-bender actuator, to which an oscillation (70 Hz with an amplitude of 50

nm (~ 5 % UME tip electrode radius)) was applied. In turn, this was mounted on a 3D-piezoelectric positioner controlled by a PC running custom LabVIEW code (LabVIEW 9.0, National Instruments), which was also used for data acquisition. The tip-substrate separation was controlled by monitoring the damping of the oscillation amplitude of the tip upon intermittent-contact between the tip and surface (typically by 5 %).[47]

2.6.3. SECM: Theory

Determination of mass transport parameters: positive feedback approach curve

The steady-state diffusion limited UME tip current in bulk solution, $i_{\mathrm{UME,bulk}} = 4nFaDc$, where n is the number of electrons transferred per redox event and F is the Faraday constant, was used to normalised UME tip currents measured close to the substrate electrode, at distance, d. The normalised tip-substrate separation, $L = d/a$, is reliably determined from normalised diffusion-limited positive feedback currents, $I_{\mathrm{UME,lim}}$:[62]

$$I_{\mathrm{UME,lim}}(L,\mathrm{RG}) = \alpha(\mathrm{RG}) + \frac{\pi}{4\beta(\mathrm{RG})\arctan(L)} + \left(1-\alpha(\mathrm{RG})-\frac{1}{2\beta(\mathrm{RG})}\right)\left(\frac{2}{\pi}\arctan(L)\right) \quad \text{(Eq. 2.5)}$$

with

$$\alpha(\mathrm{RG}) = \ln 2 + \ln 2\left(1-\frac{2}{\pi}\arccos\left(\frac{1}{\mathrm{RG}}\right)\right) - \ln 2\left(1-\left(\frac{2}{\pi}\arccos\left(\frac{1}{\mathrm{RG}}\right)\right)^2\right) \quad \text{(Eq. 2.6)}$$

and

$$\beta(\mathrm{RG}) = 1 + 0.639\left(1-\frac{2}{\pi}\arccos\left(\frac{1}{\mathrm{RG}}\right)\right) - 0.186\left(1-\left(\frac{2}{\pi}\arccos\left(\frac{1}{\mathrm{RG}}\right)\right)^2\right) \quad \text{(Eq. 2.7)}$$

Determination of kinetic and thermodynamic parameters: analytical model

Kinetic and thermodynamic properties for the redox processes in the substrate voltammetry SECM configuration are obtained by comparison of experimental curves to an analytical expression. The analytical expressions for the normalised tip current measured in both the competition and substrate generation/tip collection (SG/TC) modes for an oxidation process are given by the following:[15]

$$I_{\mathrm{comp,oxi}}(E_{\mathrm{sub}}, L) =$$

$$\xi^2\left[\frac{\pi}{2\beta(\mathrm{RG})L(2\xi^2\theta_{\mathrm{sub}}+2\theta_{\mathrm{sub}}{}^{\alpha}/\lambda^{o'}+\xi^2+1)}+\frac{1}{\xi\theta_{\mathrm{sub}}+1}\left(\frac{I_{\mathrm{UME,lim}}(L)}{\xi^2}-\frac{\pi}{2\beta(\mathrm{RG})L(\xi^2+1)}\right)\right] \quad \text{(Eq. 2.8)}$$

$$I_{\mathrm{sgtc,oxi}}(E_{\mathrm{sub}}, L) =$$

$$-\xi^2\left[\frac{\pi}{2\beta(\mathrm{RG})L(2/\theta_{\mathrm{sub}}+2\theta_{\mathrm{sub}}{}^{\alpha-1}/\lambda^{o'}+\xi^2+1)}+\frac{\xi\theta_{\mathrm{sub}}}{\xi\theta_{\mathrm{sub}}+1}\left(\frac{I_{\mathrm{UME,lim}}(L)}{\xi}-\frac{\pi}{2\beta(\mathrm{RG})L(\xi^2+1)}\right)\right] \quad \text{(Eq. 2.9)}$$

with

$$\theta_{\mathrm{sub}} = \exp(F(E_{\mathrm{sub}} - E^{0'})/RT \quad \text{(Eq. 2.10)}$$

and

$$\lambda^{0'} = k^{0'}d/D_{\mathrm{ox}} \quad \text{(Eq. 2.11)}$$

and

$$\xi = \sqrt{\frac{D_{\mathrm{ox}}}{D_{\mathrm{red}}}} \quad \text{(Eq. 2.12)}$$

where, ξ is the dimensionless diffusion coefficient ratio and $\lambda^{0'}$ is the dimensionless ET rate constant.

The analytical expressions for the normalised tip current vs. substrate potential in competition and SG/TC modes for a reduction process are given by:[15]

$$I_{\mathrm{comp,red}}(E_{\mathrm{sub}}, L) =$$

$$-\left[\frac{\pi}{2\beta(\mathrm{RG})L(2/\theta_{\mathrm{sub}} + 2\theta_{\mathrm{sub}}{}^{\alpha-1}/\lambda^{o'} + \xi^2 + 1)} + \frac{\xi\theta_{\mathrm{sub}}}{\xi\theta_{\mathrm{sub}} + 1}\left(I_{\mathrm{UME,lim}}(L) - \frac{\pi}{2\beta(\mathrm{RG})L(\xi^2 + 1)}\right)\right] \quad \text{(Eq. 2.13)}$$

$$I_{\mathrm{sgtc,red}}(E_{\mathrm{sub}}, L) =$$

$$\frac{\pi}{2\beta(\mathrm{RG})L(2\xi^2\theta_{\mathrm{sub}} + 2\theta_{\mathrm{sub}}{}^{\alpha}/\lambda^{o'} + \xi^2 + 1)} + \frac{1}{\xi\theta_{\mathrm{sub}} + 1}\left(\frac{I_{\mathrm{UME,lim}}(L)}{\xi} - \frac{\pi}{2\beta(\mathrm{RG})L(\xi^2 + 1)}\right) \quad \text{(Eq. 2.14)}$$

2.6.4. CVs for the Oxidation of TTF and Reduction of TCNQ

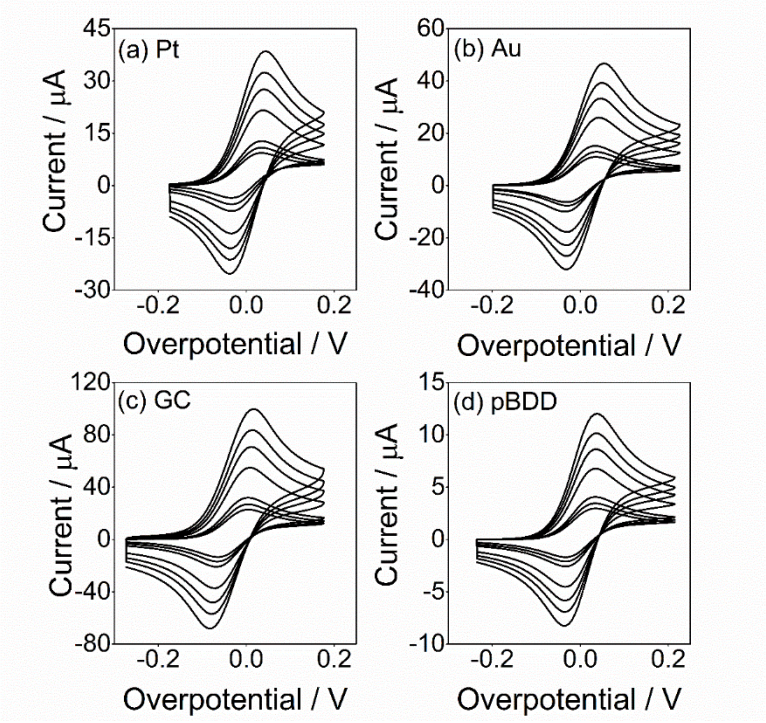

Figure 2.9 CVs for the oxidation of 1.0 mM TTF in CH_3CN (0.1 M Bu_4NPF_6) at (a) Pt (a_{Pt} = 1.0 mm), (b) Au (a_{Au} = 1.0 mm), (c) GC (a_{GC} = 1.5 mm) and (d) pBDD (a_{pBDD} = 0.5 mm) with scan rate, v, in a range of 0.05 to 1.0 V s^{-1}.

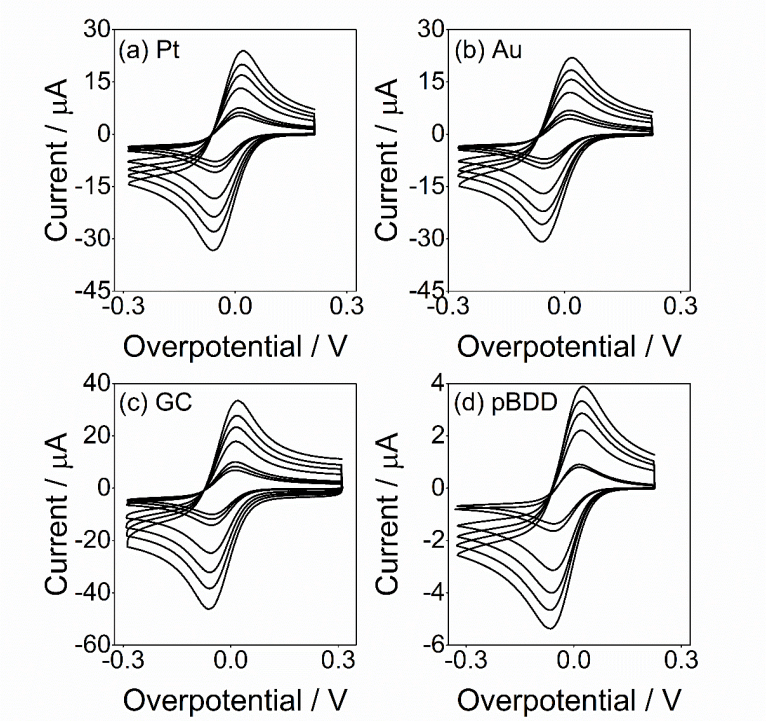

Figure 2.10 CVs for the reduction of 1.0 mM TCNQ in CH_3CN (0.1 M Bu_4NPF_6) at (a) Pt (a_{Pt} = 1.0 mm), (b) Au (a_{Au} = 1.0 mm), (c) GC (a_{GC} = 1.5 mm) and (d) pBDD (a_{pBDD} = 0.5 mm) with v in a range of 0.05 to 1.0 V s^{-1}.

Determination of the Diffusion Coefficients of TTF and TCNQ

CVs for the oxidation of 1.0 mM TTF and reduction of 1.0 mM TCNQ taken at a Pt UME (a = 1.0 μm) are shown in Figure 2.11(a) and (b), respectively. The measured diffusion-limited current, i_{UME}, gave diffusion coefficients, D_{TTF} = 2.10 × 10^{-5} cm^2 s^{-1} and D_{TCNQ} = 1.66 × 10^{-5} cm^2 s^{-1}.

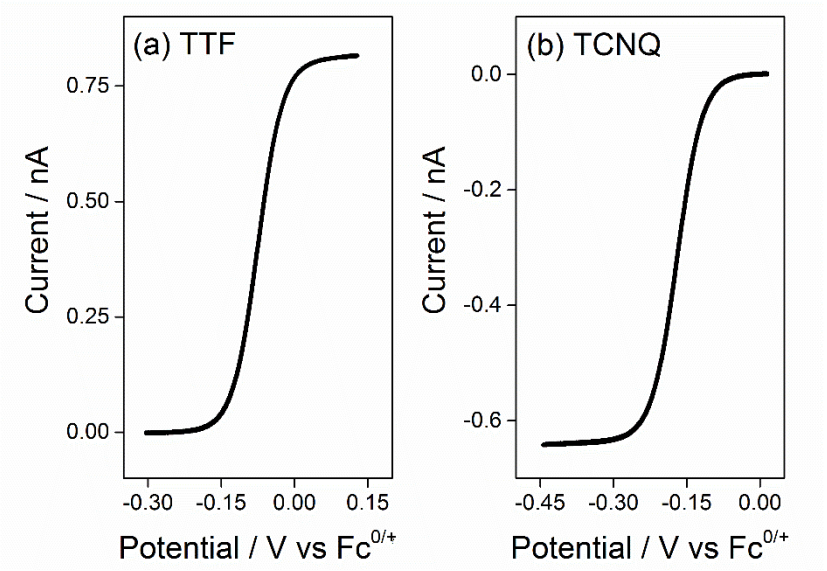

Figure 2.11 CVs for the (a) oxidation of 1.0 mM TTF and (b) reduction of 1.0 mM TCNQ in CH_3CN (0.1 M Bu_4NPF_6) with v = 0.05 V s^{-1} at a 1.0 μm-radius Pt UME.

2.6.5. Determination of the Diffusion Coefficients of $TTF^{\bullet+}$ and $TCNQ^{\bullet-}$

Voltammetric studies in the SECM configuration are very sensitive to differences in the diffusion coefficient, D, values of the oxidised and reduced forms of the redox couple. It is rare for the diffusivities of both redox forms to be the same, particularly in organic (non-conventional) solvents, studied herein. Accurate determination of these values are very important for accurate quantitative kinetic studies,[15,19,20,48,63] especially if one is seeking to measure the kinetics of fast processes that are close to the diffusion-limit.

To accurately determine D of $TTF^{\bullet+}$ and $TCNQ^{\bullet-}$, SECM-chronoamperometric measurements are employed with a Pt UME in both feedback[48] and SG/TC modes.[19] The UME tip responses can be analysed to give the D ratio of the oxidised to reduced form of

the redox couple, γ, when the redox couple undergoes a simple diffusion-controlled one ET process, with no kinetic complications and adsorption effects.[17,19,48] In the feedback configuration, γ has no effect on the steady-state current measured at the UME tip[48] because the feedback steady-state limiting-current merely depends on the redox competition between the substrate and tip electrodes in the solution. Hence, the feedback mode limiting-current can be used to precisely determine the tip-substrate separation for a pair of feedback and SG/TC limiting-currents taken at the same tip position. Under the SG/TC SECM-chronoamperometric configuration, $TTF^{\bullet+}$ or $TCNQ^{\bullet-}$ is electrogenerated at a diffusion-controlled rate from the precursor in bulk (TTF or TCNQ), at a macroscopic Pt substrate. The $TTF^{\bullet+}$ or $TCNQ^{\bullet-}$ diffusion front is intercepted by the UME tip positioned close to the substrate. Although the macroscopic substrate electrode will have a transient form, the redox mediator diffusional cycling between the UME tip and substrate will be in a quasi-steady-state limited by the diffusion of $TTF^{\bullet+}$ or $TCNQ^{\bullet-}$. Therefore, the limiting-current measured in the SG/TC mode can be used to determine γ from a simple modification of an empirically derived equation for the positive feedback mode:[64]

$$I_{\mathrm{UME,lim}}(L) = \gamma\left[0.68 + 0.78377/L + 0.3315\exp(-1.0672L)\right] \quad \text{(Eq. 2.15)}$$

2.6.6. FTACV Experimental and Simulated Data for the Oxidation of TTF at Au and GC Macroelectrodes

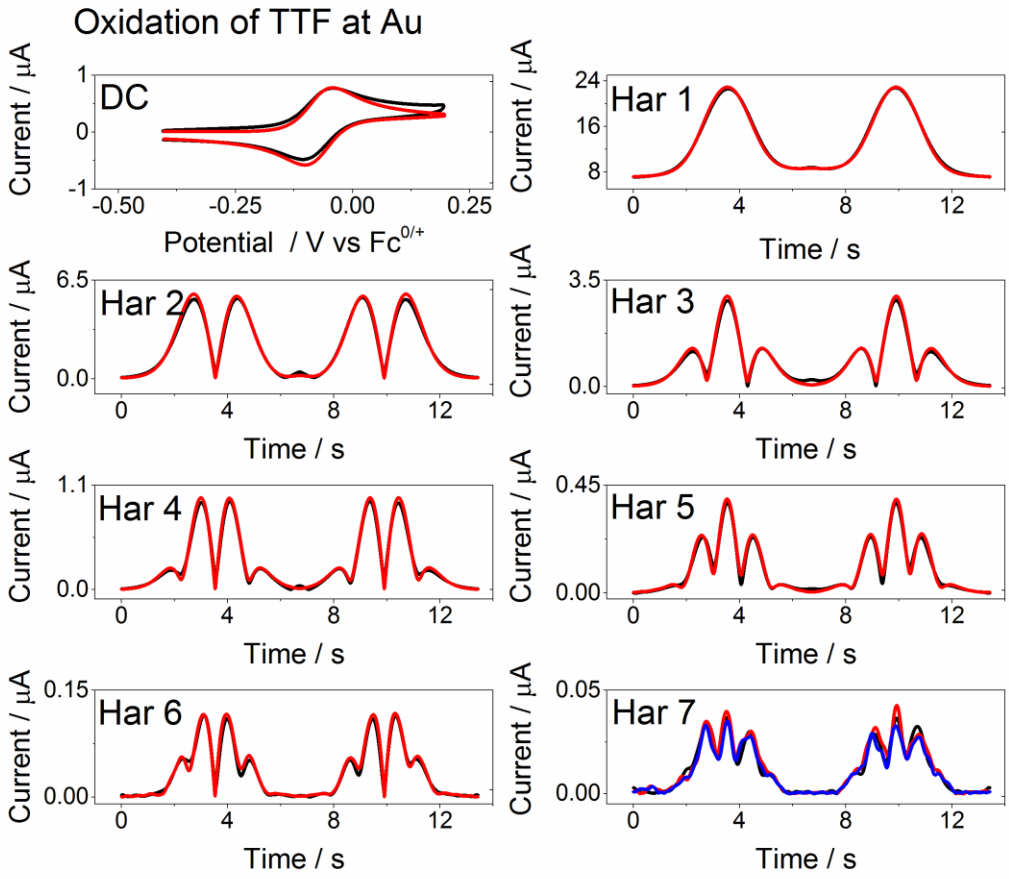

Figure 2.12 Comparison of experimental (black lines) and simulated (red lines, $\Psi = 0.994$) FTACV curves for the one-electron oxidation of 0.25 mM TTF in CH_3CN (0.1 M Bu_4NPF_6) at an Au macroelectrode. Simulation parameters: $k^0 = 1000$ cm s^{-1} (reversible), $\alpha = 0.50$, $R_u = 500$ ohm, $A = 0.00785$ cm^2, $f = 228.0$ Hz, $\Delta E = 80.0$ mV, $D_{TTF} = 2.10 \times 10^{-5}$ cm^2 s^{-1}, $D_{TTF}^{\bullet+} = 1.80 \times 10^{-5}$ cm^2 s^{-1}, $v_{AC} = 0.07$ V s^{-1} and $v_{DC} = 0.1$ V s^{-1}. The blue line shows the 7th AC harmonic component response for $k^0 = 1.5$ cm s^{-1} with all other simulation parameters the same and represents the upper kinetic limit of detection.

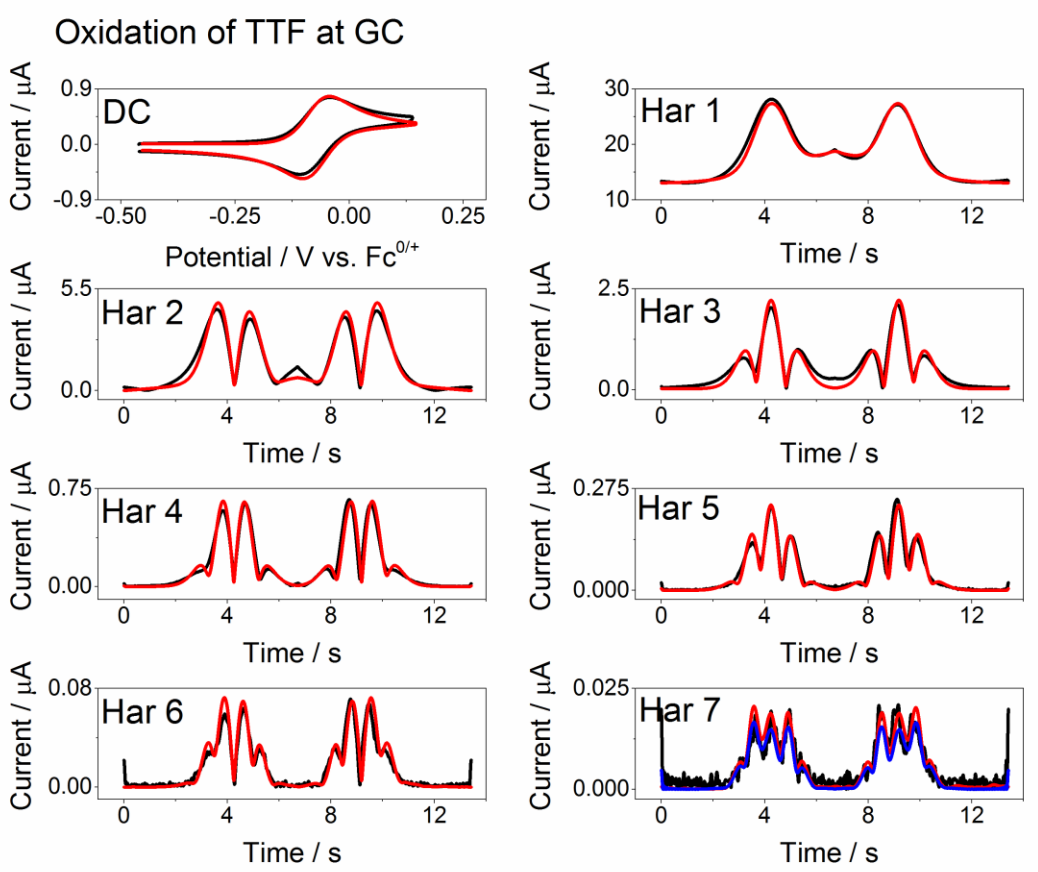

Figure 2.13 Comparison of experimental (black lines) and simulated (red lines, $\Psi = 0.975$) FTACV curves for the one-electron oxidation of 0.25 mM TTF in CH_3CN (0.1 M Bu_4NPF_6) at a GC macroelectrode. Simulation parameters: $k^0 = 1000$ cm s^{-1} (reversible), $\alpha = 0.50$, $R_u = 525$ ohm, $A = 0.00785$ cm^2, $f = 228.0$ Hz, $\Delta E = 80.0$ mV, $D_{TTF} = 2.10 \times 10^{-5}$ cm^2 s^{-1}, $D_{TTF}^{\bullet+} = 1.80 \times 10^{-5}$ cm^2 s^{-1}, $v_{AC} = 0.09$ V s^{-1} and $v_{DC} = 0.1$ V s^{-1}. The blue line shows the 7th AC harmonic component response for $k^0 = 1.0$ cm s^{-1} with all other simulation parameters the same and represents the upper kinetic limit of detection.

2.6.7. FTACV Experimental and Simulated Data for Reduction of TCNQ at Pt, Au, GC and pBDD Macroelectrodes

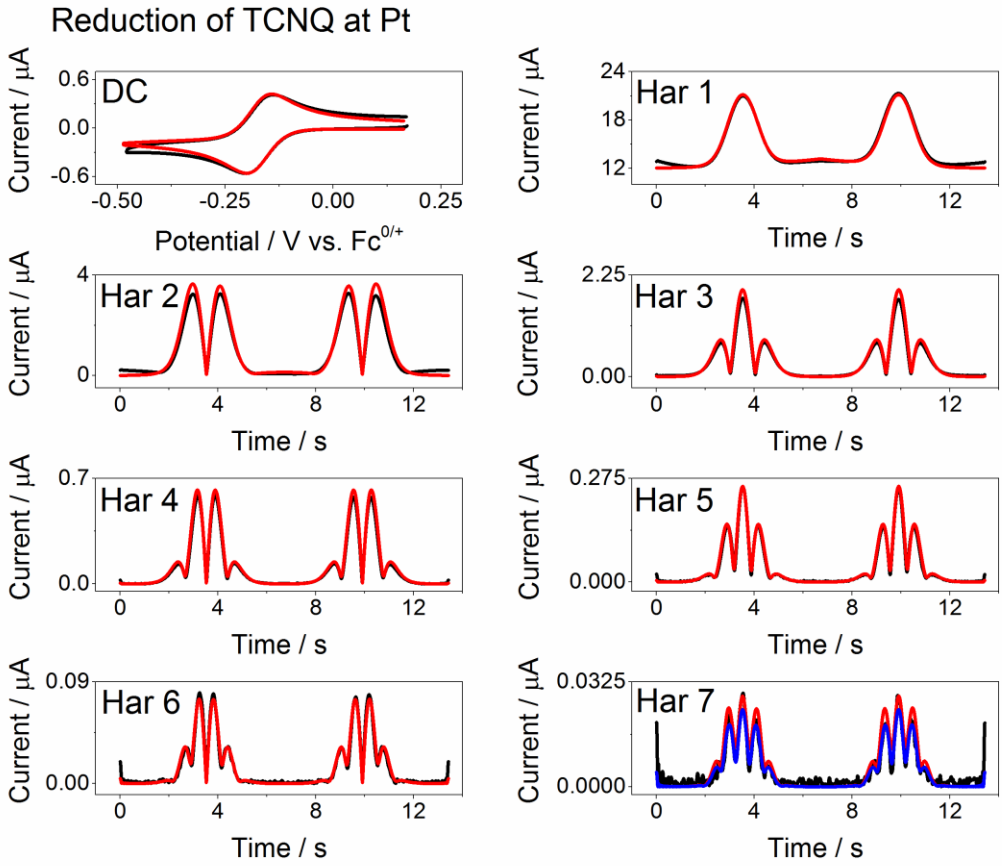

Figure 2.14 Comparison of experimental (black lines) and simulated (red lines, $\Psi = 0.990$) FTACV curves for the one-electron oxidation of 0.20 mM TCNQ in CH_3CN (0.1 M Bu_4NPF_6) at a Pt macroelectrode. Simulation parameters: $k^0 = 1000$ cm s^{-1} (reversible), $\alpha = 0.50$, $R_u = 550$ ohm, $A = 0.00785$ cm^2, $f = 228.0$ Hz, $\Delta E = 80.0$ mV, $D_{TCNQ} = 1.66 \times 10^{-5}$ cm^2 s^{-1}, $D_{TCNQ}^{\bullet-} = 1.53 \times 10^{-5}$ cm^2 s^{-1} and $v_{AC} = v_{DC} = 0.1$ V s^{-1}. The blue line shows the 7th AC harmonic component response for $k^0 = 1.2$ cm s^{-1} with all other simulation parameters the same and represents the upper kinetic limit of detection.

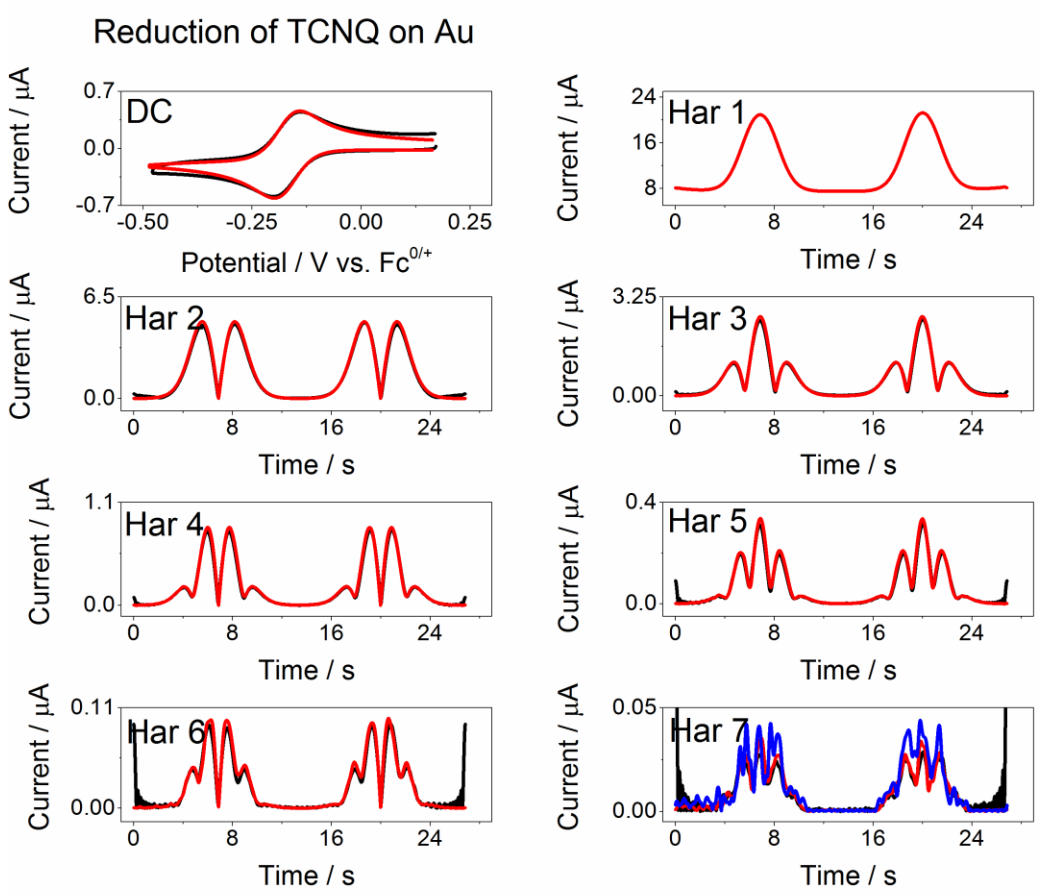

Figure 2.15 Comparison of experimental (black lines) and simulated (red lines, $\Psi = 0.990$) FTACV curves for the one-electron oxidation of 0.20 mM TCNQ in CH_3CN (0.1 M Bu_4NPF_6) at a Au macroelectrode. Simulation parameters: $k^0 = 1.0$ cm s^{-1}, $\alpha = 0.50$, $R_u = 485$ ohm, $A = 0.00785$ cm^2, $f = 228.0$ Hz, $\Delta E = 80.0$ mV, $D_{TCNQ} = 1.66 \times 10^{-5}$ cm^2 s^{-1}, $D_{TCNQ}^{\bullet-} = 1.53 \times 10^{-5}$ cm^2 s^{-1}, $v_{AC} = 0.05$ V s^{-1} and $v_{DC} = 0.1$ V s^{-1}. The blue line shows the 7th AC harmonic component response for a reversible process ($k^0 = 1000$ cm s^{-1}) with all other simulation parameters the same.

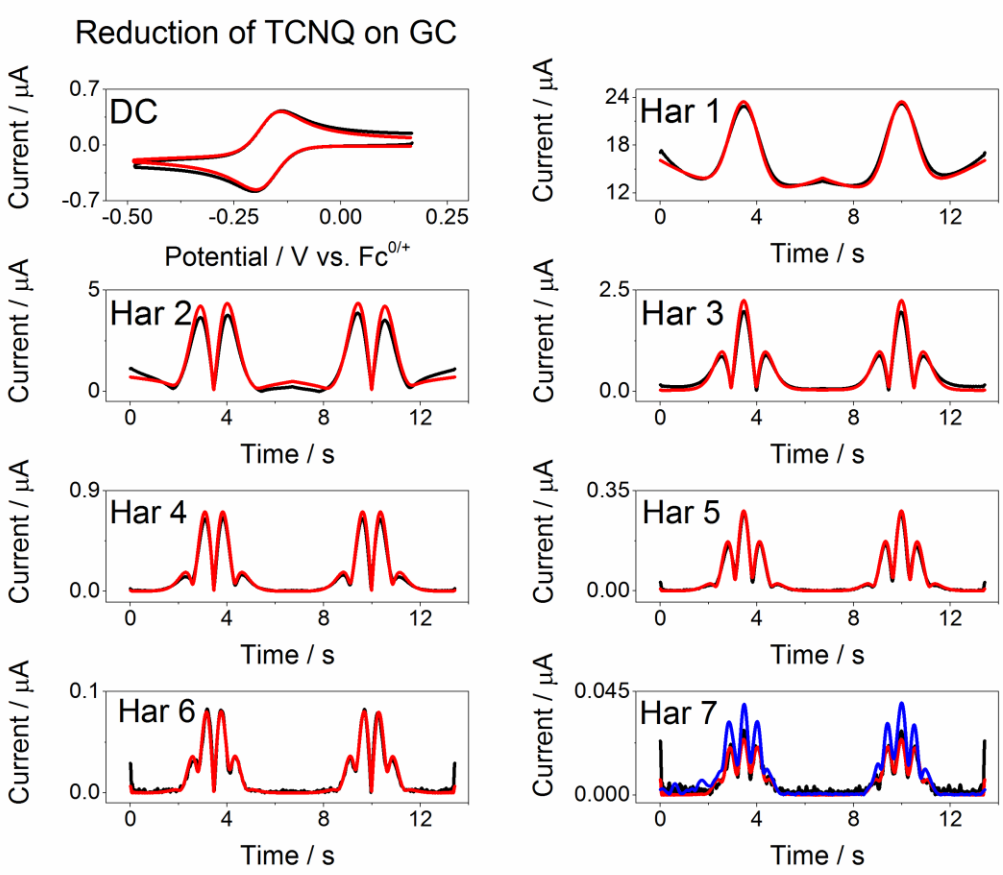

Figure 2.16 Comparison of experimental (black lines) and simulated (red lines, $\Psi = 0.981$) FTACV curves for the one-electron oxidation of 0.20 mM TCNQ in CH_3CN (0.1 M Bu_4NPF_6) at a GC macroelectrode. Simulation parameters: $k^0 = 1.0$ cm s^{-1}, $\alpha = 0.50$, $R_u = 475$ ohm, $A = 0.00785$ cm^2, $f = 228.0$ Hz, $\Delta E = 80.0$ mV, $D_{TCNQ} = 1.66 \times 10^{-5}$ cm^2 s^{-1}, $D_{TCNQ}^{\bullet-} = 1.53 \times 10^{-5}$ cm^2 s^{-1} and $v_{AC} = v_{DC} = 0.1$ V s^{-1}. The blue line shows the 7th AC harmonic component response for a reversible process ($k^0 = 1000$ cm s^{-1}) with all other simulation parameters the same.

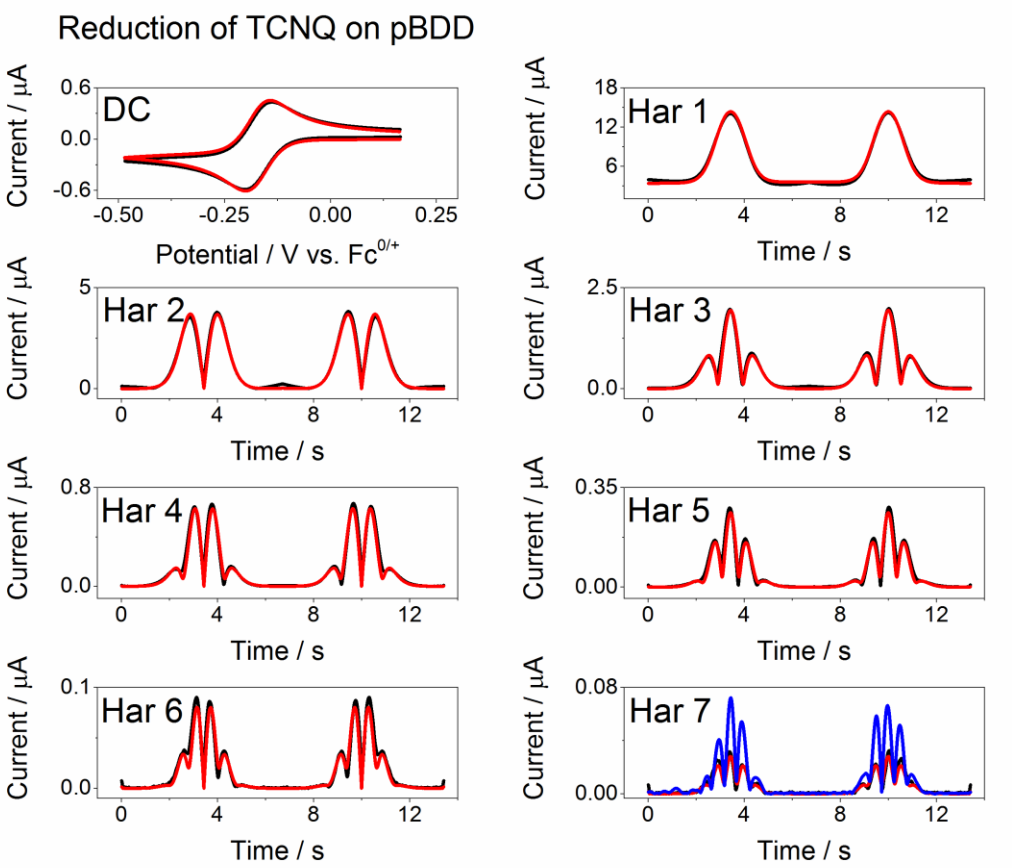

Figure 2.17 Comparison of experimental (black lines) and simulated (red lines, $\Psi = 0.979$) FTACV curves for the one-electron oxidation of 0.20 mM TCNQ in CH_3CN (0.1 M Bu_4NPF_6) at a pBDD macroelectrode. Simulation parameters: $k^0 = 0.4$ cm s^{-1}, $\alpha = 0.50$, $R_u = 300$ ohm, $A = 0.00785$ cm^2, $f = 228.0$ Hz, $\Delta E = 80.0$ mV, $D_{TCNQ} = 1.66 \times 10^{-5}$ cm^2 s^{-1}, $D_{TCNQ}^{\bullet-} = 1.53 \times 10^{-5}$ cm^2 s^{-1} and $v_{AC} = v_{DC} = 0.1$ V s^{-1}. The blue line shows the 7th AC harmonic component response for a reversible process ($k^0 = 1000$ cm s^{-1}) with all other simulation parameters the same.

2.7. References

(1) Marcus, R. A. *Annu. Rev. Phys. Chem.* **1964**, *15* (1), 155–196.

(2) Chen, S.; Liu, Y.; Chen, J. *Chem. Soc. Rev.* **2014**, *43* (15), 5372.

(3) Nicholson, R. S.; Shain, I. *Anal. Chem.* **1964**, *36* (4), 706–723.

(4) Wipf, D. O.; Kristensen, E. W.; Deakin, M. R.; Wightman, R. M. *Anal. Chem.* **1988**, *60* (4), 306–310.

(5) Hsueh, C.; Brajter-Toth, A. *Anal. Chem.* **1993**, *65* (12), 1570–1575.

(6) Sher, A. A.; Bond, A. M.; Gavaghan, D. J.; Harriman, K.; Feldberg, S. W.; Duffy, N. W.; Guo, S.-X.; Zhang, J. *Anal. Chem.* **2004**, *76* (21), 6214–6228.

(7) Bond, A. M.; Duffy, N. W.; Guo, S.-X.; Zhang, J.; Elton, D. *Anal. Chem.* **2005**, *77* (9), 186–195.

(8) Zhang, J.; Guo, S.-X.; Bond, A. M. *Anal. Chem.* **2007**, *79* (6), 2276–2288.

(9) Aoki, K. *Electroanalysis* **1993**, *5* (8), 627–639.

(10) Forster, R. J. *Chem. Soc. Rev.* **1994**, *23* (4), 289.

(11) Bard, A. J.; Mirkin, M. V; Unwin, P. R.; Wipf, D. *J. Phys. Chem.* **1992**, *96*, 1861–1868.

(12) Amemiya, S.; Bard, A. J.; Fan, F.-R. F.; Mirkin, M. V.; Unwin, P. R. *Annu. Rev. Anal. Chem.* **2008**, *1*, 95–131.

(13) Sun, P.; Laforge, F. O.; Mirkin, M. V. *Phys. Chem. Chem. Phys.* **2007**, *9*, 802–823.

(14) Mirkin, M. V.; Nogala, W.; Velmurugan, J.; Wang, Y. *Phys. Chem. Chem. Phys.* **2011**, *13*, 21196–21212.

(15) Nioradze, N.; Kim, J.; Amemiya, S. *Anal. Chem.* **2011**, *83* (3), 828–835.

(16) Liu, Y.; Holzinger, A.; Knittel, P.; Poltorak, L.; Gamero-Quijano, A.; Rickard, W. D. . A.; Walcarius, A.; Herzog, G. G.; Kranz, C.; Arrigan, D. W. M. M. *Anal. Chem.* **2016**, *88* (13), 6689–6695.

(17) Tan, S.-y.; Zhang, J.; Bond, A. M.; Macpherson, J. V.; Unwin, P. R. *Anal. Chem.* **2016**, *88* (6), 3272–3280.

(18) Eckhard, K.; Chen, X.; Turcu, F.; Schuhmann, W. *Phys. Chem. Chem. Phys.* **2006**, *8* (45), 5359.

(19) Martin, R. D.; Unwin, P. R. *Anal. Chem.* **1998**, *70* (2), 276–284.

(20) Mampallil, D.; Mathwig, K.; Kang, S.; Lemay, S. G. *Anal. Chem.* **2013**, *85* (12), 6053–6058.

(21) Wilson, N. R.; Clewes, S. L.; Newton, M. E.; Unwin, P. R.; Macpherson, J. V. *J. Phys. Chem. B* **2006**, *110* (11), 5639–5646.

(22) Patten, H. V.; Meadows, K. E.; Hutton, L. A.; Iacobini, J. G.; Battistel, D.; McKelvey, K.; Colburn, A. W.; Newton, M. E.; Macpherson, J. V.; Unwin, P. R. *Angew. Chem. Int. Ed.* **2012**, *51* (28), 7002–7006.

(23) Patten, H. V.; Lai, S. C. S.; Macpherson, J. V.; Unwin, P. R. *Anal. Chem.* **2012**, *84* (12), 5427–5432.

(24) Rao, T. N.; Fujishima, A. *Diam. Relat. Mater.* **2000**, *9* (3–6), 384–389.

(25) Pleskov, Y. V. *Russ. J. Electrochem.* **2002**, *38* (12), 1275–1291.

(26) Macpherson, J. V. *Phys. Chem. Chem. Phys.* **2015**, *17* (5), 2935–2949.

(27) Neufeld, A. K.; O'Mullane, A. P. *J. Solid State Electrochem.* **2006**, *10* (10), 808–816.

(28) Velmurugan, J.; Sun, P.; Mirkin, M. V. *J. Phys. Chem. C* **2009**, *113* (1), 459–464.

(29) Bond, A. M.; Bano, K.; Adeel, S.; Martin, L. L.; Zhang, J. *ChemElectroChem* **2014**, *1* (1), 99–107.

(30) Bano, K.; Bond, A. M.; Zhang, J. *Anal. Chem.* **2015**, *87* (16), 8387–8393.

(31) Carter, M. T.; Osteryoung, R. A. *J. Electrochem. Soc.* **1994**, *141* (7), 1713.

(32) Fuller, J.; Carlin, R. T.; Osteryoung, R. A. *J. Electrochem. Soc.* **1997**, *144* (11), 3881.

(33) Lehmann, M. W.; Evans, D. H. *J. Phys. Chem. B* **1998**, *102* (eq 5), 9928–9933.

(34) Rongfeng, Z.; Evans, D. H. *J. Electroanal. Chem.* **1995**, *385* (2), 201–207.

(35) Lehmann, M. W.; Evans, D. H. *Anal. Chem.* **1999**, *71* (10), 1947–1950.

(36) Bano, K.; Nafady, A.; Zhang, J.; Bond, A. M.; Inam-ul-Haque. *J. Phys. Chem. C* **2011**, *115* (49), 24153–24163.

(37) Ekanayake, C. B.; Wijesinghe, M. B.; Zoski, C. G. *Anal. Chem.* **2013**, *85* (8), 4022–4029.

(38) Zoski, C. G.; Luman, C. R.; Fernández, J. L.; Bard, A. J. *Anal. Chem.* **2007**, *79* (13), 4957–4966.

(39) Sun, P.; Mirkin, M. V. *Anal. Chem.* **2006**, *78* (18), 6526–6534.

(40) Yu, Y.; Sun, T.; Mirkin, M. V. *Anal. Chem.* **2016**, *88* (23), 11758–11766.

(41) Norton, J. D.; Benson, W. E.; White, H. S.; Pendley, B. D.; Abruna, H. D. *Anal. Chem.* **1991**, *63* (18), 1909–1914.

(42) Hutton, L. A.; Iacobini, J. G.; Bitziou, E.; Channon, R. B.; Newton, M. E.; Macpherson, J. V. *Anal. Chem.* **2013**, *85* (15), 7230–7240.

(43) Hutton, L.; Newton, M. E.; Unwin, P. R.; Macpherson, J. V. *Anal. Chem.* **2009**, *81* (3),

1023–1032.

(44) Lagrange, J.-P.; Deneuville, A.; Gheeraert, E. *Diam. Relat. Mater.* **1998**, *7* (9), 1390–1393.

(45) Baer, C. D.; Stone, N. J.; Sweigart, D. A. *Anal. Chem.* **1988**, *60* (2), 188–191.

(46) Bond, A. M.; Oldham, K. B.; Snook, G. A. *Anal. Chem.* **2000**, *72* (15), 3492–3496.

(47) McKelvey, K.; Edwards, M. A.; Unwin, P. R. *Anal. Chem.* **2010**, *82* (15), 6334–6337.

(48) Martin, R. D.; Unwin, P. R. *J. Electroanal. Chem.* **1997**, *439* (1), 123–136.

(49) Li, J.; Bentley, C. L.; Bond, A. M.; Zhang, J. *Anal. Chem.* **2016**, *88* (4), 2367–2374.

(50) Amatore, C.; Savéant, J. M.; Tessier, D. *J. Electroanal. Chem. Interfacial Electrochem.* **1983**, *147* (1–2), 39–51.

(51) Zhao, S.-F.; Horne, M.; Bond, A. M.; Zhang, J. *The Journal of Physical Chemistry C*. October 27, 2016, pp 23989–24001.

(52) Dumitrescu, I.; Edgeworth, J. P.; Unwin, P. R.; Macpherson, J. V. *Adv. Mater.* **2009**, *21* (30), 3105–3109.

(53) Chen, R.; Nioradze, N.; Santhosh, P.; Li, Z.; Surwade, S. P.; Shenoy, G. J.; Parobek, D. G.; Kim, M. A.; Liu, H.; Amemiya, S. *Angew. Chem. Int. Ed.* **2015**, *54* (50), 15134–15137.

(54) Macpherson, J. V. In *Electrochemistry of Carbon Electrodes*; Bartlett, P. N., Alkire, R. C., Lipkowski, J., Eds.; Wiley-VCH, 2016; pp 163–210.

(55) Blase, X.; Bustarret, E.; Chapelier, C.; Klein, T.; Marcenat, C. *Nat. Mater.* **2009**, *8* (5), 375–382.

(56) Bond, A. M.; Duffy, N. W.; Elton, D. M.; Fleming, B. D. *Anal. Chem.* **2009**, *81* (21), 8801–8808.

(57) Bard, A. J.; Faulkner, L. R. *Electrochemical Methods: Fundamentals and Applications*, 2nd ed.; Wiley: New York, 2001.

(58) Brett, C. M. A.; Brett, A. M. O. *Electrochemistry: Principles , Methods , and Applications*; 1994.

(59) Morris, G. P.; Simonov, A. N.; Mashkina, E. A.; Bordas, R.; Gillow, K.; Baker, R. E.; Gavaghan, D. J.; Bond, A. M. *Anal. Chem.* **2013**, *85* (24), 11780–11787.

(60) Simonov, A. N.; Morris, G. P.; Mashkina, E. A.; Bethwaite, B.; Gillow, K.; Baker, R. E.; Gavaghan, D. J.; Bond, A. M. *Anal. Chem.* **2014**, *86* (16), 8408–8417.

(61) Mashkina, E. A.; Simonov, A. N.; Bond, A. M. *J. Electroanal. Chem.* **2014**, *732*, 86–92.

(62) Lefrou, C. *J. Electroanal. Chem.* **2006**, *592* (1), 103–112.

(63) Ghilane, J.; Lagrost, C.; Hapiot, P. *Anal. Chem.* **2007**, *79* (19), 7383–7391.

(64) Mirkin, M. V.; Fan, F.-R. F.; Bard, A. J. *J. Electroanal. Chem.* **1992**, *328* (1–2), 47–62.

Chapter 3

Impact of Adsorption on Scanning Electrochemical Microscopy (SECM) Voltammetry and Implications for Nanogap Measurements

Since its introduction by A. J. Bard in 1986, scanning electrochemical microscopy (SECM) has positioned itself as a tool for the investigation of interfacial physiochemical processes with a wide variety of applications including quantitative measurement of fast electron transfer kinetics. The emergence of nanogap electrode geometries substantiates the need for more vigorous data analysis procedures especially when surface effects such as adsorption play an important role. This chapter, published in *Analytical Chemistry*, demonstrates SECM as a platform for the quantitative measurement of adsorption of a redox couple at the substrate electrode and the glass that encapsulates the SECM probe. A finite element method model is developed to predict the non-steady-state SECM voltammetric response with result from these surface effects. Its implications on the apparent electron transfer kinetics and interpretation of mass transport parameters are subsequently discussed.

Impact of Adsorption on Scanning Electrochemical Microscopy (SECM) Voltammetry and Implications for Nanogap Measurements

Sze-yin Tan,[†‡] *Jie Zhang,*[‡] *Alan M. Bond,*[‡] *Julie V. Macpherson,*[†] *Patrick R. Unwin**[,†]

[†] Department of Chemistry, University of Warwick, Coventry, West Midlands CV4 7AL, United Kingdom

[‡] School of Chemistry, Monash University, Clayton, Victoria 3800, Australia

*p.r.unwin@warwick.ac.uk

3.1. Abstract

Scanning electrochemical microscopy (SECM) is a powerful tool that enables quantitative measurements of fast electron transfer (ET) kinetics when coupled with modelling predictions from finite-element simulations. However, the advent of nanoscale and nanogap electrode geometries that have an intrinsically high surface area-to-solution volume ratio realises the need for more rigorous data analysis procedures, as surface effects such as adsorption may play an important role. The oxidation of ferrocenylmethyl trimethylammonium ($FcTMA^+$) at highly oriented pyrolytic graphite (HOPG) is used as a model system to demonstrate the effects of reversible reactant adsorption on the SECM response. Furthermore, the adsorption of $FcTMA^{2+}$ species onto glass, which is often used to encapsulate ultramicroelectrodes employed in SECM, is also found to be important and affects the voltammetric tip response in a nanogap geometry. If a researcher is unaware of such effects (which may not be readily apparent in slow to moderate scan voltammetry) and analyses SECM data assuming simple ET kinetics at the substrate and an inert insulator support around the tip, the result is the incorrect assignment of tip-substrate heights, kinetics and thermodynamic parameters. Thus, SECM kinetic measurements, particularly in a nanogap configuration where the ET kinetics are often very fast (only just distinguishable from reversible), require that such effects are fully characterised. This is

possible by expanding the number of experimental variables, including the voltammetric scan rate and concentration of redox species, among others.

3.2. Introduction

A long-term interest in electrochemistry has been the measurement of increasingly fast electron transfer (ET) kinetics at electrode/electrolyte interfaces to gain deeper fundamental understanding of heterogeneous interfacial ET.[1–3] Although considerable insight on interfacial ET can be gained from immobilised redox systems,[4–8] the overwhelming majority of studies deal with soluble redox species, which have to diffuse to and from the electrode. An important aspect to the study of fast ET kinetics in such systems is the need for high mass transport rates, so that this does not completely limit the current.[9–12] The introduction of ultramicroelectrode (UME) techniques from the 1980's onwards has offered many advantages including reduced ohmic effects, fast response times and high mass transport rates under both steady-state and transient conditions.[13,14] Hydrodynamic UMEs[10,11,15,16] and, particularly, the development of scanning electrochemical microscopy (SECM)[9,12,17,18] provide even higher mass transport rates under steady-state conditions.

In SECM ET kinetic measurements, a UME is positioned near a second (substrate) working electrode and both electrodes are biased externally to investigate the potential-dependent ET kinetics at one of the two electrode/electrolyte interfaces. High mass transport conditions prevail due to the shuttling of the oxidised and reduced forms of the redox couple between the two electrodes. With diffusion-limited redox shuttling (diffusion coefficient, D), the steady-state mass transport coefficient, k_t, becomes a function of tip-substrate separation, d ($k_t \sim D/d$),[19] so that high mass transport rates are obtained by decreasing the UME size and tip-substrate distances. This has fuelled the trend of miniaturising electrochemical systems, leading to the development of nanoelectrodes[20–26] and various nanogap systems.[27–33]

When using nanoscale electrochemical systems for quantitative kinetic measurements, precise knowledge of electrode geometry and the physicochemical

characteristics of electrochemical cells is imperative. For example, unaccounted for irregularities in the electrode shape from idealised models,[34] tip recession[35–37] or 'lagooned' geometries[38,39] may produce highly erroneous determination (overestimation) of ET kinetic parameters.[40] Significant efforts have thus aimed at developing easy and reproducible electrode preparation procedures and better means of geometric characterisation.[35,39,41–43] In this context, well-defined nanostructures such as graphene oxide flakes,[20] carbon nanotubes[23–26,44] and nanowires[25,44] are attractive in that the geometry of the electrodes, as used, can often be characterised by techniques such as atomic force microscopy, and related methods. Beyond the precise geometric characterisation of nanoscale electrodes, an intrinsic property of nanogap electrochemical cells is the very high surface area-to-solution volume ratio within (semi-) confined geometries. In this situation, even the weak adsorption of redox-active species may have a profound impact on the electrochemical response.

The significance of adsorption has been reported by Lemay et. al. using lithographically-fabricated nanometer wide thin-layer electrochemical cells (TLCs). In this configuration, two planar electrodes (electron-beam evaporated metal thin-films) are used to create high surface area-to-solution volume ratio nanogap electrochemical cells and electrochemical correlation spectroscopy used to investigate the redox cycling of small populations of molecules. It has been found that simple outer-sphere redox molecules such as $[Ru(NH_3)_6]^{3+}$ and 1,1-ferrocene dimethanol adsorb at Pt electrodes, and play a role in limiting electrochemical response times,[30,46] dominate noise properties[47] and at low solute concentrations, decrease current fluctuations[48,49] in these cells. Indeed, early TLC studies considered the effect of redox adsorption on electrode materials in dual electrode cells with gaps on the ~ µm to ~ 10 µm scale.[50–52] A significant difference between TLCs and SECM is that TLC studies never consider the insulator that encapsulates the electrode and are limited to redox cycling experiments. A significant advantage of SECM, particularly substrate voltammetry SECM, considered herein, is the versatility to determine thermodynamic and kinetic properties at a plethora of electrode materials that would be difficult to fabricate into the TLC configuration such as graphene,[53] highly oriented pyrolytic graphite (HOPG)[28] and carbon nanotubes.[44]

This chapter shows how adsorption can greatly affect SECM voltammetric experiments, as well as highlighting how SECM can be used to reveal and quantify adsorption in electrochemical systems, building on earlier SECM adsorption studies in other situations.[19] The focus is ferrocenylmethyl trimethylammonium, $FcTMA^+$, which undergoes an apparently simple one-electron oxidation, and has been used to study a wide range of electrode materials as an example of a fast outer-sphere redox couple.[28,32] However, it has also been demonstrated that ferrocene and its derivatives can adsorb onto electrode surfaces.[30,48,49,54,55] The substrate voltammetry configuration of SECM[27,28] is used to probe the adsorption and electrochemistry of $FcTMA^+$ at HOPG electrodes, a system that has received recent attention as one with apparently ultrafast kinetics.[28] The unequal diffusivities of $FcTMA^+$ and its oxidised form, $FcTMA^{2+}$, are carefully considered as this significantly affects the steady-state limiting-current magnitudes measured in SECM[56,57] and nanogap configurations.[27,29] Lastly, the findings are applied to typical nanoscale SECM geometries and discuss the impact of electrode and glass adsorption on the SECM voltammetric response and the effect on kinetic and thermodynamic parameters deduced from such measurements.

3.3. Theory and Simulations

COMSOL Multiphysics 4.4 (COMSOL, AB, Sweden) finite-element method modelling was used to solve the time-dependent mass transport problem in a 2D-axisymmetric cylindrical SECM geometry (Figure 3.1(a)). The following diffusion equation applies throughout:

$$\frac{\partial c_i}{\partial t} = D_i\left(\frac{\partial^2 c_i}{\partial r^2} + \frac{1}{r}\frac{\partial c_i}{\partial r} + \frac{\partial^2 c_i}{\partial z^2}\right) \quad \text{(Eq. 3.1)}$$

where c_i and D_i represent the concentration and diffusion coefficient of the redox species, i, ($FcTMA^+$ or $FcTMA^{2+}$), and r and z are the radial distance from the centre and the normal distance to the electrode, respectively.

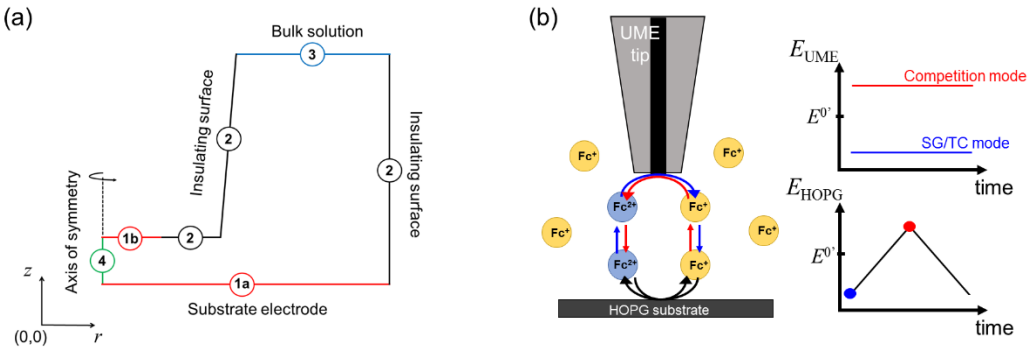

Figure 3.1 (a) Schematic (not to scale) of the 2D-axissymetric SECM simulation domain and (b) diagram of the experimental protocol for substrate voltammetry SECM.

The following redox process is considered at the HOPG substrate electrode:

$$FcTMA^{+}_{soln} \underset{k_{red,HOPG}}{\overset{k_{ox,HOPG}}{\rightleftharpoons}} FcTMA^{2+}_{soln} + e^{-} \quad \text{(Eq. 3.2)}$$

where $k_{ox,HOPG}$ and $k_{red,HOPG}$ are the first-order heterogeneous oxidation and reduction rate constants given by the Butler-Volmer relationship:

$$k_{ox,HOPG} = k^{0}_{HOPG} \exp\left[(1-\alpha) f \eta_{HOPG}\right] \quad \text{(Eq. 3.3)}$$

$$k_{red,HOPG} = k^{0}_{HOPG} \exp\left[-\alpha f \eta_{HOPG}\right] \quad \text{(Eq. 3.4)}$$

where k^{0}_{HOPG} is the standard rate constant for the $FcTMA^{+/2+}$ process at the HOPG substrate, α is the transfer coefficient (assumed reasonably to be 0.5) and $f = \frac{F}{RT}$ is a collection of constants where F is the Faraday constant, R is the universal gas constant and T is the absolute temperature. $\eta_{HOPG} = E_{HOPG}(t) - E^{0`}$, is the overpotential; $E_{HOPG}$ is the potential applied to the HOPG substrate electrode and $E^{0`}$ is the formal potential of the redox couple.

The adsorption of $FcTMA^{+}$ on HOPG is assumed to be reversible:

$$FcTMA^{+}_{soln} \underset{k_{des,HOPG}}{\overset{k_{ads,HOPG}}{\rightleftharpoons}} FcTMA^{+}_{ads} \quad \text{(Eq. 3.5)}$$

where $k_{ads,HOPG}$ and $k_{des,HOPG}$ are the adsorption and desorption rate constants, respectively, such that the equilibrium adsorption constant is:

$$K_{ads,HOPG} = \frac{k_{ads,HOPG}}{k_{des,HOPG}} \quad \text{(Eq. 3.6)}$$

The flux of $FcTMA^+$ at the HOPG/electrolyte interface (Figure 3.1(a), label 1(a)) depends on the ET process and adsorption:

$$-\mathbf{n}.\mathbf{N}_{FcTMA^+,HOPG} = -k_{ox,HOPG}c_{FcTMA^+} + k_{red,HOPG}c_{FcTMA^{2+}} - \frac{\partial\theta_{HOPG}\Gamma^0{}_{HOPG}}{\partial t} \quad \text{(Eq. 3.7)}$$

$FcTMA^{2+}$ does not adsorb appreciably at the HOPG electrode (*vide infra*) and so only the ET kinetics are important:

$$-\mathbf{n}.\mathbf{N}_{FcTMA^{2+},HOPG} = k_{ox,HOPG}c_{FcTMA^+} - k_{red,HOPG}c_{FcTMA^{2+}} \quad \text{(Eq. 3.8)}$$

where $\mathbf{n}$ is the unit normal vector to the substrate surface, while $\mathbf{N}_{FcTMA^+,HOPG}$ and $\mathbf{N}_{FcTMA^{2+},HOPG}$ represent the flux of the reduced and oxidised species to the substrate electrode surface. θ_{HOPG} is the fraction of occupied adsorption sites on the HOPG surface and $\Gamma^0{}_{HOPG}$ is the monolayer surface concentration of $FcTMA^+$ (5×10^{-10} mol cm^{-2}).[54]

The amount of $FcTMA^+$ adsorbed is assumed to follow a Langmuir isotherm:

$$\theta_{HOPG} = \frac{K_{ads,HOPG}c_{FcTMA^+}}{1 + K_{ads,HOPG}c_{FcTMA^+}} \quad \text{(Eq. 3.9)}$$

The following redox process is considered at the UME tip surface:

$$FcTMA^+{}_{soln} \underset{k_{red,UME}}{\overset{k_{ox,UME}}{\rightleftharpoons}} FcTMA^{2+}{}_{soln} + e^- \quad \text{(Eq. 3.10)}$$

The following Butler-Volmer relationship is applied:

$$k_{ox,UME} = k^0{}_{UME} \exp\left[(1-\alpha) f \eta_{UME}\right] \quad \text{(Eq. 3.11)}$$

$$k_{red,UME} = k^0{}_{UME} \exp\left[-\alpha f \eta_{UME}\right] \quad \text{(Eq. 3.12)}$$

where k^0_{UME} is the standard rate constant for ET at the Pt UME, set high to ensure reversibility (25 cm s^{-1}).[22] $\eta_{UME} = E_{UME} - E^{0`}$, $E_{UME} >> E^{0`}$ in the competition mode and $E_{UME} << E^{0`}$ in the SG/TC mode, with E_{UME} fixed to drive the reaction of interest.

For $t > 0$, the redox flux at the Pt UME tip surface (Figure 3.1(a), label 1(b)) is defined by:

$$-\mathbf{n}.\mathbf{N}_{FcTMA^+,UME} = \mathbf{n}.\mathbf{N}_{FcTMA^{2+},UME} = -k_{ox,UME}c_{FcTMA^+} + k_{red,UME}c_{FcTMA^{2+}} \quad \text{(Eq. 3.13)}$$

Other boundary conditions are shown in Figure 3.1(a), where insulating surfaces (label 2) are described by $\mathbf{n}.\mathbf{N}_{FcTMA^+} = \mathbf{n}.\mathbf{N}_{FcTMA^{2+}} = 0$, the bulk solution boundary (label 3) is given by $c_{FcTMA^+} = c_{FcTMA^+}{}^0$ and $c_{FcTMA^{2+}} = 0$ and label 4 represents the axis of symmetry.

The substrate and tip current were calculated from:

$$i_{HOPG} = 2\pi F \int_0^{a_{HOPG}} \left(-k_{ox,HOPG}c_{FcTMA^+} + k_{red,HOPG}c_{FcTMA^{2+}}\right) r dr \quad \text{(Eq. 3.14)}$$

$$i_{UME} = 2\pi F \int_0^{a_{UME}} \left(-k_{ox,UME}c_{FcTMA^+} + k_{red,UME}c_{FcTMA^{2+}}\right) r dr \quad \text{(Eq. 3.15)}$$

Typically, 100,000 triangular mesh elements were in each simulation with the greatest mesh resolution at the electrode boundaries and edges where the concentration gradient is steepest.[58]

3.4. Experimental

3.4.1. Chemicals

Ferrocenylmethyl trimethylammonium hexafluorophosphate, $[FcTMA^+][PF_6^-]$ was synthesised in-house via an exchange reaction of $FcTMA^+I^-$ (Strem Chemicals, Ltd.) with $AgPF_6$ (Strem Chemicals, Ltd.). KCl (99 %) was purchased from Sigma-Aldrich and used without further purification. All solutions were prepared using high purity water (Millipore

Corp. purification system), with a resistivity *ca*. 18.2 MΩ cm at 25 ^{o}C. 1.0 M KCl was added as the supporting electrolyte in all solutions.

3.4.2. Electrode Materials

A Pt disk macroelectrode (radius, a_{Pt} = 0.1 cm) was obtained from CH Instruments, Inc. A Pt disk UME was fabricated in-house using an established procedure,[59] involving heat sealing of a 12.5 µm-radius microwire (Goodfellow, UK) in a borosilicate glass capillary under vacuum. The microwire was connected with solder to a larger copper wire inserted into the capillary.[59] The end of the UME was polished flat and conically polished to obtain an RG value - ratio of the radius of the insulating glass sheath to that of the active electrode - of *ca.* 10. Prior to use, the UME was polished with an alumina slurry (0.05 µm) on a soft microfiber polishing pad (MicroCloth, Buehler Ltd.) and then on a clean wet microfiber pad, to produce the finished electrode surface. ZYA grade HOPG was acquired from GE Advanced Ceramics, USA. The HOPG sample was placed on a silicon wafer, coated with chromium (2 nm) and gold (60 nm) using Acheson Electrodag (Agar Scientific, 1415M). An external electrical contact was created by lowering a metal pin onto the exposed gold surface using a micropositioner. Fresh HOPG basal surfaces were prepared by gently pressing down Scotch tape on to the sample and pulling-off the top layers, as reported extensively in the literature.[33,60–63]

3.4.3. CV and SECM Instrumentation

Cyclic voltammetry (CV) was carried out for the oxidation of 0.4 mM $FcTMA^{+}$ (1 M KCl) in aqueous solution in a 3-electrode configuration using a CHI 760C potentiostat (CH Instruments, Inc.) where a HOPG substrate, a Pt wire and a AgCl-coated Ag wire were used as a working, counter and reference electrodes, respectively. The reference electrode was thus Ag/AgCl (1 M KCl). A 20 µL droplet of electrolyte solution was placed on the HOPG surface (area of *ca.* 0.165 cm^2) with the counter and reference electrode placed into the droplet.[63] An advantage of this electrochemical cell is that it can be assembled and used within seconds of sample cleavage,[63] minimising surface contamination.

Intermittent-contact (IC)-SECM setup was used for substrate voltammetry SECM measurements.[64,65] Salient details of tip positioning are given in Section 3.7.1. A 4-electrode SECM configuration was adopted with the Pt UME tip and HOPG substrate as the working electrodes, and the same counter and reference electrodes as mentioned above. For this purpose, a CHI 760C bipotentiostat was used. Scan rates applied to the HOPG substrate ranged from 0.05 to 10 V s^{-1}. Potentials applied to the UME tip were either 0.8 V (to detect $FcTMA^+$ by diffusion-limited oxidation) or 0.1 V (to detect $FcTMA^{2+}$ by diffusion-limited reduction) for the competition (shielding) mode or SG/TC mode, respectively. A droplet configuration was also used in this case and all measurements were made within 10 minutes of HOPG cleavage and droplet placement, such that evaporation of water from the electrolyte solution was negligible.

3.5. Results and Discussion

3.5.1. Adsorption of $FcTMA^+$ on HOPG Electrodes

Macroscopic CVs for the oxidation of $FcTMA^+$ (0.4 mM in 1 M KCl) at HOPG in the droplet configuration[63] gave half-wave potentials, $E_{1/2,app}$ at 0.38 V (vs. Ag/AgCl 1 M KCl) (Figure 3.2(a)). The ΔE_p values decreased monotonically from 51 mV at 0.05 V s^{-1} to 40 mV at 10 V s^{-1} (see Figure 3.8(a)). These values are smaller than 57 mV, expected for purely diffusion-controlled voltammograms at 25 ^{0}C, and seen for CVs for the oxidation of $FcTMA^+$ (0.4 mM in 1 M KCl) at a macroscopic Pt electrode (Figure 3.2(b)). Note the low background current for the voltammetry at HOPG compared to Pt due to the much lower capacitance of the HOPG/aqueous interface.[60] With further information presented below, these characteristics are indicative of a diffusional redox system that is complicated by ET from weakly adsorbed species.

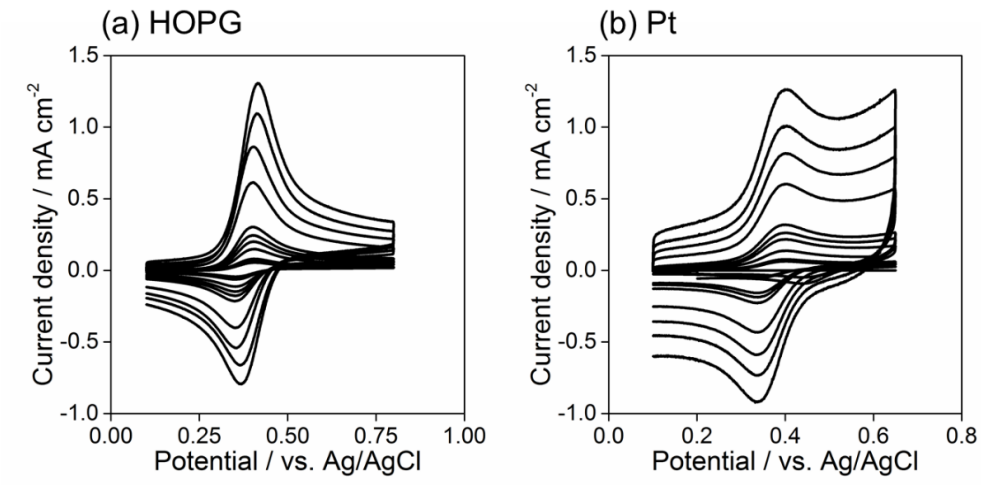

Figure 3.2 CVs for the one-electron oxidation of 0.4 mM $FcTMA^+$ in aqueous 1 M KCl supporting electrolyte at a (a) freshly cleaved ZYA grade HOPG and (b) Pt macroelectrode at different scan rates (50 mV s^{-1} to 10 V s^{-1}).

The peak currents of the forward potential scan were larger than those of the reverse potential scan with the difference increasing with scan rate (see Section 3.7.2., Figure 3.8(b)). However, at low scan rates (< 1 V s^{-1}), the ratio of forward to reverse peaks tends to 1 and ΔE_p only differs a small amount from the purely diffusional response (see above). Without running a wide range of scan rates, and focusing on relatively slow scan speeds, one could mistake this process for one that only involves diffusion (no adsorption),[28] especially as electrode placement and supporting electrolyte concentration may be critical in determining ΔE_p in small volume (droplet) electrochemical cells.[63] Comparison of experimental to computed diffusional waves (using precise diffusion coefficients) showed that the experimental currents exceeded the simulated ones (see Section 3.7.2., Figure 3.8(c)), whereas the reverse scan voltammetry fitted quite well. Thus, while $FcTMA^+$ adsorbs at the HOPG electrode, $FcTMA^{2+}$ that is produced does not adsorb appreciably and a significant proportion of $FcTMA^{2+}$produced by the oxidation of adsorbed $FcTMA^+$, diffuses away from the electrode on this timescale.

This type of behaviour has previously been reported for ferrocene and its derivatives on other electrode materials such as platinum[30] and glassy carbon,[54] but not recognised on HOPG.[28] As shown further herein, it is essential to acknowledge $FcTMA^+$

adsorption if one is to achieve accurate kinetic analysis. Examination of the macroscale droplet CVs, and the excess charge compared to a diffusional process,[55] allows us to estimate the $FcTMA^+$ surface coverage at the beginning of the experiment to be *ca.* 0.9×10^{-10} mol cm^{-2} (18 %) for a bulk concentration of 0.4 mM $FcTMA^+$ (1 M KCl). For the purpose of the analysis herein, this is a reasonable estimate; a more accurate value results from SECM measurements (see below).

Substrate voltammetry SECM was employed for a quantitative analysis of the amount of $FcTMA^+$ adsorbed onto the HOPG surface. In this work, 0.4 mM $FcTMA^+$ (1 M KCl) was used throughout. The UME tip (radius, a_{UME} = 12.5 µm) was positioned at a fixed distance from the HOPG substrate surface and E_{HOPG} was scanned from 0.1 to 0.8 V (50 mV s^{-1}) to oxidise $FcTMA^+$ to $FcTMA^{2+}$. At E_{UME} = 0.8 V, the UME tip gives the positive feedback response (E_{HOPG} = 0.1 V). As the substrate potential is positively scanned, the UME tip competes with the substrate to oxidise $FcTMA^+$ and this is known as competition mode. In the substrate generation/tip collection (SG/TC) mode (E_{UME} = 0.1 V), the tip current rises from zero as the UME tip collects $FcTMA^{2+}$ produced at the HOPG substrate electrode during the voltammetric sweep (Figure 3.1(b)). Hence, a pair of competition and SG/TC voltammograms at the same tip position can be taken at a set of tip-substrate separations to change the inter-electrode mass transport rate and effective surface area-to-solution volume ratio, and thus the sensitivity of the system to adsorption compared to diffusion.

Figure 3.3(a(i) and (ii)) shows four pairs of competition and SG/TC voltammograms (each pair measured at the same tip-substrate distance is shown in the same colour) taken at different tip-substrate heights, d = 2.58, 3.71, 4.59 and 5.98 µm (determined from positive feedback limiting-current at the beginning of the competition mode scan (discussed later)). Note that the substrate voltammograms were close to those seen without a tip present (see above). The tip currents were normalised with respect to the steady-state diffusion-limited tip current for the oxidation of $FcTMA^+$ in the bulk solution. Noticeably, the tip current measured in the competition mode was always smaller than its SG/TC counterpart and, in both configurations, voltammograms deviate significantly from

those expected for the adsorption-free voltammetric response (see Section 3.7.3., Figure 3.9(b)). This was especially noticeable for the SG/TC mode.

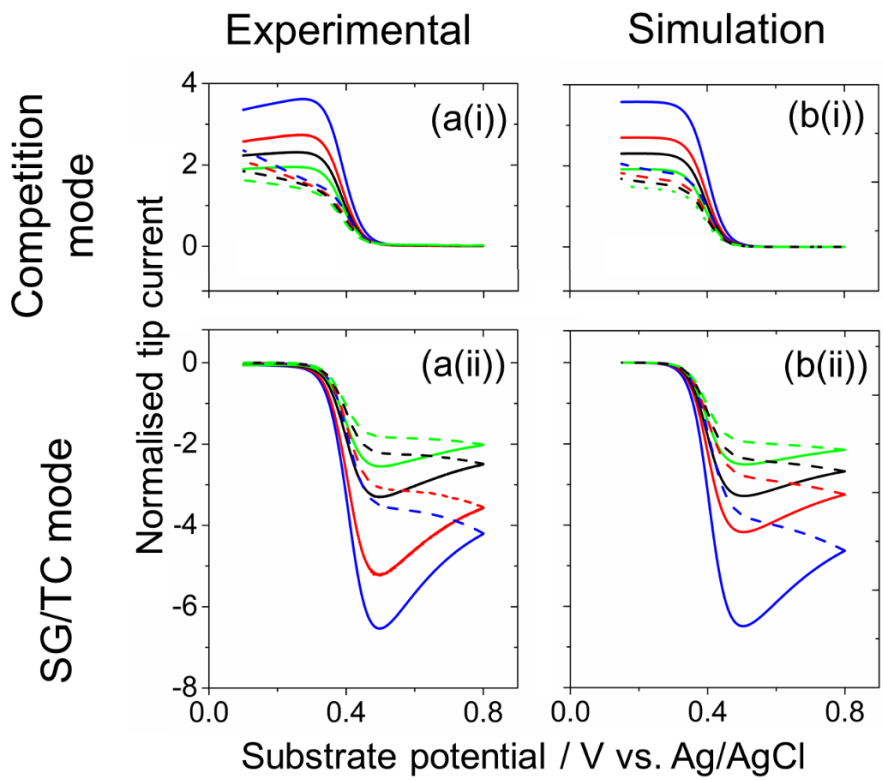

Figure 3.3 Experimental (a) and simulated (b) tip current-substrate potential curves for the competition and SG/TC modes for the one-electron oxidation of 0.4 mM $FcTMA^+$ in 1 M KCl supporting electrolyte in aqueous media at an HOPG surface (ZYA grade) at different normalised tip-substrate heights (L = 0.209 (blue), 0.297 (red), 0.367 (black), 0.478 (green)) at 50 mV s^{-1}. Solid and dashed lines show the forward and reverse curves, respectively. Simulation parameters can be found in the text.

Simulated voltammograms considering $FcTMA^+$ adsorption onto the HOPG substrate electrode are shown in Figure 3.3(b). The simulation parameters were as follows: k^0_{UME} = 25 cm s^{-1} (reversible), k^0_{HOPG} = 10 cm s^{-1} (reversible), α = 0.5, $E^{0`}$ = 0.38 V, D_{FcTMA^+} = 6.7 × 10^{-6} cm^2 s^{-1} (determined from steady-state voltammetry (see Section 3.7.4.) and $D_{FcTMA^{2+}}$ = 6.1 × 10^{-6} cm^2 s^{-1} (determined by SECM chronoamperometry in feedback and SG/TC mode (see Section 3.7.5.). The amount of adsorbed $FcTMA^+$ on the HOPG substrate was determined to be 1.13 × 10^{-10} mol cm^{-2} (22 %) by comparison of experimental

and simulated tip voltammograms, with most parameters fixed, and only those ($K_{ads,HOPG}$) relating to adsorption variable. Note that the adsorption of $FcTMA^+$ on platinum has previously been observed[30,32] and is not ruled out. However, it is minor (undetectable) under our experimental conditions, and the theoretical model assumes that the HOPG adsorption process dominates, with negligible adsorption of $FcTMA^+$ at the Pt UME tip.

In the competition mode, as noted above (see Figure 3.1(b)), the UME tip is held at a potential that oxidised $FcTMA^+$ to $FcTMA^{2+}$ at a diffusion-limited rate, while the substrate potential was cycled between 0.1 and 0.8 V at 50 mV s^{-1}. The UME tip competition voltammograms show a typical diffusion-limited (positive feedback) current on the forward wave, indicated by the solid line (Figure 3.3(a(i))). As the HOPG substrate potential was anodically scanned such that $FcTMA^+$ was oxidised to $FcTMA^{2+}$, the UME tip current decreased (competition with the substrate for $FcTMA^+$). Interestingly, by comparing simulations for all tip-substrate heights, the positive feedback limiting-currents, measured with and without reactant adsorption on the substrate, give the same values (see Section 3.7.3., Figure 3.9(a(i)) and (b(i))). This is because the positive feedback limiting-current merely depends on the redox competition between the substrate and tip electrodes for $FcTMA^+$ in solution. Hence, the experimental positive feedback UME tip limiting-currents can be used to accurately determine the tip-substrate separations without complications from $FcTMA^+$ adsorption processes. However, even though simulations with and without $FcTMA^+$ adsorption on the substrate gave equivalent limiting-currents, the $E_{1/2,app}$ values were shifted positively by 17, 13, 12 and 9 mV at d = 2.58, 3.71, 4.59 and 5.98 μm, respectively, compared to the diffusion only simulations. This is because $FcTMA^+$ adsorbed on the HOPG surface at the start of the voltammetric sweep is gradually released during the sweep, particularly in the later part of the voltammogram. Thus, adsorption of $FcTMA^+$ on the HOPG substrate subtly affects the voltammetric wave-shape.

On the reverse competition mode potential scan, the currents are not retraceable (dashed lines in Figure 3.3(a(i)) and (b(i))) but the experimental and simulations are closely similar when adsorption of $FcTMA^+$ at the HOPG substrate is taken into account. This occurs due to $FcTMA^{2+}$ reconversion to $FcTMA^+$ at the HOPG substrate where the latter adsorbs. This accounts for the generally smaller UME tip current measured on the reverse

substrate potential scan (0.8 V to 0.1 V) in the competition mode. Without substrate adsorption of $FcTMA^+$, the forward and reverse tip current responses (with the substrate potential scan) are much closer; see Section 3.7.3, Figure 3.9.

In the SG/TC mode, the UME tip is used to amperometrically detect substrate-generated $FcTMA^{2+}$ as the HOPG substrate potential was cycled from 0.1 to 0.8 V at 50 mV s^{-1} to oxidise $FcTMA^+$ to $FcTMA^{2+}$. The resultant tip current-substrate potential curves are peak shaped (Figure 3.3(a(ii))), rather than the typical sigmoidal response observed for this mode without adsorption of $FcTMA^+$ at the substrate electrode (see Section 3.7.3., Figure 3.9(b(ii))). An increase of UME tip current was observed as the substrate potential was anodically scanned, reaching a maximum value at a potential ~ 0.49 V vs. Ag/AgCl (1 M KCl) before decreasing as the substrate potential was further increased. The surplus of $FcTMA^+$ present on the HOPG substrate surface at the start of the voltammetric experiment results in a higher flux of $FcTMA^{2+}$ species to the tip surface during the anodic potential sweep. This is clear from Figure 3.10(a) and (b) which shows the concentration profiles for $FcTMA^+$ in the tip-substrate gap at E_{HOPG} = 0.5 V (close to the peak potential) on the anodic sweep for the SG/TC mode without and with reactant adsorption on the substrate electrode. The concentration of $FcTMA^+$ near the UME tip is higher than the bulk concentration with $FcTMA^+$ adsorption at the substrate.

On the reverse cathodic sweep of the substrate potential, the measured UME tip currents are smaller and tend to resemble the steady-state diffusion-controlled response. This is because $FcTMA^+$ adsorption no longer affects the tip response. A comparison of SG/TC tip voltammogram simulations, with and without surface adsorption effects, can be found in Section 3.7.3., Figure 3.9(a(ii)) and (b(ii)), respectively. The substantial contribution from $FcTMA^+$ adsorption to the SG/TC tip current-substrate potential response is seen at all tip-substrate heights, with the effect increasingly significant at closer tip-substrate separations.

As tip-substrate heights can be determined accurately from the positive feedback limiting-current of the competition mode voltammetric response (see above), the magnitude of peak currents measured in the SG/TC mode can be fitted to provide accurate measurement of reactant ($FcTMA^+$) adsorption on the HOPG substrate when matched with

simulations. Via this method, Γ_{HOPG} = 1.1 × 10^{-10} mol cm^{-2} is estimated at a bulk concentration of 0.4 mM $FcTMA^+$.

Next, the effect of scan rate on substrate voltammetry SECM is briefly investigated. Figure 3.4(a) and (b) shows typical experimental data and simulations for 3 pairs of competition and SG/TC mode tip responses taken at the same tip-substrate height (L = 0.209) but at different scan rates (50 mV s^{-1}, 0.1 and 0.5 V s^{-1}), indicated by the different colours. At higher scan rates, the surplus concentration of $FcTMA^{2+}$ generated at the HOPG surface (from adsorbed $FcTMA^+$) does not have sufficient time to diffuse out of the tip-substrate gap, where $t_{diff(escape)} \sim (a_{UME}RG)^2/D$. Hence, peak currents are no longer observed in the SG/TC mode at scan rates ≥ 0.5 V s^{-1}, but the current is massively enhanced compared to the adsorption-free case. Again, experiments and simulations are in close agreement using only the adsorption parameters for $FcTMA^+$ as a variable.

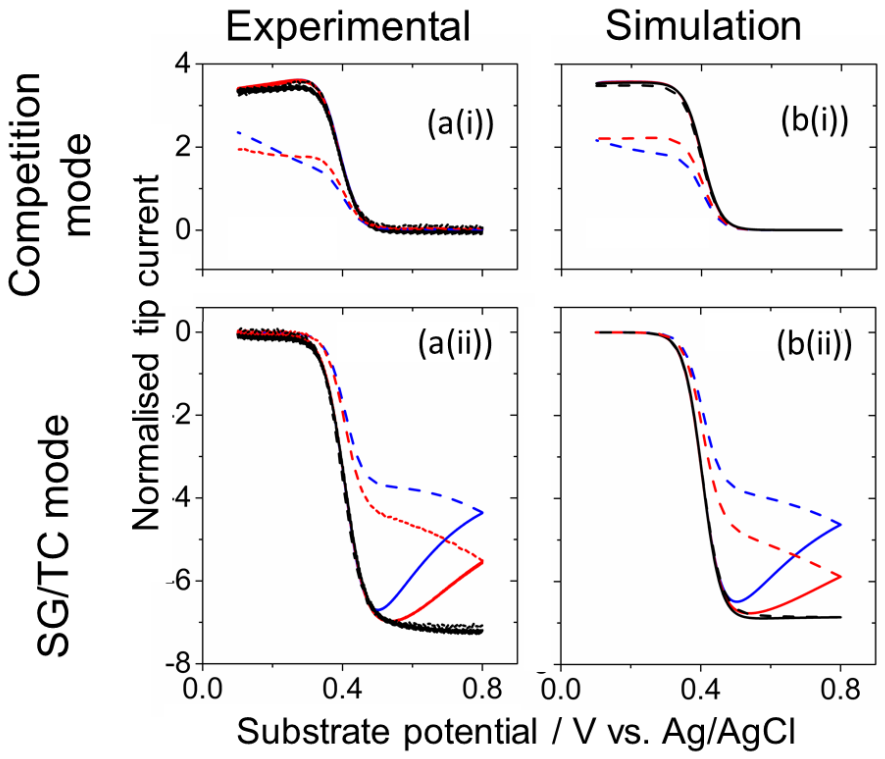

Figure 3.4 Experimental (a) and simulated (b) tip current-substrate potential curves for the competition and SG/TC modes for the one-electron oxidation of 0.4 mM $FcTMA^+$ in 1 M KCl supporting electrolyte in aqueous media at an HOPG surface (ZYA grade) at different scan rates (50 (blue), 100 (red), 500 (black) mV s^{-1}) at L = 0.209. Solid and dashed lines show the forward and reverse curves, respectively. All other simulation parameters are identical to those used in Figure 3.3.

3.5.2. Other Considerations and Impact on Nanogap Simulations

In light of our experimental results, the findings are applied to substrate voltammetry SECM at typical nanogap geometries[28] where a UME tip of a_{UME} = 0.5 µm with RG = 2 is held at typical normalised tip-substrate distances, L = 0.1 - 0.3. In absolute terms these are much smaller (50 – 150 nm) than those employed above. Furthermore, the possibility of increased $FcTMA^+$ adsorption on the substrate due to prolonged exposure times (to air) and the adsorption of the redox couple on glass, commonly used to isolate the UME tip will be considered. The following parameters apply throughout: k^0_{UME} = 25 cm s^{-1} (reversible),[22] $\alpha = 0.5$, $D_{FcTMA^+} = 6.7 \times 10^{-6}$ cm^2 s^{-1} and $D_{FcTMA^{2+}} = 6.1 \times 10^{-6}$ cm^2 s^{-1}, c_{FcTMA^+} = 0.4 mM and $\Gamma^0_{HOPG,FcTMA^+} = 5.0 \times 10^{-10}$ mol cm^{-2}.

Effect of $FcTMA^+$ adsorbed on HOPG

Although most of the SECM measurements were taken within minutes of surface cleavage, it is also interesting to consider the impact of HOPG exposure to air. It is shown that the behaviour of some redox couples change significantly over time,[60,62,63] for a variety of reasons attributed to surface contamination, delamination, surface oxidation and other factors, and it is also known that HOPG is susceptible to atmospheric contamination.[60] Some experiments, such as SECM measurements, where one has to assemble the HOPG sample in a cell before conducting the experiment, may result in unavoidable contamination of the surface, as well as damage to the sample from compression in a cell.[60]

As shown in Section 3.7.6., Figure 3.13, the amount of $FcTMA^+$ adsorbed on HOPG increased to 2.0×10^{-10} mol cm^{-2} ($FcTMA^+$ bulk concentration of 0.4 mM) after one hour exposure of a cleaved surface to air. Figure 3.5(a) shows simulated forward scan tip responses for the competition and SG/TC modes where $\Gamma_{HOPG,FcTMA^+}$ was systematically increased (1.1×10^{-10} (22 %), 1.53×10^{-10} (30 %), 2.0×10^{-10} (40 %) and 2.6×10^{-10} (50 %) mol cm^{-2}). Other simulation parameters include: L = 0.1 (50 nm) and k^0_{HOPG} = 5 cm s^{-1}. The black curves are the tip voltammetric response with no surface adsorption effects, for

comparison. In this ideal case, it can be seen that the positive feedback limiting-current (beginning of the competition mode scan) is larger than that of the SG/TC curve, which is expected because $FcTMA^{2+}$ has a smaller diffusion coefficient than $FcTMA^{+}$.[27,29,56,57] When there is $FcTMA^{+}$ adsorption on HOPG, the positive feedback limiting-currents (Figure 3.5(a (i))) remain unchanged from the control (adsorption-free) voltammogram (see earlier). Similar to the above microgap experiments above, $E^{0'}$ values are positively shifted by 4 mV for all adsorption values considered.

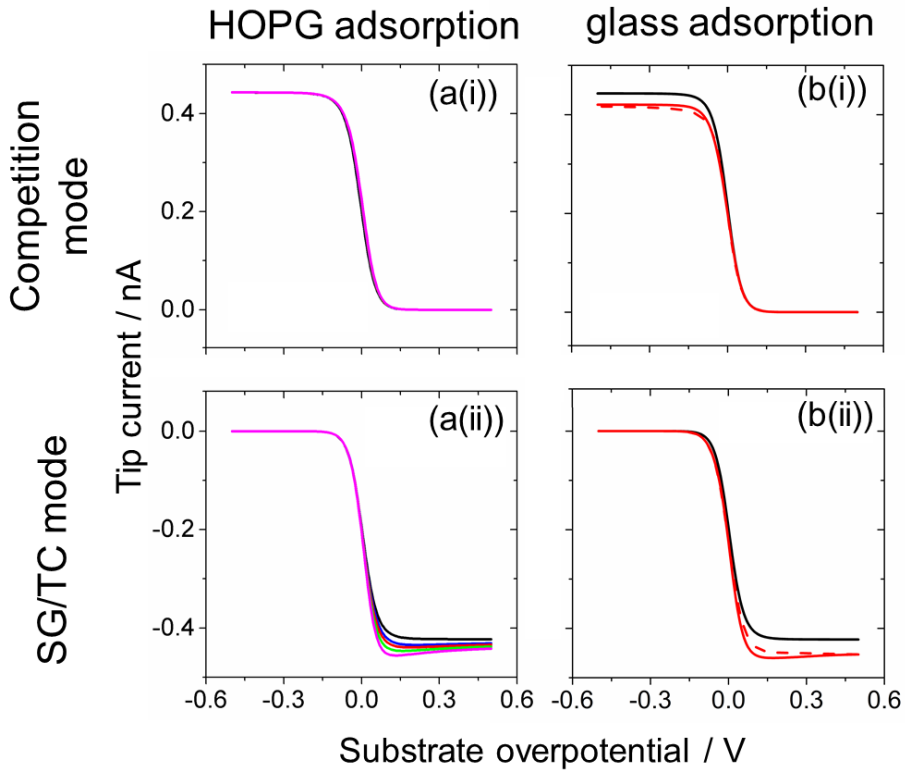

Figure 3.5 Simulated nanogap substrate voltammetry SECM tip current-substrate potential responses for: (a) varying values of $\Gamma_{HOPG,FcTMA^+}$ (1.1×10^{-10} (22 %), 1.53×10^{-10} (30 %), 2.0×10^{-10} (40 %) and 2.6×10^{-10} (50 %) mol cm^{-2}); and (b) full adsorption model (red). In both parts, the black curves represent the adsorption-free tip response. Solid and dashed lines show the forward and reverse curves, respectively. Simulation parameters: $L = 0.1$, $k^0 = 5$ cm s^{-1}, $v = 50$ mV s^{-1}, $a_{UME} = 0.5$ µm, RG = 2, $\alpha = 0.5$, $D_{FcTMA^+} = 6.7 \times 10^{-6}$ cm s^{-1} and $D_{FcTMA^{2+}} = 6.1 \times 10^{-6}$ cm s^{-1}.[1] Glass adsorption parameters are given by $\Gamma^{0}_{glass} = 2.3 \times 10^{-9}$ mol cm^{-2}, $K_{ads,glass} = 2.56 \times 10^{6}$ cm^3 mol^{-1} and $K_{12} = 9 \times 10^{6}$ M^{-1} s^{-1}.

In the SG/TC mode (Figure 3.5(a(ii))), tip currents are larger than expected and increase as the amount of adsorbed $FcTMA^+$ is increased, due to the increased flux of $FcTMA^{2+}$ toward the SECM tip from the oxidation of substrate-adsorbed $FcTMA^+$. In this situation, the larger tip current enhancement would lead to an underestimation of tip-substrate distance (if adsorption was neglected by a researcher). Moreover, the tip voltammogram with adsorption is steeper, which would result in an overestimation of the kinetic parameter, k^0. When fitted to an adsorption-free analytical model, essentially reversible ($k^0_{app} \geq 14$ cm s^{-1}) responses are found for all SG/TC curves, rather than $k^0 = 5$ cm s^{-1} that was actually applied to the simulations. Kinetic analyses for the voltammograms in Figure 3.5(a) are summarised in Section 3.7.9, Table 3.1, where the simulated voltammograms with different amounts of $FcTMA^+$ adsorption on HOPG are analysed as though they were adsorption-free (as a researcher might naively assume), and the resulting error in tip-substrate separation (underestimated), kinetics (overestimated) and thermodynamic parameter, $E^{0'}$, are revealed.

Adsorption of redox active species on glass

UME voltammetry in a drop of solution was used to determine adsorption isotherms for $FcTMA^+$ and $FcTMA^{2+}$ at the solution-glass interface (Section 3.7.1.).[66] The highly-charged $FcTMA^{2+}$ species was found to adsorb strongly on glass surfaces (see Section 3.7.7.). In this part of the simulations, the boundary condition on the glass that surrounds the UME tip is modified to include $FcTMA^{2+}$ adsorption and the well-known fast lateral charge propagation that occurs within surface-attached redox molecules,[67–71] especially ferrocenes at high surface coverage.[71] A detailed description of the boundary condition applied can be found in Section 3.7.8.

Figure 3.5(b) shows simulated results that consider both $FcTMA^+$ adsorption on HOPG and $FcTMA^{2+}$ adsorption on glass. Again, for comparative purposes, the black curves show the limiting case of no adsorption on any surface. Within this framework, at the same tip-substrate distances, the positive feedback tip limiting-currents (at the beginning of the competition mode potential scan) were always smaller than those in the SG/TC mode. This has previously been seen experimentally and the anomalous limiting-

current magnitudes were attributed to the presence of an organic contaminant layer, which had selective charge permeability in favour of the $FcTMA^+$ species.[28] Evidently, a similar effect can be observed, at least qualitatively, by considering the known adsorption of $FcTMA^+$ on HOPG and $FcTMA^{2+}$ on the UME glass sheath.

The UME tip positive feedback limiting-current obtained in the competition mode was always lower than the simulated adsorption-free counterpart. This is because the oxidation of $FcTMA^+$ by glass-bound $FcTMA^{2+}$ essentially 'competes' with the oxidation of $FcTMA^+$ at the UME tip surface. This is evident by the shallower concentration gradient of $FcTMA^+$ at the tip/glass interface compared to the adsorption-free counterpart (Figure 3.6(a)). Conversely, a higher UME tip limiting-current is obtained for the SG/TC case compared to the simulated adsorption-free counterpart. This is because ET between the UME tip-generated $FcTMA^+$ and glass-bound $FcTMA^{2+}$ provides an additional 'feedback' loop, which further enhances the flux of $FcTMA^{2+}$ to the UME tip surface on top of the above mentioned increased flux of $FcTMA^{2+}$ due to the oxidation of substrate-adsorbed $FcTMA^+$ (Figure 3.6(b)).

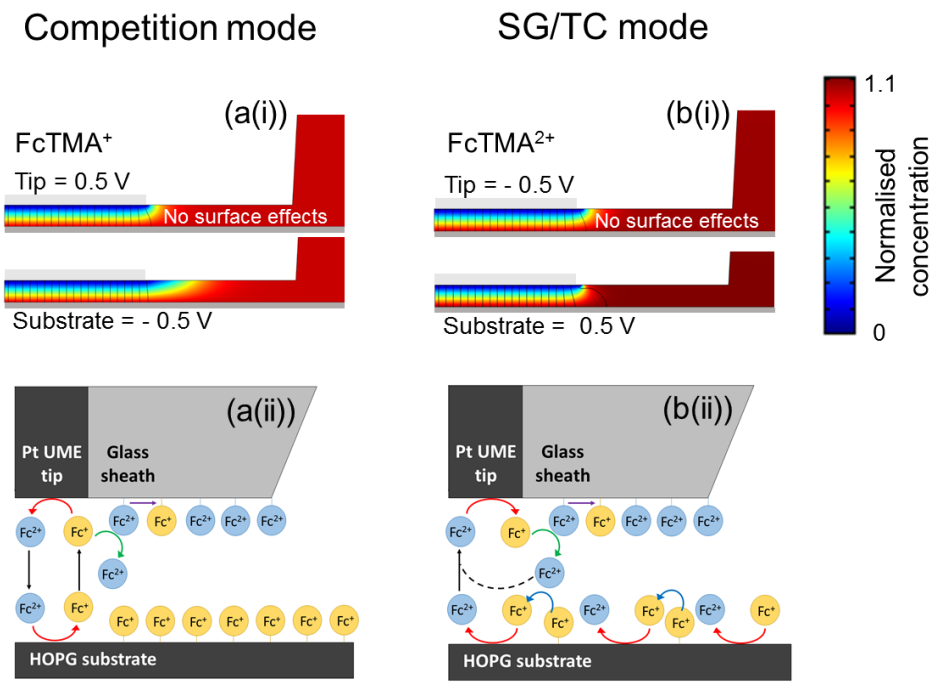

Figure 3.6 (i) Concentration profiles of (a) $FcTMA^+$ in the competition mode and (b) $FcTMA^{2+}$ in the SG/TC mode, with the parameters defined in Figure 3.5(b). (ii) Illustrations of the redox adsorption processes occurring in the (a) competition and (b) SG/TC modes.

Figure 3.7(a) shows results for systematically varied substrate kinetic values (k^0_{HOPG} = 0.5, 1.0, 10 cm s^{-1}) at a fixed distance, L = 0.1 (50 nm) for the full adsorption model. For all k^0 values employed, a tip current enhancement of ~7.3 times (competition mode) and ~7.9 times (SG/TC mode) with respect to $i_{UME,bulk}$, was observed. The resulting 'apparent' tip-substrate separations are 53 and 45 nm for the competition and SG/TC mode, respectively. Analysis of these curves with an adsorption-free analytical model is summarised in Section 3.7.9., Table 3.2, again to illustrate the kinetics and distances derived if a researcher assumed this was a simple redox process. It can be seen that both the competition and SG/TC modes give different distances (see above) and that the SG/TC mode overestimates the kinetics while the competition mode gives an underestimation. Interestingly, this has been seen experimentally,[28] but the effects were attributed to the presence of a contaminant layer.

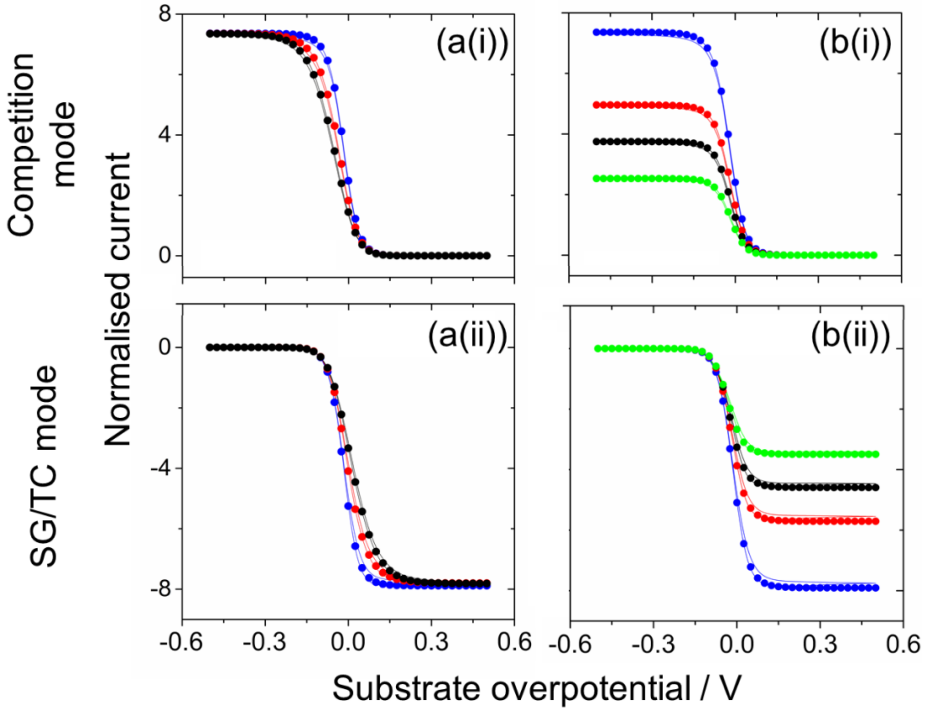

Figure 3.7 Simulated nanogap substrate voltammetry SECM tip current-substrate potential responses in (i) competition and (ii) SG/TC modes showing the effects of (a) substrate ET kinetics on the shape of the voltammograms (10 cm s^{-1} (blue), 1 cm s^{-1} (red) and 0.5 cm s^{-1} (black)) at L = 0.1; and (b) tip-substrate separation (50 nm (blue), 75 nm (red), 100 nm (black) and 150 nm (green)) for k^0_{HOPG} = 5 cm s^{-1}. Dotted lines represent the analytical adsorption-free fitting where parameters are summarised in Section 3.7.9., Table 3.2 and Table 3.3. All other simulation parameters are identical to those used in Figure 3.5. Also see Section 3.7.8.

Figure 3.7(b) shows simulated UME tip responses when the tip height, L is varied (0.1, 0.15, 0.2, 0.3) with k^0_{HOPG} fixed at 5 cm s^{-1}. Again, these voltammograms fitted well with the adsorption-free analytical model and the results are summarised in Section 3.7.9., Table 3.3. For all tip-substrate heights considered, a higher k^0 value and a smaller gap was observed in the SG/TC mode compared to the competition mode. k^0 values determined from SG/TC mode curves are overestimated and are close to the maximum kinetic limit of detection. A trend of decreasing k^0 with increasing tip-substrate heights was observed, similar to previous experimental observations,[28] where the trend of slower kinetics was attributed to selective permeability of a contaminant layer on HOPG surfaces towards $FcTMA^+$. This work however shows that such a trend can (at least partly) be explained by known adsorption phenomena of the redox couple itself.

Lastly, note that the simulated voltammograms (Figure 3.7) show that these new adsorption processes introduce some hysteresis between the forward and reverse scans in both the competition and SG/TC modes, which has also commonly been seen experimentally in nanogap systems,[28,32] indicating that extraneous redox adsorption phenomenon may be widespread in this configuration and needs to be clearly quantified if these methods are to be accurately interpreted.

3.6. Conclusions

This chapter considers the impact of adsorption phenomena on the SECM substrate electrode and tip (insulating support) with several significant outcomes. First, it is shown that substrate voltammetry SECM can be used to quantify adsorption of a redox couple at a substrate electrode. Such effects can readily be seen by changing the voltammetric scan rate applied to the substrate electrode, to achieve a non-steady-state response. Second, it is shown that it is importance of understanding surface adsorption effects on the glass that surrounds the UME tip, particularly in nanogap voltammetric measurements. The increased surface area-to-solution volume ratio of nanogap experiments makes understanding the adsorption properties of the surface probe essential in order to extract reliable kinetic data, especially if the electrode kinetics are fast (close to the diffusion-limit).

A holistic model for SECM has been developed that carefully considers the unequal diffusivities of $FcTMA^+$ and $FcTMA^{2+}$, herein, and the adsorption of the reactant, $FcTMA^+$ onto the HOPG substrate. The adsorption of highly-charged $FcTMA^{2+}$ species onto the insulating glass sheath that encapsulates the UME was also considered along with direct ET between $FcTMA^+$ in solution and glass-bound $FcTMA^{2+}$, which significantly affects the magnitude of limiting-currents measured. The implication of these findings has been discussed for the case where a researcher would be unaware of such surface adsorption effects and analysed the response purely in terms of ET kinetics at the substrate electrode. The effects discussed lead to incorrect kinetic parameters, underestimation in the competition mode and overestimation in the SG/TC mode, as well as, incorrect thermodynamic assignments.

For some of the nanogap electrode dimensions considered here, it is possible that other effects such as from the electrical double layer (EDL) will come into play and cannot be ignored. Recently, White et. al.[32] showed that limiting-currents can be strongly affected (reduced) by the EDL at cell thickness ≤ 100 nm even for typical supporting electrolyte concentrations (200 mM) where the EDL is usually assumed to have negligible effect on mass transport. This work also found hysteresis in voltammograms taken at slow scan rates with a slight variability of the experimental voltammetric responses at low electrolyte concentrations and at thin cell thicknesses attributed to the adsorption of $FcTMA^+$ at the Pt electrode surface.[32] There are further effects, such as ion transport in nanogap geometries which also need further consideration in order to fully understand the SECM nanogap configuration.

3.7. Supporting Information

3.7.1. Additional Experimental Details

SECM Instrumentation

A home-built scanning electrochemical microscope (SECM) was mounted on a vibration-isolation table inside a Faraday cage. The UME tip was mounted in a tip holder on a piezo-

bender actuator, to which an oscillation (70 Hz with a magnitude of 150 nm (~ 1 % UME tip electrode radius)) was applied. In turn, this was mounted on a 3D-piezoelectric positioner controlled by a PC running custom LabVIEW code (LabVIEW 9.0, National Instruments), which was also used for data acquisition. The tip-substrate separation was controlled by monitoring the damping of the oscillation amplitude of the UME tip upon intermittent contact between the tip and surface (typically 5 %).

Adsorption of $FcTMA^+$ and $FcTMA^{2+}$ to Glass

Bulk electrolysis of $FcTMA^+$ solutions (1 M KCl) was carried out quantitatively (monitored by steady-state voltammetry at a 12.5 µm-radius Pt UME tip) in a two-compartment cell. Both compartments were filled with known concentrations of $FcTMA^+$ solution separated by a P4 frit to minimise mixing of the solutions in the separate compartments. Two carbon fibre felt cloths of large area served as the working and counter electrodes in the separate compartments. An AgCl-coated Ag wire reference electrode was placed into the same compartment as the working electrode and a working electrode bias of 0.8 V was applied to electrochemically-generate $FcTMA^{2+}$.

To probe the possible adsorption of $FcTMA^+$ and $FcTMA^{2+}$ to glass, UME voltammetry in a drop of solution on a glass surface was employed, which provides a reasonably high surface area-to-volume ratio to be able to detect relatively low surface coverages.[1] A UME was manually lowered close to a glass substrate surrounded by a moat of water to minimise droplet evaporation. A 3.5 µL drop of $FcTMA^+$ or $FcTMA^{2+}$ solution (1 M KCl) of known concentration was placed onto the glass substrate positioned below the UME. The typical area of glass covered by the drop was 0.14 cm^2. Following the deposition of the droplet, sufficient time must be allowed for the adsorption process to attain equilibrium and, particularly, for the diffusion front to propagate through the droplet so that the concentration of solute in the droplet becomes uniform.[66] The diffusion-limited current measured at the UME, which was typically 0.5 mm from the glass surface, was used to monitor the concentration of $FcTMA^+$ or $FcTMA^{2+}$ (solute) in the droplet (in separate experiments). Knowing the initial and final concentration values allowed an estimation of solute adsorbed on the surface compared to that remaining in bulk solution.[66]

3.7.2. Cyclic Voltammetry at HOPG

Figure 3.8(a) shows a plot of ΔE_p versus scan rate, v. ΔE_p decreases with increasing v as the mixed diffusion-adsorption process becomes increasingly biased towards the adsorbed species. Analysis of CVs for the oxidation of $FcTMA^+$ on HOPG further revealed larger forward wave peak currents compared to the reverse peak currents (Figure 3.8(b)) with the difference increasing with increasing v. This is indicative of the weak adsorption of $FcTMA^+$ onto the HOPG electrode. Figure 3.8(c) shows a comparison of an experimental voltammogram to a simulated diffusion-controlled response at a v = 10 V s^{-1}. The planar diffusion simulations were carried out with the MECSim (Monash Electrochemistry Simulator) computer program written in Fortran[72] (see caption for simulation parameters) using fitting procedures described in reference[73]. The much higher current on the forward scan, seen experimentally, is indicative of the oxidation of electrode-adsorbed $FcTMA^+$, as well as $FcTMA^+$ from solution.

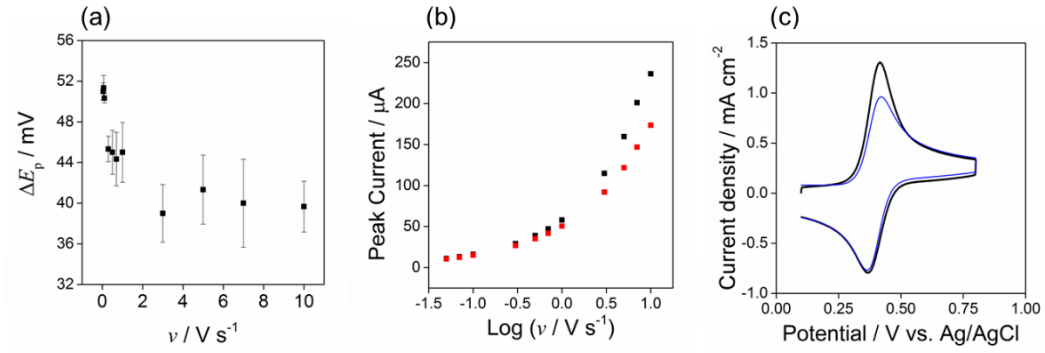

Figure 3.8 (a) Plot of ΔE_p vs. v. (b) Plot of forward peak currents (black) and reverse peak currents (red) vs. log v. (c) Experimental voltammogram (black) compared to the corresponding simulated diffusional wave (blue) at v = 10 V s^{-1}. Simulation parameters: k^0 = 100 cm s^{-1} (reversible), α = 0.5, A = 0.165 cm^2 (area of droplet calculated using procedure in reference[55]), D_{FcTMA^+} = 6.7 × 10^{-6} cm^2 s^{-1} and $D_{FcTMA^{2+}}$ = 6.1 × 10^{-6} cm^2 s^{-1}, C_{dl} = 8 μF cm^{-2}.

3.7.3. Simulated SECM Voltammograms for a 12.5 µm-radius UME Tip

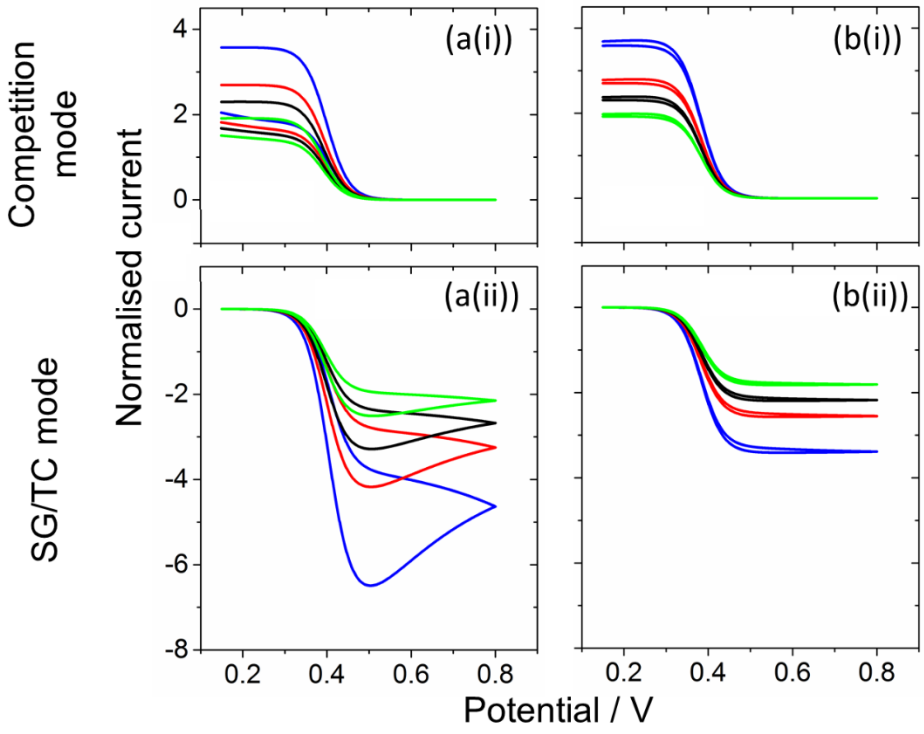

Figure 3.9 Simulated substrate voltammetry SECM tip current-substrate potential responses for the competition (i) and SG/TC (ii) modes for a one-electron oxidation process at the substrate electrode at different normalised tip-substrate distances (L = 0.209 (blue), 0.297 (red), 0.367 (black) and 0.478 (green)) for (a) adsorption of reactant (present in bulk at a concentration of 0.4 mM) occurs on the substrate electrode (reverse potential sweeps produce lower currents compared to the forward potential sweep) and (b) a typical adsorption-free case is considered. Simulation parameters: k^0_{UME} = 25 cm s^{-1} (reversible), k^0_{HOPG} = 10 cm s^{-1} (reversible), $E^{0`}$ = 0.38 V, D_{FcTMA^+} = 6.7 × 10^{-6} cm^2 s^{-1}, $D_{FcTMA^{2+}}$ = 6.1 × 10^{-6} cm^2 s^{-1}, Γ_{HOPG} = 1.13 × 10^{-10} mol cm^{-2} and $K_{ads,HOPG}$ = 7.4 × 10^5 cm^3 mol^{-1}.

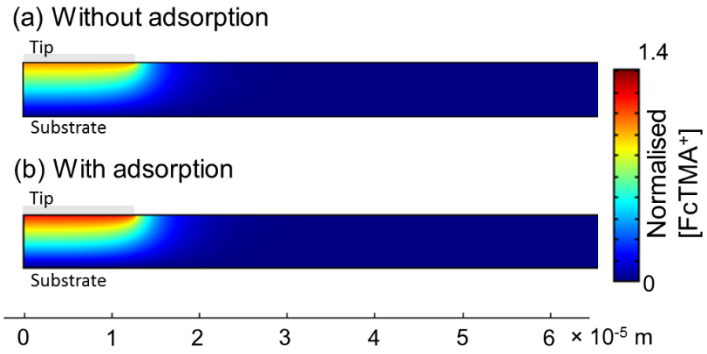

Figure 3.10 Concentration profiles of $FcTMA^+$ under the tip at E_{HOPG} = 0.5 V on the forward sweep for the SG/TC mode (a) without and (b) with $FcTMA^+$ adsorption on the SECM substrate.

3.7.4. Determination of the Diffusion Coefficient of $FcTMA^+$

CVs for the oxidation of 1.5 mM $FcTMA^+$ (1 M KCl) (Figure 3.11) gave voltammograms which were close to reversible on the time-scale of steady-state UME voltammetry. The measured diffusion-limited current (forward wave) gave a diffusion coefficient, D_{FcTMA^+} = (6.74 ± 0.03) × 10^{-6} cm^2 s^{-1} with $E_{1/2}$ of 0.38 ± 0.01 V vs. Ag/AgCl (1 M KCl).

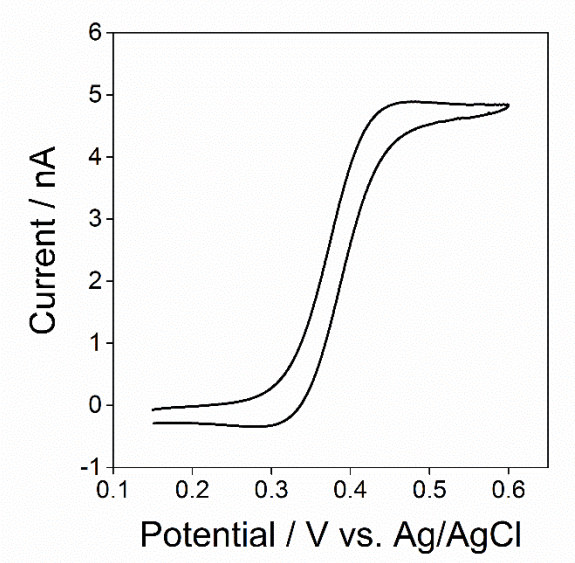

Figure 3.11 Typical CV for the oxidation of 1.5 mM $FcTMA^+$ in 1 M KCl supporting electrolyte at a 12.5 µm-radius Pt UME at a scan rate of 50 mV s^{-1}.

3.7.5. Determination of the Diffusion Coefficient of $FcTMA^{2+}$

Although voltammetric studies usually assume the same *D* value for both oxidised and reduced forms of a redox couple,[28] this is rarely the case and accurate determination of these values can be very important for quantitative kinetic studies,[27,29,56,57] especially if one is looking at measuring the kinetics of fast processes that are close to the diffusion-limit.

In order to accurately determine *D* of $FcTMA^{2+}$, SECM-chronoamperometric measurements are employed with a 12.5 μm-radius Pt UME in both the feedback[56] and SG/TC[57] mode. The responses can be analysed to give the ratio of diffusion coefficients of the oxidised to reduced form of a redox mediator couple, γ, when the redox couple undergoes a simple diffusion-controlled one-electron transfer, without any kinetic complications and adsorption effects.[56,57]

Under feedback conditions, γ has no effect on the steady-state current but can affect the way steady-state in reached.[57] Therefore, the normalised steady-state limiting-current determined in the feedback mode can be used to precisely determine the tip-substrate separation for the pair of feedback and SG/TC steady-state limiting tip currents taken at the same height. Under SG/TC conditions, $FcTMA^{2+}$ is electrogenerated at a diffusion-controlled rate from the precursor in bulk solution, $FcTMA^{+}$, at a Pt macroscopic substrate:

$$\text{Substrate reaction: } FcTMA^{+} \xrightarrow{-e^{-}} FcTMA^{2+} \quad \text{(Eq. 3.16)}$$

$FcTMA^{2+}$ diffuses away from the substrate and part of the diffusion field is intercepted by the UME tip. At the UME, $FcTMA^{2+}$ undergoes a diffusion-controlled reduction to $FcTMA^{+}$:

$$\text{Tip reaction: } FcTMA^{2+} \xrightarrow{+e^{-}} FcTMA^{+} \quad \text{(Eq. 3.17)}$$

Although the macroscopic substrate electrode will have a transient form, the redox mediator diffusional cycling between the tip and substrate attains a quasi-steady-state. A simple modification of an empirically derived equation for the positive feedback mode[74] can be used to describe the normalised steady-state collection current-distance data:

$$I = \gamma\left[0.68 + 0.78377 / L + 0.3315\exp(-1.0672L)\right] \quad \text{(Eq. 3.18)}$$

where I is the normalised current measured at the UME tip, γ is the diffusion coefficient ratio of oxidised to reduced forms of the redox couple and L is the normalised distance between the tip and substrate. γ was found to be 0.91 from best fit.

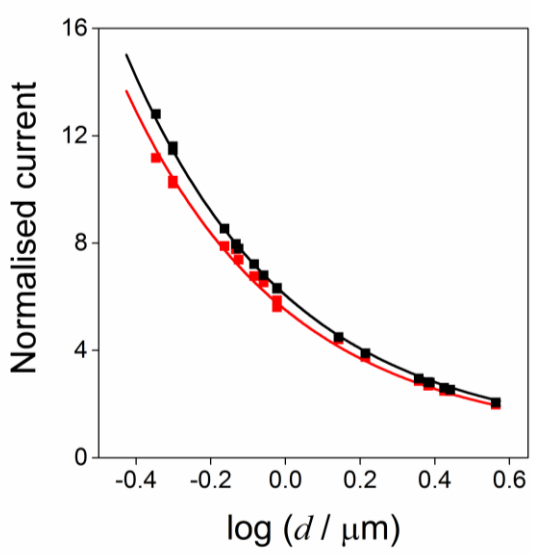

Figure 3.12 Steady-state feedback (black) and SG/TC (red) normalised UME tip current vs. distance characteristics for the $FcTMA^{+/2+}$ redox couple. The dotted line represents experimental results and solid lines indicate the γ-independent steady-state theory (black) and the theoretical SG/TC behaviour for γ = 0.91 (red).

3.7.6. Cyclic Voltammetry on 'Aged' HOPG Electrodes

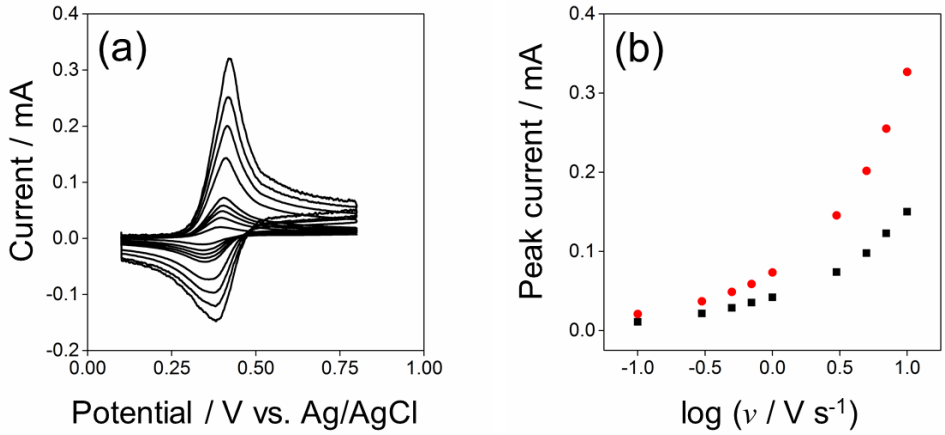

Figure 3.13 (a) CVs for the oxidation of 0.4 mM $FcTMA^+$ (1 M KCl) at 'aged' (1 hour exposure to air) ZYA grade HOPG in the droplet configuration (area of droplet was 0.162 cm^2). $E_{1/2,app}$ was found to be 0.38 V vs. Ag/AgCl (1 M KCl) with ΔE_p = 48 ± 6 mV (for all scan rates employed). (b) A plot of forward (red) and reverse (black) peak currents at different scan rate values. The peak current difference increases with increasing scan rate and is larger than at freshly cleaved HOPG surfaces (see Figure 3.8(b)). The surface coverage was estimated to be ca. 2.0×10^{-10} mol cm^{-2} with 0.4 mM $FcTMA^+$ in bulk solution.

3.7.7. Determination of $FcTMA^+$ and $FcTMA^{2+}$ Adsorption on Glass

An UME was used to monitor amperometrically the concentration of either $FcTMA^+$ or $FcTMA^{2+}$ (in separate experiments) in a small droplet of solution (3.5 µL) placed on a glass surface where the concentrations can be determined from measurements of the diffusion-limited current, i_{UME}. The droplet of solution was surrounding by a moat of supporting electrolyte solution to prevent evaporation.[66]

A decrease in limiting-current, Δi_{UME} can be ascribed to analyte adsorption onto the glass surface, Γ_{glass} (mol cm^{-2}):[66]

$$\Gamma_{glass} = (V / A)(\Delta i_{UME} / 4nFa_{UME}D_i) \quad \text{(Eq. 3.19)}$$

where V is the volume of the drop and A is the glass area of which it covers.

As shown in Figure 3.14(a), there was essentially no change in i_{UME} measured in a drop of $FcTMA^+$ solution on glass. In contrast, $FcTMA^{2+}$ evidently adsorbed much more strongly on glass surfaces. The $FcTMA^{2+}$ adsorption data fitted reasonably well to a Langmuir isotherm (over the concentration range of the experiment), Figure 3.14(b), with $\Gamma^0_{glass} = 2.3 \pm 0.8 \times 10^{-9}$ mol cm^{-2} and $K_{ads,glass} = 2.6 \pm 0.4 \times 10^6$ cm^3 mol^{-1}.

The strong adsorption on glass of $FcTMA^{2+}$ compared to $FcTMA^+$ may seem surprising, but other divalent cation molecules, such as tris (2,2'-bipyridine) ruthenium (II) strongly adsorbs from aqueous on glass at similar neutral pH to these measurements, especially at higher electrolyte concentration.[75] The much stronger adsorption of multivalent cations compared to monovalent ions, and the enhancement by supporting electrolyte is well-established.[76,77]

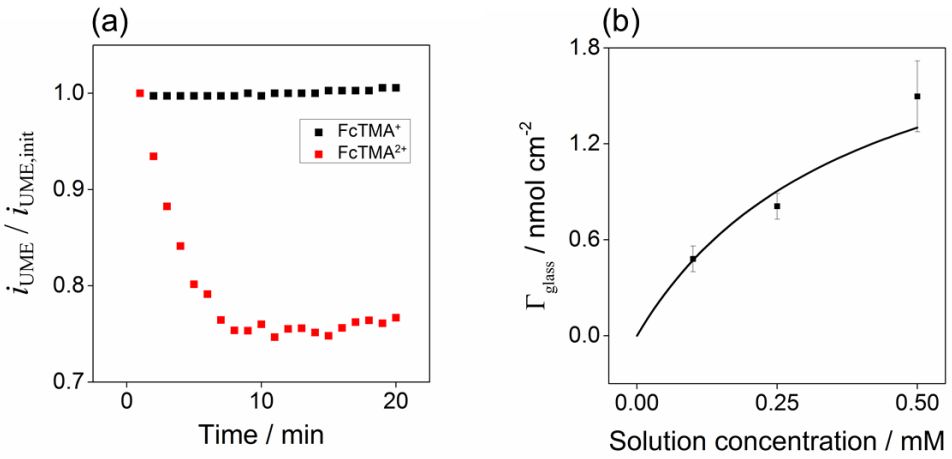

Figure 3.14 (a) Data showing the change in concentration in a 3.5 µL droplet of $FcTMA^+$ (black) and $FcTMA^{2+}$ (red) solution on glass. (b) Amount of $FcTMA^{2+}$ adsorbed on glass, Γ_{glass} as a function of remaining solution concentration of $FcTMA^{2+}$.

3.7.8. Additional Simulation Details

As shown experimentally, $FcTMA^{2+}$ adsorbs onto glass surfaces, which can be represented by the following:

$$FcTMA^{2+}_{soln} \underset{k_{des,glass}}{\overset{k_{ads,glass}}{\rightleftharpoons}} FcTMA^{2+}_{ads} \qquad \text{(Eq. 3.20)}$$

where $k_{ads,glass}$ and $k_{des,glass}$ are the rate constants for the adsorption and desorption of $FcTMA^{2+}$ onto the glass sheath surrounding the Pt UME tip.

In the SECM experiments, for $t > 0$, the flux due to adsorption of the $FcTMA^{2+}$ at the glass sheath ($a_{UME} < r < a_{UME} \times RG$, $z = d$) is defined by:

$$-\mathbf{n}.\mathbf{N}_{FcTMA^{2+},glass} = -\Gamma^{0}_{glass}\left[k_{ads,glass}(1-\theta_{glass})c_{FcTMA^{2+}_{soln}} - k_{des,glass}\theta_{glass}\right] \quad \text{(Eq. 3.21)}$$

where Γ^{0}_{glass} is the saturation value at maximum surface concentration, determined to be 2.3×10^{-9} mol cm^{-2} (from glass adsorption experiments, see Section 3.7.7), the equilibrium adsorption constant for the glass surface, $K_{ads,glass} = \dfrac{k_{ads,glass}}{k_{des,glass}}$ was found to be 2.6×10^{6} mol cm^{-3} from experiments described herein (reasonably assuming a Langmiurian isotherm) with $k_{ads,glass}$ set sufficiently large as to maintain equilibrium (1×10^{9} cm^{3} mol^{-1} s^{-1}), which is reasonable for this process which involves mainly Van der Waals electrostatic interactions of $FcTMA^{2+}$ with the surface. θ_{glass} is the fractional surface coverage of $FcTMA^{2+}$ on the glass.

Redox mediators immobilised onto the glass (non-conducting) surface can undergo various charge transfer processes, such as direct electron transfer (ET) between surface and redox molecules in the solution and charge exchange between the redox active species which are immobilised along the surface.[67–71] In order to account for this in a simple manner, a species, $FcTMA^{2+*}$ is introduced, that is generated in solution by reaction at the glass surface through the following ET process:

$$FcTMA^{+}_{soln} \xrightarrow{K_{12}} FcTMA^{2+*}_{soln} \quad \text{(Eq. 3.22)}$$

where K_{12} is the $FcTMA^{+/2+}$ homogeneous self-exchange rate constant (9×10^{6} M^{-1} s^{-1}).[19]

For $t > 0$, the flux due to the redox reaction of $FcTMA^{+}$ in solution producing $FcTMA^{2+*}$ via reaction at the glass sheath is defined by:

$$-\mathbf{n}.\mathbf{N}_{FcTMA^{+},glass} = -K_{12}c_{FcTMA^{+}_{soln}}\Gamma^{0}_{glass}\theta_{glass} \quad \text{(Eq. 3.23)}$$

$$-\mathbf{n}.\mathbf{N}_{FcTMA^{2+*},glass} = -\left[-K_{12}c_{FcTMA^{+}soln}\Gamma^{0}{}_{glass}\theta_{glass}\right] \quad \text{(Eq. 3.24)}$$

Here, the $FcTMA^{+}$ species in solution can be oxidised by surface-confined $FcTMA^{2+}$ species on the glass (the glass surface assumed to be unchanged by the ET process) to generate the $FcTMA^{2+*}$ species. This is labeled as such, as it does not participate in any glass adsorption processes, and diffuses away from the glass surface for detection at the tip electrode (in substrate voltammetry experiments). This simplification is reasonable for the demonstrative proposes herein given the well-known fast lateral charge propagation within surface attached molecules,[12-18] especially ferrocenes at high surface coverage,[13] which would rapidly restore $FcTMA^{+}$ produced in the charge transfer reaction back to $FcTMA^{2+}{}_{ads}$. Furthermore, the sharp concentration gradient in the solution near the tip/glass boundary makes it reasonable to assume that any flux of $FcTMA^{2+}$ species generated from this process at the glass surface will quickly diffuse away and will then contribute to the flux at the substrate or tip electrode.

3.7.9. Kinetic Analysis of Nanogap SECM Simulations

Table 3.1 Fitting parameters from Figure 3.5(a), $L = 0.1$ and $\Delta E^{0`} = E^{0`}{}_{app} - E^{0`}$.

Simulated data	Adsorption-free fitting					
$\Gamma_{HOPG,FcTMA^{+}}$ / mol cm^{-2}	$\Delta E^{0`}$ / mV		$k^{0}{}_{app}$ / cm s^{-1}		d_{app} / nm	
	Competition mode	SG/TC mode	Competition mode	SG/TC mode	Competition mode	SG/TC mode
0	0	0	5.0	5	50	50
1.1×10^{-10} (22 %)	4	0	5.0	≥14	50	49
1.53×10^{-10} (30 %)	4	0	4.8	≥14	50	48
2.0×10^{-10} (40 %)	4	0	4.6	≥14	50	47
2.6×10^{-10} (50 %)	4	0	4.0	≥14	50	46

Table 3.2 Fitting parameters from Figure 3.7(a), L = 0.1.

Simulated data	Adsorption-free fitting					
k^0 / cm s^{-1}	$\Delta E^{0`}$ / mV		k^0_{app} / cm s^{-1}		d_{app} / nm	
	Competition mode	SG/TC mode	Competition mode	SG/TC mode	Competition mode	SG/TC mode
10	3	0	5.0	≥ 14.0	53	45
5	3	-5	3.0	≥ 14.0	53	45
1	0	-6	0.8	1.2	53	46
0.5	-9	-9	0.5	0.5	53	47

Table 3.3 Fitting parameters from Figure 3.7(b), k^0 = 5 cm s^{-1}

Simulated data	Adsorption-free fitting					
L	$\Delta E^{0`}$ / mV		k^0_{app} / cm s^{-1}		d_{app} / nm	
	Competition mode	SG/TC mode	Competition mode	SG/TC mode	Competition mode	SG/TC mode
0.1	3	-5	3.0	≥ 15.0	53	45
0.15	3	-7	3.0	≥ 10.0	83	66
0.2	3	-10	2.2	≥ 8.0	117	83
0.25	2	-12	1.9	≥ 7.0	154	99
0.3	2	-15	1.6	≥ 6.0	190	112

3.8. References

(1) Marcus, R. A. *Annu. Rev. Phys. Chem.* **1964**, *15* (1), 155–196.

(2) Gosavi, S.; Marcus, R. A. *J. Phys. Chem. B.* **2000**, *104*, 2067–2072.

(3) Chen, S.; Liu, Y.; Chen, J. *Chem. Soc. Rev.* **2014**, *43* (15), 5372.

(4) Forster, R. J.; Faulkner, L. R. *J. Am. Chem. Soc.* **1994**, *116*, 5444–5452.

(5) Forster, R. J. *Langmuir* **1995**, *11*, 2247–2255.

(6) Forster, R. J. *Anal. Chem.* **1996**, *68* (18), 3143–3150.

(7) Chidsey, C. E. D.; Murray, R. W. *Science* **1986**, *231*, 25–31.

(8) Chidsey, C. E. D. *Science* **1991**, *251*, 919–922.

(9) Bard, A. J.; Mirkin, M. V; Unwin, P. R.; Wipf, D. *J. Phys. Chem.* **1992**, *96*, 1861–1868.

(10) Macpherson, J. V.; Marcar, S.; Unwin, P. R. *Anal. Chem.* **1994**, *66*, 2175–2179.

(11) Macpherson, J. V; Jones, C. E.; Unwin, P. R. *J. Phys. Chem. B* **1998**, *102*, 9891–9897.

(12) Amemiya, S.; Bard, A. J.; Fan, F.-R. F.; Mirkin, M. V.; Unwin, P. R. *Annu. Rev. Anal. Chem.* **2008**, *1*, 95–131.

(13) Aoki, K. *Electroanalysis* **1993**, *5* (8), 627–639.

(14) Forster, R. J. *Chem. Soc. Rev.* **1994**, *23* (4), 289.

(15) Martin, R. D.; Unwin, P. R. *J. Electroanal. Chem.* **1995**, *397*, 325–329.

(16) Macpherson, J. V; Beeston, M. A.; Unwin, P. R.; Hughes, N. P.; Littlewood, D. *J. Chem. Soc. Faraday Trans.* **1995**, *91*, 1407–1410.

(17) Sun, P.; Laforge, F. O.; Mirkin, M. V. *Phys. Chem. Chem. Phys.* **2007**, *9*, 802–823.

(18) Mirkin, M. V.; Nogala, W.; Velmurugan, J.; Wang, Y. *Phys. Chem. Chem. Phys.* **2011**, *13*, 21196–21212.

(19) Unwin, P. R.; Bard, A. J. *J. Phys. Chem.* **1991**, *95*, 7814–7824.

(20) Zhang, B.; Fan, L.; Zhong, H.; Liu, Y.; Chen, S. *J. Am. Chem. Soc.* **2013**, *135*, 10073–10080.

(21) Cox, J. T.; Zhang, B. *Annu. Rev. Anal. Chem.* **2012**, *5*, 253–272.

(22) Sun, P.; Mirkin, M. V. *Anal. Chem.* **2006**, *78* (18), 6526–6534.

(23) Heller, I.; Kong, J.; Heering, H. A.; Williams, K. A.; Lemay, S. G.; Dekker, C. *Nano Lett.* **2005**, *5*, 137–142.

(24) Dumitrescu, I.; Unwin, P. R.; Macpherson, J. V. *Chem. Commun.* **2009**, 6886–6901.

(25) Dudin, P. V; Snowden, M. E.; Macpherson, J. V; Unwin, P. R. *ACS Nano* **2011**, *5*, 10017–10025.

(26) Güell, A. G.; Meadows, K. E.; Dudin, P. V; Ebejer, N.; Macpherson, J. V; Unwin, P. R. *Nano Lett.* **2014**, *14* (1), 220–224.

(27) Nioradze, N.; Kim, J.; Amemiya, S. *Anal. Chem.* **2011**, *83* (3), 828–835.

(28) Liu, Y.; Holzinger, A.; Knittel, P.; Poltorak, L.; Gamero-Quijano, A.; Rickard, W. D. . A.; Walcarius, A.; Herzog, G. G.; Kranz, C.; Arrigan, D. W. M. M. *Anal. Chem.* **2016**, *88* (13), 6689–6695.

(29) Mampallil, D.; Mathwig, K.; Kang, S.; Lemay, S. G. *Anal. Chem.* **2013**, *85* (12), 6053–6058.

(30) Mampallil, D.; Mathwig, K.; Kang, S.; Lemay, S. G. *J. Phys. Chem. Lett.* **2014**, *5*, 636–640.

(31) Fan, L.; Liu, Y.; Xiong, J.; White, H. S.; Chen, S. *ACS Nano* **2014**, *8* (10), 10426–10436.

(32) Xiong, J.; Chen, Q.; Edwards, M. A.; White, H. S. *ACS Nano* **2015**, *9*, 8520–8529.

(33) Byers, J. C.; Paulose Nadappuram, B.; Perry, D.; McKelvey, K.; Colburn, A. W.; Unwin, P. R. *Anal. Chem.* **2015**, *87* (20), 10450–10456.

(34) Mirkin, M. V; Bard, A. J. *Anal. Chem.* **1992**, *64* (19), 2293–2302.

(35) Chang, J.; Leonard, K. C.; Cho, S. K.; Bard, A. J. *Anal. Chem.* **2012**, *84*, 5159–5163.

(36) Lazenby, R. A.; McKelvey, K.; Peruffo, M.; Baghdadi, M.; Unwin, P. R. *J. Solid State Electrochem.* **2013**, *17* (12), 2979–2987.

(37) Nioradze, N.; Chen, R.; Kim, J.; Shen, M.; Santhosh, P.; Amemiya, S. *Anal. Chem.* **2013**, *85*, 6198–6202.

(38) Oldham, K. *Anal. Chem.* **1992**, *64*, 646–651.

(39) Zhang, B.; Galusha, J.; Shiozawa, P. G.; Wang, G.; Bergren, A. J.; Jones, R. M.; White, R. J.; Ervin, E. N.; Cauley, C. C.; White, H. S. *Anal. Chem.* **2007**, *79*, 4778–4787.

(40) Penner, R. M.; Heben, M. J.; Longin, T. L.; Lewis, N. S. *Science* **1990**, *250*, 1118–1121.

(41) Shao, Y.; Mirkin, M. V; Fish, G.; Kokotov, S.; Palanker, D.; Lewis, A. *Anal. Chem.* **1997**, *69*, 1627–1634.

(42) Li, Y.; Bergman, D.; Zhang, B. *Anal. Chem.* **2009**, *81*, 5496–5502.

(43) Nogala, W.; Velmurugan, J.; Mirkin, M. V. *Anal. Chem.* **2012**, *84*, 5192–5197.

(44) Dumitrescu, I.; Edgeworth, J. P.; Unwin, P. R.; Macpherson, J. V. *Adv. Mater.* **2009**, *21* (30), 3105–3109.

(45) Lee, H. B. R.; Baeck, S. H.; Jaramillo, T. F.; Bent, S. F. *Nano Lett.* **2013**, *13*, 457–463.

(46) Kang, S.; Mathwig, K.; Lemay, S. G. *Lab Chip* **2012**, *12*, 1262–1267.

(47) Kätelhön, E.; Krause, K. J.; Mathwig, K.; Lemay, S. G.; Wolfrum, B. *ACS Nano* **2014**, *8* (5), 4924–4930.

(48) Zevenbergen, M. A. G.; Singh, P. S.; Goluch, E. D.; Wolfrum, B. L.; Lemay, S. G. *Anal. Chem.* **2009**, *81*, 8203–8212.

(49) Singh, P. S.; Chan, H.-S. M.; Kang, S.; Lemay, S. G. *J. Am. Chem. Soc.* **2011**, *133*, 18289–18295.

(50) Hubbard, A. T.; Anson, F. C. *J. Electroanal. Chem.* **1965**, *9*, 163–164.

(51) Hubbard, A. T.; Anson, F. C. *Anal. Chem.* **1966**, *38*, 1601–1603.

(52) Hubbard, A. T.; Osteryoung, R. A.; Anson, F. C. *Anal. Chem.* **1966**, *38*, 692–697.

(53) Chen, R.; Nioradze, N.; Santhosh, P.; Li, Z.; Surwade, S. P.; Shenoy, G. J.; Parobek, D. G.; Kim, M. A.; Liu, H.; Amemiya, S. *Angew. Chem. Int. Ed.* **2015**, *54* (50), 15134–15137.

(54) Bond, A. M.; Mclennan, E. A.; Stojanovic, R. S.; Thomas, F. G. *Anal. Chem.* **1987**, *59*, 2853–2860.

(55) Cuharuc, A. S.; Zhang, G.; Unwin, P. R. *Phys. Chem. Chem. Phys.* **2016**, *18* (6), 4966–4977.

(56) Martin, R. D.; Unwin, P. R. *J. Electroanal. Chem.* **1997**, *439* (1), 123–136.

(57) Martin, R. D.; Unwin, P. R. *Anal. Chem.* **1998**, *70* (2), 276–284.

(58) Patten, H. V.; Meadows, K. E.; Hutton, L. A.; Iacobini, J. G.; Battistel, D.; McKelvey, K.; Colburn, A. W.; Newton, M. E.; Macpherson, J. V.; Unwin, P. R. *Angew. Chem. Int. Ed.* **2012**, *51* (28), 7002–7006.

(59) Baer, C. D.; Stone, N. J.; Sweigart, D. A. *Anal. Chem.* **1988**, *60* (2), 188–191.

(60) Patel, A. N.; Collignon, M. G.; O'Connell, M. A.; Hung, W. O. Y.; McKelvey, K.; Macpherson, J. V.; Unwin, P. R. *J. Am. Chem. Soc.* **2012**, *134* (49), 20117–20130.

(61) Patel, A. N.; Tan, S.-y.; Unwin, P. R. *Chem. Commun. (Camb).* **2013**, *49* (78), 8776–8778.

(62) Güell, A. G.; Cuharuc, A. S.; Kim, Y.; Zhang, G.; Tan, S.-y.; Ebejer, N.; Unwin, P. R. *ACS Nano* **2015**, *9* (4), 3558–3571.

(63) Zhang, G.; Cuharuc, A. S.; Güell, A. G.; Unwin, P. R. *Phys. Chem. Chem. Phys.* **2015**, *17*, 11827–11838.

(64) McKelvey, K.; Edwards, M. A.; Unwin, P. R. *Anal. Chem.* **2010**, *82* (15), 6334–6337.

(65) McKelvey, K.; Snowden, M. E.; Peruffo, M.; Unwin, P. R. *Anal. Chem.* **2011**, *83*, 6447–6454.

(66) Unwin, P.; Bard, A. *Anal. Chem.* **1992**, *64*, 113–119.

(67) Zhang, J.; Slevin, C. J.; Morton, C.; Scott, P.; Walton, D. J.; Unwin, P. R. *J. Phys. Chem.*

B. **2001**, *105*, 11120–11130.

(68) Zhang, J.; Unwin, P. R. *J. Am. Chem. Soc.* **2002**, *124*, 2379–2383.

(69) O'Mullane, A. P.; Macpherson, J. V.; Unwin, P. R.; Cervera-Montesinos, J.; Manzanares, J. A.; Frehill, F.; Vos, J. G. *J. Phys. Chem. B.* **2004**, *108*, 7219–7227.

(70) Whitworth, A. L.; Mandler, D.; Unwin, P. R. *Phys. Chem. Chem. Phys.* **2005**, *7*, 356–365.

(71) Hauquier, F.; Ghilane, J.; Fabre, B.; Hapiot, P. *J. Am. Chem. Soc.* **2008**, *130*, 2748–2749.

(72) Bond, A. M.; Duffy, N. W.; Elton, D. M.; Fleming, B. D. *Anal. Chem.* **2009**, *81* (21), 8801–8808.

(73) Sher, A. A.; Bond, A. M.; Gavaghan, D. J.; Harriman, K.; Feldberg, S. W.; Duffy, N. W.; Guo, S.-X.; Zhang, J. *Anal. Chem.* **2004**, *76* (21), 6214–6228.

(74) Mirkin, M. V.; Fan, F.-R. F.; Bard, A. J. *J. Electroanal. Chem.* **1992**, *328* (1–2), 47–62.

(75) Powell, H. V; Schnippering, M.; Mazurenka, M.; Macpherson, J. V; Mackenzie, S. R.; Unwin, P. R. *Langmuir* **2009**, *25*, 248–255.

(76) Tadros, T. F.; Lyklema, J. *J. Electroanal. Chem. Interfacial Electrochem.* **1968**, *17*, 267–275.

(77) Porus, M.; Labbez, C.; Maroni, P.; Borkovec, M. *J. Chem. Phys.* **2011**, *135*, 64701.

Chapter 4

Probing Electrode Heterogeneity using Fourier-Transformed Alternating Current Voltammetry: Application to a Dual-Electrode Configuration

In Chapter 2, the capabilities of Fourier-transformed large amplitude alternating current voltammetry (FTACV) to measure fast electron transfer (ET) kinetics are shown to be comparable to microscopic techniques such as scanning electrochemical microscopy. However, a key advantage of scanning probe techniques is their capability to measure ET with high spatial resolution, hence discriminating electrochemical heterogeneities on electrode surfaces. This chapter contains an article and its supporting information published in *Analytical Chemistry*. It describes the development of FTACV as a tool for kinetic selectivity/discrimination of a mixed response from a redox reaction that occurs at different rates at different electrode materials or structures. This is first investigated by simulation followed by an experimental demonstration utilising a model dual-electrode configuration.

Probing Electrode Heterogeneity using Fourier-Transformed Alternating Current Voltammetry: Application to a Dual-Electrode Configuration

Sze-yin Tan,[†,‡] *Patrick R. Unwin,*[‡] *Julie V. Macpherson,*[‡] *Jie Zhang,*[*,†] *Alan M. Bond,*[*,†]

[†] School of Chemistry, Monash University, Clayton, Victoria 3800, Australia

[‡] Department of Chemistry, University of Warwick, Coventry CV4 7AL, United Kingdom

* jie.zhang@monash.edu and alan.bond@monash.edu

4.1. Abstract

Quantitative studies of electron transfer processes at electrode/electrolyte interfaces, originally developed for homogeneous liquid mercury or metallic electrodes, are difficult to adapt to the spatially heterogeneous nanostructured electrode materials that are now commonly used in modern electrochemistry. In this study, the impact of surface heterogeneity on Fourier-transformed alternating current voltammetry (FTACV) has been investigated theoretically under the simplest possible conditions where no overlap of diffusion layers occurs and where numerical simulations based on a 1D diffusion model are sufficient to describe the mass transport problem. Experimental data that meet these requirements can be obtained with the aqueous $[Ru(NH_3)_6]^{3+/2+}$ redox process at a dual-electrode system comprised of electrically coupled but well-separated glassy carbon (GC) and boron-doped diamond (BDD) electrodes. Simulated and experimental FTACV data obtained with this electrode configuration and where distinctly different heterogeneous charge transfer rate constants (k^0 values) apply at the individual GC and BDD electrode surfaces, are in excellent agreement. Principally, due to the far greater dependence of the AC current magnitude on k^0, it is straight forward with the FTACV method to resolve electrochemical heterogeneities which are ~1-2 order of magnitudes apart, as applies in the $[Ru(NH_3)_6]^{3+/2+}$ dual-electrode configuration experiments, without prior knowledge of the individual kinetic parameters (k^0_1 and k^0_2) and the electrode size ratio (θ_1:θ_2). In direct

current voltammetry, a difference in k^0 of > 3 orders of magnitude is required to make this distinction.

4.2. Introduction

Interfacial charge transfer represents a fundamental component of dynamic electrochemistry and has been studied in detail at a myriad of electrode materials using numerous techniques and data analysis strategies. To date, most quantitative investigations of electron transfer (ET) have been assumed to have taken place with fully homogenous electrode surfaces. However, in practice liquid mercury electrodes represent one of the few examples of such an ideal surface and for this and other reasons it was widely used in many early electrode kinetic studies. Unfortunately, the toxicity of mercury has severely restricted its use in recent times.

Currently, the most commonly used metallic electrode materials include platinum and gold. Platinum is a favoured material due to its electrochemical inertness and ease of fabrication into many electrode geometries such as nanotips[1,2] and nanoparticles.[3] However, recent studies have shown a direct correlation between local electrochemical activity and surface structure at polycrystalline platinum surfaces.[4,5] Gold electrodes have been used in both polycrystalline and single crystal forms and have also been successfully employed in the preparation of modified electrodes known as self-assembled monolayers but are known to produce heterogeneous surface packing densities and defects which directly affect charge transfer processes leading to ET kinetic dispersion.[6–9]

Advances in material science have seen the emergence of the field of carbon electrochemistry where materials such as glassy carbon (GC),[10] carbon nanotubes (CNTs),[11–13] graphene,[14,15] graphite,[16] and boron-doped diamond[17,18] play an important role. Many of these carbon-based materials inevitably provide heterogeneous electrode surfaces. In terms of electrode kinetics, the ET capabilities at sp^2 carbon-based materials have been extensively debated. The long-standing view was that fast ET only occurred at edge sites, defects and open ends of CNTs, although this hypothesis is not supported when subjected to the scrutiny of modern scanning probe microscopy techniques.[10,14–16,19] The

carbon electrode response can be further complicated by the presence of surface oxides or adsorbates,[16,20] time-dependent effects[14,16] and redox-dependent behavior.[14,17] Boron-doped diamond has also found significant use as an electrode material for its durability in harsh environments and biological compatibility.[18] The uptake of boron dopants into the diamond crystallographic structure is grain-dependent and results in a heterogeneously doped electrode.[21–23] Polycrystalline boron-doped diamond (pBDD) has been shown to possess facet-dependent ET behaviour due to the boron dopant densities,[22,23] and is further complicated by variations in non-diamond sp^2 carbon incorporation during synthesis particularly at grain boundaries.[18]

Heterogeneities in many electrode surface structures are widely acknowledged[24–27] but are often neglected due to complicated analysis requirements or limitations of the electrochemical technique in identifying kinetic dispersion. Furthermore, the assumption of fully overlapping diffusion zones on the voltammetric timescale is often invoked as the reason for assuming conformance to predictions for a homogenous surface.[25,28] However, the assumption of surface homogeneity and use of a theoretical model based in this faulty premise can lead to an erroneous determination of the ET kinetics.

To date, the impact of electrode heterogeneity on electrode kinetics when the oxidised and reduced forms of an electroactive couple are both soluble in solution has been described with respect to the techniques of chronoamperometry[29–31] and cyclic voltammetry (CV)[25,32–35] with the diffusion domain approximation[25,29,31,36,37] being widely implemented to describe mass transport. This approach has been used to predict the surface coverage of nanoparticle-modified electrodes where the nanoparticles and supporting electrode possess different ET rates.[25,27,38]

In this study, the technique of Fourier-transformed large amplitude alternating current voltammetry (FTACV) is introduced as a tool for the discrimination of surface heterogeneities. Significantly, all FTACV higher order harmonic data used are derived from a single experiment and hence exactly all the same electrode conditions apply unlike with direct current voltammetric (DCV) measurements where each data set is obtained at variable scan rates so that analysis is potentially complicated by experiment-to-experiment variation in the electrode condition.[39] The use of FTACV to resolve the two distinctly

different heterogeneous charge transfer kinetics (k^0 values) associated with data derived from a dual (GC + pBDD) electrode configuration for the simple one-electron $[Ru(NH_3)_6]^{3+/2+}$ redox process is demonstrated, without requiring former knowledge of the size ratios of the two electrodes or the individual ET properties. This model study reveals much higher sensitivity for the detection of surface heterogeneity by FTACV compared to traditional DCV techniques, which is principally a result of the much larger dependence of the AC harmonic currents on k^0. While carefully avoided in this study, a similar scenario is expected to apply under circumstances where overlapping in diffusion layers is present, and this study thus serves as a platform and reference for future applications of FTACV to more complicated systems.

4.3. Theory and Simulations

4.3.1. The Technique of FTACV

In the form of this technique used in this study, a sine wave is superimposed onto the direct current (DC) potential ramp used in conventional direct current cyclic voltammetry (DC CV). A Fourier-transform (FT) algorithm is then applied to convert data from the time to frequency domain to give the power spectrum. The fundamental (1^{st}) harmonic is the component that has the same frequency, *f*, as applied in the alternating current (AC) waveform while higher harmonic components have frequencies, 2*f*, 3*f*, 4*f*, etc. There is also an aperiodic DC components located near 0 Hz which resembles, but is not identical, to the conventional DC CV response. The aperiodic DC and AC harmonic components are resolved by selecting the regions of interest from the power spectrum using frequency band filtering and applying inverse FT to the selected signals and nulling the remaining signals (Figure 4.1).[40,41] FTACV data is analysed by fitting the resolved AC harmonic components in the time domain to suitable models, analogous to procedures employed in traditional DCV methods.

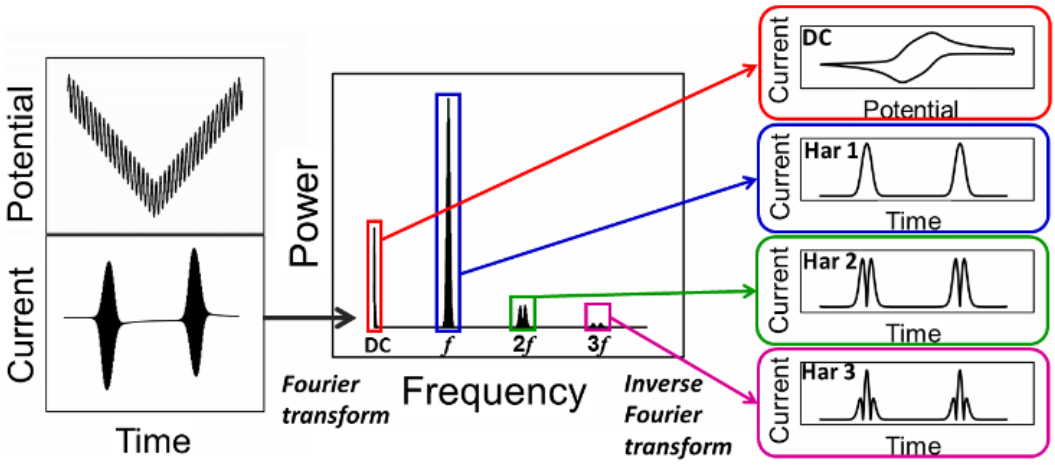

Figure 4.1 Schematic showing the potential waveform employed and experimental protocols of FTACV.

Typically, a sine wave amplitude, ΔE, value in the range of 50 to 200 mV is used to detect higher order harmonics in large amplitude FTACV. In the present study, ΔE = 160 mV was chosen for the experimental study, which provides access to 12 AC harmonics with excellent signal-to-noise ratio without excessive broadening of the current response as occurs with values of ΔE in excess of 200 mV.[42] The highest measurable harmonic is the most kinetically sensitive. The experimental frequency selected was 9.98 Hz which allows the $[Ru(NH_3)_6]^{3+/2+}$ process to be treated as reversible at the GC electrode but quasi-reversible at the pBDD electrode. The capacitance current was included in the simulations using a fourth order polynomial as previously described.[43,44]

4.3.2. FTACV Simulations

In order to probe the implications of surface heterogeneity in voltammetry, the surface of a heterogeneous electrode containing two distinctly different kinetic regimes can be modelled in terms of two regions, sharing a total area, A_{total}. The fractions of the total area of the two regions can be denoted by θ_1 and θ_2 (= $1 - \theta_1$). This chapter is concerned with comparing the voltammetric response for the reduction of a simple outer-sphere ET process at a model heterogeneous surface under both DC and AC conditions where no overlap of diffusion layers occurs. The simplest electrode configuration envisage that meets these

requirements and also generates a summed response from two distinctly different ET rates is based on two electronically coupled but well-spaced electrodes constructed from different electrode materials.

DC CV and FTACV simulations were carried out with the Monash ElectroChemistry Simulator (MECSim) program written in Fortran.[44,45] Fick's 2nd law of planar diffusion was numerically solved to obtain information on the time and spatial-dependence of the concentration of the oxidised ($[Ru(NH_3)_6]^{3+}$) and reduced ($[Ru(NH_3)_6]^{2+}$) species associated with a one-electron charge transfer process. The electrode kinetics at both electrodes were assumed to obey the Butler-Volmer relationship which describes the potential-dependence of the ET rate at the electrode/electrolyte interface as follows:

$$\text{Electrode 1: } \mathrm{Ox} + e^- \underset{k_{\mathrm{ox},1}}{\overset{k_{\mathrm{red},1}}{\rightleftharpoons}} \mathrm{Red} \quad \text{(Eq. 4.1)}$$

$$\text{Electrode 2: } \mathrm{Ox} + e^- \underset{k_{\mathrm{ox},2}}{\overset{k_{\mathrm{red},2}}{\rightleftharpoons}} \mathrm{Red} \quad \text{(Eq. 4.2)}$$

In the above equations, $k_{\mathrm{red},i}$ and $k_{\mathrm{ox},i}$ are the reduction and oxidation rate constants for each electrode material, i, given by:

$$k_{\mathrm{red},i} = k^0{}_i \exp\left[\frac{-\alpha_i F\eta}{RT}\right] \text{(Eq. 4.3)}$$

$$k_{\mathrm{ox},i} = k^0{}_i \exp\left[\frac{(1-\alpha_i) F\eta}{RT}\right] \text{(Eq. 4.4)}$$

where α_i and $k^0{}_i$ are the transfer coefficient (reasonably assumed to be 0.5 in this case) and the standard rate constant at the formal reversible potential, $E^{0\prime}$, of the redox couple. F is the Faraday constant, R is the universal constant, and T is the absolute temperature. $\eta = E(t) - E^{0\prime}$, is the overpotential and $E(t)$ is the potential applied to the electrode at time, t. In all simulations unless otherwise stated, $E^{0\prime} = 0$ V and $\alpha_i = 0.5$.

For the voltammetric experiments described herein, the potential applied to the electrode, $E(t)$, is given by the sum of the DC voltage ramp, $E_{DC}(t)$ and a sinusoidal component, $E_{AC}(t)$:

$$E(t) = E_{DC}(t) + E_{AC}(t) \quad \text{(Eq. 4.5)}$$

At any time, t, the potential is given by:

$$0 \le t \le t_s : E_{DC}(t) = E_{init} + vt \quad \text{(Eq. 4.6)}$$

$$t_s < t \le 2t_s : E_{DC}(t) = E_{init} + 2vt_s - vt \quad \text{(Eq. 4.7)}$$

$$0 \le t \le 2t_s : E_{AC}(t) = \Delta E \sin(2\pi ft) \quad \text{(Eq. 4.8)}$$

where E_{init} is the initial potential applied to the electrode, v is the DC potential scan rate, t_s is the time taken to complete a sweep in a single direction, and ΔE and f are the amplitude and frequency of the AC waveform, respectively. In this work, ΔE = 160.0 mV and f = 10.0 Hz are used for all FTACV simulations and ΔE = 0 and f = 0 are used for conventional DC CV simulations.

The current, I, is calculated from:

$$I(t) = -FA_{total}D\left[\theta_1\left(\frac{\partial c_1}{\partial x}\right)_{x=0} + \theta_2\left(\frac{\partial c_2}{\partial x}\right)_{x=0}\right] \quad \text{(Eq. 4.9)}$$

where A_{total} is the total area of the electrode, D is the diffusion coefficient, c is the concentration of the redox species and x is the spatial coordinate, with x = 0 defining the electrode surface.

4.3.3. Theory for DC CV and FTACV at a Single Electrode

The following parameters apply throughout: v = 0.1 V s^{-1}, c^0 = 1 mM, $D_{ox} = D_{red}$ = 1 × 10^{-5} cm^2 s^{-1}, $E^{0\prime}$ = 0.0 V, α = 0.5 and T = 298.2 K, ΔE = 160.0 mV and f = 10.0 Hz (or ΔE = 0 and f = 0 for conventional DC CV).

Figure 4.2(a) illustrates the simulated current density for DC CVs with k^0 = 10, 1, 0.1, 10^{-2}, 10^{-3}, 10^{-4}, and 10^{-5} cm s^{-1}. On inspection, it is seen that DC CVs with $k^0 > 5 \times 10^{-2}$ cm s^{-1} are virtually indistinguishable (reversible) at v = 0.1 V s^{-1} and give a separation in the reduction and oxidation peaks (ΔE_p values) of 56.2 mV. The voltammograms differ as expected with smaller k^0 values resulting in larger ΔE_p values, slightly diminished peak currents and changes in shape. In fact, realistically only k^0 values less than 5×10^{-2} cm s^{-1} can be accurately determined under the DC CV conditions relevant to Figure 4.2(a) from ΔE_p analysis in conjunction with the Nicholson method[46,47] or preferably by comparison of experimental and simulated data.

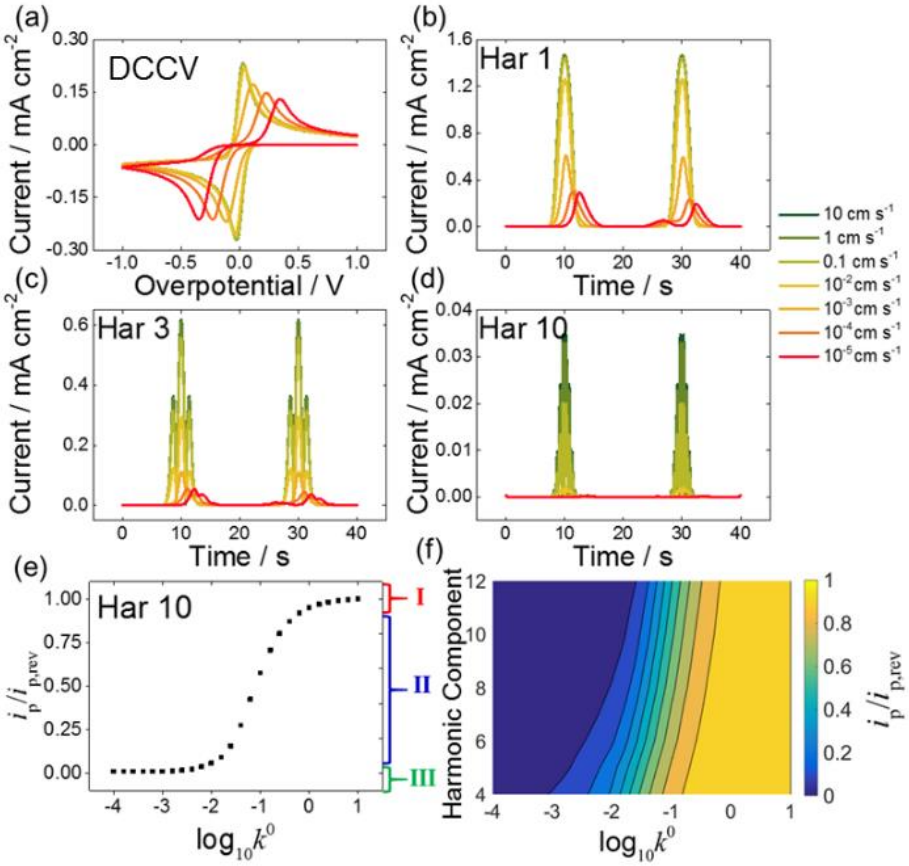

Figure 4.2 Simulation of the (a) DC CV and the (b) 1st, (c) 3rd and (d) 10th AC harmonic voltammetric response for a reduction process at a homogeneously active electrode surface having k^0 values of 10, 1, 0.1, 10^{-2}, 10^{-3}, 10^{-4} and 10^{-5} cm s^{-1}. (e) Plot of normalised peak current as a function of k^0 for the 10th AC harmonic component. (f) Surface plot of the normalised peak current as a function of k^0 for the 4th to 12th AC harmonic components. Simulation parameters are as follows: v = 0.1 V s^{-1}, c^0 = 1 mM, $D_{ox} = D_{red} = 1 \times 10^{-5}$ cm^2 s^{-1}, $E^{0\prime}$ = 0.0 V, α = 0.5 and T = 298.2 K, ΔE = 160.0 mV and f = 10.0 Hz (or ΔE = 0 and f = 0 for conventional DC CV).

Figure 4.2(b)-(d) show the simulated fundamental, 3rd and 10th AC harmonic component as a function of k^0. The FTACV simulations are carried out with identical simulation parameters as in the DC case but with ΔE = 160.0 mV and f = 10.0 Hz. In FTACV and in contrast to DC CV, the peak current magnitudes decay rapidly as k^0 becomes progressively smaller. The peak shapes also become less symmetrical with smaller k^0 values.

Figure 4.2 (e) shows how the peak current, i_p, derived from the central lobe, changes with k^0 for the 10th AC harmonic component. Three kinetic regimes with different characteristics can be identified. k^0 values which results in i_p > 90% of the reversible (k^0 = 1000 cm s^{-1}) peak current, $i_{p,rev}$, in the 10th AC harmonic, fall in Regime I (k^0 > 0.6 cm s^{-1}, in this example). At the other end of the kinetic spectrum, Regime III consists of k^0 values which results in i_p < 10% $i_{p,rev}$, for the 10th AC harmonic and hence close to zero current. In this example, k^0 < 0.02 cm s^{-1} represents Regime III. Intermediate Regime II consists of k^0 values which constitutes the most sensitive range for the determination of k^0 values. The kinetic regimes are also harmonic-dependent as shown in Figure 4.2(f) for ΔE = 160.0 mV and f = 10.0 Hz, with the sensitivity towards higher k^0 values increasing with higher order AC harmonic components and of course frequency.[48]

Importantly, the optimal kinetically sensitive range of Regime II achievable with FTACV is higher than DC CV (for the same DC potential sweep scan rate) and is tunable by changing f. Increasing ΔE also increases the accessibility of higher AC harmonic components.[49] Higher kinetic sensitivity can be achieved by increasing the scan rate in DC CV, but is accompanied by an increase in double layer charging that reduces the reliability of the measurements and requires multiple experiments.[46] Use of higher order AC harmonic components, in contrast, allows measurements to be made that are devoid of charging current and all data are obtained from a single experiment. All these advantages combined with AC current magnitudes being far more sensitive to k^0 than in a DCV case will be retained in studies considered below that are aimed at detection of kinetic dispersion arising from a heterogeneous electrode configuration.

4.3.4. Theory for DC CV and FTACV at Dual-Electrode Surfaces

Simulations at the dual-electrode configuration with no overlap of diffusion layers simply require the summation of the responses calculated for each individual electrode using the model given in the above section.

Figure 4.3(a) provides a series of simulated DC CVs based on the assumption that the total electrode surface is composed of two electrode materials having equal areas (θ_1 = θ_2 = 0.5), but exhibiting different values of k^0. Both electrodes are assumed to be sufficiently large so that mass transport can be modelled by linear diffusion to the whole electrode surface. Under these circumstances, the observed current magnitude of the dual-electrode is the weighed sum (of the individual electrode areas) of the current measured at the individual electrodes (ohmic, iR_u, effects where R_u is the uncompensated resistance, are assumed to be negligible). With all other voltammetric parameters unchanged, it is clear that the magnitude of difference in k^0 values of the two electrode materials, provided both processes are not reversible, will have a significant effect on the shape of the dual-electrode voltammograms.

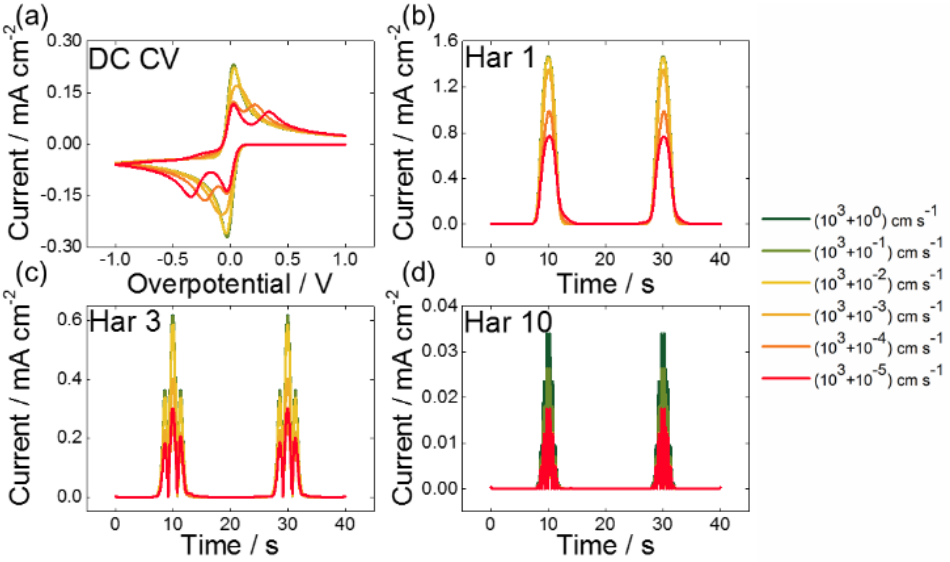

Figure 4.3 Simulation of the (a) DC CV and the (b) 1st, (c) 3rd and (d) 10th AC harmonic voltammetric response for a reduction process at a heterogeneously active electrode surface (θ_1 = θ_2 = 0.5) with k^0_1 maintained at 10^3 cm s^{-1} and k^0_2 varied (10^{-1} to 10^{-5} cm s^{-1}). See Figure 4.2 for other simulation parameters.

Under DC CV conditions, with both k^0_1 and $k^0_2 > 5 \times 10^{-2}$ cm s^{-1}, only a single process is detected with the dual-electrode with $\Delta E_p = 56.2$ mV as expected for a reversible process. Under these circumstances, no kinetic resolution of the two ET processes is observed. With small differences in k^0, i.e. $k^0_1 = 5 \times 10^{-2}$ cm s^{-1} and $k^0_2 = 10^{-3}$ cm s^{-1}, peak broadening is evident along with a slightly diminished peak current magnitude. Peak broadening under DC CV conditions is often associated with a kinetically limited process, and analysis of k^0 dependence on ΔE_p by the Nicholson method[3,46,47] would result in the underestimation of ET kinetic if the surface heterogeneity is not considered. Further increasing the difference in k^0 values ($k^0_1 > 5 \times 10^{-2}$ cm s^{-1} and $k^0_2 < 10^{-4}$ cm s^{-1}) gives rise to two well-separated processes (two reduction and two oxidation peaks are observed). The impact of the θ_1:θ_2 ratio on the DC CV response is shown in Figure 4.7 (Section 4.7.1.) .

In the case of the fundamental AC harmonic component (Figure 4.3(b)), with k^0_1 maintained at 10^3 cm s^{-1} (Regime I) and $k^0_2 < k^0_1$ is varied (10^{-1} to 10^{-5} cm s^{-1}), broadening of the peak response is detected with two well-resolved processes detected with sufficiently small k^0_2 values. Importantly, as seen in the 3th and 10th AC harmonic components displayed in Figure 4.3(c) and (d), respectively, the larger current contributions from the process with k^0_1 start to dominate the dual-electrode responses as k^0_2 values move from Regime I to III. When the process with k^0_2 lies in Regime III, it contributes little current and the AC harmonic i_p approaches predictions for a process with k^0_1 only. For the simulation parameters considered in Figure 4.3(c) and (d), Regime III corresponds to $k^0_2 <$ 0.02 cm s^{-1} for the 10th AC harmonic. In fact, the 10th AC harmonic simulations displayed in Figure 4.4 show that i_p values are directly proportional to the area of the fast (k^0_1 reversible) electrode material when $k^0_2 \leq 10^{-2}$ cm s^{-1}. Significantly, $k^0_2 = 10^{-2}$ cm s^{-1} generates a close to reversible process on the DC CV timescale (0.1 V s^{-1}) and also because no equivalent Regime III is ever available, the slower process cannot be easily discriminated against under any conditions by DCV techniques.

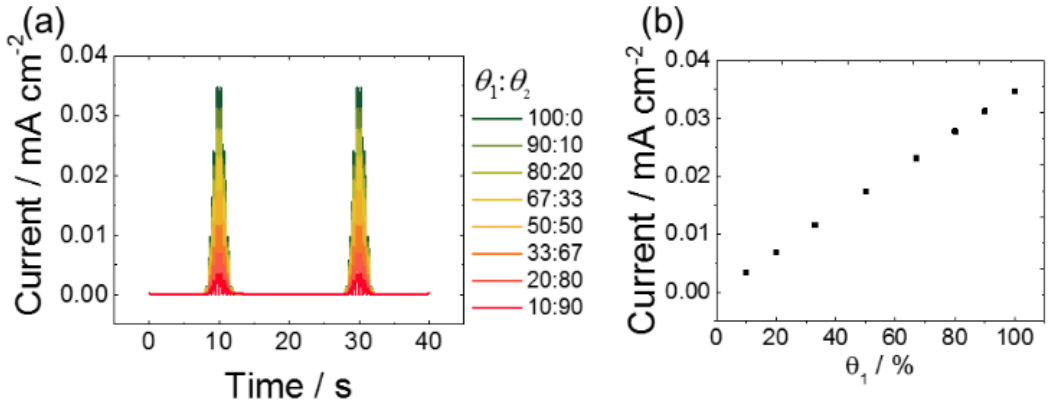

Figure 4.4 (a) Simulated 10th AC harmonic component for a reduction process at a heterogeneously active electrode surface as a function of θ_1:θ_2 ratio with k^0_1 = 1000 cm s^{-1} (Regime I) and k^0_2 = 10^{-2} cm s^{-1} (Regime III). (b) Simulated 10th AC harmonic i_p as a function of θ_1. See Figure 4.2 for other simulation parameters.

The simulated voltammograms described above assume diffusion to the electrode is at the linear limit, with no overlap of the diffusion regimes of the two electrode materials. Under the experimental conditions employed, this is valid for electrode radii ≥ 10 μm with the 6th and higher AC harmonic components (see Section 4.7.2., Figure 4.8). Furthermore, the overall uncompensated resistance in the dual-electrode system is considered to be negligible. Although, this analysis represents the simplest possible heterogeneous electrochemical configuration available, it demonstrates the significant differences in the capabilities of detection of such phenomena by the DCV and FTACV methods. Importantly, the major difference is that the magnitude of AC currents in the higher harmonic components are extremely sensitive to kinetics and this factor facilitates resolution of k^0 and effective area parameters as demonstrated experimentally below.

4.4. Experimental

4.4.1. Chemicals

Hexaammineruthenium (III) chloride ($Ru(NH_3)_6Cl_3$; 98 %) and potassium chloride (KCl; 99 %) were purchased from Sigma-Aldrich and used as received. All solutions were prepared using water purified with a Millipore Milli-Q purification system (resistivity ca. 18.2 MΩ cm at 25 ^oC). 1 M KCl was added as supporting electrolyte. All voltammetric experiments were undertaken at 25 ± 1 °C and the solutions were deaerated with N_2 for at least 10 mins prior to undertaking electrochemical measurements.

4.4.2. Electrode Materials

A GC (0.5 mm-radius) macrodisk working electrode was obtained from CH Instruments, Texas. The oxygen-terminated pBDD electrode (0.5 mm-radius) was provided by Element 6, Harwell, UK. The in-house procedure for micromachining and glass sealing pBDD macrodisk electrodes is described in detail elsewhere.[3,17] Prior to use, all working electrodes were initially polished with an aqueous alumina slurry (0.05 μm) on a soft microfiber polishing pad (MicroCloth, Buehler Ltd.) and then subsequently on a clean wet microfiber pad, carefully cleaned with water, sonicated for a few seconds and dried under nitrogen to produce a clean reproducible electrode surface. Ag/AgCl (1 M KCl) and a Pt wire were used as the reference and counter electrodes, respectively.

4.4.3. FTACV Instrumentation

A CHI 760E electrochemical workstation (CH Instruments Inc.) and home-built instrumentation[40] were used for the DC CV and FTACV experiments, respectively. All FTACV experiments were recorded using a sine wave perturbation of amplitude, ΔE = 160.0 mV and frequency, f = 9.98 Hz. The Fourier-transformed resolved higher order harmonic data was quantitatively modelled using the Monash Electrochemistry Simulator (www.garethkennedy.net/MECSim).

4.5. Results and Discussion

4.5.1. DC CV with Individual and Dual (GC + pBDD) Electrode Configurations

Experimentally, studies on the one-electron reduction of $[Ru(NH_3)_6]^{3+}$ to $[Ru(NH_3)_6]^{2+}$ are considered in highly conducting 1 M KCl aqueous electrolyte. The ET kinetics for the $[Ru(NH_3)_6]^{3+/2+}$ redox couple are highly facile at conventional metallic electrode materials with $k^0_{Pt} = 17.0 \pm 0.9$ cm s^{-1} at platinum[1,2] and $k^0_{Au} = 13.5 \pm 2.0$ cm s^{-1} at gold[2] determined from tip-voltammetry scanning electrochemical microscopy (SECM). Furthermore, pipette-based techniques such as scanning electrochemical cell microscopy applied at carbon-based electrode materials such as highly oriented pyrolytic graphite (HOPG) and single-walled carbon nanotubes (SWCNTs) has shown $k^0_{HOPG} > 0.5$ cm s^{-1} (Ref [50]) and $k^0_{SWCNT} = 7 \pm 2$ cm s^{-1} (metallic)[13] and 4 ± 2 cm s^{-1} (semi-conducting).[13] Intermittent-contact SECM experiments have also revealed two distinct regions of ET activity at pBDD electrodes, associate with the high and low boron-doped regions resulting in $k^0_{pBDD} = 3.3 \times 10^{-2}$ cm s^{-1} and 0.7×10^{-2} cm s^{-1}, repectively.[22] $k^0_{pBDD} = 1.5 \times 10^{-2}$ cm s^{-1} has also been measured using FTACV which is considered to represent an overall (average) value for the entire electrode surface.[48]

Figure 4.12 (Section 4.7.4.) shows DC CVs for the reduction of $[Ru(NH_3)_6]^{3+}$ in an aqueous solution containing 1 M KCl as supporting electrolyte where both the GC and pBDD electrodes have the same size (1 mm-dia. ($\theta_1 = \theta_2 = 0.5$)). The slightly different DC CV shapes in the experimental responses at the individual GC and pBDD electrodes arise from differences in capacitance and hence double layer capacitance (C_{dl}) background currents of the two materials ($C_{dl,GC} \sim 25$ μF cm^{-2} and $C_{dl,pBDD} \sim 5$ μF cm^{-2}). Under the DC CV conditions employed, the $[Ru(NH_3)_6]^{3+/2+}$ process is found to be essentially reversible ($\Delta E_p = 62 \pm 2$ mV for all v values employed) at the GC electrode (Figure 4.9) and quasi-reversible (ΔE_p increases from 73 mV at 0.05 V s^{-1} to 93 mV at 10 V s^{-1}) at the pBDD electrode (Figure 4.10). The ΔE_p data corresponds to $k^0_{GC} \geq 0.14$ cm s^{-1} and $k^0_{pBDD} = 0.02$ cm s^{-1} when determined from the Nicholson method[46,47,51] which is in good agreement with literature.[1,2,13,22,48,50]

As expected, the dual (GC + pBDD) electrode current values are equal to the sum of those obtained at the individual electrodes (Figure 4.12).[52] Note that this is only expected under the condition of negligible ohmic drop effects, as applies in this study where $R_\Omega \leq$ 20 Ω (high supporting electrolyte concentration in aqueous media).

4.5.2. FTACV with Individual and Dual (GC + pBDD) Electrode Configurations

FTACV was applied to the $[Ru(NH_3)_6]^{3+/2+}$ redox process at individual GC and pBDD electrodes using a sine wave perturbation of ΔE = 160.0 mV and f = 9.98 Hz. $E^{0\prime}$ = -0.197 V vs. Ag/AgCl (1 M KCl) was determined from the potential of the current minima and maxima of the central region of the even and odd harmonics, respectively. Excellent agreement between experimental data at the GC electrode and simulated data, for what can be regarded as a reversible process on the FTACV timescale used, is shown for the 1st to 12th AC harmonic components in Figure 4.11 (Section 4.7.5.). In this study, the upper kinetic limit of detection is reasonably defined as the k^0 value at which the major peak current magnitude of the highest (12th) harmonic examined is 90 % of that predicted for a reversible process, which gives $k^0_{GC} \geq 0.6$ cm s^{-1}.

Comparison between experimental and simulated data for the quasi-reversible $[Ru(NH_3)_6]^{3+/2+}$ process at pBDD is displayed in Figure 4.14 (see SI, Section 4.7.5.) leads to the conclusion that $k^0_{pBDD} = 0.026$ cm s^{-1}. At this electrode surface, experimental currents are well removed from those predicted for the reversible case. Under the experimental conditions considered herein, $k^0_{pBDD} = 0.026$ cm s^{-1} falls into Regime III with respect to the 12th AC harmonic, whereas under the same experimental conditions, the behavior at GC lies in Regime I for this harmonic.

The least squares correlation, Ψ, is also reported to quantify the agreement between experimental and simulated data and is given by:

$$\Psi = 1 - \left[\frac{1}{H} \left(\sum_{h=1}^{H} \sqrt{\frac{\sum_{i=1}^{N} \left[(f_h^{exp}(x_i) - f_h^{sim}(x_i))^2 \right]}{\sum_{i=1}^{N} f_h^{exp}(x_i)^2}} \right) \right] \quad \text{(Eq. 4.10)}$$

where h is the number of the AC harmonic component, H is the total number of AC harmonic components considered and $f_h^{exp}(x_i)$ and $f_h^{sim}(x_i)$ are the experimental and simulated functions in the corresponding AC harmonic, respectively and N is the number of data points.

Results from FTACV experiments for the $[Ru(NH_3)_6]^{3+/2+}$ process when measured at a dual (GC + pBDD) electrode ($\theta_1 = \theta_2 = 0.5$) configuration, are compared to those derived from the individual GC and pBDD electrodes in Figure 4.5, in the total current vs. time and 1st and 12th AC harmonic current components formats. In the fundamental harmonic (Figure 4.5(b)), significant variation is detected in the GC (much larger) and pBDD (much smaller) non-faradaic background current regions. As in the DC CV data (see above), this arises from the substantial difference in the double layer capacitances. Significantly, the faradaic current measured at the GC electrode in the 12th AC harmonic component is very much larger than the essentially zero value found at the pBDD electrode even though both electrodes have the same area (Figure 4.5(c)). This is expected on the basis of the much slower kinetics at pBDD compared to GC electrodes and the strong dependence of current magnitudes on k^0 in FTACV. Furthermore, the 12th AC harmonic component is devoid of the background current.

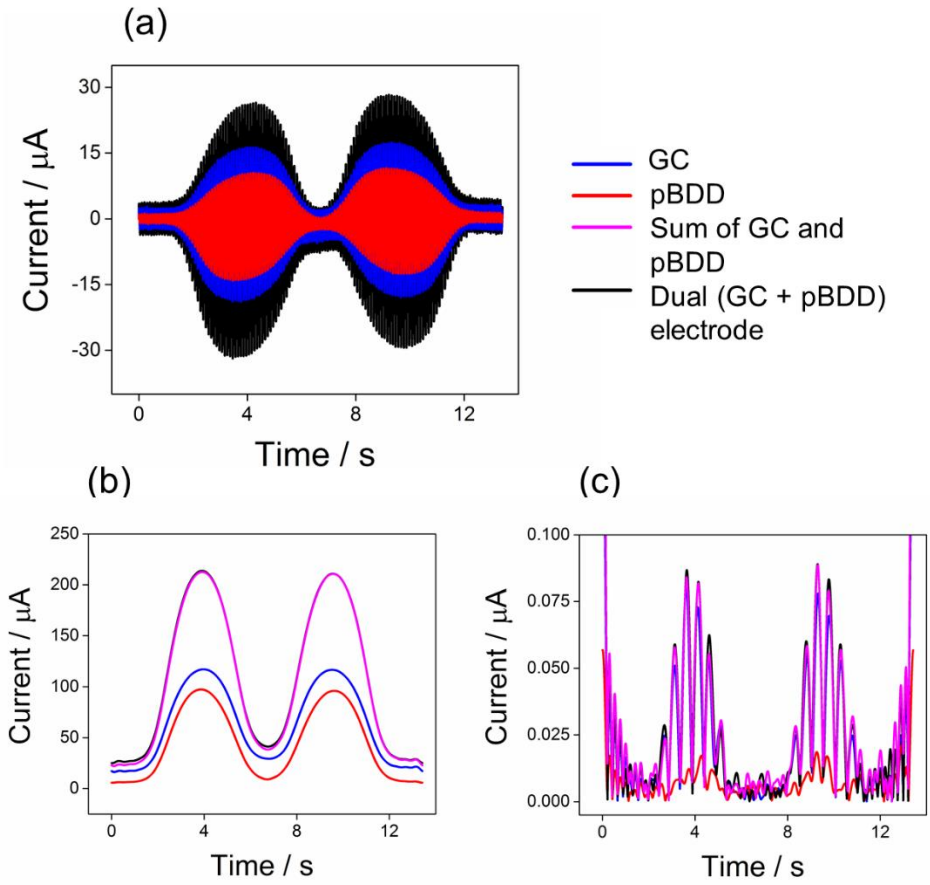

Figure 4.5 (a) Plot of total current vs. time, (b) 1st and (c) 12th AC harmonic component curves for the reduction of 1 mM $[Ru(NH_3)_6]^{3+}$ in 1 M KCl aqueous solution using a GC (blue), pBDD (red) and dual (GC + pBDD) electrode (black). The magenta lines represent the sum of the current responses from the individual GC and pBDD electrodes. Instrumentally set parameters are as follows: v = 0.09 V s^{-1}, ΔE = 160.0 mV and f = 9.98 Hz.

It is also noted that in the absence of any influences of ohmic drop, as applies in these experiments, the dual-electrode displays current values for both double layer capacitance and faradaic currents equal to the sum of those from the individual GC and pBDD electrodes. All the above observations imply it should be far easier to deconvolve the voltammetric response from a heterogeneous surface into those obtained from the individual components in terms of rate constants and relative electrode areas by analysis of the FTACV harmonic behaviour than would be the case using DCV methods.

4.5.3. Deconvolution of Individual Electrode Responses Derived from the Dual (GC + pBDD) Electrode Configuration

The following protocol can be easily applied to accurately determine the values of θ_1, θ_2, k^0_1 and k^0_2, originating from the dual heterogeneity in an electrode surface under the conditions that one process is reversible (k^0_1 is too fast to measure and lies in Regime I) and the second process is quasi-reversible with a k^0_2 value that lies in Regime III on the 12th AC harmonic timescale, as is applicable in the dual (GC + pBDD) electrode configuration. Of course, if both processes lie in Regime II or overlap of diffusion layers occur, then clearly solving the inverse problem requires considerably more sophisticated deconvolution protocols. However, it is argued on the basis of this model study that the FTACV method, with its strong dependence of current magnitude on k^0, is always likely to be superior. Future work will attempt to address other scenarios more commonly encountered in practice with the present work being essentially a proof of principle of the proposed superiority of the FTACV method.

Step 1: Parameters such as D, A and c^0 as is usually the case are assumed to be accurately known from other methods. In the scenario being considered, the experimental peak current measured in the 12th AC harmonic component is directly proportional to the area of the electrode that exhibits fast ET (large k^0_1). Therefore, θ_1 is determined when solving the inverse problem by fitting the experimental 12th AC harmonic component of the dual-electrode system to reversible kinetics (assuming $\alpha = 0.5$).

Step 2: Subtract the simulated current-time data (where k^0_1 is reversible and θ_1 is determined from Step 1) from the experimental dual-electrode current-time data. The remaining current data represents the proportion of experimental current that corresponds to the electrode surface that exhibits slower ET kinetics (k^0_2) with $\theta_2 = 1 - \theta_1$.

Step3: Apply FTACV procedures to the residual experimental currents and estimate k^0_2 through theory-experimental comparison.

Figure 4.6 illustrates the application of the analysis protocol summarised above to elucidate the kinetic (k^0_1, k^0_2) for the $[Ru(NH_3)_6]^{3+/2+}$ electrode process and relative

electrode areas (θ_1, θ_2) contributing to surface heterogeneities at the model dual-electrode system (GC and pBDD) assuming $k^0{}_1$ and $k^0{}_2$ lie within the kinetic Regimes I and III, respectively, in the highest achievable AC harmonic components (12th, in this case). In this exercise, values of $D_{ox} = D_{red} = 6.8 \times 10^{-6}$ cm^2 s^{-1} for $[Ru(NH_3)_6]^{3+}$ and $[Ru(NH_3)_6]^{2+}$, respectively, were taken from Ref[48] , A is known to be 0.0157 cm^2 and T = 298.2 K. Other simulation parameters: α = 0.5 (reasonable assumed), along with instrumentally set parameters such as v = 0.09 V s^{-1}, ΔE = 160.0 mV and f = 9.98 Hz.

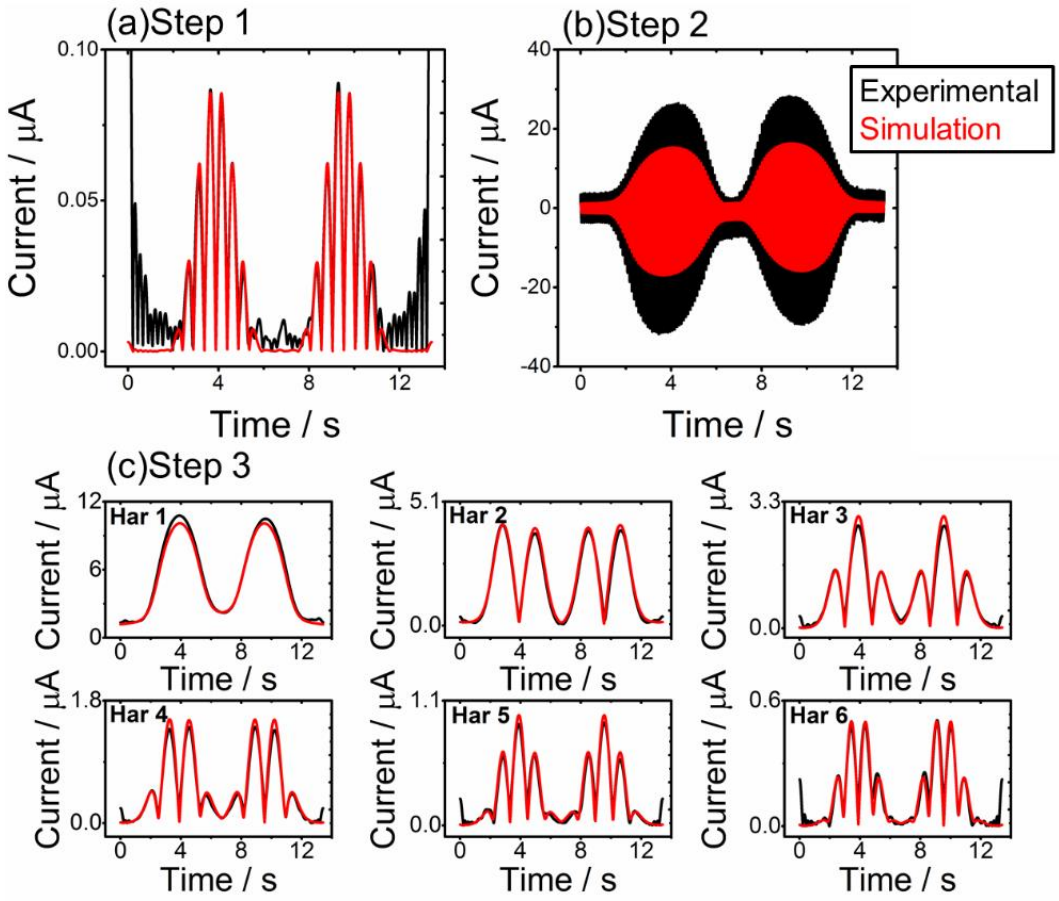

Figure 4.6 (a) Step 1, (b) Step 2 and (c) Step 3 of the FTACV protocol to determine the electrode size ratio (θ_1: θ_2) and the value of $k^0{}_2$ for the $[Ru(NH_3)_6]^{3+/2+}$ redox process at a dual-electrode comprising a GC and pBDD electrode. Simulation parameters are as follows: v = 0.09 V s^{-1}, c^0 = 1 mM, $D_{Ru(NH_3)_6^{3+}} = D_{Ru(NH_3)_6^{2+}} = 6.8 \times 10^{-6}$ cm^2 s^{-1}, $E^{0\prime}$ = -0.197 V, α = 0.5, T = 298.2 K, ΔE = 160.0 mV and f = 9.98 Hz and A_{total} = 0.0157 cm^2. Kinetic and size parameters derived from experimental-simulation comparisons are $k^0{}_1 > 0.6$ cm s^{-1}, $k^0{}_2 = 0.024$ cm s^{-1}, $\theta_1 = 0.487$ and $\theta_2 = 0.513$.

Figure 4.6(a) shows a theory-experimental comparison for the 12th AC harmonic component derived from the total dual-electrode current (**Step 1**). Setting k^0_1 = 1000 cm s^{-1} (reversible), and assuming no contribution from the second process, allows θ_1 to be determined as 0.487 (Ψ = 0.987) versus the known values of 0.50. Next, the simulated current data calculated for the reversible process is subtracted from the total dual-electrode current data (**Step 2**) as shown in Figure 4.6(b). The residual current data is subjected to FT procedures and k^0_2 is determined with θ_2 = 0.513 using the 1st to 6th AC harmonic components in the theory-simulation comparison where k^0_2 lies in Regime II and can be confidently assigned, as discussed earlier (Figure 4.2(f)). Figure 4.6(c) (**Step 3**) shows excellent agreement between experimental (black) and simulation (red, Ψ = 0.982) for the remaining current data that represents the portion of the electrode surface that exhibits slow ET kinetics with k^0_2 = 0.024 cm s^{-1} being determined in this part of the exercise. This value is in excellent agreement with k^0_{pBDD} = 0.026 cm s^{-1} determined from the individual pBDD electrode (see Section 4.7.5., Figure 4.14).

4.6. Conclusions

The technique of FTACV has been shown to be superior to DCV for probing the impact of heterogeneous electrode surfaces on electrode kinetics, predominately because the current magnitude of the AC method is far more sensitive to k^0. Detection and quantitation relies on the ability to access a unique set of higher order AC harmonic components that are devoid of background changing currents with all data being obtained from a single FTACV experiment.

In an initial model study using the $[Ru(NH_3)_6]^{3+/2+}$ redox process, the total response from a dual-electrode system comprising a GC and pBDD electrode was successfully deconvolved to reveal k^0_{GC} > 0.6 cm s^{-1} and k^0_{pBDD} = 0.024 cm s^{-1}, as predicted from literature[22,48] and measurements on the individual electrodes. Even though the analysis procedure described herein applies to a highly-simplified example, the general principle has been established for solving of the inverse problem for cases where overlap of diffusion layers and other complications will be more tractable using AC rather than DC methods of

voltammetry. Cases of interest in future work will involve studies in ionic liquids at heterogeneous carbon electrode where diffusion coefficient values of the order of 10^{-8} cm^2 s^{-1} will be encountered. Under these circumstances, greatly diminished overlap of diffusion layers of the neighbouring active sites, will occur on the typical voltammetric timescale and detection of the impact of surface heterogeneities could be commonly expected at, say, pBDD electrodes or even polycrystalline metal electrodes and at array electrodes where regions of activity and spacing of electrodes can be expected to vary the electrochemical response significantly.

4.7. Supporting Information

4.7.1. Effect of ϑ_1:ϑ_2 on Cyclic Voltammetry

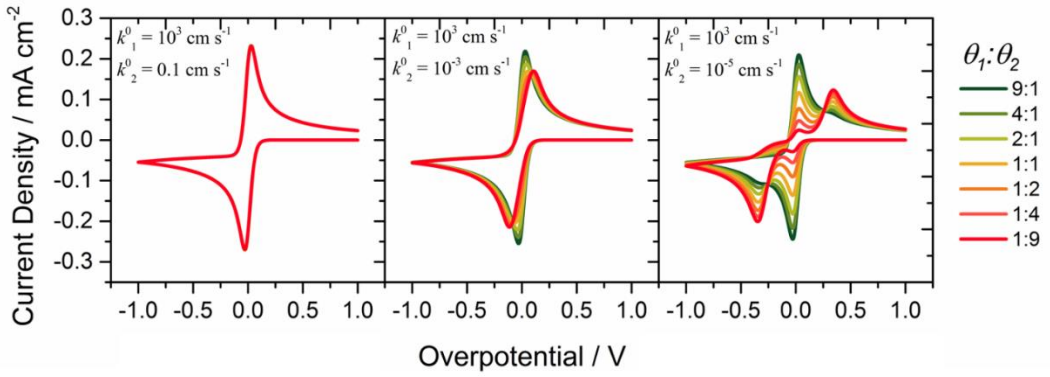

Figure 4.7 Simulated DC CV for a reduction process at a heterogeneously active electrode (containing two distinctly different kinetic regimes, k^0_1 and k^0_2) as a function of the fractional ratio of the areas of the two regions (θ_1:θ_2). Simulation parameters are as follows: v = 0.1 V s^{-1}, c^0 = 1 mM, D_{ox} = D_{red} = 1 × 10^{-5} cm^2 s^{-1}, $E^{0\prime}$ = 0.0 V, α = 0.5 and T = 298.2 K.

4.7.2. FTACV Conditions for Planar Diffusion

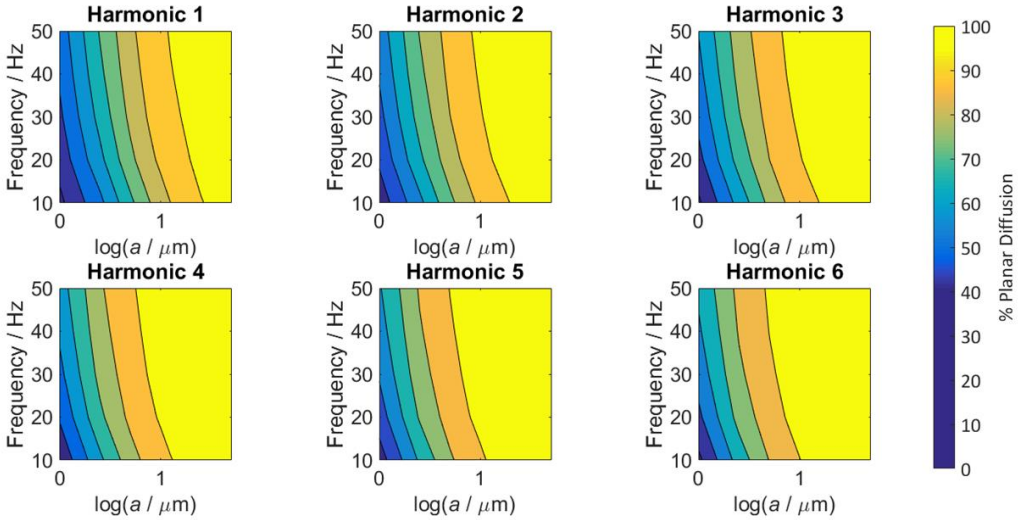

Figure 4.8 Simulated 1st to 6th AC harmonic components showing how the peak currents deviate from a planar diffusion response as a function of frequency, f and electrode radii, a. Other simulation parameters include: v = 0.1 V s^{-1}, c^0 = 1 mM, D_{ox} = D_{red} = 1 × 10^{-5} cm^2 s^{-1}, $E^{0'}$ = 0.0 V, α = 0.5, T = 298.2 K and ΔE = 160.0 mV.

Fourier-transformed large amplitude alternating current voltammetry (FTACV) simulations carried out in the Monash ElectroChemistry Simulator (MECSim) comprise the solution of Fick's 2nd Law for planar diffusion given by:

$$\frac{\partial c}{\partial t} = D\left(\frac{\partial^2 c}{\partial x^2}\right) \quad \text{(Eq. 4.11)}$$

where c is the concentration, t is the time, D is the diffusion coefficient and x is the spatial coordinate.

This approximation is valid when the electrode of interest is of an order of magnitude larger than the diffusion layer thickness, $\delta \sim \sqrt{Dt}$. As the different AC harmonic components denote different voltammetric timescales, i.e. higher AC harmonics represent shorter timescale measurements, it is interesting to consider how the AC harmonic peak currents deviate from a purely planar diffusion response as the electrode size is systematically decreased such that radial diffusion effects start to contribute to the overall diffusion.

This is achieved by comparing simulations for FTACV carried out in MECSim to equivalent simulations carried out in DigiElch where the time-dependent mass transport problem is solved in cylindrical coordinates (*r*, *z*) as shown:

$$\frac{\partial c}{\partial t} = D\left(\frac{\partial^2 c}{\partial r^2} + \frac{1}{r}\frac{\partial c}{\partial r} + \frac{\partial^2 c}{\partial z^2}\right) \text{(Eq. 4.12)}$$

Figure 4.8 shows a comparison of simulated 1st to 6th AC harmonic components peak currents, i_p from MECSim (1D) and DigiSim (2D). The peak currents are reported as the percentage of the $i_{p,2D}$ that is due to planar diffusion contributions as a function of electrode radii, *a* and AC sine wave frequency, *f*.

4.7.3. DC CV at Individual GC and pBDD Electrodes

DC CVs for the $[Ru(NH_3)_6]^{3+/2+}$ redox process at a glassy carbon (GC) electrode shows reversible behaviour and gave a half-wave potential, $E_{1/2}$ = -0.196 ± 0.001 V vs. Ag/AgCl (1 M KCl) as shown in Figure 4.9 . The linear relationship (R^2 = 0.999) between the reduction peak current, i_p and the square root of the potential scan rate, $v^{1/2}$ is indicative of a diffusion-controlled reversible process (Figure 4.9(b)) and is further reinforced by a separation in the reduction and oxidation peak potential, ΔE_p = 62 ± 2 mV for all *v* considered (Figure 4.9(c)).

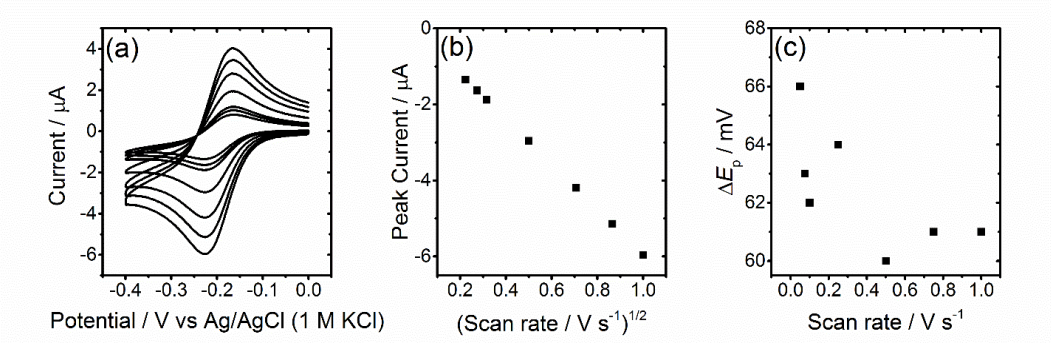

Figure 4.9 (a) DC CV for the reduction of 1 mM $[Ru(NH_3)_6]^{3+}$ (1 M KCl aq.) at a GC electrode (1 mm-dia.) with v = 0.05−1.0 V s^{-1}. (b) Plot of i_p against $v^{1/2}$. (c) Plot of ΔE_p against v.

DC CVs for the $[Ru(NH_3)_6]^{3+/2+}$ redox process at a polycrystalline boron doped diamond (pBDD) electrode is shown in Figure 4.10(a). Quasi-reversible behaviour is observed as ΔE_p increases from 73.0 mV at 0.05 V s^{-1} to 93.0 mV at 10 V s^{-1} (Figure 4.10 (c)).

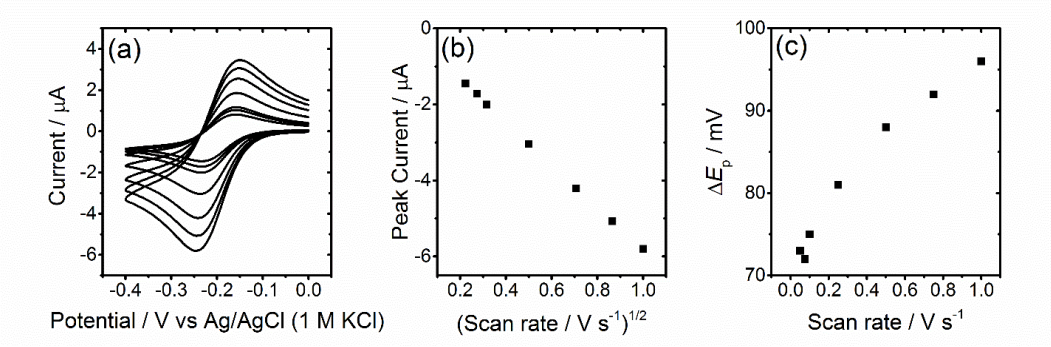

Figure 4.10 (a) DC CV for the reduction of 1 mM $[Ru(NH_3)_6]^{3+}$ (1 M KCl aq.) at a pBDD electrode (1 mm-dia.) with v = 0.05−1.0 V s^{-1}. (b) Plot of i_p against $v^{1/2}$. (c) Plot of ΔE_p against v.

4.7.4. DC CV at a Dual (GC + pBDD) Electrode

DC CVs for the $[Ru(NH_3)_6]^{3+/2+}$ redox process at a dual (GC + pBDD) electrode is shown in Figure 4.11(a). The combined currents from the GC (which shows reversible behaviour) and pBDD (which displays quasi-reversible behaviour) electrodes result in an overall quasi-reversible behaviour at the dual-electrode with no indication of surface heterogeneities.

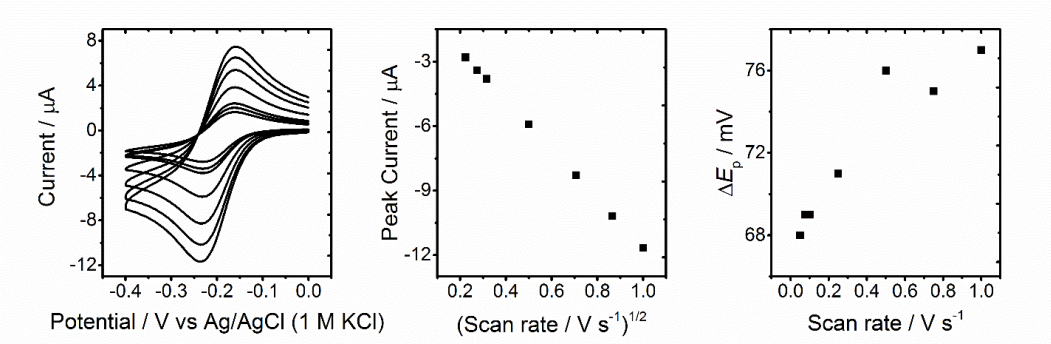

Figure 4.11 (a) DC CV for the reduction of 1.0 mM $[Ru(NH_3)_6]^{3+}$ (1.0 M KCl aq.) at a dual GC + pBDD electrode at v = 0.05−1.0 V s^{-1}. (b) Plot of i_p against $v^{1/2}$. (c) Plot of ΔE_p against v.

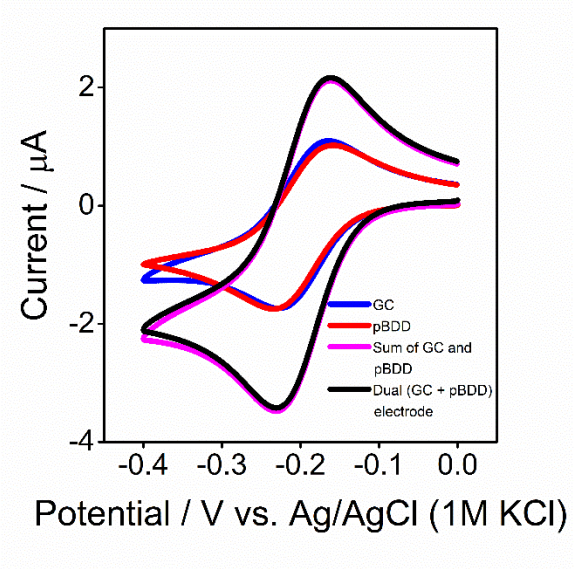

Figure 4.12 DC CV for the reduction of 1 mM $[Ru(NH_3)_6]^{3+}$ in 1 M KCl aqueous solution with v = 0.1 V s^{-1} using a GC (blue) and pBDD (red) electrode compared to a dual (GC + pBDD) electrode (black) and the sum of the individual electrodes (magenta).

4.7.5. FTACV at Individual GC and pBDD Electrodes

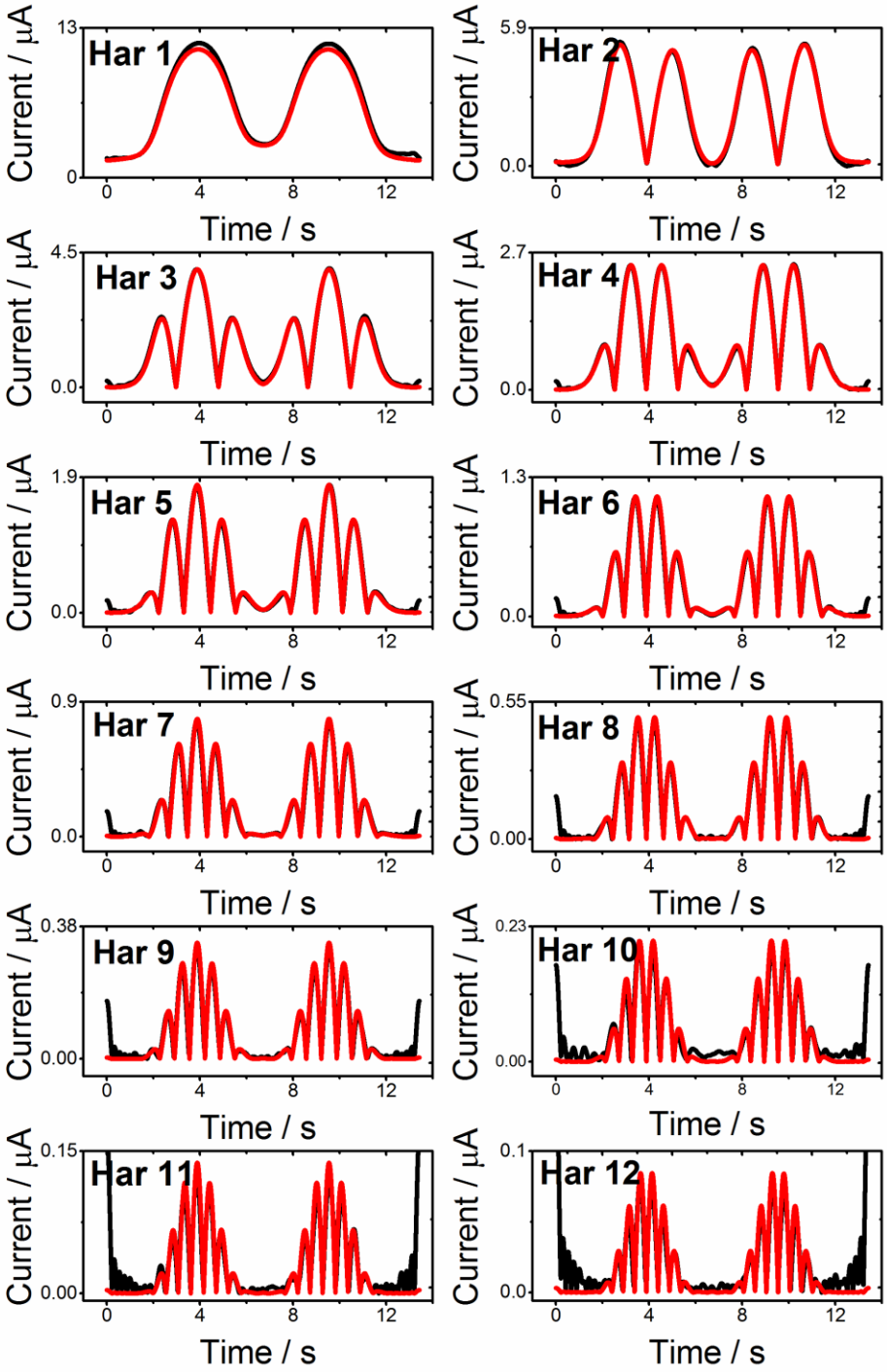

Figure 4.13 Comparison of experimental (black) and simulated (red, $\Psi = 0.992$) FTACV curves (1st to 12th harmonic) for the one-electron reduction of 1.0 mM $[Ru(NH_3)_6]^{3+}$ (1 M KCl aq.) at a GC macroelectrode. Simulation parameters: $k^0 = 1000$ cm s^{-1} (reversible), $\alpha = 0.5$, $R_\Omega = 30$ Ω, $A = 0.00785$ cm^2, $f = 9.98$ Hz, $\Delta E = 160.0$ mV, $v = 0.09$ V s^{-1} and $D_{Ru(NH_3)_6^{3+}} = D_{Ru(NH_3)_6^{2+}} = 6.8 \times 10^{-6}$ cm^2 s^{-1}.

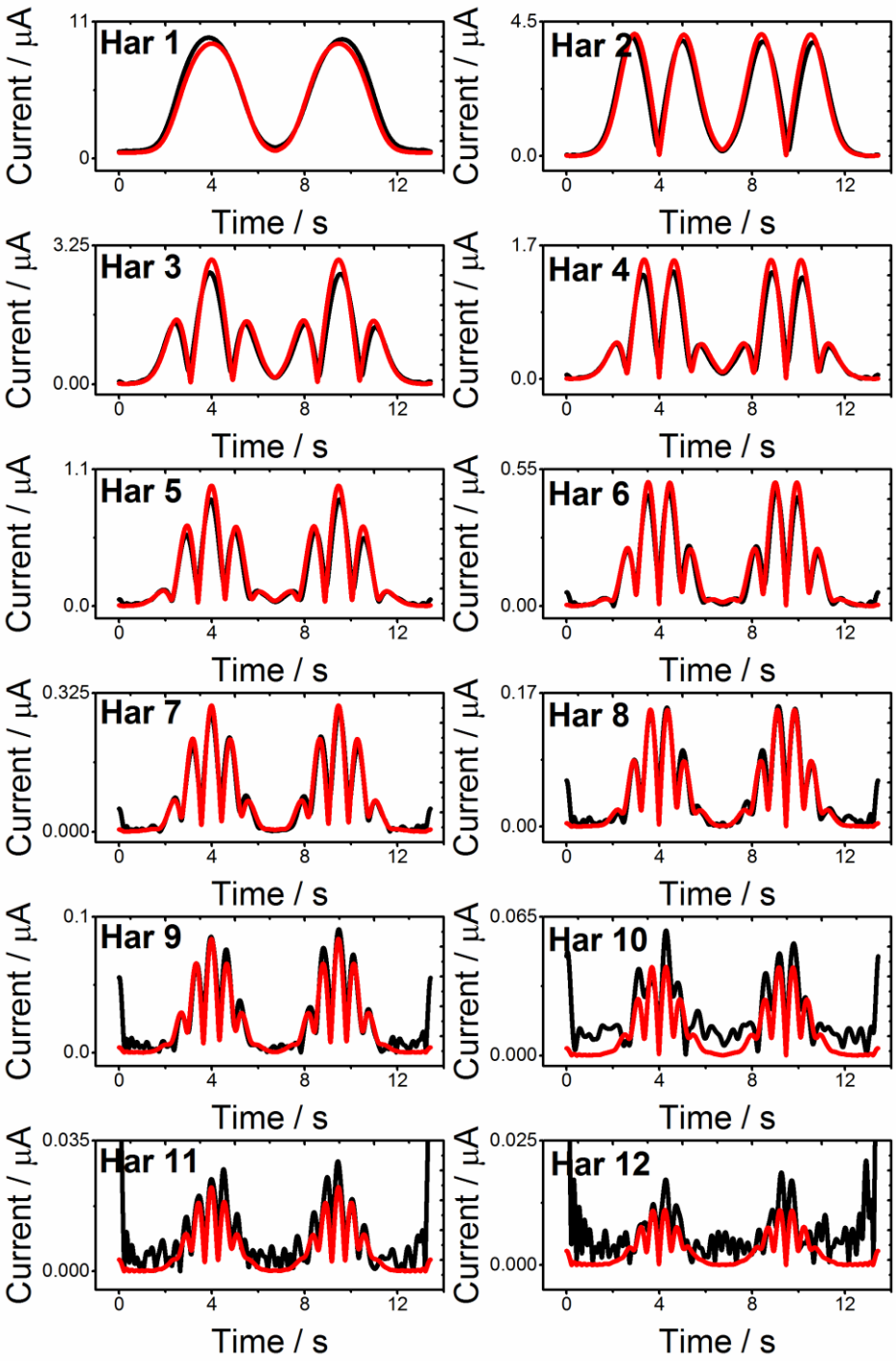

Figure 4.14 Comparison of experimental (black) and simulated (red, $\Psi = 0.932$) FTACV curves (1st to 12th harmonic) for the one-electron reduction of 1.0 mM $[Ru(NH_3)_6]^{3+}$ (1 M KCl aq.) at a pBDD macroelectrode. Simulation parameters: $k^0 = 0.026$ cm s^{-1}, $\alpha = 0.5$, $R_\Omega = 20$ Ω, $A = 0.00785$ cm^2, $\Delta E = 160.0$ mV, $f = 9.98$ Hz, $v = 0.09$ V s^{-1} and $D_{Ru(NH_3)_6^{3+}} = D_{Ru(NH_3)_6^{2+}} = 6.8 \times 10^{-6}$ cm^2 s^{-1}.

4.8. References

(1) Sun, P.; Mirkin, M. V. *Anal. Chem.* **2006**, *78* (18), 6526–6534.

(2) Velmurugan, J.; Sun, P.; Mirkin, M. V. *J. Phys. Chem. C* **2009**, *113* (1), 459–464.

(3) Hutton, L.; Newton, M. E.; Unwin, P. R.; Macpherson, J. V. *Anal. Chem.* **2009**, *81* (3), 1023–1032.

(4) Aaronson, B. D. B.; Chen, C. H.; Li, H.; Koper, M. T. M.; Lai, S. C. S.; Unwin, P. R. *J. Am. Chem. Soc.* **2013**, *135* (10), 3873–3880.

(5) Aaronson, B. D. B.; Lai, S. C. S.; Unwin, P. R. *Langmuir* **2014**, *30* (7), 1915–1919.

(6) Benítez, G.; Vericat, C.; Tanco, S.; Lenicov, F. R.; Castez, M. F.; Vela, M. E.; Salvarezza, R. C. *Langmuir* **2004**, *20* (12), 5030–5037.

(7) Lee, L. Y. S.; Sutherland, T. C.; Rucareanu, S.; Lennox, R. B. *Langmuir* **2006**, *22* (9), 4438–4444.

(8) Murphy, J. N.; Cheng, A. K. H.; Yu, H.; Bizzotto, D. *Society* **2009**, No. 14, 4042–4050.

(9) Eckermann, A. L.; Feld, D. J.; Shaw, J. A.; Meade, T. J. *Coord. Chem. Rev.* **2010**, *254* (15–16), 1769–1802.

(10) Patel, A. N.; Tan, S.-y.; Miller, T. S.; Macpherson, J. V; Unwin, P. R. *Anal. Chem.* **2013**, *85* (24), 11755–11764.

(11) Dumitrescu, I.; Unwin, P. R.; Macpherson, J. V. *Chem. Commun.* **2009**, *7345* (45), 6886.

(12) Byers, J. C.; Güell, A. G.; Unwin, P. R. *J. Am. Chem. Soc.* **2014**, *136* (32), 11252–11255.

(13) Güell, A. G.; Meadows, K. E.; Dudin, P. V; Ebejer, N.; Macpherson, J. V; Unwin, P. R. *Nano Lett.* **2014**, *14* (1), 220–224.

(14) Güell, A. G.; Cuharuc, A. S.; Kim, Y.; Zhang, G.; Tan, S. -y.; Ebejer, N.; Unwin, P. R. *ACS Nano* **2015**, *9* (4), 3558–3571.

(15) Unwin, P. R.; Güell, A. G.; Zhang, G. *Acc. Chem. Res.* **2016**, *49* (9), 2041–2048.

(16) Patel, A. N.; Collignon, M. G.; O'Connell, M. A.; Hung, W. O. Y.; McKelvey, K.; Macpherson, J. V.; Unwin, P. R. *J. Am. Chem. Soc.* **2012**, *134* (49), 20117–20130.

(17) Hutton, L. A.; Iacobini, J. G.; Bitziou, E.; Channon, R. B.; Newton, M. E.; Macpherson, J. V. *Anal. Chem.* **2013**, *85* (15), 7230–7240.

(18) Macpherson, J. V. *Phys. Chem. Chem. Phys.* **2015**, *17* (5), 2935–2949.

(19) Lhenry, S.; Leroux, Y. R.; Hapiot, P. *Anal. Chem.* **2012**, *84* (17), 7518–7524.

(20) McCreery, R. L. *Chem. Rev.* **2008**, *108* (7), 2646–2687.

(21) Wilson, N. R.; Clewes, S. L.; Newton, M. E.; Unwin, P. R.; Macpherson, J. V. *J. Phys.*

Chem. B **2006**, *110* (11), 5639–5646.

(22) Patten, H. V.; Meadows, K. E.; Hutton, L. A.; Iacobini, J. G.; Battistel, D.; McKelvey, K.; Colburn, A. W.; Newton, M. E.; Macpherson, J. V.; Unwin, P. R. *Angew. Chem. Int. Ed.* **2012**, *51* (28), 7002–7006.

(23) Tomlinson, L. I.; Patten, H. V.; Green, B. L.; Iacobini, J.; Meadows, K. E.; McKelvey, K.; Unwin, P. R.; Newton, M. E.; Macpherson, J. V. *Electroanalysis* **2016**, 1–7.

(24) Belding, S. R.; Dickinson, E. J. F.; Compton, R. G. *J. Phys. Chem. C* **2009**, *113* (25), 11149–11156.

(25) Davies, T. J.; Banks, C. E.; Compton, R. G. *J. Solid State Electrochem.* **2005**, *9* (12), 797–808.

(26) Davies, T. J.; Compton, R. G. *J. Electroanal. Chem.* **2005**, *585*, 63–82.

(27) Streeter, I.; Baron, R.; Compton, R. G. *J. Phys. Chem. C* **2007**, *111* (45), 17008–17014.

(28) Ward, K. R.; Lawrence, N. S.; Hartshorne, R. S.; Compton, R. G. *Phys. Chem. Chem. Phys.* **2012**, *14* (20), 7264–7275.

(29) Dickinson, E. J. F.; Streeter, I.; Compton, R. G. *J. Phys. Chem. B* **2008**, *112* (13), 4059–4066.

(30) Belding, S. R.; Compton, R. G. *J. Phys. Chem. C* **2010**, *114* (18), 8309–8319.

(31) Dickinson, E. J. F.; Streeter, I.; Compton, R. G. *J. Phys. Chem. C* **2008**, *112* (31), 11637–11644.

(32) Lee, H. J.; Beriet, C.; Ferrigno, R.; Girault, H. H. *J. Electroanal. Chem.* **2001**, *502*, 138–145.

(33) Ordeig, O.; Banks, C. E.; Davies, T. J.; Campo, J. del; Muñoz, F. X.; Compton, R. G. *J. Electroanal. Chem.* **2006**, *592* (2), 126–130.

(34) Amatore, C.; Savéant, J. M.; Tessier, D. *J. Electroanal. Chem. Interfacial Electrochem.* **1983**, *147* (1–2), 39–51.

(35) Godino, N.; Borrise, X.; Muñoz, F. X.; Del Campo, F. J.; Compton, R. G. *J. Phys. Chem. C* **2009**, *113* (25), 11119–11125.

(36) Chevallier, F. G.; Compton, R. G. *Electroanalysis* **2006**, *18* (23), 2369–2374.

(37) Ordeig, O.; Banks, C. E.; Davies, T. J.; Del Campo, J.; Mas, R.; Muñoz, F. X.; Compton, R. G. *Analyst* **2006**, *131* (3), 440–445.

(38) Davies, T. J.; Moore, R. R.; Banks, C. E.; Compton, R. G. *J. Electroanal. Chem.* **2004**, *574* (1), 123–152.

(39) Guo, S.-X.; Bond, A. M.; Zhang, J. *Rev. Polarogr.* **2015**, *61* (1), 21–32.

(40) Bond, A. M.; Duffy, N. W.; Guo, S.-X.; Zhang, J.; Elton, D. *Anal. Chem.* **2005**, *77* (9), 186–

195.

(41) Bond, A. M.; Elton, D.; Guo, S.-X.; Kennedy, G. F.; Mashkina, E.; Simonov, A. N.; Zhang, J. *Electrochem. commun.* **2015**, *57*, 78–83.

(42) Gavaghan, D. J.; Myland, J. C.; Oldham, K. B. *J. Electroanal. Chem.* **2001**, *516* (1–2), 2–9.

(43) Harris, A. R.; Zhang, J.; Konash, A.; Elton, D.; Hyland, M.; Bond, A. M. *J. Solid State Electrochem.* **2008**, *12* (10), 1301–1315.

(44) Bond, A. M.; Duffy, N. W.; Elton, D. M.; Fleming, B. D. *Anal. Chem.* **2009**, *81* (21), 8801–8808.

(45) Sher, A. A.; Bond, A. M.; Gavaghan, D. J.; Harriman, K.; Feldberg, S. W.; Duffy, N. W.; Guo, S.-X.; Zhang, J. *Anal. Chem.* **2004**, *76* (21), 6214–6228.

(46) Nicholson, R. S. *Anal. Chem.* **1965**, *37* (11), 1351–1355.

(47) Zhang, G.; Cuharuc, A. S.; Güell, A. G.; Unwin, P. R. *Phys. Chem. Chem. Phys.* **2015**, *17*, 11827–11838.

(48) Bano, K.; Zhang, J.; Bond, A. M.; Unwin, P. R., Macpherson, J. V. *The Journal of Physical Chemistry C*. **2015**, 119 (22), 12464-12472.

(49) Lee, C.-Y.; Elton, D.; Brajter-Toth, A.; Bond, A. M. *Electroanalysis* **2013**, *25* (4), 931–944.

(50) Lai, S. C. S.; Patel, A. N.; McKelvey, K.; Unwin, P. R. *Angew. Chem. Int. Ed.* **2012**, *51* (22), 5405–5408.

(51) Velický, M.; Bissett, M. A.; Toth, P. S.; Patten, H. V.; Worrall, S. D.; Rodgers, A. N. J.; Hill, E. W.; Kinloch, I. A.; Novoselov, K. S.; Georgiou, T.; Britnell, L.; Dryfe, R. A. W. *Phys. Chem. Chem. Phys.* **2015**, *17* (27), 17844–17853.

(52) Lee, C.-Y.; Guo, S.-X.; Bond, A. M.; Oldham, K. B. *J. Electroanal. Chem.* **2008**, *615* (1), 1–11.

Chapter 5

Probing Electrode Heterogeneity using Fourier-Transformed Alternating Current Voltammetry: Protocol Development

In the previous chapter, Fourier-transformed large amplitude alternating current voltammetry (FTACV) data analysis strategy was developed to aid kinetic selectivity for a redox reaction complicated by electrochemical heterogeneities. The detection and quantification of a mixed kinetic response relies on the ability of FTACV to access a unique set of higher order AC harmonic components. Chapter 5 contains a manuscript and supporting information published in *Electrochimica Acta*, which describes the further development of the FTACV strategy designed in Chapter 4 and generalises its application. This is achieved by taking advantage of individual AC harmonic components which display different levels of kinetic sensitivity. The limits of detection for both electrode kinetics and domain size are also reported.

Probing Electrode Heterogeneity using Fourier-Transformed Alternating Current Voltammetry: Protocol Development

Sze-yin Tan,[†,‡] *Patrick R. Unwin,*[‡] *Julie V. Macpherson,*[‡] *Jie Zhang,*[*,†] *Alan M. Bond,*[*,†]

[†] School of Chemistry, Monash University, Clayton, Victoria 3800, Australia

[‡] Department of Chemistry, University of Warwick, Coventry CV4 7AL, United Kingdom

* jie.zhang@monash.edu and alan.bond@monash.edu

5.1. Abstract

Fourier-transformed large amplitude alternating current voltammetry (FTACV) provides a sensitive analytical tool for the discrimination of electrode reactions that are complicated by surface heterogeneity. This chapter builds on the ideas developed in Chapter 4, to show how the FTACV response at a dual-electrode system comprised of different electrode materials having different heterogeneous charge transfer ($k^0{}_1$ and $k^0{}_2$) can be resolved into its individual electrode kinetics components without prior knowledge of the electrode size ratio (θ_1:θ_2). This is possible when one process is reversible and the other is quasi-reversible, achievable by careful selection of the FTACV frequency. The applicability of the FTACV method over a wide range of electrode kinetic values and size ratios is considered for conditions under which numerical simulations based on a 1D diffusion model are adequate to describe the mass transport problem.

5.2. Introduction

Modern developments in material science has seen the advent of composite electrode materials which are highly heterogeneous in nature. Consequently, understanding the voltammetric response of electrochemically heterogeneous electrode surfaces has become

essential.[1–7] However, the analysis of electrochemical responses at heterogeneous surfaces remains challenging due to the often random nature of surface-to-surface variations.

The previous chapter reported the use of Fourier-transformed large amplitude alternating current voltammetry (FTACV)[8–12] to resolve the heterogeneous charge transfer kinetics (k^0 values) associated with the simple one-electron $[Ru(NH_3)_6]^{3+/2+}$ process derived at a dual (glassy carbon (GC) + polycrystalline boron-doped diamond (pBDD)) electrode configuration, a model system representing an electrode surface with two distinctly different activity domains[13]. The FTACV method was shown to provide advantages over techniques such as chronoamperometry[14,15] and direct current voltammetry (DCV)[2,3,16] for the elucidation of electrode kinetics at heterogeneous electrode surfaces due to the strong dependence of current magnitude on k^0 in all AC harmonics.[10,11,17] The high kinetic sensitivity of the FTACV method on k^0 allowed differences in the heterogeneous rate constants (k^0_1 and k^0_2 values) that differ by ~1-2 orders of magnitude in a dual-electrode configuration to be quantified and resolved into their individual responses. Significantly, all FTACV higher order harmonic data analysed to determined k^0 values are derived from a single experiment[10] using the same electrode. In contrast, in traditional DCV, each data set is obtained in separate experiments at different scan rates such that the computation of k^0 values is likely to be complicated by experiment-to-experiment variabilities.[18]

In this chapter, a generalised application of the FTACV model[13] reported in Chapter 4 is developed so that the standard rate constants, k^0_1 and k^0_2, and size ratios, θ_1:θ_2, of two different activity domains of a dual-electrode surface do not limit the deconvolution of the current measured into the individual components. This is achievable provided that k^0_1 is fully reversible and k^0_2 is quasi-reversible on the FTACV timescale chosen. This outcome is possible as data obtained from a single FTACV experiment can be analysed with respect to each individual AC harmonic component which display a different level of kinetic sensitivity (different measurement timescales).

The applicability of this model is experimentally demonstrated with the deconvolution of the electrochemical response from a dual (Pt + pBDD) electrode configuration for the simple one-electron $FcCH_2OH^{0/+}$ process. Conditions under which FTACV data can be treated by a 1D diffusion model are also discussed.

5.3. Theory and Simulations

The common form of the FTACV technique and the one used in this chapter comprises a sinusoidal potential waveform of amplitude, ΔE / V, and frequency, f / Hz, superimposed onto a linear potential ramp, E_{DC}. The current includes the fundamental frequency component along with the higher order components, 2f, 3f, 4f, etc. which are resolved using a Fourier transform (FT) – band filtering – inverse FT sequence of operation.[8–12] The FTACV data are then analysed by comparison of the resolved AC harmonic components to suitable models, analogous to the strategy adopted in modern DCV methods.

This chapter is concerned with the voltammetric response for the oxidation of redox-active molecules undergoing simple outer-sphere electron transfer (ET) at a model surface containing two types of active sites under both DC and AC voltammetric conditions where no overlap of diffusion layers occurs between the two regions. In order to probe the implications of electrode surface heterogeneities on the voltammetric response, a surface consisting two distinctly different kinetic properties (k^0_1, α_1, k^0_2 and α_2) can be modelled in terms of two regions which share a total surface area, $A_{total.}$ The fractions of the total area of the two regions can be related by θ_1 and θ_2 (= $1-\theta_1$). Fick's 2nd law of planar diffusion was numerically solved to obtain time and spatial-dependence information for the concentration of the reduced species associated with the charge transfer process given by:

$$\frac{\partial c_i}{\partial t} = D\left(\frac{\partial^2 c_i}{\partial x^2}\right) \quad \text{(Eq. 5.1)}$$

where D is the diffusion coefficient of the electroactive species of interest and c_i is the concentration of the electroactive species of interest at electrode material, i.

The electrode kinetics at both electrodes were assumed to obey the Butler-Volmer relationship which describes the potential-dependence of the ET rate at the electrode/electrolyte interface as follows:

$$\mathrm{Red} \underset{k_{\mathrm{red},i}}{\overset{k_{\mathrm{ox},i}}{\rightleftharpoons}} \mathrm{Ox} + e^- \quad \text{(Eq. 5.2)}$$

In the above equation, k_{ox} and k_{red} are the oxidation and reduction rate constants given by:

$$k_{ox,i} = k^0{}_i \exp\left[\frac{(1-\alpha_i)F\eta}{RT}\right] \text{(Eq. 5.3)}$$

$$k_{red,i} = k^0{}_i \exp\left[\frac{-\alpha_i F\eta}{RT}\right] \text{(Eq. 5.4)}$$

In Eq. 5.3 and 5.4, α and k^0 are the transfer coefficient (reasonably assumed to be 0.50 in this case) and the standard heterogeneous charge transfer rate constant at the formal reversible potential, $E^{0\prime}$, of the redox couple, F is the Faraday constant, R is the universal constant, T is the absolute temperature and $\eta = E(t) - E^{0\prime}$ where $E(t)$ is the potential applied to the electrode at time, t. In all simulations, $E^{0\prime} = 0$ V and $\alpha_i = 0.50$.

For the voltammetric experiments described herein, $E(t)$ is given by the sum of the DC voltage ramp, $E_{DC}(t)$ and a sinusoidal component, $E_{AC}(t)$:

$$E(t) = E_{DC}(t) + E_{AC}(t) \text{ (Eq. 5.5)}$$

At any time, t, the potential is given by:

$$0 \le t \le t_s: \; E_{DC}(t) = E_{init} + vt \quad \text{(Eq. 5.6)}$$

$$t_s < t \le 2t_s: \; E_{DC}(t) = E_{init} + 2vt_s - vt \text{ (Eq. 5.7)}$$

$$0 \le t \le 2t_s: \; E_{AC}(t) = \Delta E \sin(2\pi ft) \text{ (Eq. 5.8)}$$

where E_{init} is the initial potential applied to the electrode, v is the potential scan rate, t_s is the time taken to complete a sweep in a single direction, and ΔE and f are the amplitude and frequency of the AC waveform, respectively. In this study, $\Delta E = 80.0$ mV and $f = 10.0$ Hz are used for all FTACV simulations at a potential scan rate, v_{AC}, unless stated otherwise, or $\Delta E = 0.0$ mV and $f = 0.0$ Hz for conventional direct current cyclic voltammetry (DC CV) simulations at a potential scan rate, v_{DC}.

The current, I, is calculated from:

$$I(t) = -FD\sum_{i=1}^{n} A_i \left(\frac{\partial c_i}{\partial x}\right)_{x=0} \quad \text{(Eq. 5.9)}$$

where A is the area of the electrode, n is the number of activity regions considered (2 in this case) and x is the spatial coordinate, with $x = 0$ defining the position of the electrode surface.

Figure 5.1 displays the peak currents, i_p, derived from simulated FTACV responses at a *homogeneous electrode surface* for a series of different kinetics values ($k^0 = 10^3$, 10, 5.0, 1.0, 0.5, 0.25, 0.1 and 0.05 cm s^{-1}) as a function of frequency (different measurement timescales) at ΔE = 80.0 mV. This value of ΔE was chosen as it gives access to 12 AC harmonic components with excellent signal-to-noise ratio without excessive broadening of the current response which occurs at ΔE > 200mV.[19–21] Here, the i_p values are determined from the central lobe and the average of the two central lobes of the odd and even AC harmonics, respectively.

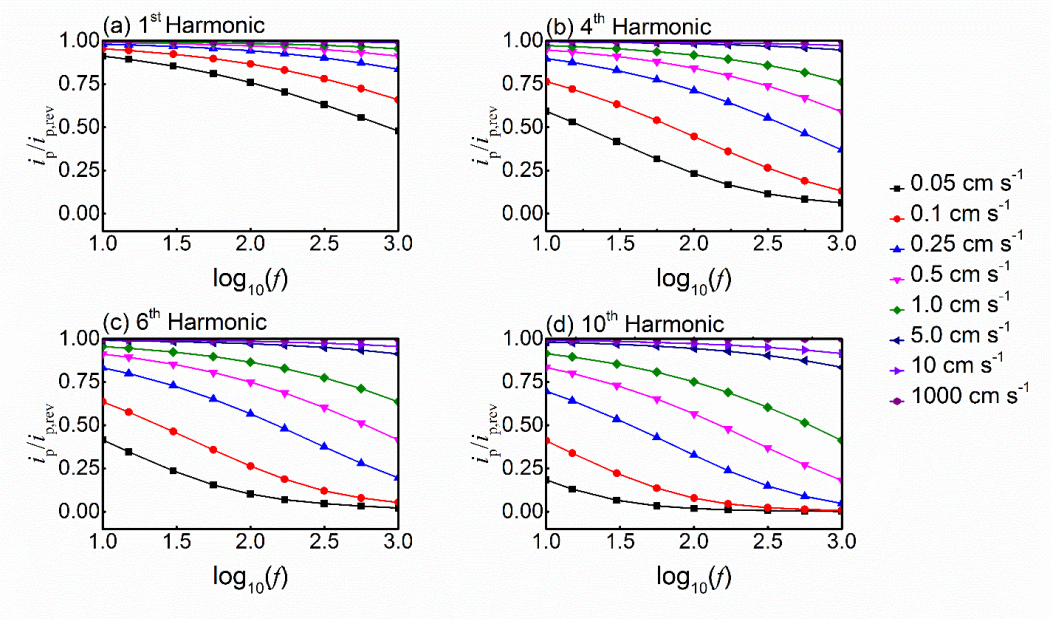

Figure 5.1 Simulated plots of $i_p/i_{p,rev}$ versus $\log_{10}f$ for the (a) 1st, (b) 4th, (c) 6th and (d) 10th AC harmonic components for an oxidation process at a homogeneous electrode surface with k^0 = 0.05, 0.1, 0.25, 0.5, 1.0, 5.0, 10 and 1000 cm s^{-1}. Simulation parameters are as follows: c^0 = 1.0 mM, D = 1.0 × 10^{-5} cm^2 s^{-1}, α = 0.50, T = 295.0 K, v_{AC} = 0.1 V s^{-1} and ΔE = 80.0 mV.

Three distinctly different kinetic regimes for each AC harmonic component can be derived from the sinusoidal data. Large k^0 values which result in large currents or $i_p > 90$ % of the value of the reversible ($k^0 = 1000$ cm s^{-1}) peak current, $i_{p,rev}$, fall into Regime I. At the slow k^0 part of the spectrum, close to zero current, Regime III is represented by small k^0 values ($i_p < 10$ % $i_{p,rev}$). The intermediate Regime II therefore consists of k^0 values which represents the kinetically sensitive range where accurate determination of k^0 values is available from simulation-experimental data comparison.[13,22] Importantly, the optimal kinetically sensitive Regime II available with FTACV comprised larger k^0 values than in direct current cyclic voltammetry (DC CV) (for the same DC scan rate, refer to Section 5.7.1., Figure 5.6, Figure 5.7 for further discussion) and is tuneable by varying *f*. For example, with reference to Figure 5.1, Regime II of harmonic 6 at $f = 10$ Hz is given by k^0 values in the range of 0.6–0.015 cm s^{-1} whereas with $f = 1000$ Hz, 6.0–0.15 cm s^{-1} represents the kinetically sensitive range. To achieve this kinetic sensitivity ($k^0 \geq 6.0$ cm s^{-1}) in DC CV, it would require a scan rate of > 500 V s^{-1} to give ΔE_p values ≥ 60 mV (distinguishable from reversible, see Figure 5.7). However, the current contributions arising from double layer charging currents are linearly dependent on *v* while faradaic currents are proportional to $v^{1/2}$ resulting in diminished faradaic-to-background current ratios at high scan rates, complicating the reliability of fast ET kinetic measurements. Further complicating these measurements will be the phenomenologically similar effects of k^0 and uncompensated resistance, which both result in increased ΔE_p values in DC CV measurements (see Section 5.7.1., Figure 5.9).

In the case of an electrochemically heterogeneous electrode surface comprising two distinctly different kinetic regions with values k^0_1 and k^0_2, assuming the electron transfer coefficient, $\alpha_1 = \alpha_2 = 0.5$ for two regions which share a total surface area, A_{total}, with the fractions of the total surface area designated by θ_1 and θ_2 (= $1-\theta_1$), it is immediately apparent that if one of the two kinetic regions fall into Regime III (zero current) where the AC current is essentially zero and the other in Regime I, the measured response will be directly proportional to the electrode area relevant to the fast (Regime I) kinetics, as considered previously.[13]

The FTACV simulations reported herein describe diffusion to an electrode in the linear limit, where no overlap of diffusion between the two electrode regions is considered. It is important to note that this assumption is valid for a wide range of electrode geometry sizes under FTACV conditions. As shown in Figure 5.11 (Section 5.7.1.), for $D = 1.0 \times 10^{-5}$ cm^2 s^{-1}, the assumption of linear diffusion is valid for electrode radii ≥ 10 μm with the 6th and higher AC harmonic components (linear diffusion constitutes ≥ 90 % of the total diffusion to the electrode surface) when the AC perturbation is given by ΔE = 80.0 mV and f = 10.0 Hz. When f is increased to 100.0 Hz, the assumption of linear diffusion is now applicable to electrode radii ≥ 3 μm.

5.3.1. Protocol for Deconvolution of a Dual-Heterogeneity FTACV Response

In this chapter, a general strategy for the deconvolution of data derived from a heterogeneous electrode, consisting of two regions with different kinetic activity, into the individual components is discussed. The protocol developed is illustrated for the case where one process is fully reversible (k^0_1 too large to be measured), and the other is quasi-reversible, having a k^0_2 value that leads to a smaller current (≤ 90 %) compared to the reversible response. In the scenario considered herein, each AC harmonic component is considered to be the sum of both processes with the fast one assigned as reversible with its response assumed to be proportional to the relevant electrode area. The slower process will display a different level of reversibility in each AC harmonic (different timescales). This allows the deconvolution of the dual-electrode response into its individual components. Parameters such as D, A_{total} and c^0 are known from independent measurements.

Step 1: The FTACV procedure is applied to the experimental current-time data to resolve it into its AC components. A high harmonic component (10th AC harmonic, in this example) can thus be fitted using a homogeneous electrode model to provide an initial estimation of the area of the electrode, A_1, that exhibits fast ET (large k^0_1). This value of A_1 will represent an ***overestimate*** but provides the best initial guess in an environment where k^0_2 contributions are smallest.

Step 2: Subtract the simulated current-time data (where k^0_1 is reversible and A_1 is the estimate value from Step 1) from the experimental dual-electrode current-time data. The residual current data provides an initial estimation of the proportion of the current associated with the quasi-reversible (slower) process.

Step 3: Apply the FTACV procedure to the residual experimental data. The calculated A_2 is from the $\theta_2 = 1 - \theta_1$ relationship and gives an initial guess as an ***underestimated*** value. An apparent harmonic-dependent k^0_2 value response will be found. However, an intermediate AC harmonic component can be selected (5^{th} AC harmonic, in this example) to give a first estimate of k^0_2. This will probably represent an ***underestimated*** value.

Step 4: Subtract the simulated current-time data (using k^0_2 and A_2 values determined from Step 3) from the experimental dual-electrode current-time data. The now residual data represents the proportion used to determine the next approximation of A_1, with k^0_1 assumed to be reversible (Step 1). Steps 1 to 4 are then repeated until the estimated values converge. The protocol is summarised in Figure 5.2.

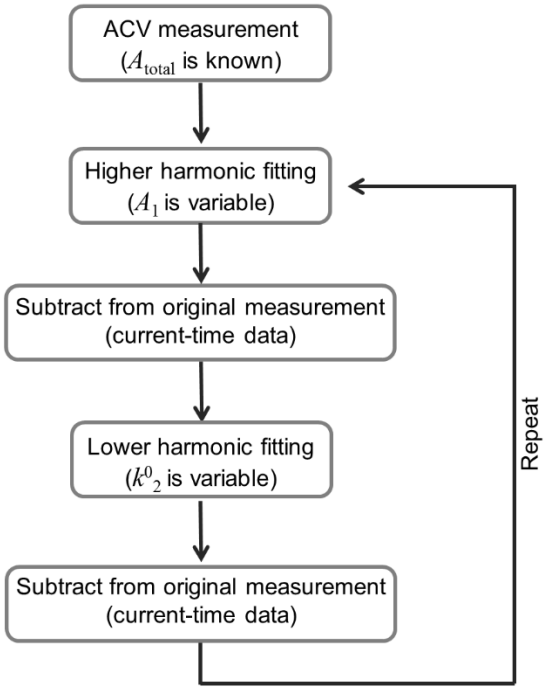

Figure 5.2 Scheme showing the protocol for the deconvolution of a dual-heterogeneity FTACV response.

5.3.2. Application to a Simulated Dual-Heterogeneity FTACV Response

The FTACV response at a dual-electrode comprising one reversible (1000 cm s^{-1}) and one quasi-reversible (0.1 cm s^{-1}) process on the AC timescale (ΔE = 80.0 mV and f = 10.0 Hz) was simulated with relative electrode areas, $\theta_1 = \theta_2 = 0.50$. Other simulation parameters included $D = 1.0 \times 10^{-5}$ cm^2 s^{-1}, v_{AC} = 0.1 V s^{-1}, α = 0.50 and T = 295.0 K. The analysis protocol was then applied to the simulated dual-electrode response to recover the kinetic (k^0_1 and k^0_2) and relative electrode area (θ_1 and θ_2) parameters associated with the individual responses. Note that the electrochemical reversibility an electron transfer reaction can be adjusted by changing the frequency of the applied sinusoidal waveform. Under the optimal condition of k^0_1 being just above the reversible limit (0.6 cm s^{-1}) and k^0_2 being just below the reversible limit (0.3 cm s^{-1}), a factor of two dispersion in this kinetic parameters is distinguishable with our protocol.

Figure 5.3(a) shows the initial (**Step 1**) comparison of the simulated 10th AC harmonic component derived from the total dual-electrode response (black) and a homogeneous model with k^0_1 set to 1000 cm s^{-1} (fully reversible) and A_1 applied as a variable (red). This gives a first estimate of θ_1 of 0.665 (versus the known value of 0.50). Next, the data calculated for the reversible process (overestimated) are subtracted from the total dual-electrode current-time data (**Step 2**) as shown in Figure 5.3(b). **Step 3** of the analysis protocol is then applied to the residual data to give the result in Figure 5.3(c). The 5th AC harmonic component of the residual dual-electrode (black) is then compared to that from a homogenous electrode model (blue) to obtain an underestimated value of k^0_2 with $\theta_2 = 0.335$ ($\theta_2 = 1-\theta_1$) and k^0_2 used as a variable to give an estimated value of 0.0715 cm s^{-1} (versus the known value of 0.1 cm s^{-1}). Next, the data for the quasi-reversible process (with the underestimated k^0_2 value) are subtracted from the total dual-electrode current-time data (**Step 4**) as shown in Figure 5.3(d). This residual current data are then subjected to the FTACV procedure. Steps 1 to 4 are repeated to obtain progressively better estimations of θ_1, θ_2 and k^0_2.

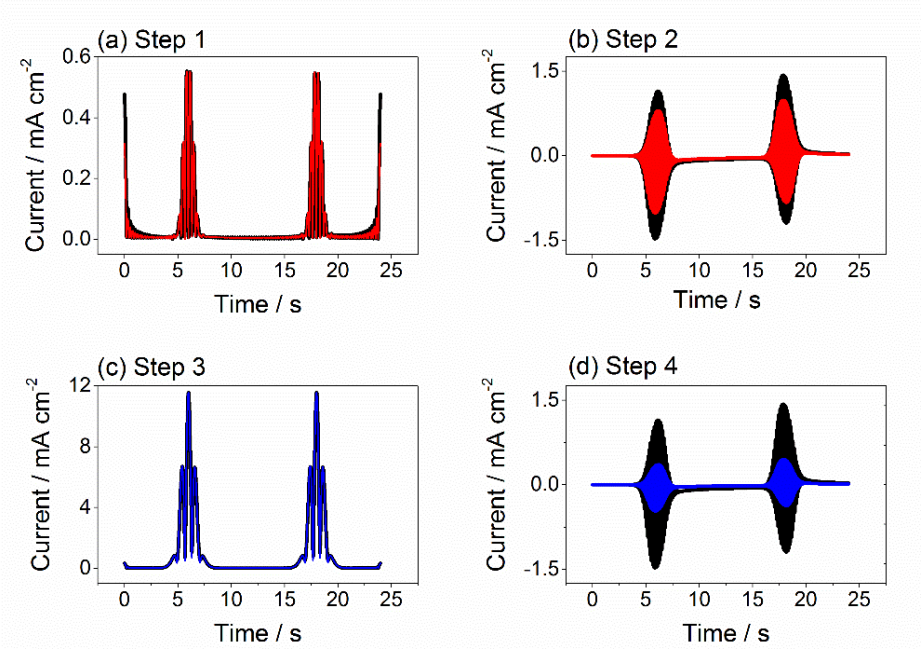

Figure 5.3 Application of Steps 1−4 of the FTACV protocol using simulated data to determine the electrode area ratio (θ_1:θ_2) and k^0_2 value at a dual-electrode configuration. Simulation parameters for the dual-electrode process (black line) are: $\theta_1 = \theta_2 = 0.50$, $k^0_1 = 1000$ cm s^{-1}, $k^0_2 = 0.10$ cm s^{-1}, $c^0 = 1.0$ mM, $D = 1.0 \times 10^{-5}$ cm^2 s^{-1}, $\alpha = 0.50$, $T = 295.0$ K, $\nu_{AC} = 0.1$ V s^{-1}, $\Delta E = 80.0$ mV and $f = 10.0$ Hz. The red lines illustrate the first estimation of $\theta_1 = 0.665$. The blue lines show the first estimate of θ_2 and k^0_2 are 0.335 and 0.0715 cm s^{-1}, respectively.

The values of θ_1 and θ_2 and k^0_2 determined using the analysis protocol described above are summarised in Table 5.1. With each protocol iteration, the values of θ_1, θ_2 and k^0_2 become closer to the known input values for the dual-electrode simulation. In this example, an estimate of $\theta_1 = 0.507$ is obtained after 10 iterations which agrees well with the known input value of 0.50 while k^0_2 is estimated to be 0.0987 cm s^{-1} versus the known value of 0.10 cm s^{-1}.

Table 5.1 Summary of data obtained using 10 iterations of the FTACV protocol applied to a simulated dual-electrode system with θ_1:θ_2 =1.0:1.0 and k^0_2 = 0.10 cm s^{-1}.

Iteration No.	θ_1	θ_2	k^0_2 / cm s^{-1}
1	0.665	0.335	0.0715
2	0.605	0.395	0.0810
3	0.571	0.429	0.0868
4	0.551	0.449	0.0900
5	0.538	0.462	0.0928
6	0.525	0.475	0.0953
7	0.518	0.482	0.0965
8	0.513	0.487	0.0975
9	0.510	0.490	0.0982
10	0.507	0.493	0.0987

The analysis protocol was also applied to other dual-electrode scenarios with individual electrode size ratios, θ_1:θ_2 = 1:9 (Case 1) and 9:1 (Case 2). Results are summarised in Table 5.3 and Table 5.4 in Section 5.7.4. Estimations of θ_1 and θ_2 values of 0.124 and 0.876 for Case 1 and 0.901 and 0.099 for Case 2 after 10 iterations and values for k^0_2 of 0.097 and 0.099 cm s^{-1}, respectively, were obtained.

These results confirm the attributes of relatively simple FTACV data analysis strategies to deconvolute a dual-heterogeneous electrochemical response without prior knowledge of the size distribution, provided that one process lies in Regime I for the highest harmonic considered, as long as mass transport can be described by linear diffusion and the uncompensated resistance, R_u is negligible. These conditions are achieved experimentally by careful selection of the AC timescale (f) and the use of highly conducting electrolyte media.

5.4. Experimental

5.4.1. Chemicals

Ferrocene methanol ($FcCH_2OH$, 97 %) and potassium chloride (KCl, 99 %) were purchased from Sigma-Aldrich and used without further purification. All solutions were prepared using water purified with a Millipore Milli-Q purification system (resistivity ca. 18.2 MΩ cm at 25 ^{0}C). 1 M KCl was added as the supporting electrolyte.

5.4.2. Electrode Materials

The Pt (0.5 mm-radius) macrodisk electrode was obtained from CH Instruments, Texas. The oxygen-terminated pBDD electrode (0.5 mm-radius) was provided by Element 6, Harwell, UK in the free-standing form, i.e. not attached to the growth substrate and polished to ~nm roughness on the growth (electrochemical measurement) face. An in-house procedure for glass sealing the pBDD macrodisk electrodes is described in detail elsewhere.[23,24] Before use, all working electrodes were polished with an aqueous alumina slurry (50 nm) on a soft microfiber polishing pad (MicroCloth, Buehler) and then subsequently on a clean wet microfiber pad, to produce clean reproducible electrode surfaces. Ag/AgCl (1 M KCl) and Pt wire served as the reference and counter electrodes, respectively. All experiments were carried out at 22 ± 1 ^{o}C.

5.4.3. FTACV Instrumentation

A CH Instruments 760E electrochemical workstation and a home-built (Monash) instrumentation[10] were used for the DC CV and FTACV measurements, respectively. All FTACV experiments were recorded using a sine wave perturbation of ΔE = 160.0 mV and f = 9.98 Hz. Experimentally, the signal-to-noise current ratio is reduced due to a 'ringing' artefact at the initial and final parts of the time domain signal which is particularly pronounced at higher AC harmonics. A larger ΔE value is used experimentally (160 mV) compared to the simulations (80 mV) to overcome this issue and provide access to 12 AC

harmonic components. The Fourier-transformed resolved higher order AC harmonic current components were quantitatively modelled using the MECSim software package (www.garethkennedy.net/MECSim).

5.5. Results and Discussion

5.5.1. DC CV and FTACV at Individual and Dual (Pt and pBDD) Electrodes

Heterogeneity in the oxidation of $FcCH_2OH$ was mimicked using a dual-electrode configuration comprising individual Pt (1 mm-diameter) and pBDD (1 mm-diameter) working electrodes which are electrically coupled but well-separated so that no overlapping of diffusion layers occurs. The ET kinetics for the $FcCH_2OH^{0/+}$ couple has been shown to be facile (reversible) at metallic electrodes ($k^0_{Pt} \geq 21.0$ cm s^{-1} [25] and $k^0_{Au} = 8 \pm 1$ cm s^{-1} [26]) while Fc derivatives such as ferrocenylmethyltrimethylammonium often display quasi-reversible behaviour at pBDD electrodes on the typical voltammetric measurement timescale, with k^0 being dependent on the local boron dopant concentration, [B], with $k^0_{BDD} \sim 0.04$ cm s^{-1} with [B] ~ 1.2×10^{21} atoms cm^{-3} and $k^0_{BDD} \sim 0.007$ cm s^{-1} with [B] ~ 1.5×10^{20} atoms cm^{-3}.[27]

Experimental DC CV measurements for the $FcCH_2OH^{0/+}$ process taken at the individual Pt and pBDD electrodes, as well as with the dual (Pt + pBDD) electrode configuration ($\theta_{Pt} = \theta_{pBDD} = 0.5$) are shown in Figure 5.4(a). The individual Pt and pBDD voltammograms differ slightly, predominately due to large differences in the double layer capacitance, C_{dl}, values ($C_{dl,Pt} = 80$ μF cm^{-2} and $C_{dl,pBDD} = 6$ μF cm^{-2}). Under the DC CV conditions employed, $FcCH_2OH$ oxidation is essentially reversible with $\Delta E_p = 61 \pm 1$ mV at $v = 0.1–1.0$ V s^{-1} at the Pt electrode (Section 5.7.2., Figure 5.12). In contrast, ΔE_p is 61 mV at a scan rate of 0.1 V s^{-1} and 79 mV at 10 V s^{-1} at the pBDD electrode (Section 5.7.2., Figure 5.13) indicating the process is quasi-reversible. The ΔE_p data from the Pt and pBDD voltammograms correspond to $k^0_{Pt} \geq 0.6$ cm s^{-1} and $k^0_{pBDD} = 0.13 \pm 0.02$ cm s^{-1} ($\alpha = 0.5$), respectively, when determined from the Nicholson method.[28,29] These k^0 values are also in accordance with FTACV measurements performed on the individual Pt and pBDD

electrodes which gave $k^0_{Pt} \geq 0.6$ cm s^{-1} (reversible) and $k^0_{pBDD} = 0.12$ cm s^{-1} (see Section 5.7.3., Figure 5.14 and Figure 5.15, respectively). As expected, the dual (Pt + pBDD) electrode response is equal to the sum of the responses at the individual electrodes (see black and purple lines, respectively, in Figure 5.4(a)). Note that these findings apply only to conditions of planar diffusion with negligible impact of resistance ($R_u \leq 100$ Ω)[6] for the experimental conditions considered herein.

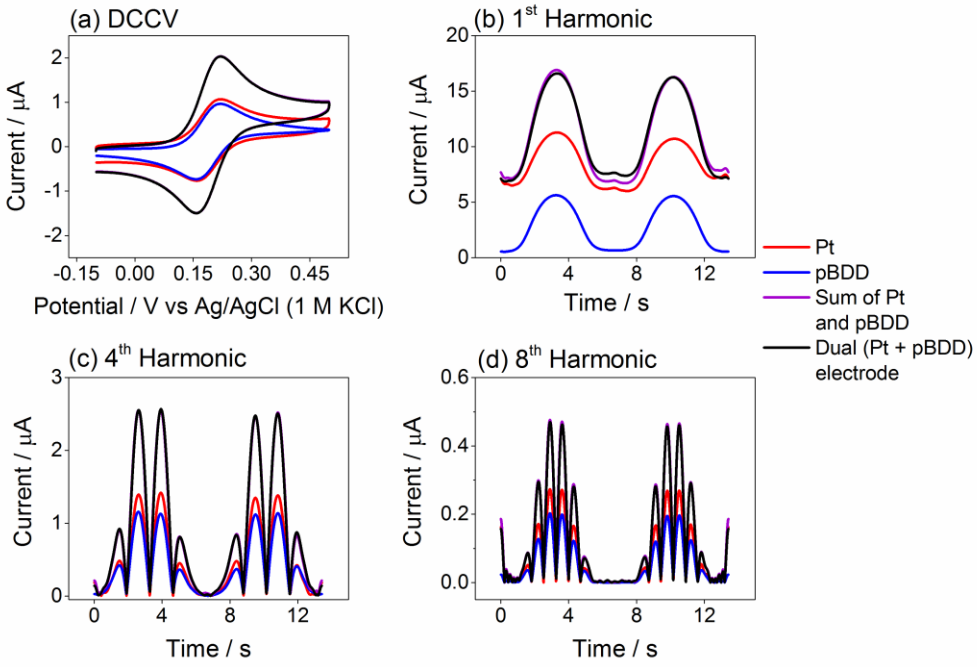

Figure 5.4 (a) DC CV, (b) 1st, (c) 4th and (d) 8th AC harmonic components for the oxidation of 0.50 mM $FcCH_2OH$ in 1 M KCl aqueous solution using individual Pt (red) and pBDD (blue) electrodes compared to a dual (Pt + pBDD) electrode configuration (black). The purple line represents the sum of the current responses from the individual Pt and pBDD electrodes. $v_{DC} = 0.1$ V s^{-1}, $v_{AC} = 0.089$ V s^{-1}, $\Delta E = 160.0$ mV and $f = 9.98$ Hz.

Figure 5.4(b), (c) and (d) show FTACV data obtained for the fundamental, 4th and 8th AC harmonic components for the $FcCH_2OH^{0/+}$ process using a sine wave perturbation of $\Delta E = 160.0$ mV and $f = 9.98$ Hz. Again, significant variation is evident in the Pt (much larger) and pBDD (much smaller) non-faradaic background regions of the fundamental component (Figure 5.4(b)). As in the DC CV data, this arises from the substantially different C_{dl} values of the electrode materials. In contrast, the 8th AC harmonic component (Figure 3(d)) is essentially devoid from background capacitance current and in this short

time domain, the magnitude of the central lobe regions are very sensitive to the electrode kinetics. On comparison of the 8th AC harmonic, it is obvious that the kinetics at the pBDD electrode are slower than at Pt. Again both Pt and pBDD current contributions additively equal the total current measured at the dual (Pt + pBDD) electrode for all AC harmonics, as in the DC CV case, as expected for planar diffusion conditions and negligible effect of R_u.

As established in the Theory Section, each AC harmonic component represents a different timescale measurement with the relative contributions of the individual currents to the total dual-electrode current being harmonic-dependent. This is evident in comparing the individual current responses at Pt and pBDD in the 4th and 8th AC harmonic in Figure 5.4(c) and (d), respectively, with their dual-electrode configuration response. This harmonic-dependent property of FTACV is exploited below to deconvolve a dual-heterogeneity response into its individual components using the protocol highlighted above (see Section 2.1).

5.5.2. Deconvolution of a Dual (Pt and pBDD) Electrode Response

FTACV data obtained with a dual (Pt + pBDD) electrode for the $FcCH_2OH^{0/+}$ process were analysed using the protocol described above to deconvolute the dual-electrode response into its individual electrode current components. In this example, the total area, A_{total}, of the dual-electrode configuration is known to be 0.0157 cm^2, c^0 = 0.50 mM and D_{FcCH_2OH} = 7.8 × 10^{-6} cm^2 s^{-1} and α_1 and α_2 are reasonably assumed to be 0.50. $k^0{}_1$ is assumed to be reversible ($\geq$ 0.6 cm s^{-1}, in this case). The 8th AC harmonic component of the experimental dual-electrode response is first analysed by a homogeneous model using A_1 as a variable to give the initial overestimated value of A_1 = 0.01399 cm^2 (versus the known values of 0.00785 cm^2) (**Step 1**) as shown in Figure 5.5(a). Next, the simulated data for the reversible process are subtracted from the experimental dual-electrode current-time data (**Step 2**, Figure 5.5(b)). In **Step 3**, the residual current is then subjected to FTACV procedures and the 4th AC harmonic is fitted to give the first underestimated value of $k^0{}_2$ = 0.055 cm s^{-1}

(versus the known value of 0.12 cm s^{-1}), using $A_2 = A_{total} - A_{1(estimation\ 1)}$, as shown in Figure 5.5(c). The current-time data for the simulated quasi-reversible process are then subtracted from the experimental dual-electrode data (**Step 4**, Figure 5.5(d)). The residual data are then subjected to FTACV procedures and Steps 1− 4 are repeated to give improved estimations of A_1, A_2 and k^0_2.

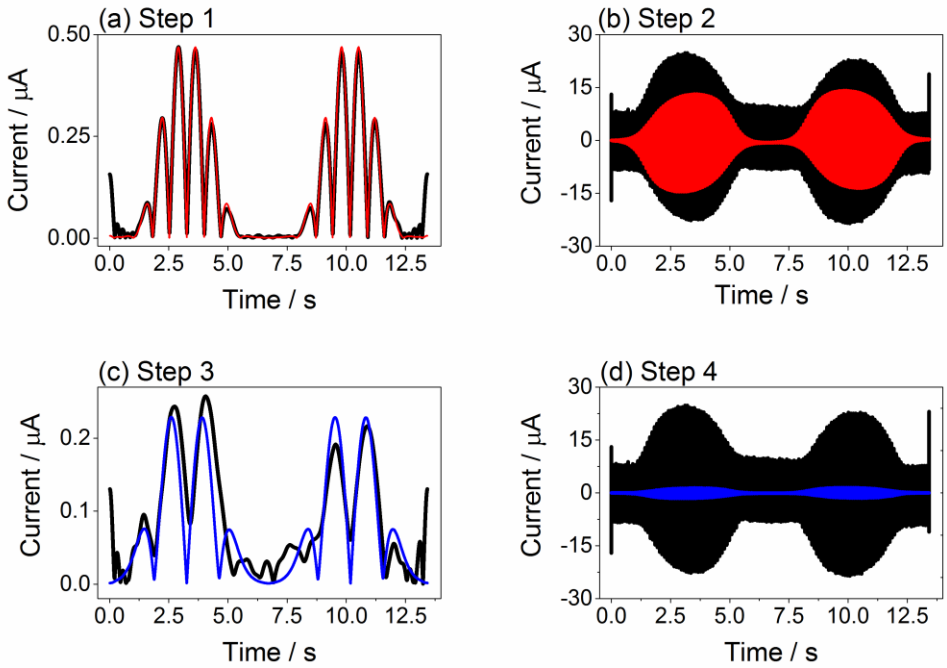

Figure 5.5 Steps 1−4 of the FTACV protocol applied to a dual (Pt + pBDD) electrode for the oxidation of 0.50 mM $FcCH_2OH$ in 1 M KCl aqueous solution. The red lines illustrate the first estimation of A_1 = 0.01399 cm^2. The blue lines illustrate the first estimation of A_2 = 0.0171 cm^2 and k^0_2 = 0.055 cm s^{-1}. Other simulation parameters: c^0 = 0.5 mM, D = 7.8 × 10^{-6} cm^2 s^{-1}, α = 0.50, T = 295.0 K, ν_{AC} = 0.089 V s^{-1}, ΔE = 160.0 mV and f = 9.98 Hz.

Table 5.2 provides a summary of the A_1, A_2 and k^0_2 values obtained from 15 iterations using the analysis protocol. The estimated values of A_1, A_2 and k^0_2 slowly converge towards the known values of 0.00785 cm^2, 0.00785 cm^2 and 0.12 cm s^{-1}, respectively. Note that the kinetic heterogeneities of the individual electrode[4] are neglected in the analysis procedure as a low frequency is chosen for the FTACV measurement to ensure uniform diffusion on the individual electrode surfaces.

Table 5.2 Summary of the FTACV protocol applied to a dual (Pt + pBDD) electrode configuration for the one-electron oxidation of 0.50 mM $FcCH_2OH$ in 1 M KCl electrolyte aqueous solution. Simulations parameter: T = 295.0 K, D_{FcCH_2OH} = 7.8 × 10^{-6} cm^2 s^{-1}, A_{total} = 0.0157 cm^2, $E^{0'}$ = 0.192 V, v_{AC} = 0.089 V s^{-1}, ΔE = 160.0 mV and f = 9.98 Hz. k^0_1 is set to mimic a reversible process (≥ 0.6 cm s^{-1}).

Iteration No.	A_1 / cm^2	A_2 / cm^2	k^0_2 / cm s^{-1}
1	0.0140	0.0017	0.055
2	0.0133	0.0024	0.060
3	0.0128	0.0029	0.065
4	0.0126	0.0031	0.072
5	0.0124	0.0033	0.080
6	0.0121	0.0036	0.087
7	0.0117	0.0040	0.096
8	0.0113	0.0044	0.105
9	0.0109	0.0048	0.109
10	0.0106	0.0051	0.111
11	0.0104	0.0053	0.114
12	0.0102	0.0055	0.116
13	0.0100	0.0057	0.117
14	0.0099	0.0058	0.118
15	0.0097	0.0060	0.119

5.6. Conclusions

FTACV is shown to be a valuable tool for probing heterogeneously active electrode surfaces. The advantages over DC methods are largely due to the much higher sensitivity of the FTACV current on electrode kinetics and access to a series of higher order harmonics. A protocol is developed and applied to the one-electron oxidation of $FcCH_2OH$ at a dual (Pt + pBDD) electrode system allowing the deconvolution and quantification of the response into its individual electrode contributions. The analysis procedure is applicable to dual heterogeneous electrode surfaces regardless of the domain size ratio when one of the processes is reversible, the other quasi-reversible and mass transport is appropriately described by 1D diffusion with overlap of diffusion layers being negligible. The probability of these conditions being met using a single heterogeneous carbon electrode, such as pBDD, will be greatly enhanced in highly viscous ionic liquid media

where the diffusion coefficients are of the order of ~10^{-8} cm^2 s^{-1} and will be considered in a future study.

5.7. Supporting Information

5.7.1. DC CV and FTACV Simulation Results

Figure 5.6 shows simulated DC CVs for an oxidation process at a homogeneously active electrode surface. It is observed that only DC CVs with an ET rate constant, $k^0 < 5.0 \times 10^{-2}$ cm s^{-1} can be distinguished from reversible at v = 0.1 V s^{-1} and give a separation of the oxidation and reduction peak potentials, ΔE_p, > 57 mV. As expected, diminishing values of k^0 result in diminished peak current, i_p, and increased ΔE_p values and slight changes in the voltammogram shape.

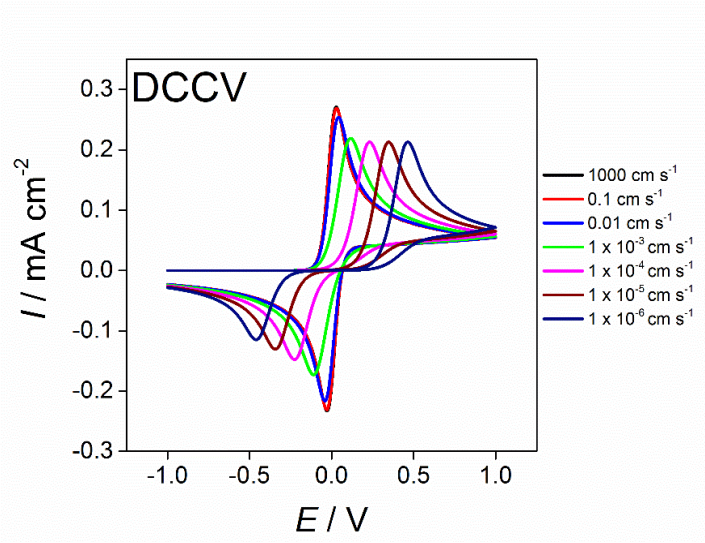

Figure 5.6 Simulations for the DC CV response for an oxidation process at a homogeneously active electrode surface having k^0 values in the range of 10^3–10^{-6} cm s^{-1}. Simulations parameters are: c^0 = 1.0 mM, D = 1.0 × 10^{-5} cm^2 s^{-1}, α = 0.50, T = 295.0 K, v_{DC} = 0.1 V s^{-1}.

Figure 5.7 shows a plot of ΔE_p versus scan rate, v, for an oxidation process at a homogeneously active electrode surface with k^0 = 6 cm s^{-1}. This demonstrates how high scan rates are required to achieve the same kinetic sensitivity with DC CV compared to the moderate scan rates needed using FTACV.

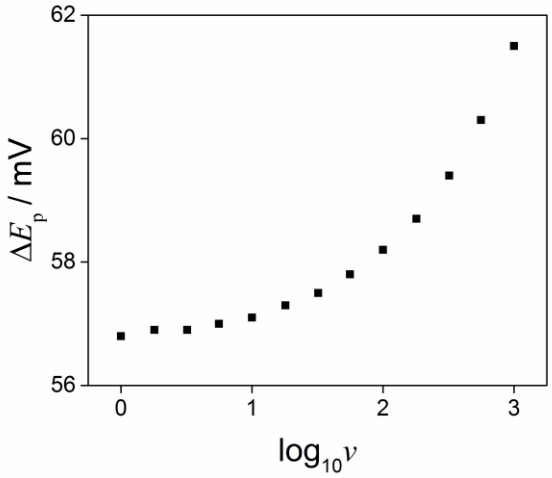

Figure 5.7 Plot of ΔE_p versus $\log_{10} v$ for an oxidation process at a homogenously active electrode having k^0 = 6 cm s^{-1}. Simulations parameters are c^0 = 1.0 mM, D = 1.0 × 10^{-5} cm^2 s^{-1}, α = 0.50 and T = 295.0 K.

Figure 5.8 shows the simulated fundamental, 3rd, 6th and 10th AC harmonic current components for an oxidation process at a homogeneously active electrode surface as a function of k^0 using FTACV. In FTACV and in contrast to DC CV, i_p magnitudes decay rapidly as k^0 values become progressively smaller. This phenomenon is harmonic-dependent as it is contingent on the timescale of the electrochemical measurement.

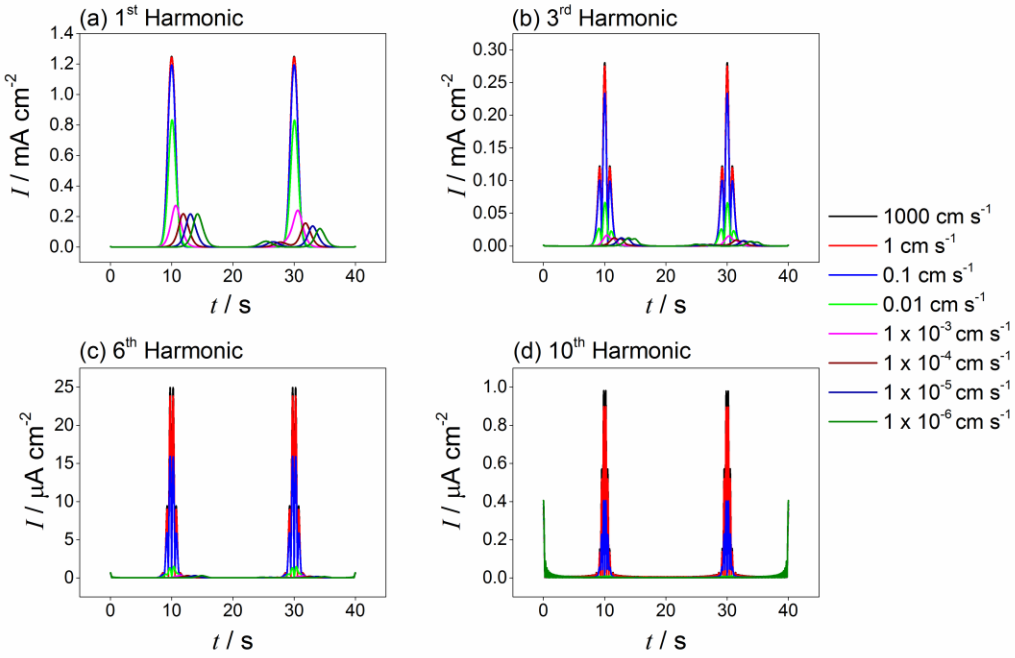

Figure 5.8 Simulations of the (a) 1st, (b) 3rd, (c) 6th and (d)10th AC harmonic components for an oxidation redox process at a homogeneous electrode surface having k^0 values in the range of 10^3–10^{-6} cm s^{-1}. Simulations parameters are: c^0 = 1.0 mM, D = 1.0 × 10^{-5} cm^2 s^{-1}, α = 0.50, T = 295.0 K, v_{AC} = 0.1 V s^{-1}, ΔE = 80.0 mV and f = 10.0 Hz.

Patterns of behaviour associated with the effect of uncompensated resistance, R_u, are far less informative with DC CV when compared to FTACV. Figure 5.9(a) shows the effect of R_u on the shape of a voltammograms with k^0 = 1000 cm s^{-1} (reversible) with v = 0.1 V s^{-1}. Clearly, the effects of slow ET kinetics and R_u distorts the DC CV response in a similar way, making it difficult to separate the influence of uncompensated resistance from kinetics[9] (see earlier, Figure 5.6). Figure 5.9(b) shows the effect of R_u on the shape of the 6th AC harmonic current component with k^0 = 1000 cm s^{-1}. It is observed that as the R_u value increase, the peak shapes start to change in a very characteristic way such that the effects of R_u and k^0 can be differentiated in FTACV. These features also exhibit harmonic-dependent sensitivity which allows for a 'unique' solution of the electrode mechanism[9].

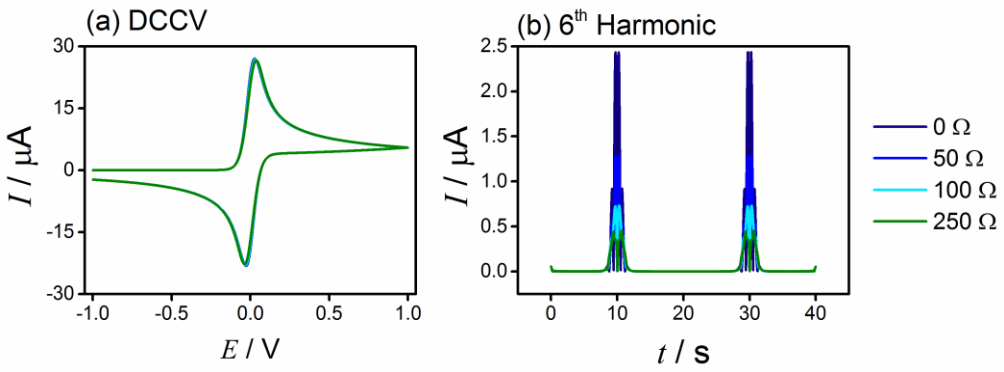

Figure 5.9 Simulations showing the effect of varying uncompensated resistance on the (a) DC CV and (b) 6th AC harmonic component response for an oxidation process at a homogenous electrode with k^0 = 1000 cm s^{-1} (reversible). Simulation parameters: c^0 = 1.0 mM, D = 1.0 × 10^{-5} cm^2 s^{-1}, A = 0.1 cm^2, α = 0.50, T = 295.0 K, v_{DC} = v_{AC} = 0.1 V s^{-1} and ΔE = 80.0 mV and f = 10.0 Hz.

Figure 5.10 shows the simulated $i_p/i_{p,rev}$ for an oxidation process as a function of ΔE (50 mV to 200 mV) for the fundamental, 4th, 6th and 12th AC harmonic. Typically, larger ΔE are employed to access higher order AC harmonic components with measurable current values. However, as observed here, increasing the ΔE values also results in a smaller kinetic sensitivity range and hence the value of ΔE used experimentally has to be carefully selected. For instance, within the example presented herein, the 12th AC harmonic currents are essentially zero at ΔE = 50 mV (Figure 5.10(d)) and hence cannot be used for any kinetic analysis. The i_p values are obtained from the central lobe of the odd AC harmonics and the average of the two central lobes of the even AC harmonic components.

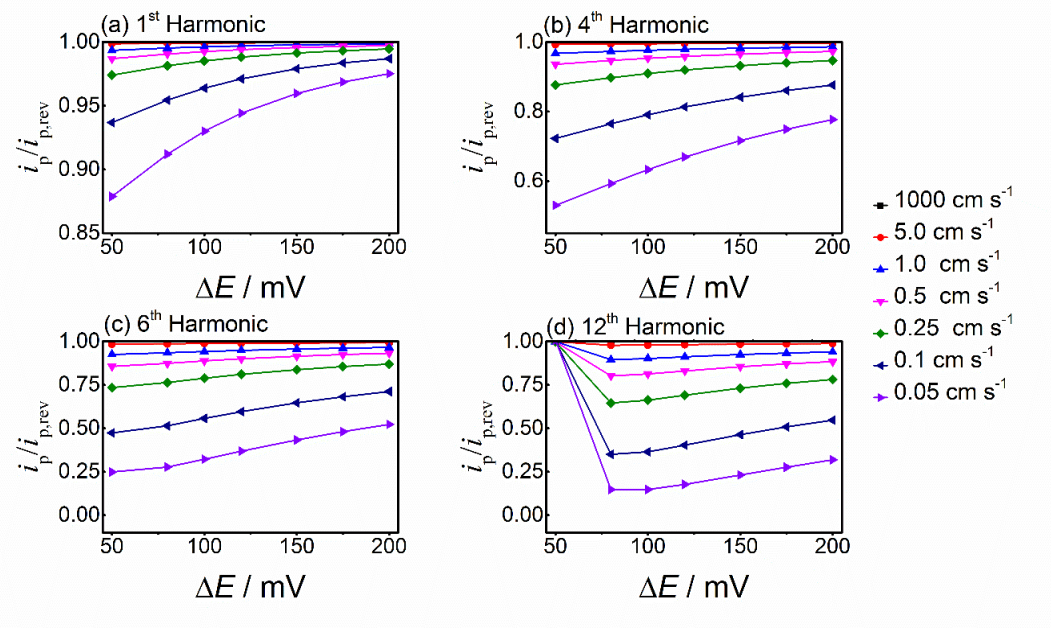

Figure 5.10 Simulations for the (a) 1st, (b) 4th, (c) 6th and (d) 12th AC harmonic component normalised peak current ($i_p/i_{p,rev}$) response for an oxidation redox process at a homogeneous electrode surface where ΔE is in the range of 50−200 mV. Other simulations parameters are: c^0 = 1.0 mM, D = 1.0 × 10^{-5} cm^2 s^{-1}, α = 0.50, T = 295.0 K, v_{AC} = 0.1 V s^{-1} and f = 10.0 Hz.

In order to determine the FTACV experimental conditions at which planar diffusion dominates the electrode response, i_p values derived from 1D simulations from MECSIM were compared to 2D simulations carried out in DigiElch digital simulation software (v. 7F, Elchsoft, Germany) for a range of electrode radii, a, (1 to 100 μm) and f (10 to 100 Hz) values as previously described[13]. The peak currents are reported as the percentage of the $i_{p,2D}$ that is due to planar diffusion contributions in Figure 5.11 for the fundamental, 6th and 10th AC harmonic component. The proportion of planar diffusion increases with the applied frequency and the higher order harmonics for a given electrode size.

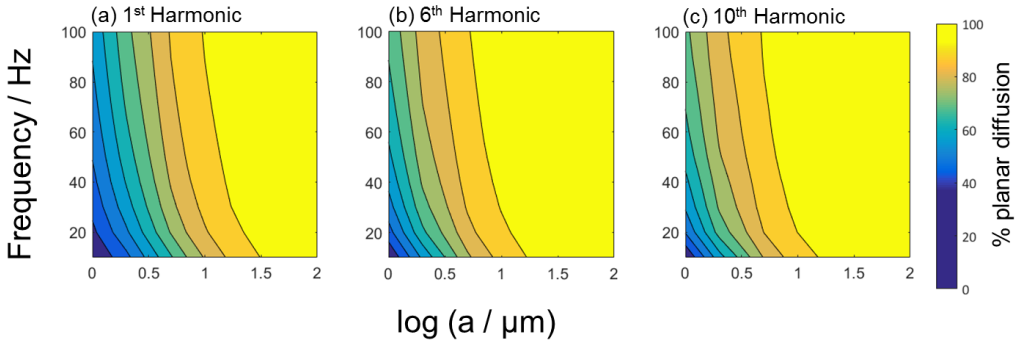

Figure 5.11 Simulated (a) 1st, (b) 6th and (c) 10th AC harmonic components showing how the currents deviate from a planar diffusion response as a function of electrode radii, *a*, for frequency, *f*, values in the range of 10−100 Hz. Other simulations parameters include: c^0 = 1.0 mM, D = 1.0 × 10^{-5} cm^2 s^{-1}, $E^{0'}$ = 0.0 V, α = 0.50, T = 295.0 K, v_{AC} = 0.1 V s^{-1} and ΔE = 80.0 mV.

5.7.2. DC CV at Individual Pt and pBDD Electrodes

The oxidation of $FcCH_2OH$ is considered in highly conducting 1 M KCl aqueous electrolyte. The DC CVs for the reversible $FcCH_2OH^{0/+}$ process at a Pt electrode are shown in Figure 5.12(a) for v_{DC} = 0.05−1.0 V s^{-1}. The mid-wave potential, E_m = 0.191 ± 0.002 V vs Ag/AgCl (1 M KCl) ~ $E^{0'}$. A linear relationship between i_p and $v^{1/2}$, is indicative of a diffusion-controlled process (Figure 5.12(b)). The reversibility of this process is confirmed by ΔE_p = 61 ± 1 mV (Figure 5.12(c)).

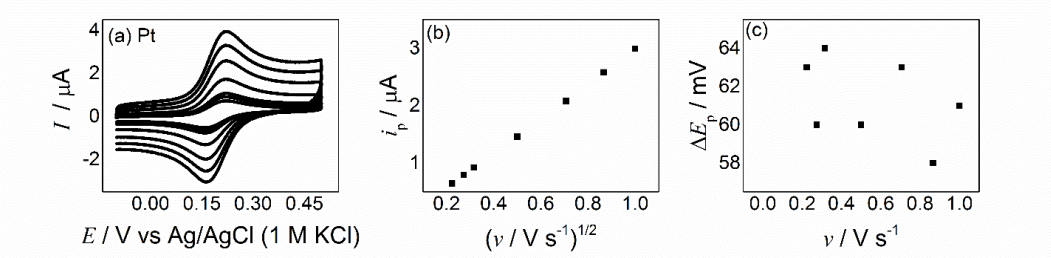

Figure 5.12 (a) DC CV for the oxidation of 0.5 mM $FcCH_2OH$ (1.0 M KCl aq.) at a Pt electrode (1 mm-diameter) with v_{DC} = 0.05, 0.075, 0.1, 0.25, 0.5, 0.75 and 1.0 V s^{-1}. (b) Plot of i_p versus $v^{1/2}$. (c) Plot of ΔE_p versus v.

DC CVs for the oxidation of $FcCH_2OH$ at a pBDD electrode are shown in Figure 5.13 (a). Quasi-reversible behaviour is observed as evident by ΔE_p values increasing from 61 mV to 79 mV at scan rates of 0.1 V s^{-1} and 10 V s^{-1}, respectively.

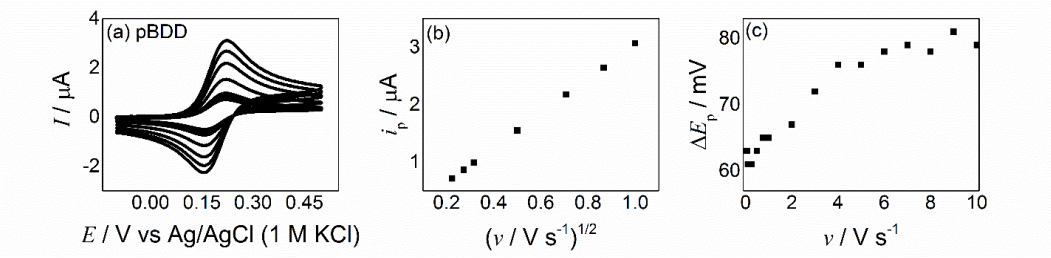

Figure 5.13 (a) DC CV for the oxidation of 0.5 mM $FcCH_2OH$ (1 M KCl aq.) at a pBDD electrode (1 mm-diameter) with v_{DC} = 0.05, 0.075, 0.1, 0.25, 0.5, 0.75 and 1.0 V s^{-1}. (b) Plot of i_p versus $v^{1/2}$. (c) Plot of ΔE_p versus v.

5.7.3. FTACV at Individual Pt and pBDD Electrodes

A sine wave perturbation of amplitude, ΔE = 160.0 mV and frequency, f = 9.98 Hz was applied. $E^{0'}$ = 0.192 V vs Ag/AgCl (1 M KCl) was determined from the potential of the minima and maxima of the central region of the even and odd harmonics, respectively. Excellent agreement between experimental data for the $FcCH_2OH^{0/+}$ redox process at the Pt electrode and simulated data for a reversible redox process on the FTACV timescale is shown in Figure 5.14. The upper kinetic limit of detection is defined in this study as the k^0 value for which the major peak current magnitude of the highest harmonic examined (12^{th} in this case) is 90 % of that predicted for the reversible process implies that $k^0_{Pt} \geq 0.6$ cm s^{-1}. A comparison of the experimental and simulated data for the quasi-reversible $FcCH_2OH^{0/+}$ process at pBDD is shown in Figure 5.15 and leads to k^0_{pBDD} = 0.12 cm s^{-1}. At this electrode surface, experimental current values are significantly smaller than those predicted for a reversible process, as demonstrated by the blue lines for the 8^{th} and 12^{th} AC harmonic components.

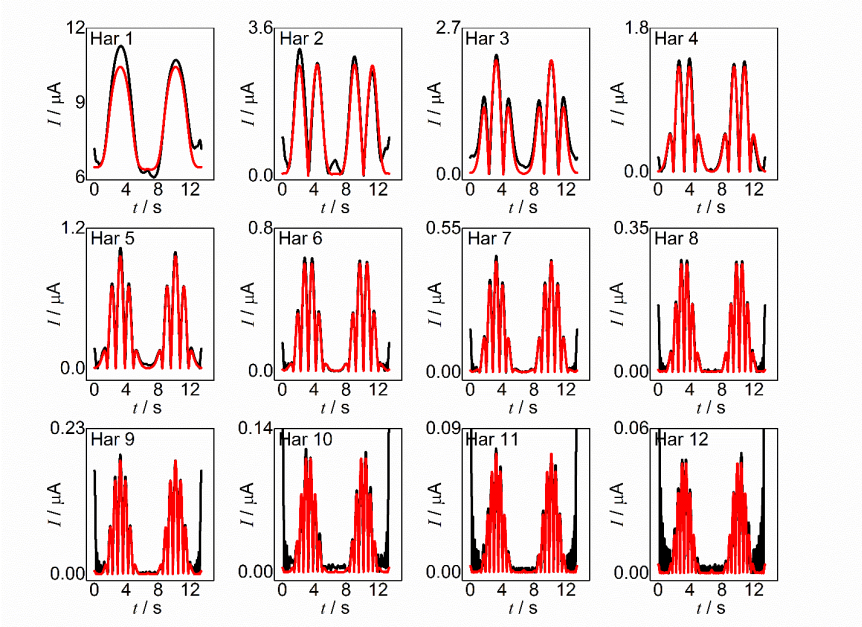

Figure 5.14 Comparison of experimental (black) and simulated (red) FTACV curves (1st to 12th AC harmonic) for the one-electron oxidation of 0.5 mM $FcCH_2OH$ (1 M KCl aq.) at a Pt macroelectrode (1 mm-diameter). Simulation parameters: k^0 = 1000 cm s^{-1} (reversible), α = 0.50, T = 295.0 K, f = 9.98 Hz, ΔE = 160.0 mV, v_{AC} = 0.09 cm s^{-1}, D = 7.8 × 10^{-6} cm^2 s^{-1}.

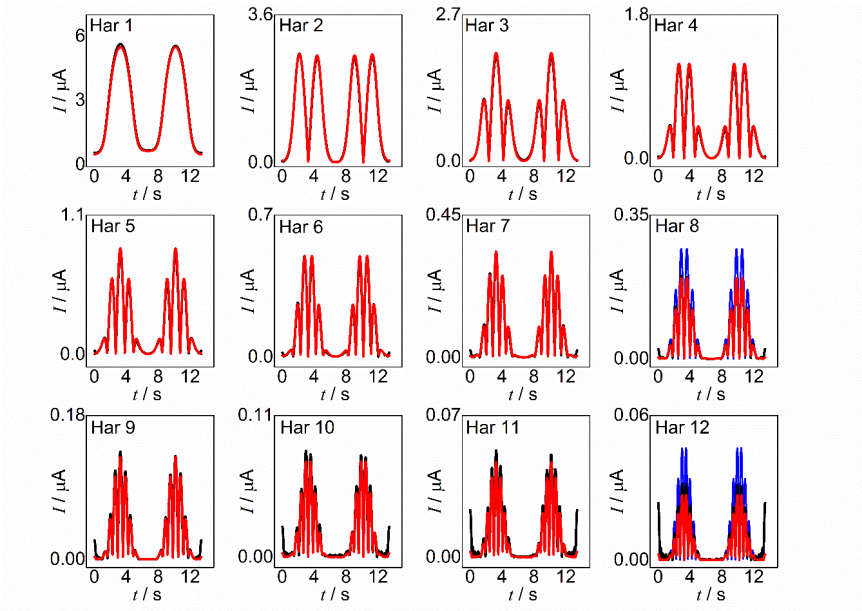

Figure 5.15 Comparison of experimental (black) and simulated (red) FTACV curves (1st to 12th AC harmonic) for the one-electron oxidation of 0.5 mM $FcCH_2OH$ (1 M KCl aq.) at a pBDD macroelectrode (1 mm-diameter). Simulation parameters: k^0 = 0.12 cm s^{-1} α = 0.50, T = 295.0 K, f = 9.98 Hz, ΔE = 160.0 mV, v_{AC} = 0.09 cm s^{-1}, D = 7.8 × 10^{-6} cm^2 s^{-1}. The blue lines show the simulated reversible (1000 cm s^{-1}) response for the 8th and 12th AC harmonic components.

5.7.4. Deconvolution of Simulated Dual-Electrode Responses

Table 5.3 provides a summary of the values of θ_1, θ_2 and k^0_2 determined using the analysis protocol described in the main text where a dual-electrode response comprising two ET processes one of which is reversible (k^0_1 =1000 cm s^{-1}) and the other quasi-reversible (k^0_2 = 0.1 cm s^{-1}) with respect to the AC timescale (f = 10.0 Hz and ΔE = 80.0 mV) is simulated with relative electrode areas of the two kinetic regions of θ_1 = 0.1 and θ_2 = 0.9, respectively.

Estimation	θ_1	θ_2	k^0_2 / cm s^{-1}
1	0.463	0.537	0.0670
2	0.337	0.663	0.0766
3	0.270	0.730	0.0825
4	0.227	0.773	0.0868
5	0.196	0.804	0.0900
6	0.173	0.827	0.0925
7	0.155	0.845	0.0943
8	0.141	0.859	0.0957
9	0.131	0.869	0.0968
10	0.124	0.876	0.0970

Table 5.4 provides a summary of the values of θ_1, θ_2 and k^0_2 determined using the analysis protocol described in the main text where a dual-electrode response comprising two ET processes one of which is reversible (k^0_1 = 1000 cm s^{-1}) and the other quasi-reversible (k^0_2 = 0.1 cm s^{-1}) with respect to the AC timescale (f = 10.0 Hz and ΔE = 80.0 mV) is simulated with relative electrode areas of the two kinetic regions of θ_1 = 0.9 and θ_2 = 0.1.

Estimation	θ_1	θ_2	k^0_2 / cm s^{-1}
1	0.930	0.070	0.0740
2	0.919	0.081	0.0830
3	0.913	0.087	0.0880
4	0.909	0.091	0.0910
5	0.907	0.093	0.0934
6	0.905	0.095	0.0952
7	0.904	0.096	0.0962
8	0.903	0.097	0.0971
9	0.902	0.098	0.0980
10	0.901	0.099	0.0990

5.8. References

(1) Amatore, C.; Savéant, J. M.; Tessier, D. *J. Electroanal. Chem. Interfacial Electrochem.* **1983**, *147* (1–2), 39–51.

(2) Davies, T. J.; Moore, R. R.; Banks, C. E.; Compton, R. G. *J. Electroanal. Chem.* **2004**, *574* (1), 123–152.

(3) Davies, T. J.; Banks, C. E.; Compton, R. G. *J. Solid State Electrochem.* **2005**, *9* (12), 797–808.

(4) Patten, H. V.; Meadows, K. E.; Hutton, L. A.; Iacobini, J. G.; Battistel, D.; McKelvey, K.; Colburn, A. W.; Newton, M. E.; Macpherson, J. V.; Unwin, P. R. *Angew. Chem. Int. Ed.* **2012**, *51* (28), 7002–7006.

(5) Güell, A. G.; Cuharuc, A. S.; Kim, Y.; Zhang, G.; Tan, S.-y.; Ebejer, N.; Unwin, P. R. *ACS Nano* **2015**, *9* (4), 3558–3571.

(6) Lee, C.-Y.; Guo, S.-X.; Bond, A. M.; Oldham, K. B. *J. Electroanal. Chem.* **2008**, *615* (1), 1–11.

(7) Lazenby, R. A.; Kelvey, K.; Unwin, P. R. *Anal. Chem.* **2013**, *85* (5), 2937–2944.

(8) Zhang, J.; Guo, S.-X.; Bond, A. M.; Marken, F. *Anal. Chem.* **2004**, *76* (13), 3619–3629.

(9) Sher, A. A.; Bond, A. M.; Gavaghan, D. J.; Harriman, K.; Feldberg, S. W.; Duffy, N. W.; Guo, S.-X.; Zhang, J. *Anal. Chem.* **2004**, *76* (21), 6214–6228.

(10) Bond, A. M.; Duffy, N. W.; Guo, S.-X.; Zhang, J.; Elton, D. *Anal. Chem.* **2005**, *77* (9), 186–195.

(11) Zhang, J.; Guo, S.-X.; Bond, A. M. *Anal. Chem.* **2007**, *79* (6), 2276–2288.

(12) Mashkina, E. A.; Simonov, A. N.; Bond, A. M. *J. Electroanal. Chem.* **2014**, *732*, 86–92.

(13) Tan, S.-y.; Unwin, P. R.; Macpherson, J. V.; Zhang, J.; Bond, A. M. *Anal. Chem.* **2017**, *89* (5), 2830–2837.

(14) Dickinson, E. J. F.; Streeter, I.; Compton, R. G. *J. Phys. Chem. C* **2008**, *112* (31), 11637–11644.

(15) Dickinson, E. J. F.; Streeter, I.; Compton, R. G. *J. Phys. Chem. B* **2008**, *112* (13), 4059–4066.

(16) Davies, T. J.; Compton, R. G. *J. Electroanal. Chem.* **2005**, *585*, 63–82.

(17) Guo, S.; Bond, A. M.; Zhang, J. *Rev. Polarogr.* **2015**, *61* (1), 21–32.

(18) Li, J.; Bentley, C. L.; Bond, A. M.; Zhang, J. *Anal. Chem.* **2016**, *88* (4), 2367–2374.

(19) Engblom, S. O.; Myland, J. C.; Oldham, K. B. *J. Electroanal. Chem.* **2000**, *480* (1–2), 120–

132.

(20) Gavaghan, D. J.; Bond, A. M. *J. Electroanal. Chem.* **2000**, *480* (1–2), 133–149.

(21) Gavaghan, D. J.; Elton, D.; Oldham, K. B.; Bond, A. M. *J. Electroanal. Chem.* **2001**, *512* (1–2), 1–15.

(22) Bano, K.; Zhang, J.; Bond, A. M. *J. Phys. Chem. C* **2014**, *118* (18), 9560–9569.

(23) Hutton, L.; Newton, M. E.; Unwin, P. R.; Macpherson, J. V. *Anal. Chem.* **2009**, *81* (3), 1023–1032.

(24) Hutton, L. A.; Iacobini, J. G.; Bitziou, E.; Channon, R. B.; Newton, M. E.; Macpherson, J. V. *Anal. Chem.* **2013**, *85* (15), 7230–7240.

(25) Yu, Y.; Sun, T.; Mirkin, M. V. *Anal. Chem.* **2016**, *88* (23), 11758–11766.

(26) Velmurugan, J.; Sun, P.; Mirkin, M. V. *J. Phys. Chem. C* **2009**, *113* (1), 459–464.

(27) Tomlinson, L. I.; Patten, H. V.; Green, B. L.; Iacobini, J.; Meadows, K. E.; McKelvey, K.; Unwin, P. R.; Newton, M. E.; Macpherson, J. V. *Electroanalysis* **2016**, 1–7.

(28) Nicholson, R. S. *Anal. Chem.* **1965**, *37* (11), 1351–1355.

(29) Zhang, G.; Cuharuc, A. S.; Güell, A. G.; Unwin, P. R. *Phys. Chem. Chem. Phys.* **2015**, *17*, 11827–11838.

Chapter 6

Conclusions and Future Work

This thesis has presented developments in strategies and methodologies for analysing advanced electrochemical processes using Fourier-transformed large amplitude alternating current voltammetry (FTACV) and scanning electrochemical microscopy (SECM)-voltammetry, with the objective to achieve detailed quantification of fast outer-sphere electron transfer kinetics at conventional (e.g. platinum or gold) and carbon (e.g. highly oriented pyrolytic graphite (HOPG) or polycrystalline boron-doped diamond (pBDD)) electrode materials.

Chapter 2 provides a comparison between the standard electron rate constants, k^0, determined from macroscopic FTACV and microscopic SECM measurements for the simple oxidation of tetrathiafulvalene (TTF) and tetracyanoquinodimethane (TCNQ). At three conventional electrode materials: Pt, Au and glassy carbon, all measurements found k^0 to be fast and close to the upper limit of detection for both electrochemical techniques. However, at the semi-metallic pBDD electrodes, both redox couples are found to be kinetically-limited due to the lower number of available charge carriers. Key differences in the techniques emerged, with FTACV measurements providing the overall kinetic values of the entire electrode while SECM allows highly localised measurements which provides

kinetic information of the region of the pBDD electrode under the UME tip. For the TTF oxidation process, two regions of distinct kinetic activity were observed using SECM, relating to regions of high and low dopant densities of pBDD. These values are in good agreement with the overall kinetic activity determined by FTACV. Interestingly, highly distorted SECM voltammograms were observed for the TCNQ reduction process, diagnostic of increasing limitations from the electrode material as the potential was scanned in the negative direction, consistent with the degenerate p-doping of pBDD. This phenomenon was attributed to the high local current density of SECM that imposes a significant challenge on charge flow through the pBDD material and was not observed with FTACV which passes a significantly lower current density (by ca. 2 orders of magnitude) during the voltammetric measurement. This study thus identifies important differences between studies of electron transfer at metallic and semi-metallic electrode materials as revealed by simple redox couples. Further understanding of the electronic structure and charge carrier mobility near the surface of pBDD could be achieved by studies with additional redox couples as well as varying boron dopant concentrations.

Numerous attempts have been made to measure the kinetics of rapid heterogeneous electron transfer reactions by a wide range of electrochemical techniques and this remains an extremely challenging area of research for electrochemists. This is because the heterogenous electron transfer rate constant can only be measured if it is smaller or comparable to the mass-transfer coefficient of the electrochemical technique employed. This has spearheaded the development of various nanostructured and nanogap systems. An intrinsic property of nanogap electrochemical cells in the high surface area-to-solution volume ratio. In this situation, precise knowledge of the physicochemical characteristics of the electrochemical system is imperative. For instance, surface effects such as weak adsorption of redox-active species may have profound impact on the voltammetric response. Chapter 3 considers the effect of adsorption on SECM voltammetric measurements. A holistic numerical simulation model for SECM has been developed that carefully considers the unequal diffusivities of $FcTMA^+$ and $FcTMA^{2+}$, and the adsorption of the reactant, $FcTMA^+$, onto the HOPG substrate. The adsorption of highly-charged $FcTMA^{2+}$ species onto the insulating glass sheath that encapsulates the UME was also considered along with direct electron transfer between $FcTMA^+$ in solution and glass-

bound $FcTMA^{2+}$, which significantly affects the magnitude of limiting-current measured. The implications of these surface effects on the interpretation of the apparent electron transfer rate constants are considered and may lead to the incorrect kinetic and thermodynamic assignments. Another surface effect, the electrical double layer (EDL), is not considered in this work but could have serious consequences on voltammetric measurements in these nanogap systems. Recently, White et. al.[1] showed that limiting-currents can be strongly affected by the EDL at cell thickness ≤ 100 nm even for typical supporting electrolyte concentrations (200 mM) where the EDL is usually assumed to have negligible effect on mass transport.

Partial blocking or spatial heterogeneities of electrode materials can result in non-linear diffusion effects when the average size of the active sites and the average distance between them are small compared to the total diffusion layer. Advances in material science has fuelled the emergence of the field of carbon electrochemistry which inevitably provide electrochemically heterogeneous electrode surfaces. Chapter 4 and 5 focuses on the development of FTACV data analysis strategies for the deconvolution of current responses complicated by kinetics heterogeneities. In an initial model study (Chapter 4) using a dual-electrode system comprising a GC and pBDD electrode, the total response from the $[Ru(NH_3)_6]^{3+/2+}$ redox process was successfully deconvolved into its individual electrode contributions. Although this represented a highly-simplified example, a general principle was established for solving this problem. Chapter 5 focuses on further developing FTACV as a tool for kinetic selectivity at heterogeneously active electrodes. This is achieved by taking advantage of the harmonic-dependent measurement timescale of FTACV to deconvolute a dual-heterogeneity electrochemical response into its individual components by implementing an iterative protocol procedure. This is successfully applied to the one-electron oxidation of $FcCH_2OH$ at a dual (Pt + pBDD) electrode system. The analysis procedure is applicable to dual heterogeneous electrode surfaces regardless of the domain size ratio when one of the processes is reversible, while the other is quasi-reversible and mass transport is appropriately described by 1D diffusion with overlap of diffusion layers being negligible. The probability of these conditions being met using a single heterogeneous carbon electrode, such as pBDD, will be markedly enhanced in highly

viscous ionic liquid media where the diffusion coefficients are of the order of ~10^{-8} cm^2 s^{-1}.

In summary, this thesis reports on the positive strides made in the development of SECM and FTACV as powerful tools for the measurement of fast electron transfer kinetics. The importance of understanding the influence of measurement technique and the electrode material electronic structure in fundamental electrochemical studies is emphasised (Chapter 2). Throughout this work, the significance of numerical simulations to predict and quantify electrochemical responses is highlighted particularly when complications from surface effects exist, such as reactant adsorption (Chapter 3) and electrode surface electrochemical heterogeneities (Chapter 4 and 5).

(1) Xiong, J.; Chen, Q.; Edwards, M. A.; White, H. S. *ACS Nano* **2015**, *9*, 8520–8529.